

Université catholique de Louvain

Faculté des Sciences Appliquées

Département des Sciences
des Matériaux et des Procédés

Unité PCPM

Thin film acoustic waveguides and resonators for gravimetric sensing applications in liquid

Membres du Jury :
Prof. Patrick Bertrand,
promoteur
Prof. Jean-Didier Legat,
président
Prof. Denis Flandre
Prof. Chris Van Hoof
Prof. Sylvain Ballandras
Dr. Andrew Campitelli

Dissertation présentée
en vue de l'obtention
du grade de Docteur en
Sciences Appliquées

par
Laurent A. Francis



en collaboration avec
IMEC vzw

Interuniversitair
Micro-Electronika
Centrum vzw
Kapeldreef 75
B-3001 Leuven

Février 2006

Science sans conscience n'est que ruine de l'âme.
François Rabelais

Il faut rire avant que d'être heureux,
de peur de mourir sans avoir ri.
Jean de la Bruyère

In Memoriam
à ma petite Bonne-Maman,
tante Liliane et oncle Robert.

Summary

The fields of health care and environment control have an ever increasing demand for sensors able to detect low concentrations of particles like (bio)molecular agents, warfare agents, and pathogen cells or solid particles contained in gaseous or liquid samples. The recent introduction of microfabricated devices in these fields gave rise to new sensors with attractive properties: rapid response, reliability, portability, ease of use, size and cost reductions. A cutting edge technology for the development of such sensors is based on guided acoustic waves, e.g. the harmonic propagation of an elastic deformation in a waveguide structure at ultrasonic frequencies extending between some MHz to a few GHz. A variation in the propagation of the acoustic signal is induced when the waveguide boundary is perturbed by an event occurring at the nanometer scale. Typical application examples are: recognition of antibodies by specific antigens, adsorption of proteins on chemically tailored surfaces, metal electrodeposition and study of polymers swelling.
In this thesis, we investigate acoustic waveguides fabricated with thin film technology for the sensing of a mass deposited from a sustaining liquid. A first part is dedicated to the Love mode structure, in which the film is coating a piezoelectric substrate, and a second part is dedicated to nanocrystalline diamond thin film membrane devices for the fabrication of higher sensitivities Lamb mode and thin Film Bulk Acoustic Resonator (FBAR) structures. The sensitivity of the Love mode device was analyzed with an equivalent transmission line model generalized to isotropic and viscoelastic layers. A variational model was developed to correlate shifts of amplitude and phase of the electrical signal as the mechanical characteristics of the sensed media are varying. During a biorecognition experiment, signal variations are attributed to the adsorption of a composite layer of viscous nature. The Love mode biosensor is seen as a sensitive rheometer where the density, the viscosity and the thickness of the adlayer influence the acoustic signal. The ratio of amplitude shift to phase shift is representative of the rigid or viscous nature of the interaction between the probing acoustic field and the probed layers. For a better determination of the surface composition, a novel integrated combination of the surface acoustic wave with an optical biosensor (i.e. surface plasmon resonance) is presented. Methodologies are explained to provide quantitative details about physisorbed proteins and about the

conformational transition of poly(N-isopropyl acrylamide) (PNIPAAm) upon thermal cycling. This method resolves independently the thickness, with a nanometer resolution, the density and the viscosity of the film, with the main consequence to provide an evaluation of the solvent content diluted in the film.
We developed mathematical expressions of the influence of interferences between the acoustic signal and electromagnetic waves generated by the transducers for the open and the closed loop configurations of the Love mode device. The interferences modify locally the value of phase shifts and, under specific circumstances, enhance the sensitivity of the open loop configuration. The location of interference peaks can be used to determine the phase velocity in the sensing area even when the interferences are strongly attenuating the acoustic signal.
The thin films guiding the acoustic energy in the Love mode structure play a major role on the dispersion characteristics of device and on the sensitivity. Three thin film materials were investigated: silicon dioxide deposited by plasma-enhanced chemical vapor deposition in a hydrogen-rich atmosphere, zinc oxide deposited by spray pyrolysis, and plasma-enhanced chemical vapor deposited silicon germanium. Still for the actual fabrication of Love mode devices, we tackled the issue of packaging with a method based on the protection of the transducers from the surrounding liquids by SU-8 walls terminated with a glass capping.
In the second part, nanocrystalline diamond as an emerging material with properties close to single-crystal diamond was investigated under the form of thin film membranes suspended to a rigid silicon frame. The unique properties of NCD (high mechanical and chemical resistance) open ways to membrane based sensors such as Flexural Plate Wave and thin Film Bulk Acoustic Resonators (FBAR). A dynamic characterization of the mechanical properties of the film and of its residual stress is presented based on the non-destructive stroboscopic analysis of deformation shapes of membranes with different lateral dimensions and placed in vibration on the first resonance modes. The results of this method are used to estimate the potential advantages of a diamond-based flexural plate wave biosensors. Finally, the properties of composite FBAR devices including a supporting thin film membrane and a piezoelectric layer, which is required for the actuation of longitudinal acoustic resonance modes, are assessed using the perturbation theory and applied to the first prototype of an actual diamond-based composite FBAR.

Acknowledgments

This thesis work could not have existed without the precious help of the following people I acknowledge: Carmen Bartic for the SU8 walls, René Ferro for the spray pyrolysis setup, Alexander Kromka for the diamond films, Jos van Mol and Claude Poleunis for the support with the RBS, Randy de Palma for the idea with the gold etching and the calibration with S-layers, Merlijn van Spengen for the storoboscopic measurements, Wanling Pan for the GHz measurements, and Cheng Zhou for the idea of the calibration with CTAB. A special thank to Jean-Michel Friedt and to Doris Steinmüller for an incredible amount of help and many fruitful discussions. I thank also Patrick Bertrand and Andrew Campitelli for their support to my research, and Jean-Didier Legat, Denis Flandre, Chris Van Hoof and Sylvain Ballandras for their participation in the evaluation Jury of this thesis.
I would like to acknowledge the F.R.I.A. (Fonds pour la Formation à la Recherche dans l'Industrie et dans l'Agriculture) for the financial support and to the Jury members who evaluated my PhD proposal for their confidence in my research. More specifically, and with respect to this grant, Hervé Buyse, Xavier Gonze, Eugène Bosmans and Joël Demarteau played a role for the granting and the renewal of the fellowship.
This thesis would be different without some inputs and improvements due to my colleagues and friends of IMEC, in particular many thanks to Harrie Tilmans, Gerard Klaasse, Tom Sterken, Phillip Ekkels, Marc Fouchier, Maria Gromova and the *Polish* team of the reliability group. My rewards for their dynamism and optimism to Sheron Shamuilia and Caroline Geuens, who – I hope – learned something in acoustics during their master studies while helping me in my own work. I am also due to Sébastien Michotte and Cédric Gustin to have provided me with useful LaTeX hints to write this text, I appreciated their friendship as well.
Thanks a lot to my friends for their psychological and philosophical support along those years and to have kept me with enough fun, especially Sébastien, Serge, Frédéric, Jean-Philippe, Julien, Cédric, and Vincent; I wish them the best success in their own enterprises.
Last, but not least, I dedicate this work to my parents, Maurice and Marie-Thérèse, as a fruit of their daily support, their trust and their *Love* for me during the last 27 years and for the many upcoming years.

List of symbols and abbreviations

Symbol

α	normalized thickness
α	acoustic signal amplitude
α	electromagnetic-acoustic waves interaction amplitude
α	material constant
a	inter-atomic distance
B	electrical susceptance
β_{ij}	structural factor
C	equivalent mechanical capacitance
C_{EM}	electromagnetic parasitic capacitance
c	speed of light
$\mathbf{c}$	elastic stiffness matrix
$\mathbf{c}^E$	elastic stiffness matrix at constant electric field
ΔA	electric signal attenuation per unit of length
$\Delta\phi$	electric signal delay phase shift per unit of length
δ	penetration depth
$\vec{D}$	electric displacement
D	sensing area length
D	plate flexural rigidity
d	corrugation depth
d	membrane center deflection
ε^S	electric permittivity matrix at constant mechanical strain
ε_d	dielectric constant of a dielectric
ε_m	dielectric function of a metal
E	Young's modulus
$\vec{E}$	electric field
$\mathbf{e}$	piezoelectric strain matrix
φ	complex coupling angle
F	constant of Faraday
f	wave frequency
f_c	wave cut-off frequency
$\mathbf{\Gamma}$	Christoffel matrix
$\overline{\mathbf{\Gamma}}$	stiffened Christoffel matrix
γ	equivalent transmission line propagation function

Symbol

G	electrical conductance
G	equivalent mechanical conductance
η	dynamic viscosity
H	delay line transfer function
h	composite layer thickness
I	electrical current
i	imaginary number $\sqrt{-1}$ (mathematical notation)
j	imaginary number $\sqrt{-1}$ (electrical notation)
K	atomic bounds rigidity constant
K_e^2	effective electromechanical coupling coefficient
$\vec{k}$	wavevector
k	wavenumber
k_x	propagation wavenumber
k_P	surface plasmon polariton wavenumber
k_z	resonance wavenumber
k^2	electromechanical coupling coefficient
λ	wavelength
λ	Lamé constant
L	equivalent mechanical inductance
L	transmission line length
L	interdigital transducers midpoints distance
$\vec{l}$	direction of propagation
μ	shear Lamé constant
M	atom mass
M	molar weight
$\mathbf{M}$	structural factor matrix
m	surface mass
m_e	mass of the electron
ν	Poisson's ratio
N_α	electric signal amplitude noise
N_ϕ	electric signal phase noise
n	electromagnetic interference mode number
n	refractive index
$\mathbf{n_e}$	number of electrons in an electrochemical reaction
Φ	electric potential
Q	quality factor

Symbol

θ	SPR dip angle
θ_C	critical angle
ρ	material density
ρ	conduction electron number density
$\vec{r}$	spatial coordinate
R_f	relative frequency
R_S	relative mass sensitivity
σ	rigid mass surface density
σ	bi-axial residual stress
$\mathbf{S}$	strain field
$\mathbf{S}$	intrinsic sensitivity matrix
S	gravimetric sensitivity
S^f	frequency gravimetric sensitivity
S_C	mass sensitivity of an FBAR
$S_{C,P}$	mass sensitivity of the piezoelectric side of an FBAR
$S_{C,LL}$	mass sensitivity of the loading layer side of an FBAR
S_P	mass sensitivity of a single layer FBAR
S_V	velocity sensitivity
$S_{\alpha,\rho\eta}$	signal amplitude to mass viscosity sensitivity
$S_{\alpha,\sigma}$	signal amplitude to mass density sensitivity
S_ϕ	phase sensitivity
$S_{\phi,\rho\eta}$	signal phase to mass viscosity sensitivity
$S_{\phi,\sigma}$	signal phase to mass density sensitivity
$S_{\rho\eta,\alpha}$	mass viscosity to signal amplitude sensitivity
$S_{\rho\eta,\phi}$	mass viscosity to signal phase sensitivity
$S_{\sigma,\alpha}$	mass density to signal amplitude sensitivity
$S_{\sigma,\phi}$	mass density to signal phase gravimetric sensitivity
S_ω	frequency sensitivity
s	spacing between corrugation
τ	delay line transit time
τ_g	delay line time of flight
T	temperature
$\mathbf{T}$	stress field
t	film thickness
t	time

Symbol

U_v	total energy stored in an acoustic resonator
$\vec{u}$	displacement field
V	wave phase velocity
V_g	wave group velocity
V_l	longitudinal wave phase velocity
V_s	shear wave phase velocity
v	shear wave particle velocity
ω	angular frequency
W	interdigital transducer width
w	corrugation width
Y	mechanical transmission line admittance
Y	electrical admittance
Z	mechanical transmission line impedance
Z	mechanical transmission line characteristic impedance
Z_c	mechanical transmission line characteristic impedance

Abbreviation

AFM	Atomic Force Microscope
APM	Acoustic Plate Mode
BAW	Bulk Acoustic Waves
BCB	BenzoCycloButene
BG	Bleustein-Guylaev
CCD	Charge-Coupled Device
DRIE	Deep Reactive Ion Etching
EM	ElectroMagnetic
FBAR	Film Bulk Acoustic Resonator
FPW	Flexural Plate Waves
IDT	InterDigital Transducer
LCST	Lower Critical Solution Temperature
NCD	NanoCrystalline Diamond
PDMS	Poly-DiMethylSiloxane
PECVD	Plasma-Enhanced Chemical Vapor Deposition
PGMEA	Propylene Glycol Monomethyl Ether Acetate
PMMA	Poly-MethylMethAcrylate
PNIPAAm	Poly-(N-IsoPropyl AcrylAmide)
PSAW	Pseudo Surface Acoustic Waves
RBS	Rutherford Back-Scattering
RUS	Resonant Ultrasound Spectroscopy
SAW	Surface Acoustic Waves
SEM	Scanning Electron Microscope
SGAW	Surface Generated Acoustic Waves
SGBW	Sensitivity Gain BandWidth
SH	Shear-Horizontal
SMR	Solidly Mounted Resonator
SPD	Spray Pyrolysis Deposition
SPR	Surface Plasmon Resonance
SSBW	Surface Skimming Bulk Waves
TSM	Thickness Shear Mode
XPS	X-ray Photoelectron Spectroscopy

Table of Contents

Page

Table of Contents **xv**

1 General introduction **1**
1.1 Biosensors . . . 1
1.2 Acoustic biosensors . . . 4
1.3 Acoustic waveguides and resonators . . . 8
1.3.1 Quartz crystal microbalance . . . 8
1.3.2 Rayleigh mode . . . 10
1.3.3 Shear-horizontal waves and Love modes . . . 11
1.3.4 Lamb mode and flexural plate waves . . . 12
1.3.5 Thin film bulk acoustic resonator . . . 14
1.3.6 Performances comparison . . . 17
1.4 The biochemical interface . . . 17
1.5 Objectives and organization of this thesis . . . 19

I Love Mode Surface Acoustic Wave Biosensors **21**

2 Sensitivity of the Love mode SAW biosensor **23**
2.1 Introduction . . . 23
2.2 Modeling . . . 26
2.2.1 State of the art . . . 26
2.2.2 Acoustic transmission lines model . . . 28
2.3 Sensitivity . . . 35
2.3.1 State of the art . . . 35
2.3.2 Electrical signal . . . 41
2.3.3 Variational model of the sensitivity . . . 42
2.3.4 Determination of the sensitivities . . . 45

2.3.5 Discrimination between rigid and viscous interactions . . . 45
2.3.6 Penetration depth and film thickness . . . 49
2.3.7 Detection levels and influence of the noise . . . 54
2.4 Conclusion . . . 58
2.5 Additional resources . . . 58

3 Fabrication, packaging and calibration of SAW biosensors 59
3.1 Love mode SAW device fabrication . . . 61
3.1.1 Basic structure of the sensor . . . 61
3.1.2 Hydrogenated PECVD silicon dioxide . . . 62
3.1.3 Spray pyrolysis deposition of zinc oxide . . . 63
3.1.4 PECVD amorphous silicon germanium . . . 69
3.2 Liquid cell design . . . 73
3.2.1 The packaging issue of SAW biosensors . . . 73
3.2.2 Liquid cell fabrication . . . 77
3.2.3 Performances of the packaging . . . 81
3.3 Experimental calibration techniques . . . 86
3.3.1 Experimental measurement of the dispersion curve 86
3.3.2 Modification of the surface density . . . 87
3.3.3 Viscosity calibration . . . 96
3.4 Conclusion . . . 97

4 Effect of interferences on the sensitivity 101
4.1 Introduction . . . 102
4.2 Modeling . . . 103
4.3 Electromagnetic interferences . . . 105
4.4 Sensitivity . . . 108
4.4.1 Definitions of the sensitivity . . . 108
4.4.2 Phase differentials without interferences . . . 109
4.4.3 Open loop configuration . . . 110
4.4.4 Closed loop configuration . . . 111
4.5 Experimental results . . . 114
4.5.1 Sensor fabrication and instrumentation . . . 114
4.5.2 Correlation of the results with the model . . . 116
4.6 Discussion . . . 121
4.6.1 Expression of the EM interaction term . . . 123

4.6.2 Sensitivity gain bandwidth 125
4.6.3 Periodicity 127
4.7 Conclusion 128

5 Combining acoustic and optical biosensors 131
5.1 Introduction 132
5.2 Operation principle of surface plasmon resonance 133
5.2.1 Plasmon surface polaritons 133
5.2.2 Surface plasmon resonance biosensor 135
5.2.3 Combining SPR and SAW methods 138
5.3 Experimental method 139
5.4 Data mining for rigid layers 141
5.4.1 Methodology 141
5.4.2 Application to S-layers 143
5.5 Data mining for soft layers 147
5.5.1 PNIPAAm and notation conventions 147
5.5.2 Methodology 150
5.5.3 Materials and Methods 152
5.5.4 Results 155
5.5.5 Discussion 158
5.6 Conclusion 165
5.7 Additional resources 166

II Thin Film Nanocrystalline Diamond Membranes 167

6 Characterization method with flexural plate waves 169
6.1 Introduction 170
6.2 Modeling 171
6.2.1 Flexural frequencies and mode shapes 172
6.2.2 Extraction of the material constant and the stress 173
6.3 Experimental methodology 174
6.3.1 Fabrication of nanocrystalline diamond membranes 174
6.3.2 Actuation and detection methods 176
6.4 Results 178
6.4.1 Dynamic characterization 178
6.4.2 Correlation with static measurements of the residual stress 182
6.5 Discussion 185

6.5.1 Critical stress and FPW frequencies 186
6.5.2 Minimum mass per area detection of diamond FPW sensors 186
6.5.3 Drawbacks of the method 189
6.6 Conclusion 190

7 Composite thin film bulk acoustic resonators 191
7.1 Introduction 191
7.2 Composite FBAR sensor 192
7.3 Theory 193
7.3.1 Relation of dispersion 193
7.3.2 Energy distribution and coupling coefficient 195
7.3.3 Mass sensitivity 196
7.3.4 Ground detection limit 199
7.4 Experimental results 203
7.4.1 Device fabrication 203
7.4.2 Electrical performances 203
7.4.3 Influence of the electrodes 206
7.4.4 Evolution of the sensitivity 209
7.5 Discussion 209
7.5.1 AlN/NCD FBAR mass sensor 209
7.5.2 FBAR-FPW sensor concept 213
7.6 Conclusion 213

8 Final conclusions and outlook 215

References 225

A Acoustic waves in solids 247
A.1 Introduction 247
A.2 Propagation of time-harmonic plane waves 249
A.2.1 Elastic fields in solids 249
A.2.2 Christoffel equation 250
A.2.3 Isotropic solids 251
A.2.4 Anisotropic solids 253
A.2.5 Piezoelectric solids 254
A.2.6 Attenuation 256
A.2.7 Slowness surfaces 257
A.3 Reflection and refraction 264

A.3.1 Snell's law 264
A.3.2 Critical angle 267
A.3.3 Acoustic impedances 267
A.4 Energy considerations 268
A.4.1 Acoustic Poynting's Theorem 268
A.4.2 Complex acoustic Poynting's Theorem 270
A.4.3 Energy transport of plane waves 270

B Electrical model of the SAW device 273

C List of scientific communications 277
C.1 Peer-reviewed publications 277
C.2 Patent 278
C.3 Conferences 278

Chapter 1

General introduction

> "And that," put in the Director sententiously, "that is the secret of happiness and virtue – liking what you've *got* to do. All conditioning aims a that: making people like their unescapable social destiny"
>
> *Aldous Huxley*
> Brave New World

1.1 Biosensors

In variety of industrial, medical, health care and consumer applications, small, reliable, disposable and inexpensive sensors able to determine the presence of specific biomolecules are needed. These sensors are better known as *biosensors*. Biosensors have been defined by the Union of Pure and Applied Chemistry (IUPAC) Commission as a subgroup of chemical sensors in which a biologically based mechanism is used for detection of an analyte [170]. Commonly, biosensors are chemical sensing devices in which a biologically derived recognition is coupled to a physical element, also called *transducer*, in which the biological event is recorded [38, 58, 141]. About 20 billion US$ are yearly spend worldwide for analytical tests [124], a reduction of costs and analysis time is possible with modern biosensors. The global market for biosensors has increased rapidly during the last decade, with an annual rate of 10% [125]. In the

future, it is quite reasonable to think this demand will still increase due to breakthroughs in bio-related areas such as health care, biotechnology, pharmaceutical, etc. Current examples are the growing use of biosensors in personal glucose testing for diabetics, cancers and HIV detection, and DNA sensing. Although the potential market for biosensors is known to be very large, the commercialization of the numerous biosensors has been slow except rare cases including glucose monitoring, single analyte enzyme electrodes for food industry and biological oxygen demand for water [45, 125].

The development limit of biosensors has been imposed by a lack in their desired performance characteristics in terms of sensitivity, dynamic range, and reproducibility. However, the potential advantages offered by biosensors technology include minimal sample preparation, high speed of analysis and the potential for *in situ* and flow stream analysis for process control [125, 208].

Biosensor components include a biological recognition element, a physical transducer, an electrical amplifier and a data processing system. Above all, a (micro)fluidics system – or *liquid cell* – serves to condition the fluids to be analyzed, to display them to the sensing area and to dispose of them. Figure 1.1 shows schematically the main components of a typical biosensor.

A wide variety of transducers have been reported in the literature. Biological sensing has been demonstrated with potentiometric and amperometric sensors using enzymatic mediation [38]. These sensors measure the electrochemical activity of the enzyme. Potentiometric systems measure the open-circuit voltage, while the amperometric systems measure the short-circuit current. Chemiresistive devices measure a change in electrical conductivity caused by a biochemical reaction.
Thermal sensors can be used to detect antibody-antigen and/or enzymatic detection. These devices are based on a change in thermal conductivity between a heater and a heat detector.
Optical fibers and waveguides have been used in many configurations including phase interferometry, optical absorption, fluorescence and surface plasmon resonance.
In electromechanical systems, tuning forks with sensitivity comparable to quartz crystal microbalances [212] have been reported. Cantilever

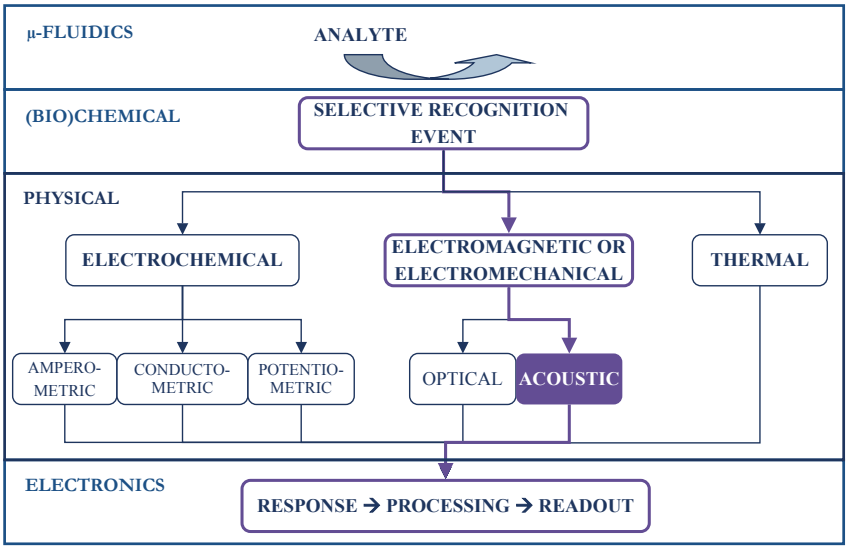


Fig. 1.1 – The biosensor platform is composed of a (bio)chemical interface where specific bio-species are adsorbed; a physical transduction transfers this recognition event to a measurable electrical signal recorded by a dedicated electronics system. The micro-fluidics condition and deliver the analyte to the sensing interface (modified after [38]).

resonators appeared with the possibility of detection of single bacteria, viruses or pH [13, 14]. The ultimate limit is probably reached with nanoelectromechanical systems (NEMS) for attogram detection and for which, ultimately, single virus detection has been proved [52, 76, 94].

1.2 Acoustic biosensors

The technological advances in microelectronics and fiber optics have dramatically increase the number of physical transducers which are available for use in biosensors. In addition, breakthroughs in biochemistry, immunochemistry and biotechnology have provided large amount of well characterized enzymes, antibodies, tissues, living cells and receptors for use in these devices. Acoustic biosensors, detailed here after, is a subset of electromechanical transduction that constitutes the main matter of this thesis. Biosensors and immunosensors based on piezoelectric materials have benefited from rapid developments during the last decade. Acoustic wave devices exist in a multitude of varieties according to the structure of the device and the polarization of the wave. Piezoelectric materials are often needed to generate acoustic waves. Figure 1.2 represents the main categories of guided acoustic waves; the corresponding devices are given by the mode of wave propagation through or on a piezoelectric substrate [46]. A main distinction is done between bulk and surface acoustic waves, depending if the wave propagates through the substrate or along its surface. The most common examples of bulk acoustic wave devices are the thickness shear mode (TSM) resonator [34], the shear-horizontal acoustic plate mode (SH-APM) [169, 201] and the thin film bulk acoustic resonator (FBAR) [17]. Examples of surface generated acoustic waves are Rayleigh mode, Bleustein-Gulyaev (BG) mode [74], shear-horizontal surface acoustic waves (SH-SAW) [6, 116, 171], Love modes [63, 67] and Lamb modes [54, 192]. Initially developed for filters and delay lines in the telecommunication field, surface acoustic wave devices have also attracted a growing interest in the sensor field [10]. The sensing principle is based on the perturbation of the elastic field propagating along the surface of the planar substrate, resulting in a measurable modification of the acoustic signal as schematically represented in Figure 1.3.

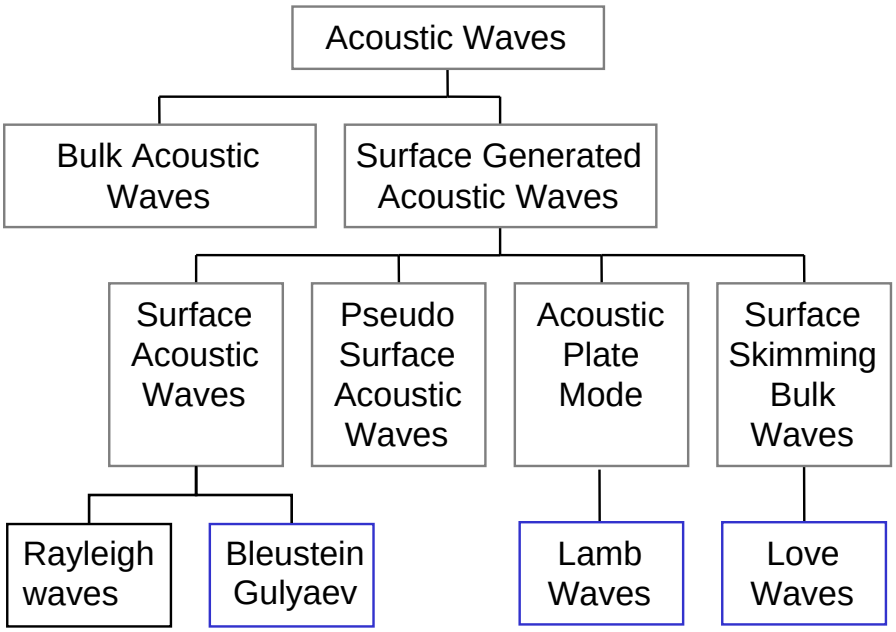


Fig. 1.2 – The acoustic wave family is broad and divided in two main categories: bulk acoustic waves (BAW) and surface generated acoustic waves (SGAW) depending of the propagation of the wave with respect to the surface. Subcategories are determined by the structure of the device and the polarization of the wave.

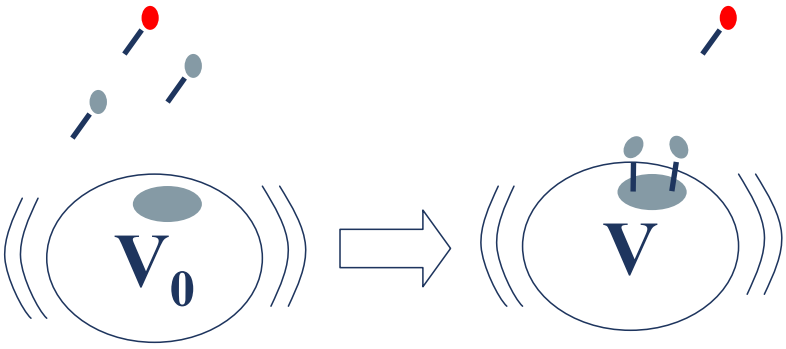


Fig. 1.3 – Schematic principle of an acoustic biosensor: an intrinsic measurable property V_0 of the acoustic device is changing to V after the specific adsorption on its surface of a perturbing element, e.g. in biosensors by a given amount of specific biomolecules.

When the SAW is shear polarized, like SH-SAW and Love-mode sensors, the acoustic energy loss due to the presence of a liquid on the surface is lower than for the Rayleigh case [99, 128]. These sensors are adequate as biosensors where the perturbation is caused by the physical adsorption of biomolecules present in solution [6, 82]. Alternatively, an indirect perturbation mechanism is based on pH changes resulting from enzymatic reactions, for instance with an urease film on the sensing surface to detect urea concentration in the human blood [115]. For any detection mechanism, the biochemical recognition results in a SAW velocity change that is monitored in real-time by the electrical transducers. The transduction itself is obtained on piezoelectric substrates thanks to interdigital transducers [202] (IDTs) that consist in a set of interdigitated electrodes with alternative electrical polarity.

Although any of these acoustic sensors could be used for mass sensing a gaseous environments, less of them can operate in aqueous environments without suffering from a large attenuation making the sensor unadequate to liquid loading. Considered from a pure mechanical point of view, a liquid loading supports the propagation of a particle displacement in a pressure wave and, therefore, the loss of acoustic energy. This energy dissipation occurs in all cases, although it can be reduced by an appropriate choice of acoustic waves. For two cases, a trapping of the acoustic wave in an evanescent wave in the liquid is possible by a shear-horizontal polarization or by an acoustic wave with a phase velocity lower than the one in the liquid. In both cases, the acoustic wave is evanescent in the liquid and therefore trapped at the solid-liquid interface. As application example, the gravimetric detection of human immunoglobulin G (IgG), depicted in Figure 1.4, is a classical target for biosensors. The molar weight of IgG is about 150 kDa, which is $2.5 \cdot 10^{10}$ ng per molecule. A tightly packed monolayer of this molecule contains of the order of 10^{12} molecules per cm^2, which corresponds to 400 ng/cm^2. Thus, a monolayer of IgG is detected at the condition that the detection limit of the acoustic biosensor is lower than this typical value.

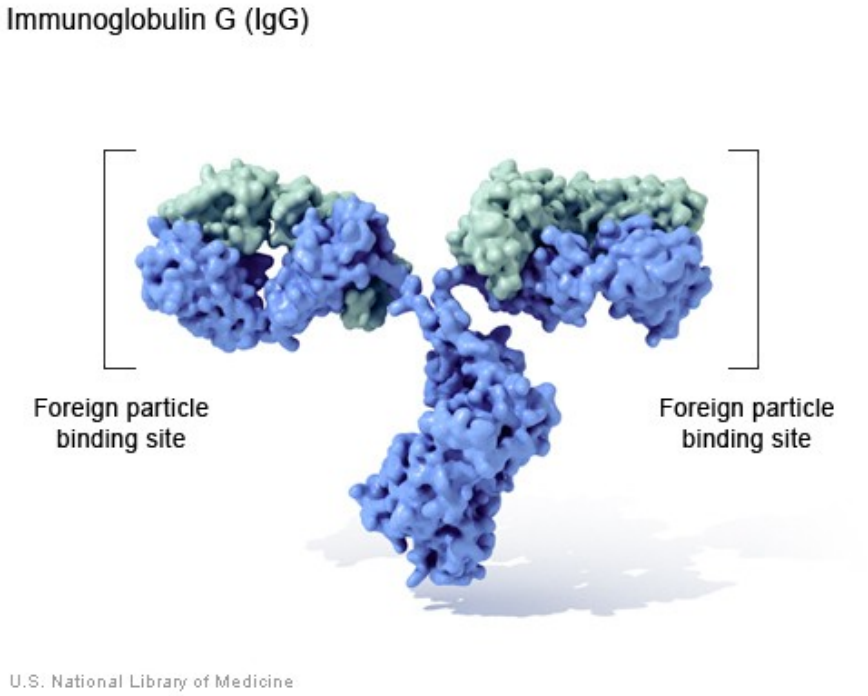


Fig. 1.4 – A representation of the immunoglobulin G (IgG) [source: `http://www1.geneticsolutions.com`. This information was provided by Clinical Tools, Inc., and is copyrighted by Clinical Tools, Inc.]

1.3 Acoustic waveguides and resonators

Acoustic waveguides are solving the propagation of harmonic elastic deformations with specific boundary conditions. In unbounded and homogeneous solids, acoustic waves can freely propagate at a phase velocity V which depends upon the polarization of the waves, according to the orientation of the displacement field with respect to the wavevector. In solid bodies, three acoustic waves can propagate, one longitudinal and two transversal (also called shear), each of them with its own velocity. For isotropic materials, the shear waves are degenerated in a single velocity and the Lamé constants λ and μ are sufficient to define the velocities of the longitudinal and the shear acoustic waves. For a material of density ρ, they are given by $\sqrt{(\lambda + 2\mu)/\rho}$ for the longitudinal one and by $\sqrt{\mu/\rho}$ for the two shear ones. More details about acoustic waves in solids is given in Appendix A.
As any kind of waves, acoustic waves are defined by a *phase velocity* V, related to the angular frequency $\omega = 2\pi f$ and the wavenumber $k = 2\pi/\lambda$ by $V = \omega/k$, and by a *group velocity* $V_g = \mathrm{d}\omega/\mathrm{d}k$. The dispersion relation links the angular frequency to the wavenumber. The acoustic wave propagation is dispersive if phase and group velocities are different.
In an infinite solid or on a free surface, acoustic waves are not dispersive; phase and group velocities are identical at all frequencies. This situation is dramatically modified when the solid is bounded or when inhomogeneities are introduced on the propagation path of the acoustic wave. For instance, by the presence of a film on a surface of the solid. At the material boundaries, for the changes in phase velocities, the acoustic wave experiences reflection and refraction. Constructive interferences between incident and reflected waves at the boundaries can be sustained at specific frequencies and for specific dimensions of the system, defining *acoustic waveguides*.
In this context, a thin film is defined as a material layer of thickness h lower than the acoustic wavelength λ. The structures related to Rayleigh, Love and Lamb modes waveguides are explained here after.

1.3.1 Quartz crystal microbalance

Bulk acoustic waves (BAW) travel in the bulk of a material and present interaction at opposite surfaces. BAW were the first to be developed as acoustic waves based sensors, they were then used for de-

tection of gases and particle matter. The more representative device is the *quartz crystal microbalance* (QCM) which was firstly developed for monitoring of thin films in microelectronics. As biosensors, these devices are used for antibody-antigen monitoring. Shear waves are used to minimize power dissipation in fluids containing biochemical species.

The QCM is based on a resonance principle, a stationary wave is generated and maintained in a plate with thickness multiple of a half-wavelength. This mode is called *thickness shear mode* (TSM). The bulk acoustic wave phase velocity and the boundary conditions (electrical and mechanical at surfaces) determine the resonance frequencies. Although in principle any kind of piezoelectric material can be employed, the QCM uses the AT-cut of quartz. This cut has been studied for more than 50 years; it provides a shear wave vibration with a resonance vibration that has the advantage to be stable in a large temperature domain. A representation of QCM is given in Figure 1.5.

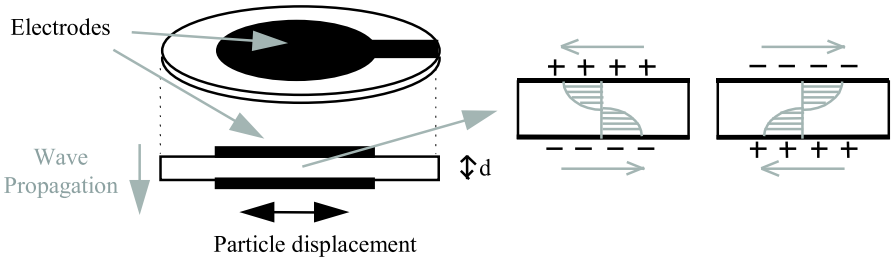


Fig. 1.5 – A bulk acoustic waves biosensor : the quartz crystal microbalance (QCM) is the typical example of BAW resonating in a *thickness shear mode* (TSM) [courtesy of A. Campitelli [30]].

QCM is called *microbalance* due to the frequency decrease when loaded by a mechanical charge at its surfaces. The QCM exhibit best sensitivity for the first modes of resonance and for higher operating frequencies. A very sensitive device could then be obtained with a very small thickness but problems to fabricate and mechanically support a thin quartz crystal impose a maximum of the sensitivity.

1.3.2 Rayleigh mode

Surface acoustic waves are known since Lord Rayleigh suggested that they *"play an important part in earthquakes, and in the collision of elastic solids."* For that reason, surface acoustic waves are equally named Rayleigh waves. These waves have displacements that decay in an exponential fashion in depth beneath the surface. Almost all of the elastic energy is concentrated within a distance of the order of a wavelength below the free surface. The particle motion on the surface and at each depth is elliptical and entirely contained in the plane perpendicular to the surface. Rayleigh waves know successful applications in the telecommunications with development of filters and delay lines. The deposition of interdigital electrodes at surface of piezoelectric media has widely opened the field of investigations for the gigahertz frequency range. As sensors, they also obtained very enthusiastic investigations and were successfully applied as temperature, pressure, acceleration, (high) voltage, polymer phase transitions and gas concentration sensors but less for biosensing applications. Indeed, the normal component of the Rayleigh waves couple easily with liquid and thus suffer from strong attenuation as they propagate.

The most unexpected mode in acoustic waveguides is the Rayleigh mode. At the opposite of many other acoustic modes, the Rayleigh mode has no counterpart in electromagnetic waves. It can be demonstrated that a free surface solves the propagation of a guided mode [160, pp. 247–253]. For a propagation in isotropic materials, the acoustic velocity V can be exactly computed or be approached by the Viktorov approximation:

$$V = \frac{0.436 + \lambda/(\lambda + 2\mu)}{0.5 + \lambda/(\lambda + 2\mu)} \sqrt{\frac{\mu}{\rho}}. \tag{1.1}$$

The Rayleigh mode is always slower than the bulk shear velocity and results from the combination of two displacements at the surface, a longitudinal and a shear perpendicular to the guiding surface. These two components are coupled and decaying within the depth of the substrate on. The displacement field is trapped at the solid interface and decaying below the surface over a distance about one wavelength. Because of these properties, the Rayleigh mode is known as *surface acoustic wave* (SAW). That denomination has extended to all others guided modes that present an entrapment of the acoustic energy at an interface.

The Rayleigh mode is not dispersive for the case of a semi-infinite homogeneous substrate. When the surface is made of a thin film above an infinite substrate, the modified Rayleigh mode obeys a dispersion relation that must be solved numerically rather than analytically [2, 3]. Because of the out-of-plane component of the displacement field, the Rayleigh mode suffers from a strong attenuation as the surface is loaded by a fluid since it creates a pressure wave dissipating energy away from the surface. This effect prevents the use of the Rayleigh mode for biosensor applications. At the opposite, guided modes with a pure shear-horizontal (SH) wave polarization, i.e. with a displacement field entirely parallel to the interface plane, are preferred in liquid sensing applications since those mode are coupled with the liquid through viscous effects in an evanescent wave and its energy remains trapped at the interface.

1.3.3 Shear-horizontal waves and Love modes

Pure shear-horizontal (SH) waves, also known as Bleustein-Gulyaev waves, exist only in some piezoelectric materials and for certain direction of propagation [74,129]. Typical piezoelectric materials are $LiTaO_3$, $Li_2B_4O_7$, $KNbO_3$, $AlPO_4$ (berlinite), CdS, $LiIO_3$, $KTiOPO_4$ (KTP), and the langasite family of crystals (langasite LGS $La_3Ga_5SiO_{14}$, langanate LGN $La_3Ga_{5.5}Nb_{0.5}O_{14}$ and langatate LGT $La_3Ga_{5.5}Ta_{0.5}O_{14}$) [19, 36, 117, 214]. These modes have usually a strong electromechanical coupling and, for such reason, are suited to pH sensing in liquids and to biosensors [19, 42, 111, 209]. They are highly sensitive to the ionic concentration, to the density and to the viscosity and to their variations of liquids. Because of their propagation in specific material cuts and their high costs for fabrication, such structures are not investigated in this thesis although they present a potential for biosensor applications.

An other specific case is the *surface skimming bulk wave* (SSBW), also called *leaky surface wave*, which is actually a bulk mode closely trapped at the surface and generated thanks to the interdigitated electrodes that acts like an endfire antenna launching a wave in the direction of the transducer's axis and that is skimming right below the surface of the crystal [4, pp. 313–315]. The excitation of bulk modes are usually not wanted since it is the source of interferences with the main SAW signal and of energy leaks for SAW resonators. For certain cuts of quartz,

the electromechanical coupling between the transducer and the SAW is almost absent and bulk wave excitation is the main transfer of energy between transducers [127]. An approximated formulation of the SSBW velocity, neglecting the piezoelectric coupling, is given by [127]:

$$V = \sqrt{\frac{c_{55}c_{66} - c_{56}^2}{\rho c_{66}}} \tag{1.2}$$

The Love mode is guided by a thin film deposited on top of a substrate supporting the propagation of SH-SAW or SSBW. Consequently, the Love mode has a shear horizontal polarization with a particle displacement perpendicular to the direction of propagation and parallel to the waveguide surface. The structure of the Love mode waveguide is sketched in Figure 1.6. The difference in mechanical properties between the two materials creates an entrapment of the acoustic energy in the thin film and a lower penetration of the acoustic wave in the substrate.

The shear Lamé constant μ of the substrate and of the film determine the dispersion of the Love mode; a large difference of the constant between the two materials lead to a strong entrapment of the acoustic energy in the layer, i.e. to a better confinement of the energy at the top surface compared to the Rayleigh mode. This latter property has been intensively used at benefit in (bio)chemical sensors, as described by an abundant literature. Applications of Love wave sensors are relatively large since the device is a generic gravimetric sensing platform: detection of pathogen agents in liquids such as virus, bacteria [185] or pathogen spores [24], determination of the viscosity of low-viscous liquid [98], adsorption of aptamer, thrombin and single-stranded DNA [72, 168], determination of the binding constant of immunoglobulin G (IgG) to proteins G and A [162], hazardous gases detection [215], discrimination of wine [165], ice formation [191], etc. This list is not exhaustive because of the great versatility of the Love mode sensor.

1.3.4 Lamb mode and flexural plate waves

So far, we have considered semi-infinite solid as substrate: the stress and strain fields of surface acoustic waves are canceling while they penetrate in the substrate. When the substrate is smaller than the pen-

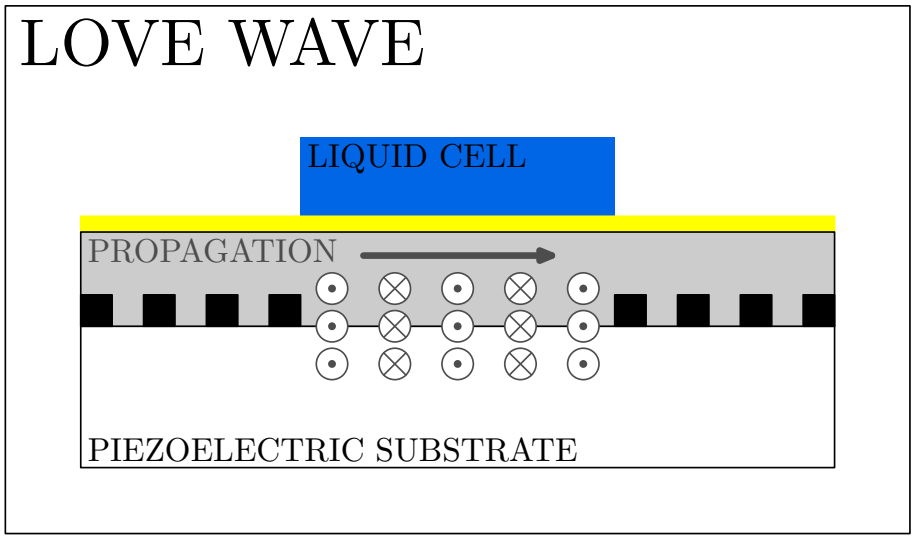


Fig. 1.6 – Schematic structure of the Love mode waveguide: a shear-horizontally polarized acoustic wave is guided by an overlayer coating of a substrate. The transduction is obtained thanks to a piezoelectric substrate with patterned interdigitated electrodes atop of it (black squares). As biosensor, a liquid cell containing the analyte is added on top of the waveguide.

etration depth, an interaction between guided modes on both sides of the substrate takes place and lead to the Lamb modes. These modes are distinguished between symmetric (S) and antisymmetric (A) modes depending of the symmetry of the displacement fields with regards to the neutral axis of the beam formed by this structure. The first antisymmetric mode (A_0) is the only mode that presents a phase velocity going to zero when the normalized thickness goes to zero. This specific property is used in liquid sensing applications.

Since it is almost impossible to handle free standing thin films because of their inherent fragility, the thin film has to be held on its sides by a frame. The thin film is a suspended membrane. Because of the rigid boundary conditions at the edges of the membrane, it will resonate at specific eigenfrequencies determined by the shape of the membrane and its material composition. The suspended membrane can be used as a mechanical resonator with a relatively high quality factor. In this configuration, the Lamb mode is called *flexural plate wave* (FPW). The FPW structure is sketched in Figure 1.7.

1.3.5 Thin film bulk acoustic resonator

Unlike the QCM, a piezoelectric thin film sandwiched between two electrodes is basically generating a bulk acoustic field with a polarization that depends upon the direction of the electrical field with respect to the crystalline orientation of the excited material. Piezoelectric thin films, such as aluminum nitride or zinc oxide, can be deposited using sputtering methods or, for AlN, with reactive sputtering from an aluminum target [136]. As deposited, these materials are oriented such that their crystalline C-axis is perpendicular to the substrate surface. Hence, electrodes deposited below and atop of the deposited thin film generate a longitudinally polarized wave once electrically excited, the acoustic wave is reflected at boundaries of the structure and will enter in resonance at frequencies determined by the thickness and the bulk longitudinal acoustic velocity of the materials and the boundary conditions applied to the structure. Typical resonance frequencies attainable are as high as 10 GHz for films with thicknesses in the order of hundreds of nanometers. This device is known as the thin Film Bulk Acoustic Resonator (FBAR) [17, 62, 157, 164, 211].

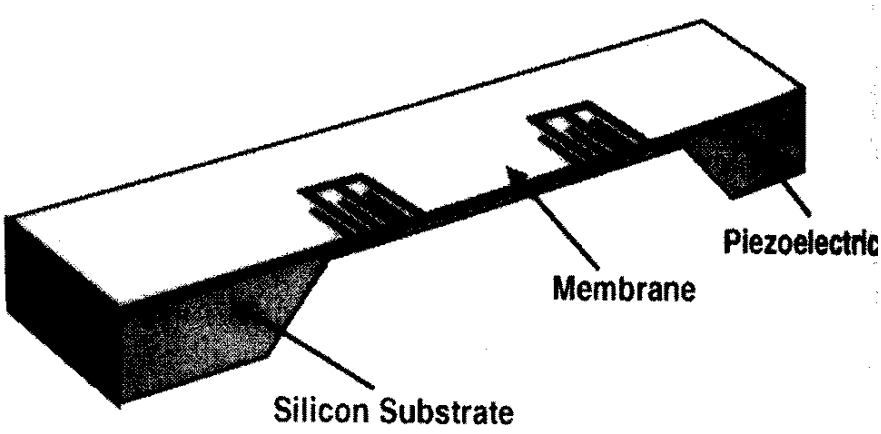


Fig. 1.7 – The flexural plate wave configuration: a thin membrane supported by a frame is placed in vibration thanks to interdigitated electrodes patterned on a piezoelectric material constituting the membrane (source: [10, page 37]).

As the FBAR concentrates efficiently the acoustic energy in a depth in the order of a few hundreds of nanometers to some micrometers, the FBAR presents a larger sensitivity than the SAW structure presented before, both in gases and liquids. The FBAR comes in two main different "flavors" schematically depicted in Figure 1.8: the solidly mounted resonator (SMR) and the membrane resonator, depending of the removal or not of the substrate below the piezoelectric film. It is important to notice that, due to the longitudinal polarization of the wave and its high phase velocity, the resonator radiates a part of its energy when loaded by a liquid, thus resulting in a dropping of its mechanical quality factor of resonance [211]. This effect is a major drawback of the FBAR with respect to surface acoustic wave devices once applied to gravimetric sensing in liquids.

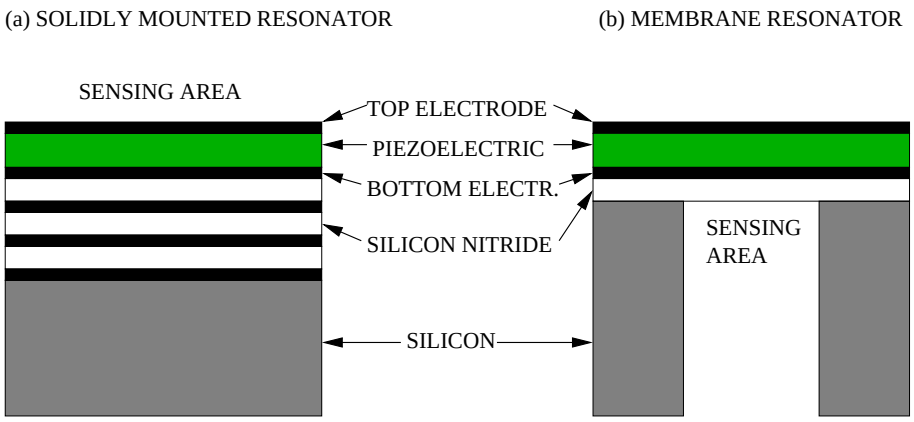


Fig. 1.8 – Schematic cross-section of the thin film bulk acoustic resonator. (a) The solidly mounted resonator (SMR) is formed by a piezoelectric layer sandwiched between two actuating electrodes and deposited atop of a Bragg reflector, consisting itself in a multilayer stack of alternating low and high acoustic velocity materials on a silicon substrate. (b) The membrane resonator is made of the same piezoelectric layer with actuation electrodes but, this time, supported by a membrane (e.g. silicon nitride) held by a silicon frame. The sensing area for the two devices is not identically located as, for the SMR, only the top electrode can serve as such while for the membrane resonator, both sides of the membrane structure are allowed as sensing surface. However, it is common use to display the analyte on the etched side of the membrane FBAR.

1.3.6 Performances comparison

Acoustic sensors used as gravimetric sensors are compared by their sensitivity S^f defined as the frequency shift $\Delta f = f - f_0$, where f_0 is the unperturbed frequency, resulting from the adsorption of a given surface mass Δm:

$$S = \frac{\Delta f}{f_0} \frac{1}{\Delta m}. \tag{1.3}$$

Therefore, the units of the gravimetric sensitivity according to this definition are m^2/kg, while its common to multiply the value of sensitivity by 10 to work in cm^2/g units.

The detection limit is the second most important characteristics of acoustic biosensors as it determines the minimum surface mass that can be detected and is directly derived from the device sensitivity once the noise on the frequency is known. This noise, N_f, is the RMS value of the frequency measured over a given period of time in stable and constant conditions. It is usually recommended to measure a signal variation higher than 3 times the noise level in order to conclude from an effective variation. From this recommendation, it comes out that the detection limit is given by:

$$\Delta m = \frac{3N_f}{f_0 S}, \tag{1.4}$$

that indicates a best detection limit for a low frequency noise, a high sensitivity and a high operating frequency. Table 1.1 compares the sensitivity and the detection limit of the main acoustic biosensors introduced previously, i.e. for the quartz crystal microbalance, the Love mode waveguide, the flexural plate wave resonator and the thin film bulk acoustic resonator.

1.4 The biochemical interface

For the biochemical interface between the physical sensing platform and the sensed environment, the sensing surface must be chemically tailored to attach selective chemical probes on the metal coating and prevent other, non-desired and non-specific, biomolecule attachment. Surface chemistry for the formation of the biochemical interface is an entire research field far beyond the scope of this thesis. Most of the methods

Device	Frequency (MHz)	Sensitivity (cm^2/g)	Detection limit (ng/cm^2)
QCM	$1 - 10$	~ 10	10
Love	$1 - 5 \cdot 10^2$	$10^2 - 10^3$	1
FPW	$1 - 10$	$10^2 - 10^3$	0.5
FBAR	$1 - 10 \cdot 10^3$	$10^3 - 10^4$	$0.01 - 0.1$

Table 1.1 – Performances of acoustic wave gravimetric sensors.

are based on organic chemistry, to form tailored surface for the selective adsorption of (bio)molecules and must be selected according to the sensing purposes of the biosensor. Main methods are based on organic coating of the sensing area. Examples are electrografted polymers [15], DEX-tran layers [12], and alkanethiols that form self-assembled monolayers (SAMs) on gold surfaces. Since that latter example is the most common used approach, it is detailed here after.

The formation of SAMs based on alkanethiols is due to the predictable binding of sulfur to gold that allows the formation of tightly packed monolayers even in the presence of many other functional groups [8]. Long-chain alkanethiols form a densely packed, crystalline or liquid-crystalline monolayer due to strong molecular interactions (van der Waals forces) between the long carbon chains [8, 181]. The other end of the alkane chain is terminated by a chemical functionality determining bonds formation to targeted biochemical species such as antibodies or antigens.

Depositing two or more alkanethiols with different terminal groups – also referred to as *mixed SAMs* – results in enhanced sensitivity, stability, and selectivity of the biochemical interface while compared to single functionality SAMs coverage of the sensing surface [59]. Mixed SAMs consists of a shorter background thiol with a terminal group that provides a neutral surface. A second alkanethiol with a lower concentration is dispersed with the background thiol and has a terminal group of interest. The terminal group of interest provides the desired biochemical activity of the tailored surface and the background thiol provides stabil-

ity to the monolayer. Mixed SAMs permit several different functional groups to be present at the same time.

1.5 Objectives and organization of this thesis

The objectives of this thesis are related to the investigation of thin film acoustic waveguides and resonators for the specific application of a biosensor, which means working in a liquid environment for the determination of the interaction between biomolecules and a chemically defined surface. The thesis is divided into two parts. The first part is related to Love mode sensors while the second part is dedicated to nanocrystalline diamond thin films.

Chapter 2 provides a theoretical investigation of the sensitivity of the Love mode biosensor. A model of the device based on transmission lines is presented and applied to the sensitivity of the biosensor to liquid and mass sensing. It is demonstrated that the electrical signal of the Love mode biosensor is a very sensitive rheometer detecting a thin and soft layer on the sensing surface. A method to discriminate between rigid and viscous layers is discussed.

Chapter 3 describes the fabrication of Love mode biosensors and the wafer-level integration of a liquid cell and their packaging. A section is dedicated to materials (hydrogenated SiO_2, ZnO and amorphous SiGe) for the realization of the guiding layer. A section is devoted to several experimental calibration methods of the device concerning the operating conditions of the device.

Chapter 4 is dedicated to the influence of interferences on the Love mode device. Theoretical expressions are given for the particular case of the electromagnetic interference which causes a different value of sensitivity as a function of the instrumentation of the sensor: at constant frequency (open loop) or at constant phase (closed loop). We show that electromagnetic interferences, often considered as noise, deliver important information related to the intrinsic sensing properties of the device. A sensitivity enhancement can result from specific conditions.

Chapter 5 introduces the combination of acoustic and optical meth-

ods, in particular the original combination of the acoustic Love mode with surface plasmon resonance for the simultaneous measurement of the biorecognition. The chapter describes theoretical methods for determining out of the combined measurement analytical values of the density and the thickness of rigid layers and the density, the viscosity and the thickness of viscous layers. Practical examples are demonstrated, in particular the conformational change of PNIPAAm, a thermosensitive polymer.

Chapter 6 details the theoretical and experimental investigation of nanocrystalline diamond for flexural plate wave sensors and a method for the dynamic characterization of stressed thin film membranes.

Chapter 7 provides a theoretical investigation of composite FBAR mass sensors to the purpose of introducing nanocrystalline diamond thin film as a functional and structural part of the sensor.

Chapter 8 summarizes the main conclusions of this thesis work.

Part I

Love Mode Surface Acoustic Wave Biosensors

Chapter 2

Sensitivity of the Love mode SAW biosensor

All you need is love, love,
love is all you need ...

The Beatles

In this chapter, we present a model of the device based on equivalent transmission lines. The model serves to calculate the properties of the waveguide mode as it propagates in a multilayered and viscoelastic structure. Variations of acoustic velocity and attenuation with surface density and liquid viscosity determine the sensitivity of the device. The results are then extended to the differentiation between rigid and viscous adsorbed layers. The acoustic signal depends on the density, the viscosity and the thickness of the adsorbed biomolecules. As consequence, the Love mode biosensor must first be designed, optimized, calibrated and interpreted as a viscosity sensor.

2.1 Introduction

Acoustic waves with a shear-horizontal polarization are well suited for sensing applications in liquids: the mechanical displacement at the surface probes within a certain volume the density, the shear stiffness and the dynamic viscosity of the composite material that has a certain thickness and is adsorbed on the surface, thus resulting in a mechanical interaction between the layer and the acoustic device. The Love mode

acoustic structure supports the guided propagation of a shear-horizontal wave in a stack of guiding layers deposited atop a piezoelectric crystal substrate. For a large velocity difference between the guiding layers and the substrate, the acoustic energy is trapped closely to the sensing area and results in the highest sensitivity of all similar acoustic structures.

A theoretical model is required to investigate the sensing properties of the Love mode structure, a model that help to optimize the design of the acoustic structure and with the selection of materials that enhance the sensitivity. The model should give a clear insight in the interaction mechanisms between the sensor and its environment for the interpretation of experimental results. A versatile and easy to implement model is, among other choices, the best to be selected. Selection criterion must be based on low computational resources needed and accuracy since these two main factors determine the appropriateness of a model for a fast calibration of the device and for a rapid processing and interpretation of experimental data.

With a shear horizontal polarization and a high mass sensitivity, Love mode surface acoustic wave (SAW) biosensors detect and quantify in real-time chemical species sustained in liquid environments [82, 99, 168, 185]. A Love mode is a guided acoustic mode generated in single or multiple layer coatings on a piezoelectric substrate [47, 63], as sketched in Figure 2.1. Love mode biosensors can be tailored in order to achieve desired parameters from both electrical and sensing points of view [107, 156]. The fine tuning of these parameters requires a set of proper methods to investigate experimentally the sensing properties and link them with theoretical models that take into account the material characteristics as well as the instrumentation and the physical effects occurring in the device during a biorecognition experiment. Experimental and theoretical techniques to evaluate the mass sensitivity are reported in the literature [81, 137, 138, 197] and our work comes in the continuation of these investigations on the sensing characteristics of the Love mode SAW biosensors.

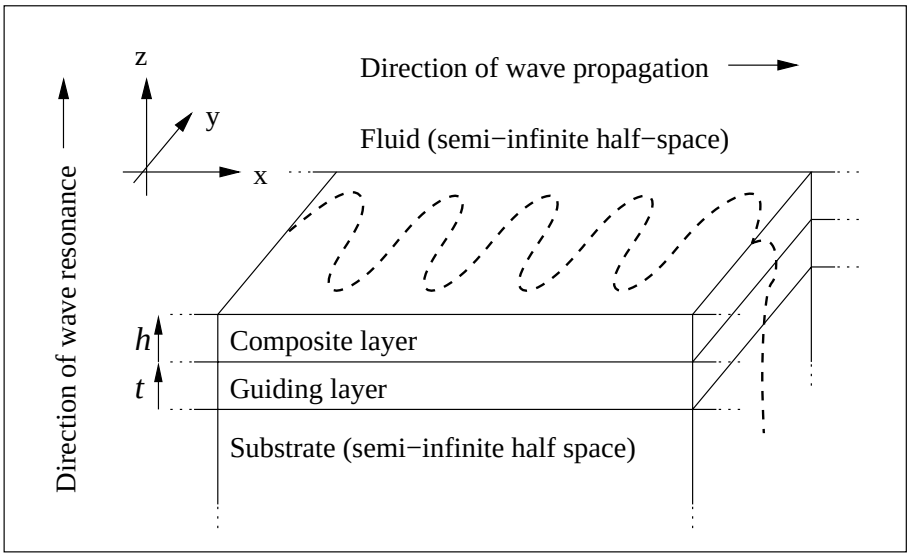


Fig. 2.1 – Schematic view of the Love mode biosensor. The acoustic structure supports the propagation along the x direction of an elastic deformation field in a stack of layers of different thicknesses. The elastic field has a shear-horizontal polarization that makes it suited for application with liquid loadings. For the model, the structure is made of a substrate with semi-infinite extension coated by a guiding layer of thickness t; the device is loaded by a fluid with semi-infinite extension above the waveguide surface and from which we assume that material is segregating to the surface as a flat and uniform composite layer of thickness h.

2.2 Modeling

Several possible models are already existing and reported in literature to determine the properties of the Love mode sensor which is a two-steps method: the first step is to determine the waveguide characteristics (propagation and attenuation of guided modes in the acoustic waveguide), and the second step is to determine how those characteristics are modified by the sensing event, according to the nature of this event. The first step is addressed in this section while the second one is detailed in the next section.

2.2.1 State of the art

The properties of surface acoustic waveguides is widely described in the literature. We report here a survey of the known methods without describing them in detail. The objective is to focus on methods able to address the physical modeling of the multilayered Love mode structure, and to determine the propagation characteristics for a device operating under liquid conditions.

A first method is the *propagation matrix* and the *generalized impedance matrix* [2, 3, 85], their principle can be extended for viscous layer loading [102].
A second method is the *effective permittivity* introduced by Milson [140], which is applied to evaluate guided modes and has been applied to determine the propagation of Rayleigh waves loaded by a viscoelastic thin film [104] and to evaluate the viscous coupling between liquids and SH acoustic plate modes [186, 213].
A third method is the *finite elements method* (FEM). This technique has been reported for the investigation of layered structures with a zinc oxide guiding layer and including the influence of the interdigitated electrodes patterns [95]. The FEM requires a relatively large amount of computation to mesh and simulate even a simplified structure but its main advantage is to take into account the effect of the mechanical loading of the electrodes, which is often neglected by other techniques.
To compensate the time consuming issue of the FEM, the periodicity of the acoustic structure is advantageously used in a combination of FEM with the *boundary elements method* (BEM, or Moment's method) in a fourth method [103, 123, 193, 194]. The FEM/BEM approach is based on

the FEM analysis of an elementary periodic cell containing the minimum periodic set of electrodes, which are excited by an harmonic potential. The motion of the cell is translated from interface to interface of the unit cell by periodic harmonic Green's functions (i.e. a linear combination of translated Dirac functions). One advantage of the method is to be able to calculate directly the admittance of the interdigital transducer.

Most of the techniques are able to establish the acoustic properties of a given structure but less of them are able to tackle with a fluid loading and eventually with a viscous liquid loading of the device. For a theoretical modeling of the Love mode structure, we have chosen to describe the layered structure of this acoustic sensor in terms of mechanical transmission lines. Transmission line methods are known and were already used with success for the analysis of resonator sensors [133, 144]. The introduction of transmission lines has been successfully attempted for the design of the electrical transducers of SAW delay lines [175–177] and, latter, for the modeling of the entire sensor in electrical simulators for the design of the driving and measuring sensor electronics [30, 108].

The transmission line model is used to determine the sensitivity of the acoustic device to density and viscosity variations of thin films and bulk materials, thus specifically applying to biosensors. Attenuation and phase shifts recorded electrically are quantified and analyzed to identify the type of interaction between the adsorbed biomolecules layer and the sensor. Acoustic devices are sensitive to mechanical perturbations, temperature changes and electrical perturbations such as pH changes, conductivity and dielectric constant of added materials. If the sensing area is electrically shielded by a grounded conducting layer, these electrical effects can be neglected, letting the device be sensitive to mainly mechanical perturbations. For the model, and to obtain an immediate correlation with biorecognition events targeted by our application, we will assume that the surface adsorbed organic layer - like proteins or polymers - is a composite material that segregates from the bulk solution on the waveguide surface as an hypothetical perfectly flat layer of given characteristics to be determined.

2.2.2 Acoustic transmission lines model

The acoustic velocity and the attenuation of the acoustic wave in the stacked structure is electrically probed thanks to interdigitated electrodes patterned on the piezoelectric material. The phase at a given frequency within the bandpass range of the delay line and the insertion loss of the acoustic device measured electrically, for instance with a network analyzer, are representative of the actual propagation characteristics of the acoustic wave along the delay line and, in particular, along the sensing path. The properties of propagation and attenuation of acoustic waves in resonator and waveguide devices are found using an analogy between mechanical structures and electromagnetic transmission lines as described in 1969 by Oliner [144]. From his description, a block approach of acoustic transmission is obtained by the formalism of electromagnetic waves on transmission lines. This approach has been applied to determine the phase velocity for the most basic Love mode structure, i.e. for a single layer deposited on a substrate and with vacuum on the top surface. The same approach is applied and expanded here to the design and the analysis of Love mode acoustic wave biosensors, that is for a substrate coated with one or more guiding layers and loaded on the top surface by a fluid. The purpose of a modeling with equivalent transmission lines is to allow the use of known techniques of microwave engineering for the development of Love mode sensors.

An implementation of the equivalent transmission line model is given here to analyze the propagation characteristics of the guided wave in the Love mode structure, including the presence of the surface adsorbed layer and the liquid from which this layer segregates. At first, each material is equivalently represented by a transmission line with a wavevector $\vec{k}$ and a characteristic impedance Z such that the shear stress $T(\vec{r})$ and shear particle velocity $v(\vec{r})$ fields at a given point $\vec{r}$ in the material are given by the superposition of incident and reflected acoustic waves:

$$T(\vec{r}) = T_+ \, e^{-\vec{k}\cdot\vec{r}} + T_- \, e^{\vec{k}\cdot\vec{r}} \tag{2.1}$$

$$v(\vec{r}) = \frac{T_+}{Z} \, e^{-\vec{k}\cdot\vec{r}} - \frac{T_-}{Z} \, e^{\vec{k}\cdot\vec{r}} \tag{2.2}$$

where T_+ and T_- are arbitrary values for the intensity of the incident and reflected waves. The equivalent representation of a viscoelastic layer in this model is given in Figure 2.2, which consists in a series inductance

L shunted by a capacitance C placed in series with a conductance G. The values of the equivalent parameters are given in mechanical terms of the layer, i.e. its density ρ, its shear stiffness μ and its dynamic viscosity η, by the following correspondence [5]:

$$L = \rho \tag{2.3}$$
$$C = \frac{1}{\mu} \tag{2.4}$$
$$G = \frac{1}{\eta} \tag{2.5}$$

from which we derive an analytical expression of the wavenumber $k = \left\|\vec{k}\right\|$ and of the characteristic impedance Z:

$$k = \frac{\mathrm{i}\omega}{V} \tag{2.6}$$
$$Z = \frac{\mu + \mathrm{i}\omega\eta}{V} \tag{2.7}$$

where $\omega = 2\pi f$ is the angular frequency, while V is the complex acoustic velocity defined by

$$V = \sqrt{\frac{\mu + \mathrm{i}\omega\eta}{\rho}}. \tag{2.8}$$

The use of transmission lines equivalent helps to build basic blocks for each constitutive layer and the behavior of the device loaded by (viscoelastic) masses segregating from a (viscous) fluid.

For waveguides, the wavevector $\vec{k}$ is decomposed in a resonance wavenumber $\vec{k}_z$ and a propagation wavenumber $\vec{k}_x$ such that $k^2 = k_x^2 + k_z^2$. The projection into both directions, propagation and resonance, is expressed in each layer by a *complex coupling angle* φ:

$$k_{jx} = k_j \sin\varphi_j \tag{2.9}$$
$$k_{jz} = k_j \cos\varphi_j \tag{2.10}$$
$$Z_{jx} = Z_j \sin\varphi_j \tag{2.11}$$
$$Z_{jz} = Z_j \cos\varphi_j \tag{2.12}$$

where the subscript j refers to a constituent layer. The *transverse resonance principle* [144] is applied to determine the propagation wavenumber: according to this principle, the coupling angles are related

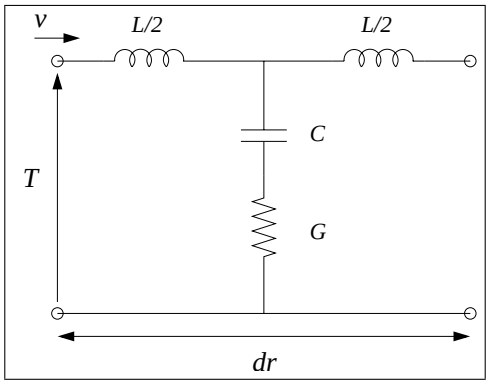


Fig. 2.2 – Differential element of the viscoelastic mechanical transmission line model: the shear stress (T) and the shear wave particle velocity (v) propagate through a symmetric differential element of length dr made of an inductance L shunted by the series connection of a capacitance C and a conductance G.

between each others such that the propagation wavenumbers k_{jx} are all equal. For a simpler notation, the k_{jx} being all identical are noted k_x.

To determine the propagation characteristics in the waveguide structure, the last step is to determine the resonance wavenumber. To that purpose, an equivalent circuit of the physical structure represented in Figure 2.3 is built by connecting in series each equivalent transmission lines of the layers stacked in the direction of resonance, as depicted in Figure 2.4. The series connection automatically solves the boundary conditions associated to the continuity of the mechanical stress and strain at materials interfaces. As a consequence, semi-infinite layers (the substrate S and the fluid F) are terminated by a matching load that accounts for the endless side while the other layers (the guiding layers G_j and the composite layers C_j) have finite dimensions, respectively t_j and h_j. One must notice that for a clearer representation, only one guiding layer and one composite layer have been schematically depicted although the model is easily extended to a larger amount of layers. Consequently, the model sees the Love mode structure as transmission lines placed in parallel in the direction of propagation, with an identical value k_x, and placed in series in the direction of resonance.

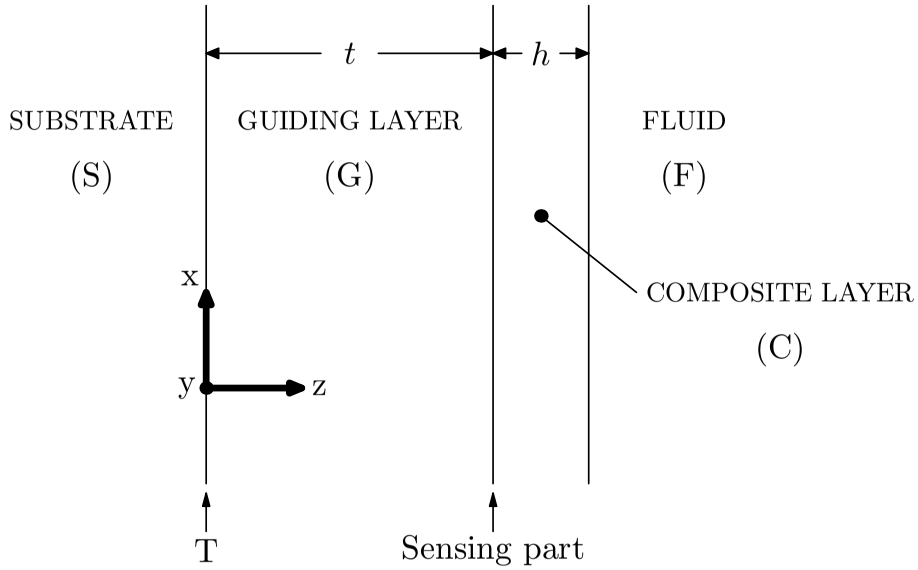


Fig. 2.3 – Schematic representation of the physical layered structure of the Love mode SAW sensor. A guided acoustic shear-acoustic wave propagates in the x direction in a stack composed of the semi-infinite piezoelectric substrate (S), a guiding layer (G) of thickness t, the composite layer (C) of thickness h that segregates from a semi-infinite fluid (F). The sensing area of the device is at the interface between the guiding layer and the adsorbed composite layer. The plane T is a reference plane used to determine the propagation characteristics of the guided acoustic wave. For clarity, only one guiding layer is represented although the practical structure might be composed of several guiding layers.

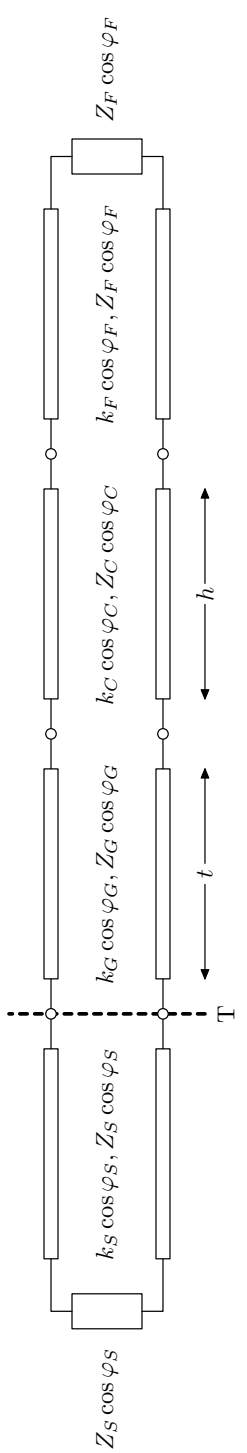


Fig. 2.4 – Equivalent transmission line model of the physical structure in the direction of resonance (z) given in Figure 2.3. The equivalent transmission lines of each part of the device implement the model of Figure 2.2 and are schematically represented by stub lines with the indication of the wavenumber k_{jz} and the characteristic impedance Z_{jz}. The lines are connected in series to satisfy the boundary conditions and the two semi-infinite layers are loaded with a matching impedance. Resonance solutions of this network are solution for a guided Love mode.

Finally, the resonance is found by measuring the impedance at a plane T located at an arbitrary position in the structure, for instance at the substrate–coating interface as sketched in Figure 2.4: the resonance is found for values of the complex coupling angle that result in opposite impedances seen in both directions at the reference plane T. These impedances are determined by applying a standard formula from the transmission line theory to calculate the input impedance of a transmission line of characteristic impedance Z_{char} and length L loaded at its end with an impedance Z_{load}:

$$Z = Z_{char}\ \frac{Z_{load} + Z_{char}\tanh\left(k_z L\right)}{Z_{char} + Z_{load}\tanh\left(k_z L\right)}.$$

A solution of the resonance wavenumber is translated to the propagation wavenumber thanks to Eqs. (2.9) and (2.10). The real and imaginary parts of a determined solution k_x are related to the attenuation and the phase velocity of a guided mode, respectively.

The value of φ is a real number if the structure has no losses, which is when all the η are null, and it becomes a complex number when the Love mode dissipates its energy while propagating in viscous layers. The building block approach performed here is of great importance to evaluate easily the impact of a modification at the surface of the sensor. Indeed, one can calculate the basic properties of the structure under any circumstances, such as in vacuum (in such case both acoustic impedance and propagation function are null) or while loaded with a rigid or a viscoelastic layer, and with or without a liquid environment.

As a practical example, the transmission line model is applied to a specific device (ST-cut quartz substrate, silicon dioxide guiding layer, gold 50 nm and water) to determine its characteristics while loaded with water for different thicknesses of a silicon dioxide guiding layer. The material parameters for the simulation are given in Table 2.1. The Love mode phase and group velocities and the signal attenuation are plotted in Figure 2.5.

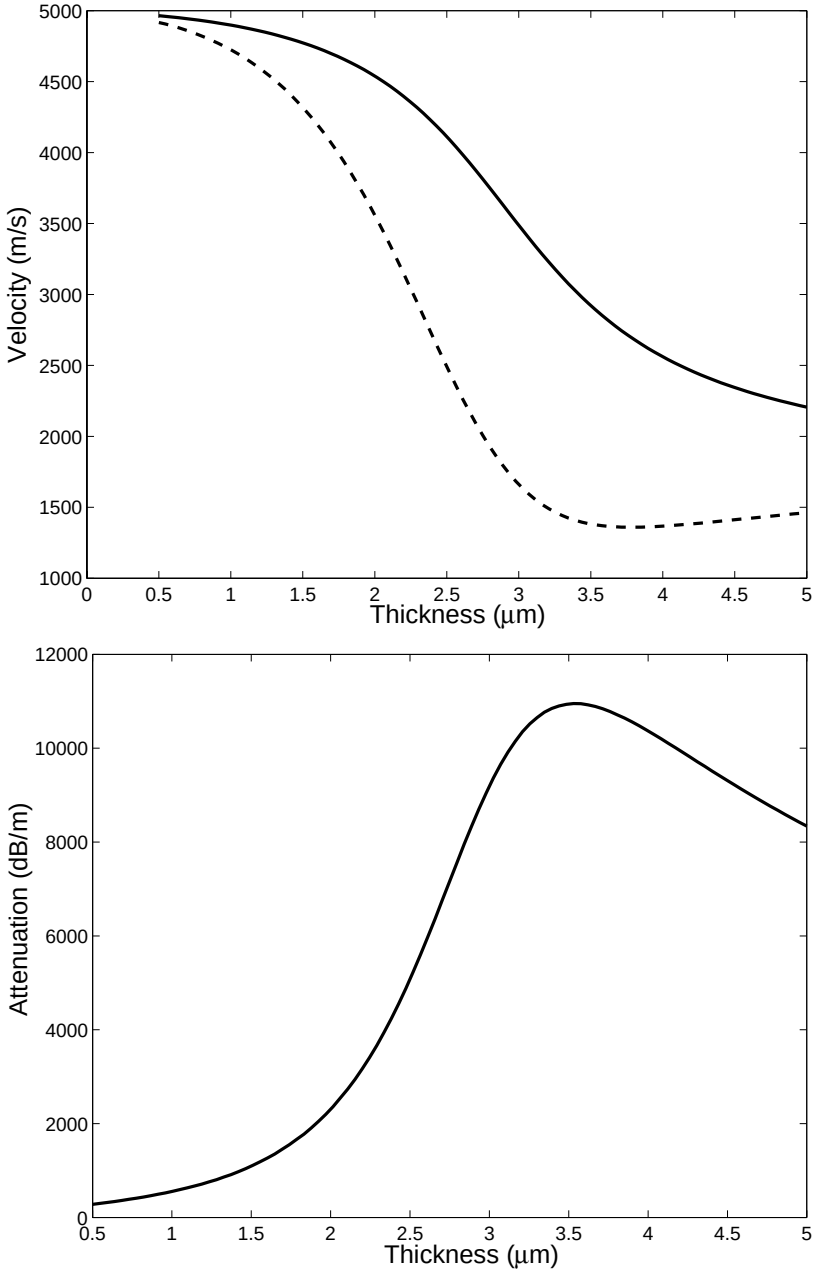


Fig. 2.5 – (top graph) Theoretical Love wave phase (solid line) and group (dashed line) velocities and (bottom graph) signal attenuation for a water loaded structure at a frequency of 123.2 MHz *vs.* the SiO_2 layer thickness.

Material	Density ρ (kg/m^3)	Shear stiffness μ (GPa)	Viscosity η ($Pa \cdot s$)
Quartz	2648	66.31	0
SiO_2	2610	8.313	0
Gold	19300	28.50	0
Water	1000	0	0.001

Table 2.1 – Materials parameters for the device simulation.

2.3 Sensitivity

This section investigates the sensitivity of the Love mode waveguide. After a review of the state of the art, a variational model of the sensitivity is presented for the specific case of mass detection in a liquid environment. The model is based on variations in amplitude and phase of the measured signal obtained thanks to the electrical transduction and is discussed as a function of the intrinsic physical changes taking place on the surface of the sensor. The sensitivity define a set of terms that relate changes in surface adsorbed mass and liquid viscosity variations and their effect on the electrical signal. The discussion is extended to the influence of rigid and viscous interactions between the acoustic wave and the probed media and expressions are given to determine the nature of this interaction on the base of the ratio between the amplitude and the phase shifts of the acoustic signal, in relation with the sensitivity. We indicate that biosensing with the Love mode waveguide is equivalent to a rheological measurement where the biomolecules forms on the sensing surface a thin viscous layer. The consequence is important in terms of data interpretation since the sensitivity is often and erroneously calibrated and compared to a rigid layer loading. A final point addresses the influence of the noise and its influence on the discrimination between rigid and viscous behaviors.

2.3.1 State of the art

The sensitivity of the acoustic sensor has been intensively investigated in the literature since its value gives the correlation between

observed, measured, electrical signals delivered by the sensor when a perturbing event takes place on the sensing area of the acoustic waveguide. A high sensitivity is linked to a strong variation of the signal for a small perturbation. Since the Love mode biosensor operates in a liquid environment, changes of the bulk properties of the liquid (density and viscosity) are probed while surface changes due to mass adsorption are equally seen by the sensor. Therefore, the actual signification of the term *sensitivity* strongly depends of the context in which the input and output variables are expressed. The output of the device can be equally considered on several aspects according to the quantified output (phase velocity, group velocity, resonance frequency for an oscillator configuration, amplitude). As example, the so-called *mass sensitivity* is defined for a change of phase velocity for a differential surface mass change Δm [137]:

$$S = \lim_{\Delta m \to 0} \frac{1}{\Delta m} \frac{\Delta V}{V_0} \tag{2.13}$$

with $\Delta V = V - V_0$, where V_0 is the unperturbed phase velocity and V its value after the surface mass change. The literature reports numerous studies of the mass sensitivity and of the viscous liquid sensitivity of the Love mode waveguide but they are rarely considered together.

The first method used to determine the mass sensitivity of the Love mode waveguide is based on the perturbation theory [4]. Wang *et al.* calculated explicitely, in 1994, the mass sensitivity of a single guiding isotropic overlayer of thickness h deposited on an isotropic substrate with the perturbation theory [197]:

$$S = \frac{-1}{\rho_L h} \left(1 + \frac{\sin(k_L h)\cos(k_L h)}{k_L h} + \frac{\rho_S}{\rho_L} \frac{\cos^2(k_L h)}{k_S h} \right)^{-1} \tag{2.14}$$

where the subscripts S and L refer to the substrate and the loading layer, respectively, and ρ is the density and k the propagation number. The sensitivity expression has a maximum at a given value of the overlayer thickness for which also the ratio of the shear sitffness of the layer to the substrate trends to zero, which condition is not physically possible. The optimum sensitivity is obtained for $\cos(k_L h) = 0$, which is the *quarter-wavelength resonance* of the overlayer. At the condition that the shear velocity in the guiding layer is much lower than the one in the substrate,

one obtains [197]:

$$S \simeq \frac{-4V_S}{V_L \rho_L \lambda_S} \tag{2.15}$$

where V_S is the bulk shear acoustic velocity of the substrate, V_L is the bulk shear acoustic velocity of the layer made of a material of density ρ_L, and λ_S is the wavelength of the surface transverse wave in the substrate.

Because the choice of materials strongly determine the actual value of sensitivity, Stevenson *et al.* [179] investigated theoretically and at the same period the choice of several guiding materials (silicon dioxide, aluminum, copper, zinc, silver, gold, lead, PMMA). From the expressions derived from the perturbation theory, it was deduced that the best sensitivity is reached for a guiding material with a low shear acoustic velocity, a low density and low acoustic losses. A material of choice suggested in the early start of the 90's is PMMA (polymethylmethacrylate) [67, 197]. In the same research group, Gizeli demonstrated theoretically the higher sensitivity of the polymer coated Love mode sensor in a comparison with bulk acoustic wave and acoustic plate mode sensors [68]. Despite a low shear velocity and a low density, the optimum thickness of PMMA has never been experimentally reached since acoustic losses in polymer materials are generally too high.

Du *et al.* investigated experimentally the sensing properties of a ST-cut quartz with a silicon dioxide guiding layer, as a function of the thickness of that latter layer [49]. Experimental devices with SiO_2 between 0 and 7.3 μm were tested. For an acoustic wavelength of 40 μm, an optimum sensitivity was obtained around 5.5 μm with a value of 380 cm^2/g. The mass sensitivity was determined by the deposition of an ultra-thin ($\leq$2 nm) gold film on the sensing area in a vacuum chamber. At that point, a discrepancy was observed between the theoretical estimation of the sensitivity obtained due to the perturbation theory and the experimental results, in particular as the guiding layer was getting thicker. In a second and latter publication [48], they showed the influence of the viscosity of the liquid on the sensing and the electrical properties of the device and concluded that it could be used as a highly sensitive, stable in liquid and with a low detection limit device. The detection of a monolayer of IgG antibody (about 400 ng/cm^2) is possible with the Love mode sensor.

At the same period, Jakoby and Vellekoop addressed the properties of Love wave sensors for biochemical and for liquid density and viscosity measurements [99]. The mass sensitivity was theoretically determined using the propagation matrix method to determine the propagation characteristics for a given structure and then by deriving mathematically these characteristics for the case of a pure mass loading (assuming a perturbing layer of vanishing thickness and of finite density). Thanks to this approach, they noticed that the sensitivity measured by frequency changes in an oscillator loop configuration differs from the sensitivity estimated from the acoustic velocity by a factor V_g/V, thus a typical 10% difference can be noted between the change of velocity and the measured change of frequency.

From material aspects, a combination of high sensitivity but high loss material with a low sensitivity and low loss material was suggested by Du *et al.* [47]. Such hybrid device combines the advantages of a high sensitivity and a low loss. As example, they studied the SiO_2/PMMA structure. A maximum sensitivity of 640 cm^2/g was measured by the deposition of a gold ultra-thin film in vacuum. However, a frequency drift due to water absorption by the PPMA in water was seen. This water adsorption is a drawback since it modifies the mechanical properties of the device as it operates in water and results in a poor long-term stability of the liquid sensor. On an other side, silicon dioxide has proved to be a stable material while operating in liquid. They suggested to use a thin film overlayer barrier to avoid this degradation of the device.

When operated in liquids, a major effect on the device signal is the influence of the product of the density and the viscosity of the loading liquid. Herrmann *et al.* investigated theoretically and experimentally a method for the separate determination of the two parameters [87]. The method is based on a corrugation of the sensing surface that results in a trapping of the liquid at the device-liquid interface. The frequency shift of the corrugated device follows the relation [87]:

$$\frac{\Delta f}{f} = -\frac{V_g}{V} S\omega\rho d \frac{w}{s+w} C \tag{2.16}$$

where S is the liquid sensitivity, s the spacing between corrugations, w the corrugation width, d the corrugation depth and C a fit parameter.

The experimental calibration of the mass sensitivity is reported with the deposition of biochemical materials on the surface in the liquid environment. Gizeli demonstrated experimentally the effect of the deposition of a lipid bilayer on a quartz substrate coated with PMMA for different thicknesses of the guiding layer [64]. The formation of the lipid bilayer is a stable process resulting in a thin film of reproducible surface density. The surface density can be calibrated easily using radiolabeled lipids. A sensitivity of 250 cm^2/g for a 1.3 μm thick guiding layer has been measured with this method. During the calibration, the change of ratio of the amplitude shift to the phase shift was increasing with increasing thickness of the PMMA guiding layer when loading the device with water and with the lipids. It was concluded at that time that this observation was linked to a different contribution from viscous and mass loading to the phase signal.

For the analysis of the sensitivity, the most classical approach is based on perturbation theory [4] but Green's function have recently been used to calculate the propagation in a layered structure with identification of the influence of the electrodes and with liquid loading [154, 174].

In 2001, Harding demonstrated experimentally that the sensitivity of the entire sensor was not identical in all points of the structure, this because of the acoustic reflectance above the interdigitated electrodes [81]. For thicknesses of the guiding layer close to the theoretical optimum, the mass sensitivity of the sensing area located between the transducers happened to be higher than the one obtained by including the transducers. In the same study, the guiding layer was a modified silicon dioxide obtained by RF sputtering of SiO_2 with different pressures of CF_4 in the deposition chamber. The resulting film incorporates a part of fluorine in various concentration according to the deposition parameters, including the possibility to obtain Si-O-F films with a graded concentration profile. The mass sensitivity, estimated by deposition of ultra-thin gold film and by coating with a layer of sheep IgG (assuming a surface density of 440 ng/cm^2), was different as the film composition was varied, indicating the modification of the acoustic shear velocity and the density caused by the presence of the fluorine atoms in the silica layer.

The mass sensitivity was assessed theoretically by McHale *et al.* in 2002 on base of the dispersion properties of the Love mode waveguide [137]. They demonstrated a formulation of the mass sensitivity based on phase and group velocities of the sensor:

$$S \simeq \frac{1}{\rho_L h} \frac{V_g - V}{V_g}, \tag{2.17}$$

while they clearly pinpointed that this expression of the mass sensitivity of the dispersive structure, based on the phase velocity, differs from a frequency mass sensitivity S^f obtained from the frequency shift in an oscillation loop:

$$S^f \simeq \frac{1}{\rho_L h} \frac{V_g - V}{V}. \tag{2.18}$$

As a conclusion on the survey of the state of the art, we state that the knowledge and the understanding of the interaction mechanisms between surface adsorbed biomolecules sustained in a liquid and the Love mode acoustic waveguide were limited to a separation between a rigid mass loading on one side and a bulk liquid mass viscosity loading on an other side. Beside that, the interpretation of the signal is often referred to the only variation of the electrical phase (or of the frequency when the sensor is inserted as the feedback element of a close loop oscillator) while neglecting, either totally or partly, effects reflected by amplitude variations of the electrical signal. In addition, theoretical or experimental quantitative methods to estimate the mass sensitivity are *most of the time* based on the assumption of the adsorption of a rigid and consistent mass on the surface caused by the presence of the biomolecules, the influence of the solvent being ignored at first. Only recently, Gizeli *et al.* [66] assumed the viscoelastic behavior of biomolecules probed acoustically and the consequences on the analysis of the electrical signal. The main consequence is that the attenuation of the acoustic wave, reflected by the amplitude of the acoustic signal, carries a determining information to resolve the exact viscosity of the adsorbed layer and, with an adequate modeling, to the quantity of biomolecules present in the probed volume.

In this thesis, we have adopted a different approach taking into account the most recent developments and understanding of the intimate mechanisms involved in the acoustic waveguide biosensor. The main hypoth-

esis, premised by the theoretical model of the multilayered structure as described in the previous section, assumes the deposition of the perturbing material under the form of a composite layer of variable composition and finite thickness. The deposited layer has viscoelastic properties comprised between the ones of a pure bulk material and the ones of the liquid from which it segregates. We believe, at this point, that our intuitive approach is likewise to represent at best the surface adsorption of the biomolecules. In the following parts of this section, we integrate in a single model the effects of surface mass and liquid loadings on both the amplitude and the phase of the electrical signal. From this analysis, the ratio of the amplitude to the phase shifts is used to evaluate the rigid or viscous nature of the adsorbed layer.

2.3.2 Electrical signal

The Love mode SAW delay line sketched in Figure 2.6 records a biochemical event occurring on the sensing area through a variation in its transfer function. The transfer function is the ratio of the electrical signal at the output interdigital transducer (IDT) to the AC electrical signal driving the input IDT [202]. The transfer function is a complex number described by an amplitude α and a phase angle ϕ. The value $-20\log_{10}(e)\alpha$ (in dB/m) is a more common description of the amplitude called the *insertion loss*.

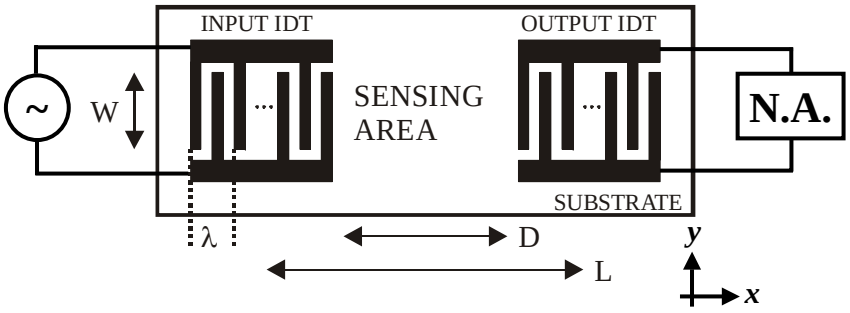


Fig. 2.6 – Schematic structure of the Love mode SAW biosensor and its instrumentation. The input interdigitated electrodes are driven by an AC voltage while the signal is recorded by a network analyzer (N.A.) at the output interdigitated electrodes.

For the analysis of the acoustic signal, variations in amplitude and in phase of the electrical signal are monitored in real-time as modifications happen: variations of the mechanical characteristics of the composite layer, of the layer thickness, or variation in the nature of the fluid. Because of such variations, the propagation wavenumber k_x changes to k'_x. The induced variations of the acoustic signal are measured through the transducers and interpreted as an electric signal attenuation per unit of length ΔA, in dB/m, given by:

$$\Delta A = 20 \log_{10} \frac{\Re(k_x)}{\Re(k'_x)} \tag{2.19}$$

and to an electrical delay phase shift per unit of length $\Delta\phi$, in 1/m, given by

$$\Delta\phi = \Im(k_x) - \Im(k'_x). \tag{2.20}$$

The quantities to compare with experimental values are obtained by multiplying the theoretical shifts by the length of the sensing path D. According to these specifications, one can see that the following relations are observed:

$$\mathrm{d}\alpha = -\lim_{k'_x \to k_x} \Delta A; \tag{2.21}$$

$$\mathrm{d}\phi = \lim_{k'_x \to k_x} \Delta\phi. \tag{2.22}$$

2.3.3 Variational model of the sensitivity

The sensitivity is the quantitative relation between the acoustic signal variations and the modifications occurring in the environment above the sensing area. In biosensing, two types of modifications are allowed: surface density and liquid viscosity. Firstly, the adsorption of biomolecules on the sensing area modifies the surface density σ and corresponds to a mass loading of the surface. For an uniform layer, the surface density is given by the product of the layer density ρ by its thickness h, i.e. $\sigma = \rho h$. Secondly, the liquid carrying the biomolecules is loading the device and is sensed trough the density ρ times the viscosity η [138].

According to our notations, we suggest the following variational

model for the sensitivity:

$$\begin{pmatrix} \mathrm{d}\phi \\ \mathrm{d}\alpha \end{pmatrix} = \begin{pmatrix} \frac{\partial\phi}{\partial\sigma} & \frac{\partial\phi}{\partial(\sqrt{\rho\eta})} \\ \frac{\partial\alpha}{\partial\sigma} & \frac{\partial\alpha}{\partial(\sqrt{\rho\eta})} \end{pmatrix} \begin{pmatrix} \mathrm{d}\sigma \\ \mathrm{d}\sqrt{\rho\eta} \end{pmatrix} \tag{2.23}$$

$$= \begin{pmatrix} k_x D & 0 \\ 0 & D \end{pmatrix} \begin{pmatrix} S_{\phi,\sigma} & S_{\phi,\rho\eta} \\ S_{\alpha,\sigma} & S_{\alpha,\rho\eta} \end{pmatrix} \begin{pmatrix} \mathrm{d}\sigma \\ \mathrm{d}\sqrt{\rho\eta} \end{pmatrix} \tag{2.24}$$

$$= \mathbf{MS} \begin{pmatrix} \mathrm{d}\sigma \\ \mathrm{d}\sqrt{\rho\eta} \end{pmatrix} \tag{2.25}$$

The two matrices allow to distinguish between structural factors ($\mathbf{M}$) and intrinsic sensing properties ($\mathbf{S}$) of the acoustic device. The components of the matrix of sensitivities $\mathbf{S}$ are calibrated experimentally or determined theoretically. The component component $S_{\phi,\sigma}$ is reported in the literature as the *mass sensitivity* (also named *gravimetric sensitivity*) as it links the surface density change to the electrical phase change as schematically depicted in Figure 2.7. The other components of $\mathbf{S}$ will be evaluated by the theoretical approach of the biosensor.

Once known, the matrix $\mathbf{S}$ can be inverted to link the experimental observed phase and attenuation changes to the actual values of surface density and viscosity changes:

$$\begin{pmatrix} \mathrm{d}\sigma \\ \mathrm{d}\sqrt{\rho\eta} \end{pmatrix} = \mathbf{S^{-1}M^{-1}} \begin{pmatrix} \mathrm{d}\phi \\ \mathrm{d}\alpha \end{pmatrix} \tag{2.26}$$

$$= \begin{pmatrix} S_{\sigma,\phi} & S_{\sigma,\alpha} \\ S_{\rho\eta,\phi} & S_{\rho\eta,\alpha} \end{pmatrix} \begin{pmatrix} \frac{1}{k_x D} & 0 \\ 0 & \frac{1}{D} \end{pmatrix} \begin{pmatrix} \mathrm{d}\phi \\ \mathrm{d}\alpha \end{pmatrix} \tag{2.27}$$

from which the following equations can be expressed:

$$\boxed{\mathrm{d}\sigma = \frac{1}{k_x D|\mathbf{S}|}\left(S_{\alpha,\rho\eta}\mathrm{d}\phi - k_x S_{\phi,\rho\eta}\mathrm{d}\alpha\right)} \tag{2.28}$$

and

$$\boxed{\mathrm{d}\sqrt{\rho\eta} = \frac{1}{k_x D|\mathbf{S}|}\left(k_x S_{\phi,\sigma}\mathrm{d}\alpha - S_{\alpha,\sigma}\mathrm{d}\phi\right)} \tag{2.29}$$

The latter equations show the influence of the attenuation due to bulk viscous loading, the factor $\mathrm{d}\alpha$, on the estimation of the actual surface density change.

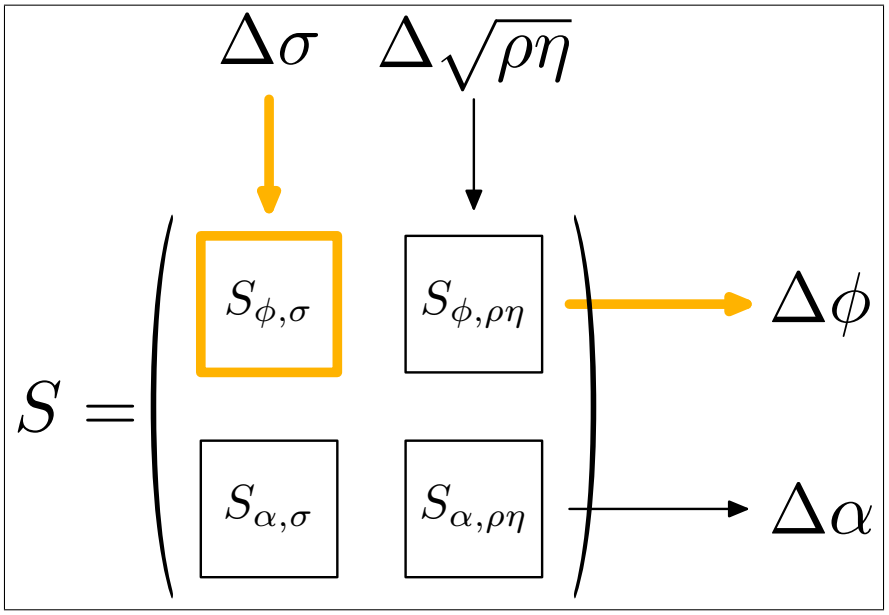


Fig. 2.7 – The sensitivity of the Love mode biosensor is modeled by a 4 components matrix. These components relate shifts of surface density $\Delta\sigma$ and mass viscosity $\Delta\sqrt{\rho\eta}$ to shifts of electrical phase $\Delta\phi$ and signal attenuation $\Delta\alpha$. The component framed in bold is the so-called *gravimetric* sensitivity, noted here $S_{\phi,\alpha}$. The gravimetric sensitivity links phase shifts to surface density shifts, it is the component usually considered in literature for the quantification of the amount of biomolecules attached to the sensing surface.

2.3.4 Determination of the sensitivities

The components of the matrix of sensitivities **S** and of the inverted matrix $\mathbf{S^{-1}}$ are given for our example as a function of the silicon dioxide thickness in Figure 2.8. The values of sensitivity were obtained by derivation of the phase velocity and attenuation with respect to the guiding layer thickness, and by varying the mass viscosity ($\sqrt{\rho\eta}$). For our dedicated example, the matrix **S** has the components:

$$S_{\phi,\sigma} = -17.9 \text{ m}^2/\text{kg} \quad (2.30)$$

$$S_{\phi,\rho\eta} = -5.18 \cdot 10^{-4} \text{ m}^2 \cdot \text{s}^{1/2}/\text{kg} \quad (2.31)$$

$$S_{\alpha,\sigma} = 3.78 \cdot 10^5 \text{ dB} \cdot \text{m/kg} \quad (2.32)$$

$$S_{\alpha,\rho\eta} = 755 \text{ dB} \cdot \text{m} \cdot \text{s}^{1/2}/\text{kg} \quad (2.33)$$

and the inverted matrix $\mathbf{S^{-1}}$ has the components:

$$S_{\sigma,\phi} = -5.68 \cdot 10^{-2} \text{ kg/m}^2 \quad (2.34)$$

$$S_{\sigma,\alpha} = -3.89 \cdot 10^{-8} \text{ kg/dB/m} \quad (2.35)$$

$$S_{\rho\eta,\phi} = 28.46 \text{ kg/m}^2/\text{s}^{1/2} \quad (2.36)$$

$$S_{\rho\eta,\alpha} = 1.35 \cdot 10^{-3} \text{ kg/dB/m/s}^{1/2} \quad (2.37)$$

2.3.5 Discrimination between rigid and viscous interactions

The mechanisms of propagation and losses are physically due to the mechanical behavior of the adsorbed layer. As indicated by the modeling, the three mechanical parameters (ρ, μ and η) of the adsorbed layer must be taken into account to determine the variation of the acoustic signal. Inversely, the acoustic signal is linked to the variations in these three parameters and in the thickness of the layer. Because of the interaction of the adsorbed layer with the moving surface of the sensor, it is known that the relaxation period (ratio η/μ) is important to differentiate two extreme cases of mechanical behavior. These two limit cases are the purely rigid and the purely viscous layer [163]. The product of the relaxation period by the frequency indicates if the adsorbed film moves in phase (rigid) or out of phase (viscous) with the acoustically driven surface. When the relaxation time is high, i.e. when $\omega\eta \gg \mu$, the

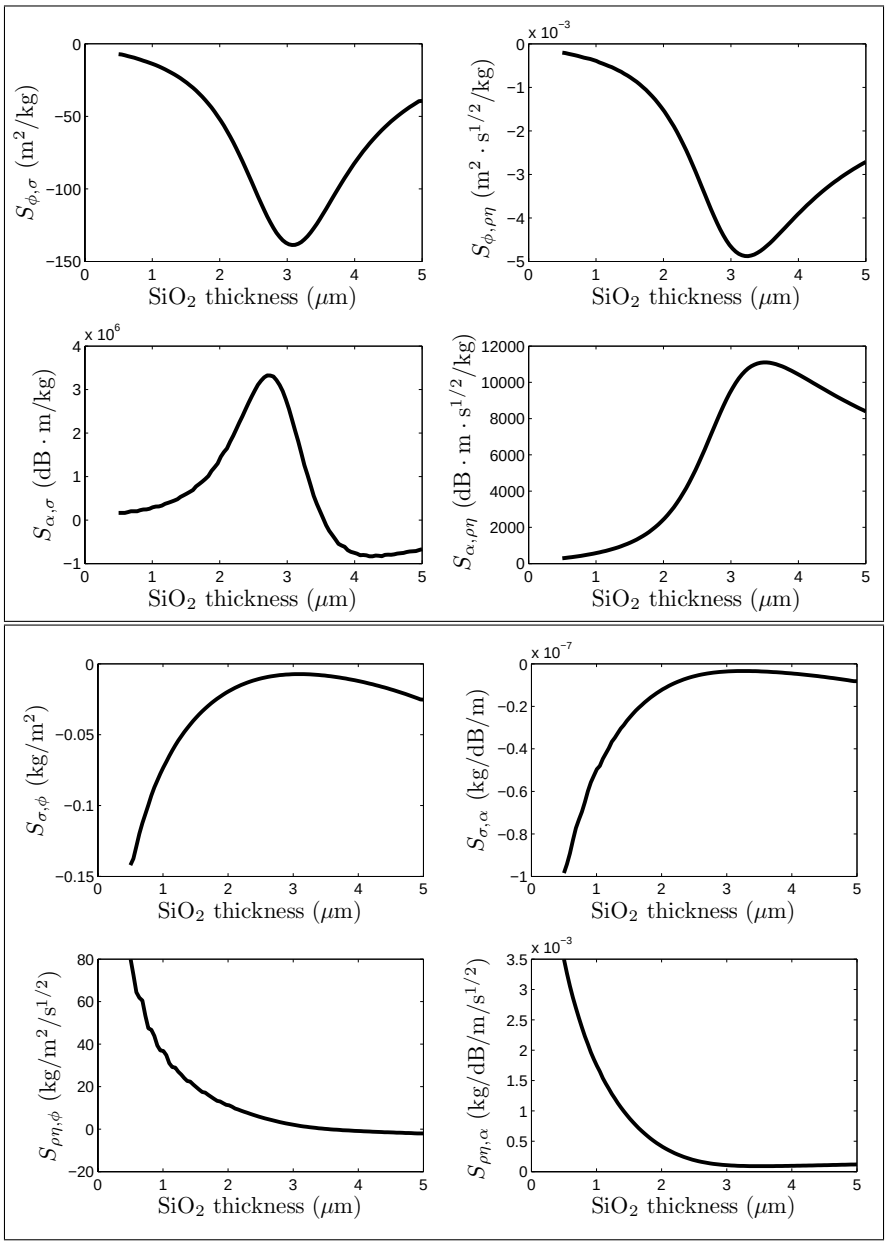


Fig. 2.8 – (top part) Components of the matrix of sensitivities $\mathbf{S}$ and (bottom part) components of the inverted matrix of sensitivities $\mathbf{S^{-1}}$ at 123.2 MHz *vs.* the SiO_2 layer thickness.

film is viscous, meaning that acoustic loss is a predominant mechanism of energy dissipation in the film, which is also a mechanism driving an important attenuation of the acoustic wave as it propagates along the perturbed part. At the opposite, when the relaxation time is low and $\omega\eta \ll \mu$, the film is considered as rigid, involving an entrapment of the acoustic energy in the film which participates effectively in the guiding of the acoustic wave.

For viscous films, it is known that the product of the density by the viscosity and the film thickness play a role in the modification of the acoustic velocity and the attenuation of the signal [138]; for rigid films, only the density and the film thickness play a role. The mechanical behavior of the film with respect to the excitation frequency is determined by the part, real or imaginary, of the propagation wavevector k_x that is predominant. For the operating frequencies of Love mode devices, typically comprised between 80 MHz and 430 MHz, a film is seen as a viscous layer till shear stiffness up to 10^5 Pa, as presented in Figure 2.9. Above this threshold, the film supports the propagation of the guided Love mode rather than its dissipation, leading to the influence of the density of the film only rather than the product of the density by the viscosity.

A possibility to experimentally discriminate between the two extreme mechanical behaviors is obtained via the ratio of the attenuation shift to the phase shift, which is a significant indicator of rigid or viscous interactions between the layer and the vibrating surface. The differentiation of the two cases is seen by canceling alternatively the contributions $\mathrm{d}\sigma$ and $\mathrm{d}\sqrt{\rho\eta}$ in (2.23). For a pure rigid loading, the ratio of the attenuation shift to the phase shift is written

$$\frac{\mathrm{d}\alpha}{\mathrm{d}\phi} = \frac{S_{\alpha,\sigma}}{kS_{\phi,\sigma}} \tag{2.38}$$

and, for a pure viscous loading, the ratio becomes

$$\frac{\mathrm{d}\alpha}{\mathrm{d}\phi} = \frac{S_{\alpha,\rho\eta}}{kS_{\phi,\rho\eta}}. \tag{2.39}$$

The model helps to plot this ratio as a function of the guiding layer thickness t in Figure 2.10 or as a function of the loading layer thickness

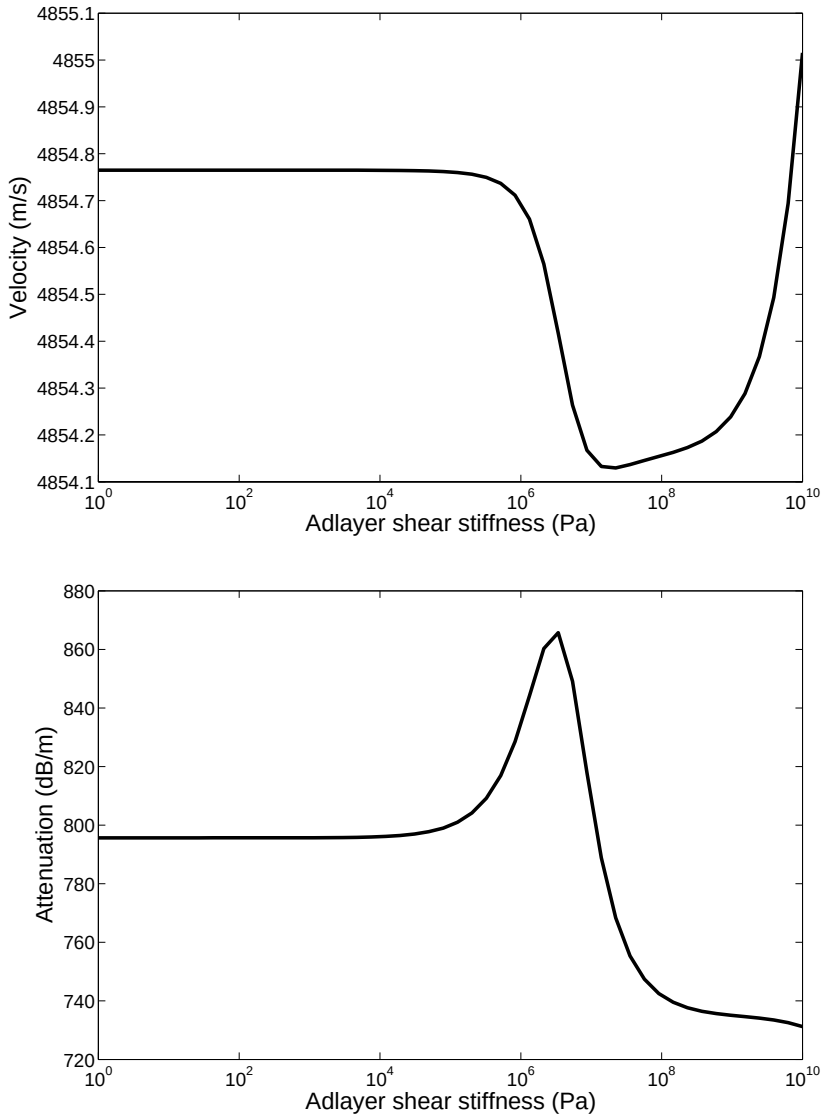


Fig. 2.9 – Viscoelastic transition of an adlayer (thickness 20 nm, density 1400 kg/m^3, viscosity 5 cP) at 123.2 MHz as a function of the shear stiffness of the layer. The transition from Newtonian to Maxwellian behavior appears for a shear stiffness equals to 3.9 MPa.

h in Figure 2.11 for a rigid layer and in Figure 2.12 for a viscous layer for two thicknesses of the guiding layer ($t = 1.2$ μm and 3.2 μm).

2.3.6 Penetration depth and film thickness

The penetration depth δ of shear waves in fluids is an indication of the thickness probed by the acoustic method. The exact value of δ for surface acoustic waveguides is determined by the real part of the wavevector in the viscous layer as determined by the transmission line equivalent model. Its value is close to the one obtained from the well-known relation [163]

$$\delta = \sqrt{\frac{2\eta_C}{\rho_C \omega}} \tag{2.40}$$

from which it slightly differs due to the coupling angle φ_C in the viscous layer. Because of an usually large velocity difference between the rigid guiding layers and the viscous layers, the real part of the coupling angles φ_C and φ_F are almost equal to zero and, therefore, the penetration depth can be identified with the expression given by Eq. (2.40). As example, δ is about 50 nm for water at a frequency of 123.2 MHz (corresponding to the central frequency of our application device).
The acoustic wave "senses" the viscous layer with an exponential decay extending to a thickness about 3δ, after which the acoustic field decays below 10% of its initial value and is neglected. This effect has an impact on the ratio $\mathrm{d}\alpha/\mathrm{d}\phi$ as seen in Figure 2.12. This effect is better appreciated when considering separately the evolution of the viscosity sensitivities, $S_{\alpha,\rho\eta}$ and $S_{\phi,\rho\eta}$, as a function of the viscous layer thickness (cfr. Figure 2.13). The two sensitivities are function of the layer thickness and present a maximum amplitude at different thicknesses: the influence of the viscous layer on the phase is reaching its maximum before the one caused on the amplitude. Such observations let us assume that considering both phase and amplitude shifts could be an opportunity to obtain extra information about the thickness of a viscous film. For a thin viscous layer ($< 0.1\delta$), the ratio $\mathrm{d}\alpha/\mathrm{d}\phi$ becomes similar to the one that would result from a rigid layer. Consequently, a small experimental ratio is not sufficient to conclude that the probed layer behaves as a viscous or a rigid layer. On the other hand, a high ratio is an unquestionable indicator of a viscous interaction, where the hypothesis of a soft layer can be assumed ($\omega\eta_C \gg \mu_C$).

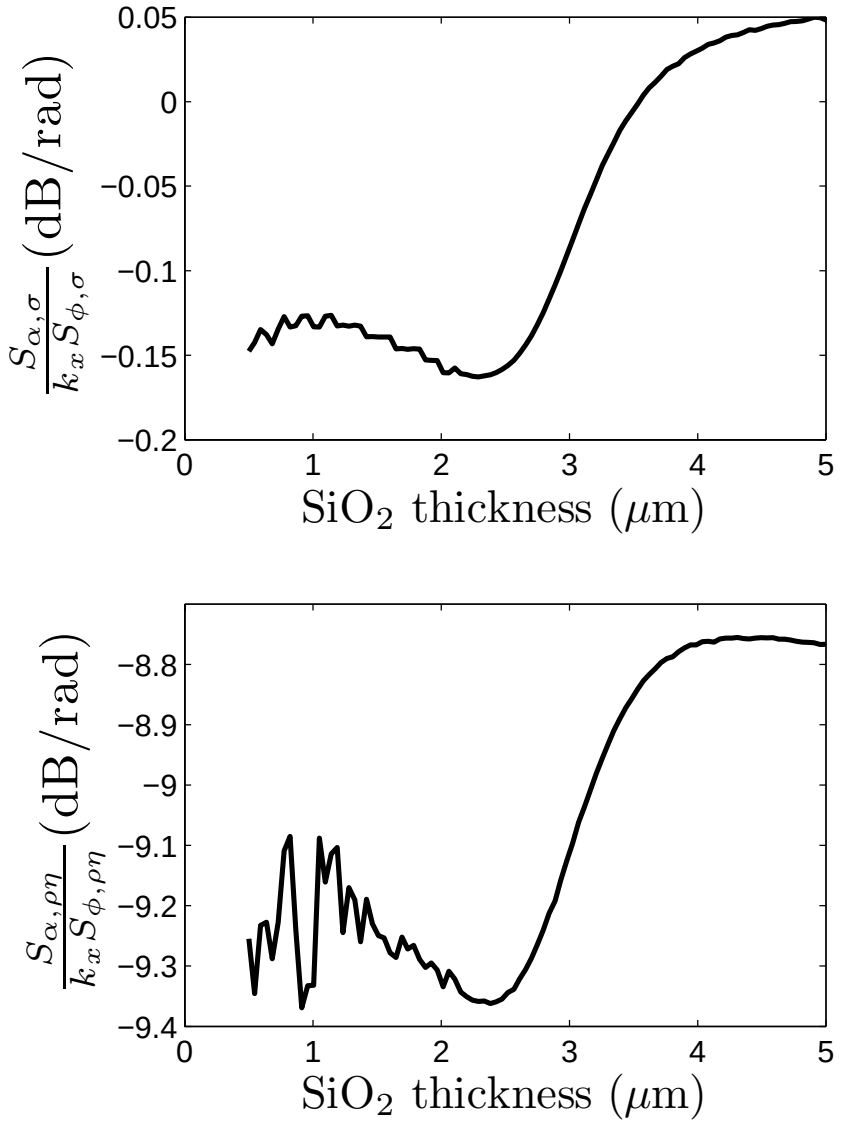


Fig. 2.10 – Theoretical ratio of the attenuation to the phase shift as a function of the SiO_2 guiding layer for (top graph) a pure rigid loading and (bottom graph) a pure viscous loading. The computation is done at fixed frequency $f_0 = 123.2$ MHz (the noise on the curves is due to numerically propagating errors). A small ratio (< 0.15 in absolute value) occurs for a rigid loading, indicating that the amplitude shift is small compared to the phase shift of the signal for such loading, while a high ratio (> 8.8 in absolute value) occurs for a viscous loading. In that latter case, the larger amplitude shift is caused by viscous losses of the acoustic energy along the sensing path.

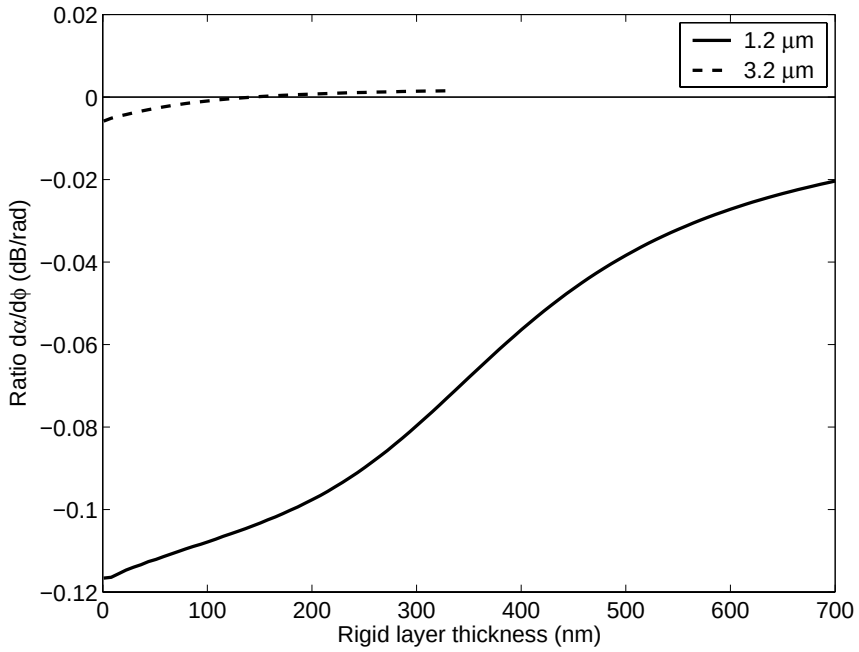


Fig. 2.11 – Theoretical ratio of the attenuation to the phase shift as a function of the thickness of a rigid layer at fixed frequency f_0 = 123.2 MHz for two thicknesses of the SiO_2 guiding layer (t =1.2 and 3.2 μm). The small ratio is diminishing as the loading layer increases

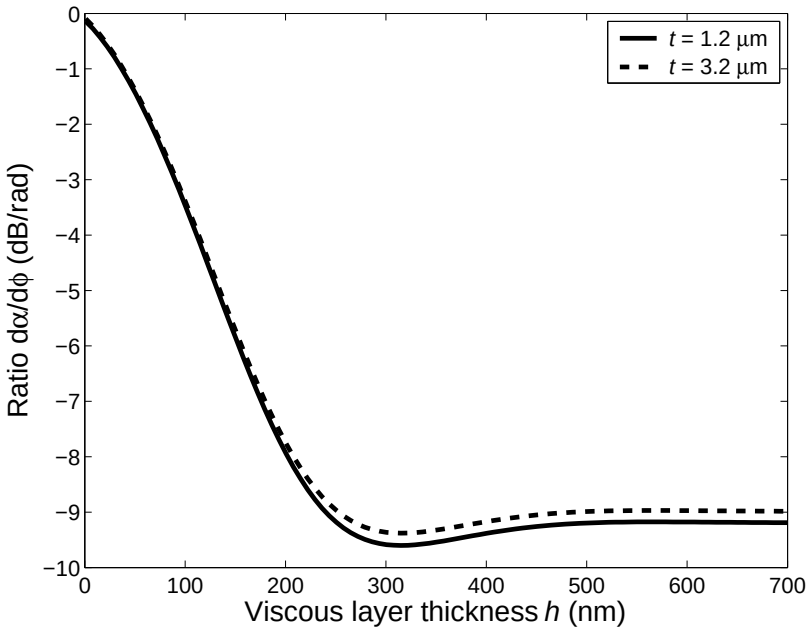


Fig. 2.12 – Theoretical ratio of the attenuation to the phase shift as a function of the thickness of a viscous layer at fixed frequency $f_0 =$ 123.2 MHz for two thicknesses of the SiO_2 guiding layer (t =1.2 and 3.2 μm). The ratio increases from 0 in the absence of loading layer till a saturation at the high value of a bulk viscous liquid when the thickness is above a certain threshold.

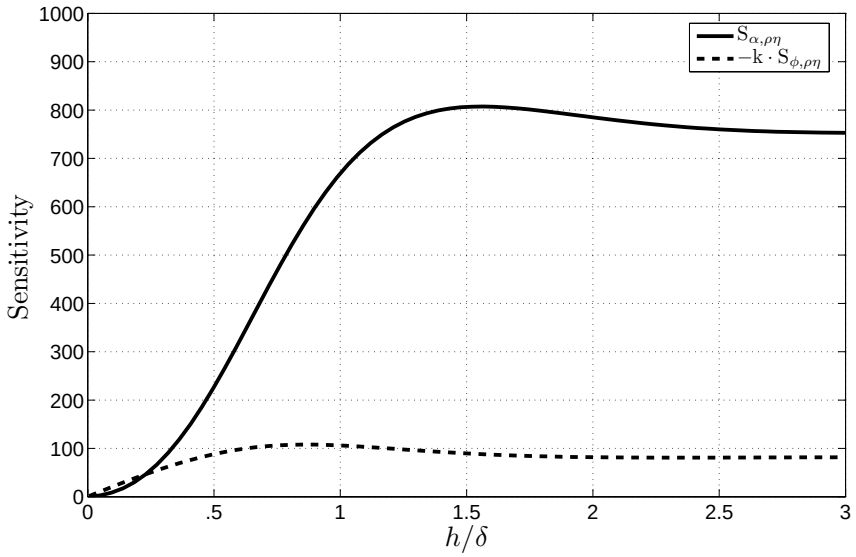


Fig. 2.13 – Values of attenuation and phase sensitivity for a viscous layer loading as a function of the normalized thickness of the loading layer at fixed frequency $f0 = 123.2$ MHz ($\eta_C = 10$ cP).

The viscosity sensitivities ($S_{\phi,\rho\eta}$ and $S_{\alpha,\rho\eta}$) given in Figure 2.8 are therefore valid only when the adsorbed layer becomes thicker than 150 nm; which is far from real biosensing scenarios where the biomolecules layer is hardly thicker than few tens of nanometers and even less.

In biosensing experiments, the exact behavior of the biomolecules is function of their own mechanical and chemical interactions, their affinity for the sensing surface and their affinity between each others and with the solvent. All these parameters influence the actual value of the relaxation period of the biofilm and result in a complex system. As a consequence, the system composed by the acoustic sensor and the surface adsorbed biomolecules is opened to a wide amount of possibilities requiring further assumptions to quantify each of these parameters. In addition, the density, the viscosity and the thickness of a viscous thin layer can not be directly estimated from the two information (insertion loss and phase) resulting from a single SAW measurement. Additional information about one of the value (density, viscosity or thickness) of the film is requested with a measurement technique compatible with surface

acoustic waves. A first possibility is a thickness estimate by AFM [35]. A second possibility is an optical measurement of the film such as ellipsometry or surface plasmon resonance. This latter possibility has been chosen and is described in Chapter 5 [61], however others combination techniques are possible and still need to be investigated.

In the assumed case that the film of biomolecules acts as a viscous layer, it appears that the Love mode biosensor performs as a rheometer. The analysis of the rheological characteristics of the adsorbed film requires an adequate modeling to fit the values of density and viscosity of the film as a function of its thickness. The sensitivity interpretation in this case is schematically depicted by Figure 2.14. Finally, it must be noticed that the best biosensor is the one for which $S_{\phi,\rho\eta}$ is at its maximum value; this optimized device will also present the worse attenuation of all while loaded by the liquid because $S_{\alpha,\rho\eta}$ will be at a maximum value too. A trade-off in the design must be considered to optimize the sensor.

2.3.7 Detection levels and influence of the noise

The minimum amount that can be detected depends of the noise on the measurement. If we denote the noise on the phase by N_ϕ and the one on the signal amplitude by N_α, we notice that in the case of a rigid layer deposition, the following relation must be followed to estimate correctly the surface density resulting from the deposition of the rigid layer from bulk viscosity changes:

$$N_\alpha \leq \left| \frac{S_{\alpha,\rho\eta}}{k_x S_{\phi,\rho\eta}} \right| \cdot N_\phi. \tag{2.41}$$

An identical relation is expressed for the corrected estimation of the bulk mass viscosity change:

$$N_\alpha \leq \left| \frac{S_{\alpha,\sigma}}{k_x S_{\phi,\sigma}} \right| \cdot N_\phi. \tag{2.42}$$

Since the ratio of the viscosity components is high, the corrected estimation of the surface density is not linked to a stringent condition; the estimation of the viscosity change is a problem since the ratio is below 1, thus resulting in a stringent reduction of the amplitude noise to correlate

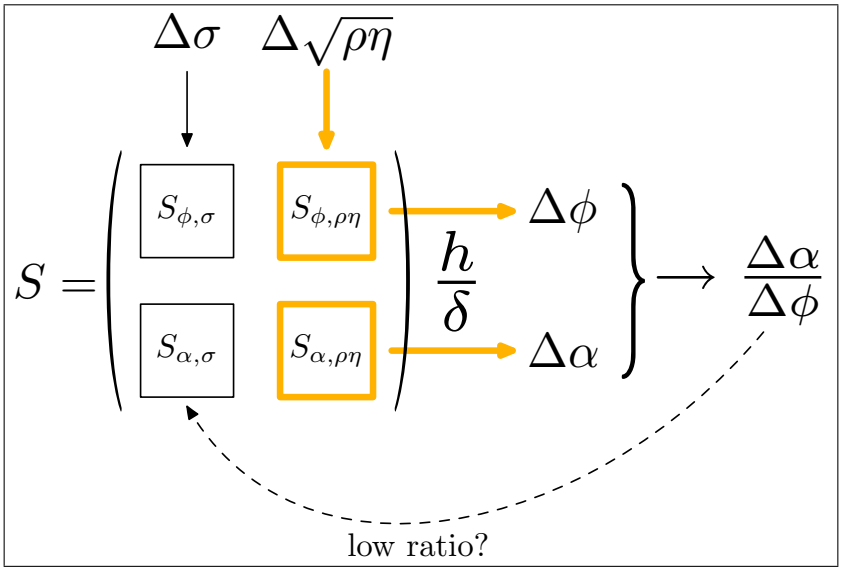


Fig. 2.14 – Schematic description of the interpretation of the Love mode biosensor when considered as a rheological sensor: the variations of amplitude and phase of the acoustic signal are caused by the adsorption on the surface of a thin and soft (i.e. viscous) layer. The density and the viscosity of this layer have both an influence on the signal change, while the ratio of attenuation to phase shifts supports the conclusion of a viscous or a rigid interaction between the adsorbed film and the acoustic probing wave: a high ratio denotes a viscous layer while a low ratio can signify a rigid or a viscous interaction. The values of mass viscosity sensitivities are function of the thickness of the film and the penetration depth unless the film gets thicker than 3 times the penetration depth. For thicker films, the sensor identifies the film to a bulk material. Because of their thickness dependency, the sensitivities are written $S_{\phi,\rho\eta}(h)$ and $S_{\alpha,\rho\eta}(h)$ for $h \leq 3\delta$.

signal changes to actual bulk viscosity variations. The actual detection limit is function of the value of both noises and the minimum mass on the surface that can be detected, σ_{min}, is given for a phase shift at least equal to 3 times the noise on both the phase and the amplitude:

$$\sigma_{min} = \frac{3}{k_x D \left|\mathbf{S}\right|} \left(S_{\alpha,\rho\eta} N_\phi - k_x S_{\phi,\rho\eta} N_\alpha\right) \tag{2.43}$$

where $|\mathbf{S}|$ is the determinant of the matrix of sensitivities. As an example, this equation is applied with the current values of sensitivity to estimate the detection limit of the device as a function of the noise on the signal. The result is plotted in Figure 2.15 and it shows that the detection limit is in the range of tens to hundreds of ng/cm^2, assuming the deposition of a rigid uniform layer.

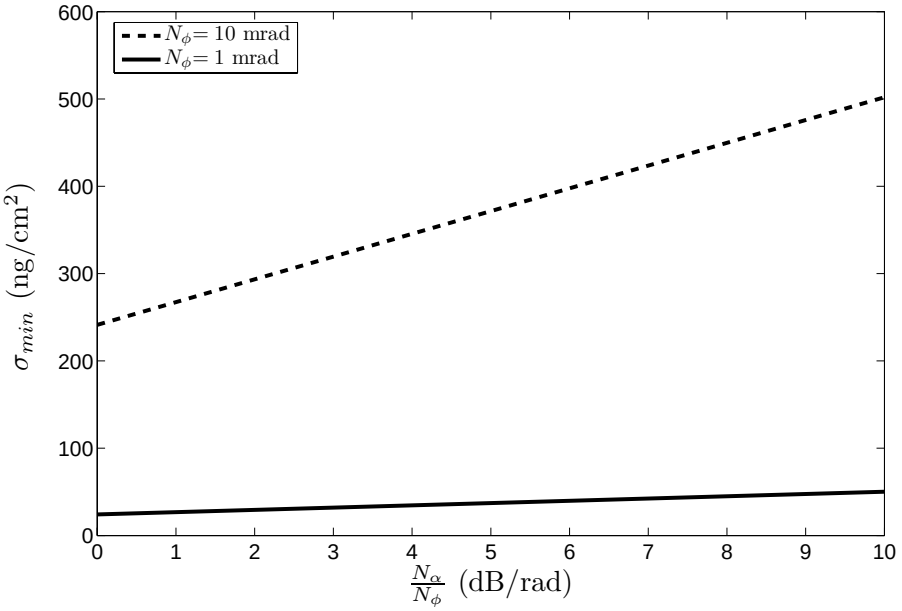


Fig. 2.15 – Influence of the noise on the detection limit: evolution of the minimum surface density detected σ_{min} as a function of the amplitude to phase noise ratio for the example device. A reduction of the noise results in a reduction of the minimum surface density detected. For a phase noise of 1 mrad, σ_{min} is about 30 ng/cm^2, which is approximatively 10% of the surface density of a densely packed and uniform IgG monolayer.

For a viscous film adsorption, the analysis is easily extended but this time by considering only one equation: the value of viscous sensitivities as a function of the adsorbed layer thickness. The following relation must be followed to estimate correctly the mass viscosity of the layer from bulk viscosity changes:

$$N_\alpha \leq \left| \frac{S_{\alpha,\rho\eta}(h)}{k_x S_{\phi,\rho\eta}(h)} \right| \cdot N_\phi. \tag{2.44}$$

This ratio is sketched in Figure 2.12: when the thickness of the layer becomes too small, the restriction on the amplitude noise is getting smaller and smaller. The relation is extremely important to determine which thickness will be impossible to resolve by the measurement. As the amplitude noise N_α is too large, the determination of the mass viscosity of the adsorbed layer can not be determined at all. This might as well happen for a given thickness of the viscous layer, indicating that the discrimination method, between rigid and viscous layers, but also between thick and thin viscous layers, can not be applied for film thicknesses below a threshold thickness h_{min} determined by:

$$\left| \frac{S_{\alpha,\rho\eta}(h_{min})}{k_x S_{\phi,\rho\eta}(h_{min})} \right| = \frac{N_\alpha}{N_\phi}. \tag{2.45}$$

As application example, let assume typical values of N_α=0.01 dB and N_ϕ=2 mrad; their ratio is equal to 5 dB/rad. According to Figure 2.12, the determination of the density of viscous films thinner than 120 nm can not be achieved. In that case, the viscosity was assumed equal to 10 cP, which is a high viscosity in comparison to water. For this high value of viscosity, the penetration depth is about 160 nm, and therefore the threshold film thickness is 75% of the penetration depth. If the viscosity of the film is varied, simulations indicate that this proportionality factor is kept constant. Therefore, for a film with a viscosity as water, for which $\delta = 50$ nm, the threshold value is about 38 nm. As conclusion, for identical values of the thickness of an adsorbed viscous layer, the identification of the density and the viscosity of the film by the Love mode biosensor is facilitated when the viscosity of the film is low. This is due to the fact that the penetration depth in low viscosity films is smaller than in high viscosity films.

2.4 Conclusion

We conclude from our approach that Love mode SAW biosensors must be considered and optimized as viscosity sensors firstly and an independent layer thickness measurement is needed to apply adequately the theoretical model. The mass sensitivity of Love mode surface acoustic wave sensors can be evaluated by different techniques based on incremental modifications of the surface density on the sensing area of the device. The most important conclusion for acoustic biosensors is the following: the acoustic signal presents a mixed contribution of the density and the viscosity interactions of the biomolecules in the adsorbed layers. Modeling is needed to extract both contributions to the acoustic signal. The calibration of the viscous sensitivity and an independent method to measure the layer thickness are needed for an adequate application of the model.

2.5 Additional resources

Matlab M-files to compute the dispersion relation and the sensitivity of Love mode SAW waveguides are archived and documented on the website `http://jmfriedt.free.fr` or available on simple request by e-mail to francisl@ieee.org.

Chapter 3

Fabrication, packaging and calibration of SAW biosensors

> Qui s'aperçoit d'avoir dit ou fait une sottise croit toujours que ce sera la dernière. Loin d'en conclure qu'il en fera bien d'autres, il conclut que celle-là l'empêchera d'en faire.
>
> *Blaise Pascal*
> Pensées

In this chapter, we address in a first part the fabrication aspects of Love mode SAW device and the influence of materials on the dispersion of the acoustic wave for different overlayers. The dispersion in the Love mode device is directly linked to the mechanical properties of the guiding layer and they determine the sensing performance of the waveguide. The main objective is to obtain a high, reproducible and stable gravimetric sensitivity with materials that do not present high acoustic losses. Three materials are investigated: silicon dioxide obtained by plasma-enhanced chemical vapor deposition (PECVD) in a hydrogen-rich atmosphere, zinc oxide obtained by spray pyrolysis deposition, and amorphous silicon germanium obtained by PECVD. These materials are selected because of a shear bulk acoustic velocity lower than the one of quartz, thus allowing their integration in Love modes supported by quartz substrates, and

because of the ability to tailor the mechanical properties with their selected deposition method.

In a second part, the packaging of the Love mode sensor is addressed. The packaging is one significant challenge facing biosensor development. For surface acoustic wave based biosensors, packaging influences the general sensing performance. The acoustic wave is generated and received thanks to interdigital transducers and the separation between the transducers defines the sensing area. Liquids used in biorecognition experiments lead to an attenuation of the acoustic signal while in contact with the transducers.
We have developed a liquid cell with an original approach based on photodefinable epoxy SU-8 that prevents the presence of liquid on the transducers, has a small disturbance effect on the propagation of the acoustic wave, does not interfere with the biochemical sensing event, and leads to an integrated sensor system with reproducible properties. The liquid cell is achieved in two steps. In a first step, the SU-8 is precisely patterned around the transducers to define 120 μm thick walls. In a second step and after the dicing of the sensors, a glass capping is placed manually and glued on top of the SU-8 walls. This design approach is an improvement compared to the classical solution consisting of a pre-molded PDMS cell that must be pressed against the device in order to avoid leaks, with negative consequences on the reproducibility of the experimental results. We demonstrate the effectiveness of our approach by protein adsorption monitoring. The packaging materials do not interfere with the biomolecules and have a high chemical resistance to resist to the chemical cleaning of the sensing surface for the reusing of the sensor. For future developments, wafer level bonding of the quartz capping onto the SU-8 walls is suggested.

In a third part, the experimental evaluation of the mass sensitivity of the Love mode SAW biosensor is investigated. We present techniques that can be classified in two approaches. The first approach is a destructive technique where the dispersion relation is recorded by a chemical wet etching procedure, which enables the continuous monitoring of the transfer function during the etching of the entire guiding layer. The second approach is based on a incremental variation of the surface density by adding or removing thin layers of different materials in known

quantities. The mass sensitivity is estimated in different cases: etching of a thin gold layer, copper electrodeposition, and surface adsorption of an ionic surfactant. We focused our techniques to the actual operating conditions of the sensor; that is on the diced and mounted sensor, in a liquid environment, and with surface density variations in the same order of magnitude as the targeted biochemical sensing application (below 1 μg/cm^2). The results obtained by these different techniques are evaluated with respect to the theoretical approach described in Chapter 2.

3.1 Love mode SAW device fabrication

This section describes the basic structure of the Love mode SAW sensor. The fabrication techniques and the integration of specific guiding thin films are presented as well. The growth of thin films can results in materials either amorphous or crystalline. In polycrystalline materials, grain boundaries and spatial inhomogeneities scatter the acoustic energy and, therefore, increase the insertion loss of the waveguide. We report here the fabrication of two amorphous materials (silicon dioxide and silicon germanium) and one polycrystalline material (zinc oxide). The reported techniques are intended to grow materials with mechanical characteristics as different as possible than the substrate in order to enhance the energy concentration in it so that the sensitivity of the acoustic structure to a surface perturbation is maximized.

3.1.1 Basic structure of the sensor

The Love mode sensor is obtained by a 500 μm thick ST-cut (42.5° Y-cut) quartz substrate with interdigital transducers patterned in 200 nm thick sputtered aluminum. Split fingers electrodes geometry help to reduce the triple transit interferences. The guiding layer is a thick overlayer of silicon dioxide (description here after). This layer was deposited by plasma enhanced chemical vapor deposition (Plasmalab 100, Oxford Plasma Technology, England) up to 5.2 μm. Because devices with thick guiding layers showed a large insertion loss while loaded with water, we used for most of the experiments a 1.2 μm thick guiding layer. The fingers of the interdigital transducers are 5 μm wide and equally spaced by 5 μm ($\lambda_0 = 40$ μm). The acoustic aperture W is equal to $80\lambda_0$ (3.2 mm), the total length of each transducer is $100\lambda_0$ (4 mm) and the distance

center to center of the IDTs is $225\lambda_0$ ($L = 9$ mm, $D = 5$ mm). The sensing area was defined by covering the space left between the edges of the IDTs by successive evaporation and lift-off of 10 nm of titanium and 50 nm of gold. The resulting Love mode device is photographed in Figure 3.1.

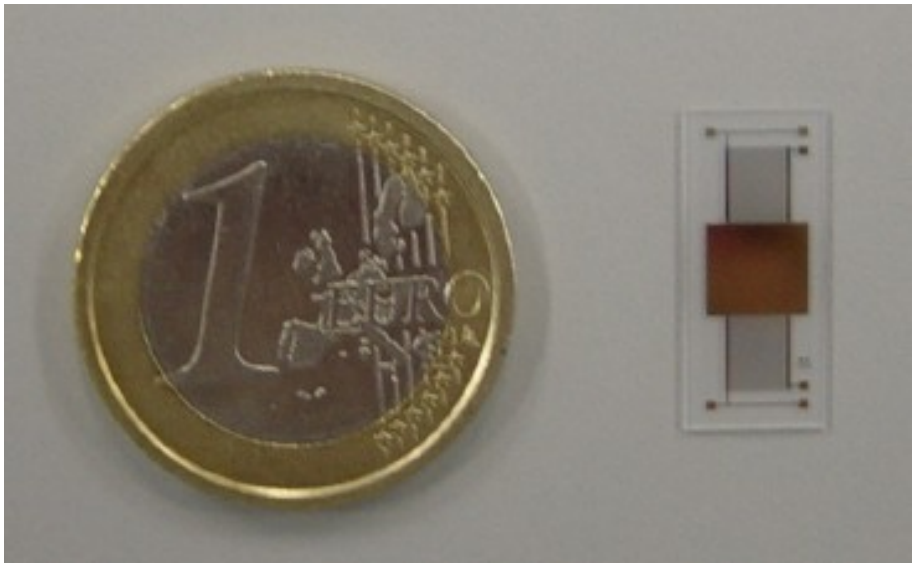


Fig. 3.1 – Photography of the Love mode device compared to a 1 € coin.

The device was packaged by using a method described in the rest of this chapter [56]. The sensor mounted and wire-bonded to an epoxy printed circuit board had its transfer function recorded by an HP4396A Network Analyzer. A home-made program was used to log the data of the Network Analyzer to a PC through the GPIB interface. The central frequency f of the transfer function is 123.5 MHz.

3.1.2 Hydrogenated PECVD silicon dioxide

The deposition of silicon dioxide by the PECVD technique has several advantages. The deposition is obtained from tetraethylorthosilicate (TEOS) and oxygen (O_2) plasma [43] or from silane (SiH_4) and nitrous oxide (N_2O) mixtures [145]. Variations in the processing parameters influence strongly the chemical characteristics of the deposited film with consequences on the mechanical and optical properties of the silicon

dioxide [43,145]. By adjusting the deposition parameters (i.e. substrate temperature, gases flow, RF power, pressure, gases dilution, etc.), one can obtain films with various characteristics but at a high cost of complicated investigations. The complexity in plasma deposition makes very difficult to directly link processing parameters to the final result and can be tackle by genetic algorithms [79].

In the present case, as the material is expected to be of fairly low mechanical stiffness, in order to reduce as much as possible the sound velocity in the guiding layer and therefore enhance the acoustic dispersion in the acoustic waveguide, silicon dioxide layers were deposited from silane and nitrous oxide diluted with hydrogen. It was reported in the literature that such deposition results in a modified material with a low refractive index and a stable integration of the hydrogen in the film [113, 187, 206]. Although it was not possible to find any reported information about the influence of hydrogen on the mechanical characteristics of the layer, our investigation indicates that the engineering of this material results in low mechanical stiffness and different growing properties when compared to other deposition parameters. A noticeable modification in the mechanical properties is seen by changing the hydrogen gas flux. The silicon dioxide obtained with a higher hydrogen flux results in a soft layer of silicon dioxide, as indicated in Table 3.1. Surface acoustic wave offer a useful method to determine mechanical properties of thin films [89,134,215]. In the present case, the extraction of the mechanical characteristics of the thin film, i.e. the shear stiffness and the density, were obtained by a least-square fitting of the Love mode dispersion of experimentally measured resonance frequencies at different wavelengths. To that purpose, test wafers were patterned with 6 different wavelengths regularly spanned (λ =18, 22, 28, 40, 76 and 120 μm) and the film thickness was measured with a DekTak stylus profilometer. A more intensive investigation with adequate analytical tools was not intended in this thesis but should be considered for future works.

3.1.3 Spray pyrolysis deposition of zinc oxide

Zinc oxide has recently been introduced has guiding material for Love mode applications. Its mechanical properties are much more suited than silicon dioxide and it has shown already a better sensitivity [37, 106].

	SiO_2 A	SiO_2 B
SiH_4 [sccm]	35	35
N_2O[sccm]	1200	1200
N_2 [sccm]	400	400
H_2 [sccm]	400	400, 600, 800
		(1/3 of time each)
Wafer T° [°C]	300	300
RF plasma power [W]	100	100
Growth rate [nm/min]	190	135
Density ρ [kg/m^3]	∼2457	2615
Shear Lamé constant μ [GPa]	∼22	8.3

Table 3.1 – Fabrication parameters and mechanical properties of PECVD SiO_2 with different hydrogen concentration during deposition.

Zinc oxide is a piezoelectric semiconductor. In order to test the efficiency, we have been interested in the deposition of zinc oxide by spray pyrolysis.
The spray pyrolysis deposition technique (SPD) of ZnO was primarily intended for the low-cost fabrication of buffer layer for solar cells and for capacitive gas sensors. The method consists in spraying a solution of a salt of the material to deposit in small droplets above the heated substrate. The technique does not need a reduced pressure. As example, zinc oxide thin films are obtained by spraying a 0.1 to 1 M solution of zinc nitrate or zinc acetate. The reactions occurring during deposition and the influence of various parameters on the morphology, crystalline orientation, conductivity and optical properties for a large variety of pure or doped thin films of noble metals, metal oxides, spinel oxides, chalcogenides and superconducting compounds are well described in the literature [18, 40, 149].

However, the application of the technique to acoustic waveguides has never been investigated although it possesses an unused potential for the realization of highly sensitive biosensors at low production costs and with a huge versatility for tailored applications. So far, the inte-

gration of SPD films on acoustic waveguides has been limited to CdS thin film gas sensor [159] and for the realization of SAW filters where the ZnO is used for its piezoelectricity [112].

The SPD setup used presently was experimental (see Figure 3.2) and the reproducibility of the films was difficult to obtain, presented a low control of the growth rate and large inhomogeneities over the substrate. Thin films were obtained by the spraying of a 0.1 M solution of zinc acetate for different times between 10 and 45 minutes and temperatures between 150 and 450 °C. The thin films were sputtered on a quartz substrate with patterned aluminum IDTs having a wavelength of 40 μm. The temperature and the spraying solution composition are important during the deposition. We tested the deposited material and it presented different morphologies according to the temperature and the time of deposition. The film thicknesses measured by Rutherford Back-Scattering (2 MeV alpha particles,$\theta = 170°$) are reported in Figure 3.3. The growth rate has a similar value of 5 ± 1 nm/min at 250 °C and 350 °C. The growth rate decreases for higher temperatures, and is 3.6 ± 1.5 nm/min at 450 °C .

Three different types of microstructure are observed, function of the deposition time and the temperature. The first type of microstructure shows ZnO conglomerates randomly distributed on the substrate surface (Figure 3.4(a)); it is typical of a low deposition time or low temperatures (below 250 °C). The second type of microstructure presents a good coverage of the substrate but a very rough surface (Figure 3.4(b)); it is seen during the deposition for any kind of time and temperature. It corresponds to the first ZnO crystals randomly oriented. The third type of microstructure happens when the deposition time is long enough, or the temperature high enough, then the C-axis orientation perpendicular to the surface is thermodynamically favored and the growth of columnar crystal takes place (Figure 3.4(c)). In the SEM picture, one sees the top of the columnar crystals. The diameter of the columns is about 100 nm, while their height can be estimated equals to the film thickness (i.e. $\sim$ 200 nm). These observations are correlated by the X-ray diffraction measurement of the samples, where the last microstructure has the highest peak intensity of the C-axis oriented crystal (not reported here).

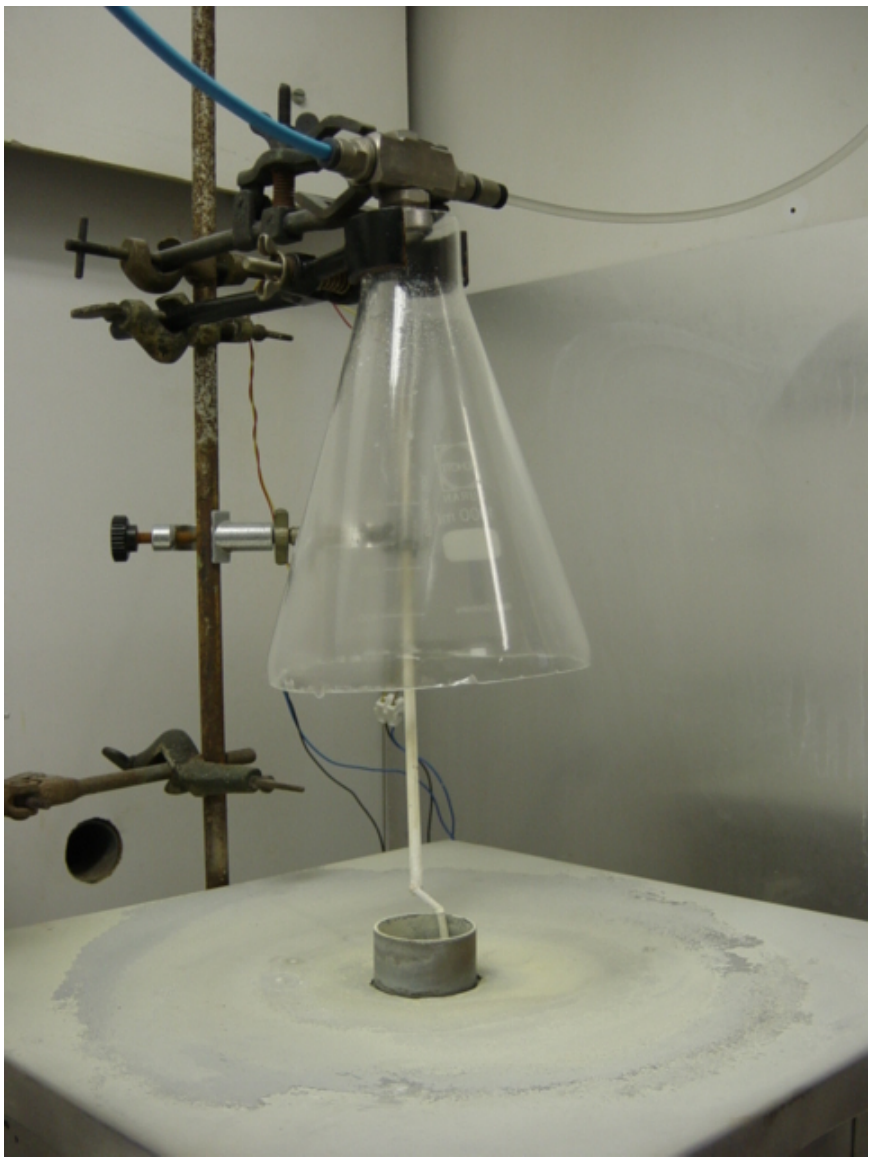


Fig. 3.2 – The spray pyrolysis deposition setup. A nozzle (top part) sprays a solution of zinc acetate over the heated substrate (bottom part).

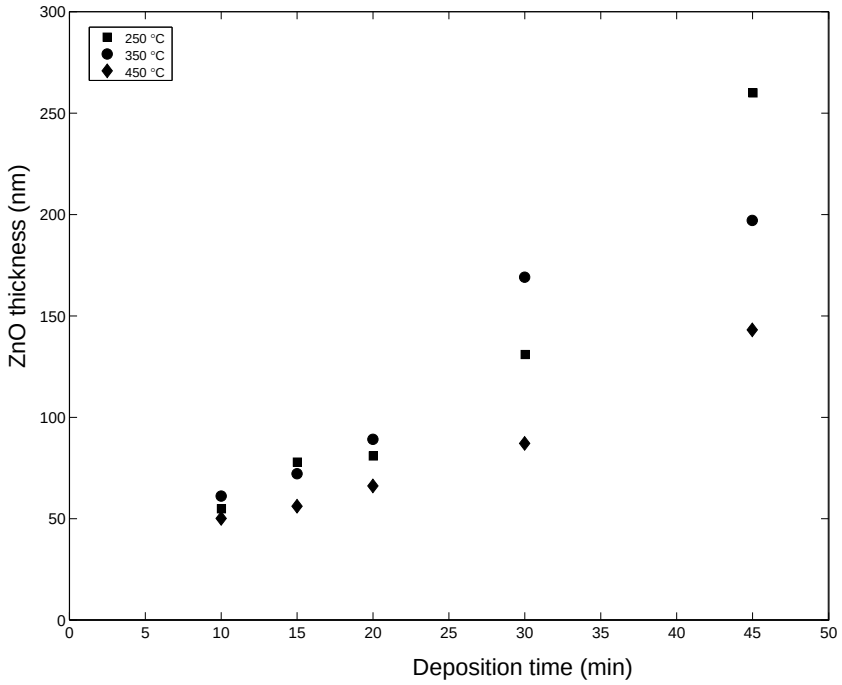
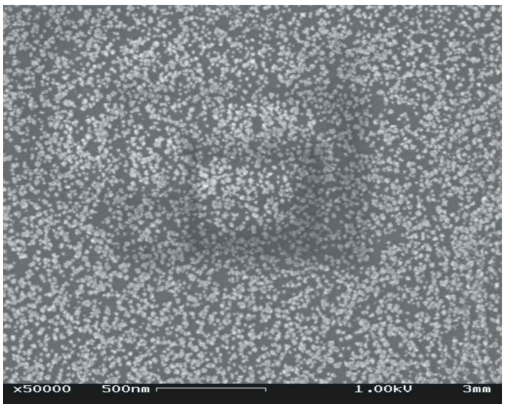
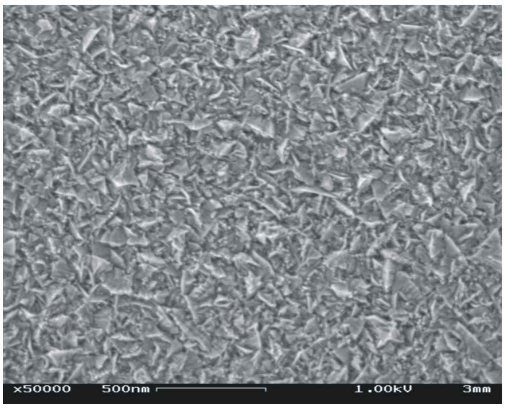


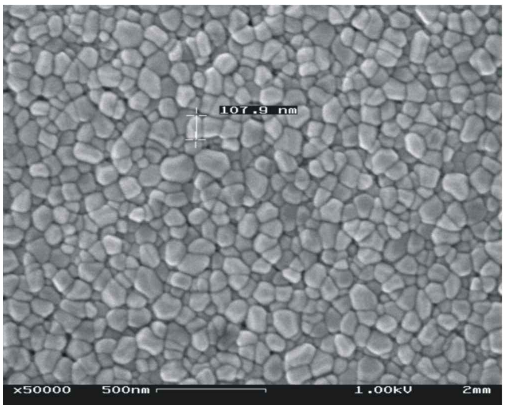
Fig. 3.3 – Thickness of the ZnO grown with different temperature as given by RBS.



(a) 150 °C, 5 min.



(b) 250 °C, 30 min.



(c) 450 °C, 20 min.

Fig. 3.4 – Scanning Electron Microscope image of ZnO grown by Spray Pyrolysis Deposition .

From a mechanical point of view, the data collected were not sufficient to extract the values of density and shear modulus. The dispersion curves are given in Figure 3.5; the dispersion is stronger for the SPD ZnO than for silicon dioxide, e.g. 4940 m/s for a 1.2 μm thick H-rich PECVD SiO_2. Since the density of ZnO (ρ = 5600 kg/m^3) is higher than SiO_2, the increased dispersion has to come from a very low shear compliance that can be originated from the presence of voids between the ZnO crystals.

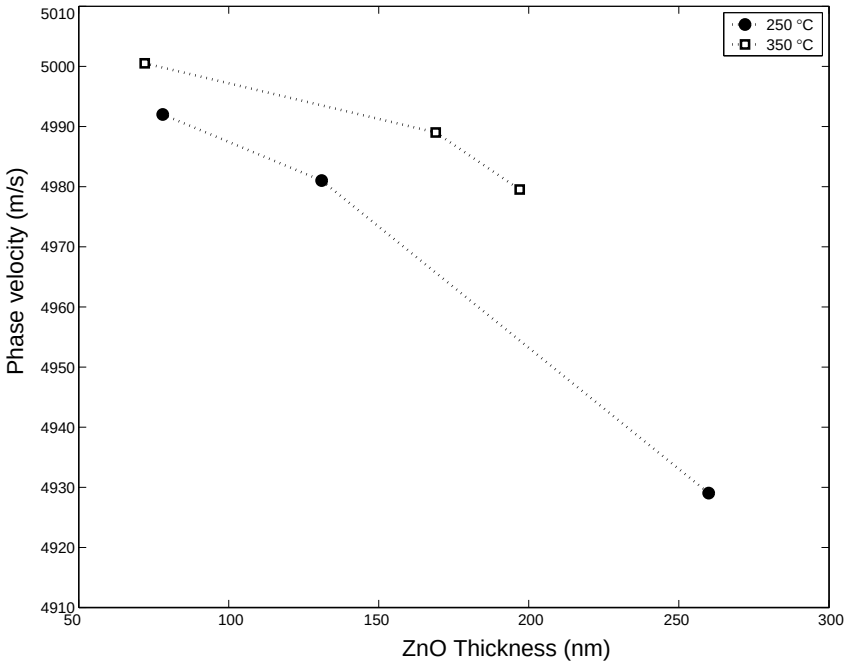


Fig. 3.5 – First Love mode velocity as a function of the thickness recorded for two SPD grown ZnO layers on a quartz substrate with shear wave propagation ($\lambda = 40$ μm).

3.1.4 PECVD amorphous silicon germanium

Silicon germanium is a material of variable composition that can be tailored during PECVD deposition. This material has initially been developed for solar cells. The actual material deposited is a-Si_xGe_{1-x}:H and the mechanical characteristics are function of the concentration of

silicon, germanium and hydrogen in the layer [69,172,204,207]. A 1 μm thick layer has been deposited by PECVD (Temperature 400 $^{\circ}C$, 100 sccm GeH_4 diluted in 10% H_2, 30 sccm SiH_4, 40 sccm H_2, 30 W for HF Power, pressure 2 Torr, growth rate 60 nm/min). The deposition on a quartz wafer was accompanied by the formation of bubbles in at the interface between the quartz substrate and the deposited SiGe layer. The bubbles are mainly located along the aluminum electrode lines as seen in Figure 3.6. The delamination of the film due to a poor adhesion and stress effects was observed too.

The material deposited presented a density of 4899 kg/m^3 and a shear stiffness of 21.56 GPa as characterized by the acoustic propagation at 6 wavelengths. The theoretical phase and frequency sensitivities are reported in Figure 3.9.

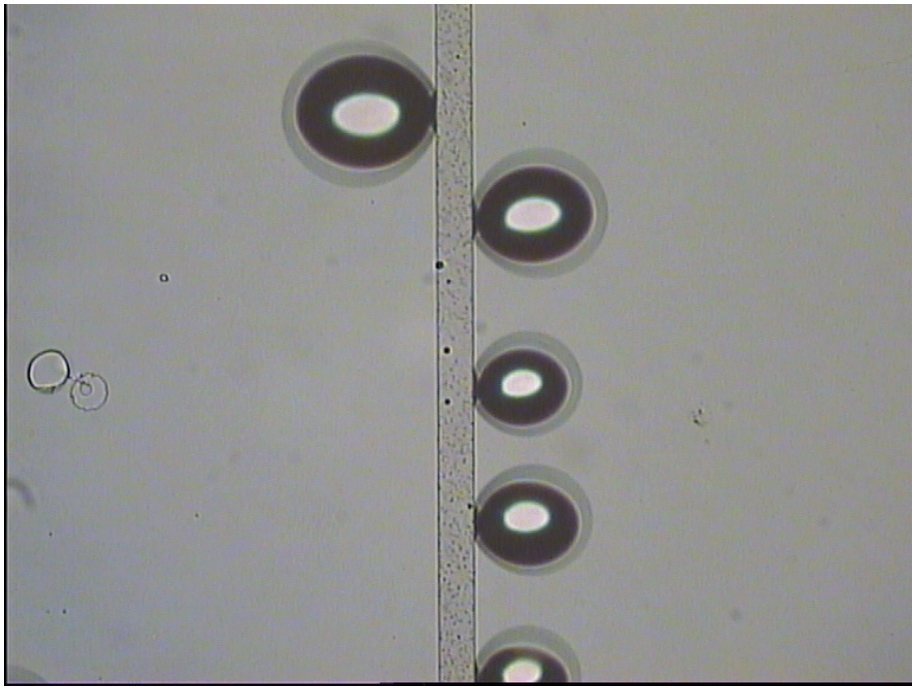


Fig. 3.6 – Bubbles formation along an aluminum line under the amorphous SiGe layer.

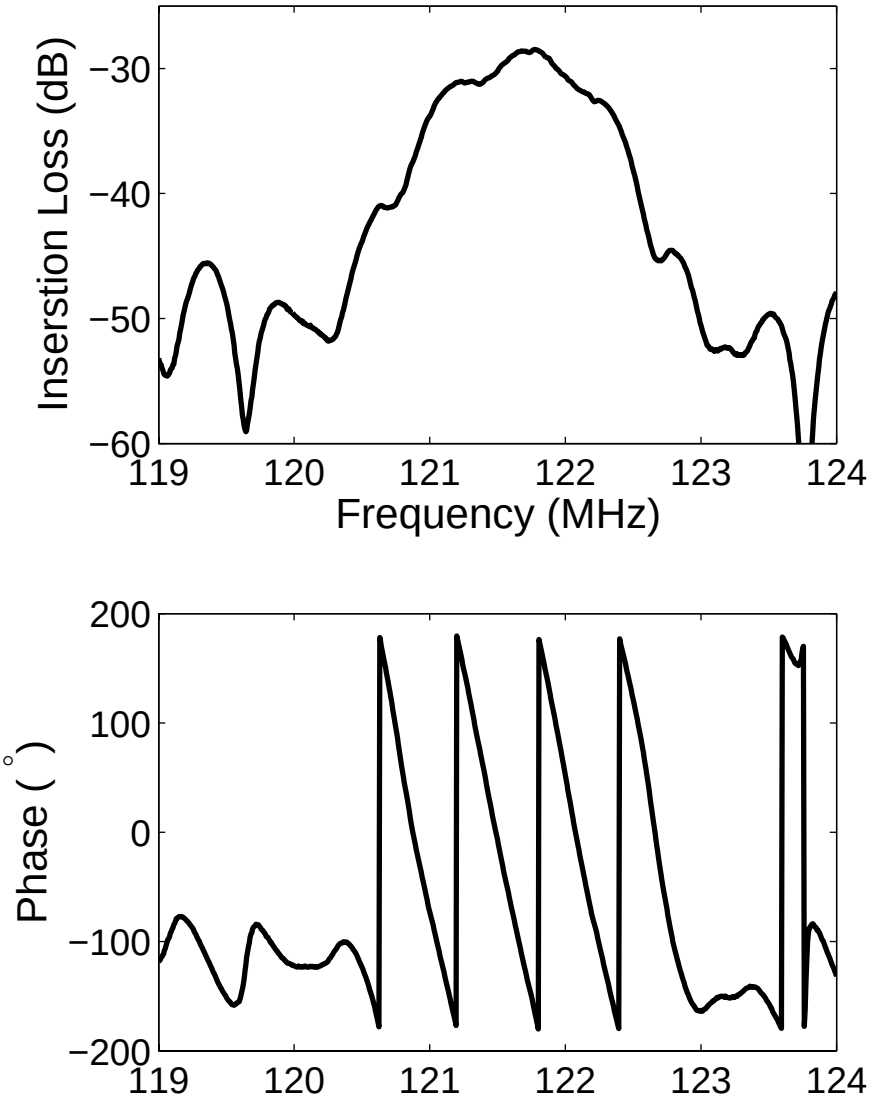


Fig. 3.7 – Transfer function for a 1 μm thick SiGe overlayer measured with transducer of periodicity 40 μm.

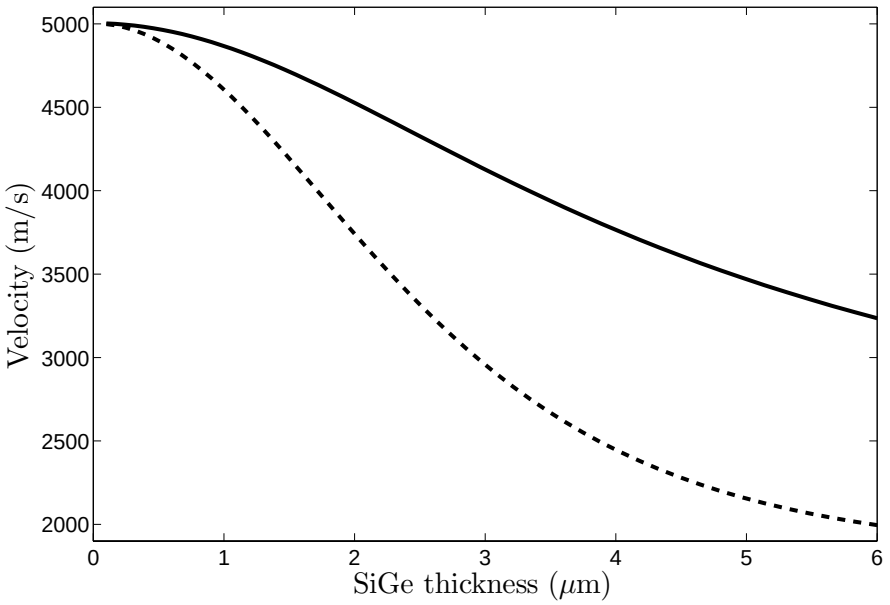


Fig. 3.8 – Phase (solid line) and group (dashed line) velocities as a function of the SiGe thickness for $\lambda = 40$ μm.

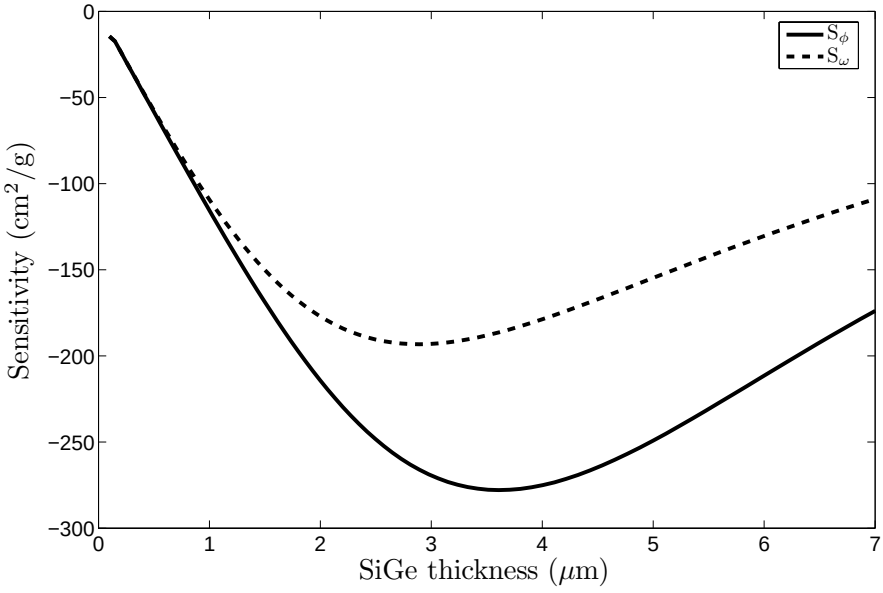


Fig. 3.9 – Theoretical phase and frequency sensitivities of the Quartz/SiGe Love mode structure *vs.* the SiGe thickness for $\lambda = 40$ μm

3.2 Liquid cell design

3.2.1 The packaging issue of SAW biosensors

The transfer function of the device, which relates the amplitude of an AC electrical signal at the output transducer to its value at the input transducer, is affected when a liquid with a high dielectric constant value is partly or fully contacting the transducers. As example, Figure 3.10 shows the effect of deionized water in contact with any of the transducers on a quartz substrate. The attenuation observed in the amplitude and the phase of the transfer function is mainly due to an extra capacitance loading of the transducers; more details related to this effect are given in Appendix B. The intensity of the attenuation is function of the value of the electromechanical coupling constant K^2 of the piezoelectric substrate. It is more intense for low K^2 substrates such as quartz than for high K^2 substrates such as lithium niobate or lithium tantalate. For Love-mode sensors, it also depends of the thickness of the guiding dielectric overlayer that acts as shielding and reduces the interaction with liquids.

In any cases, the signal attenuation affects the general performance of the sensor from the instrumentation and the sensing aspects. It results in a lack of correlation between surface changes caused by the biomolecules adsorption and the SAW velocity changes measured by phase shifts in the transfer function. Therefore, one desires a method for the efficient shielding of the IDTs against liquids that serves in the same time as liquid holder, namely a *liquid cell*. Numerous examples of liquid cell are reported in the literature [24, 66, 67, 185]. Typically, they consist in a pre-molded polydimethylsiloxane (PDMS) cell or in a mechanically drilled Teflon cell that comes in close contact with the device. The cell is mechanically pressed against the surface of the sensor in order to avoid leaks. Despite the flexibility allowed by external liquid cells, these methods miss an integration step at the device processing scale. A liquid cell integrated during the fabrication of SAW biosensors open and enhance their application: a well designed liquid cell maximizes the sensing surface and minimize interactions with the acoustic wave and with the biochemical species. Beside the liquid cell itself, Jakoby and Vellekoop suggested to circumvent the interaction issue thanks to a shielding metalization applied on the device-liquid interface [100]. They investigated

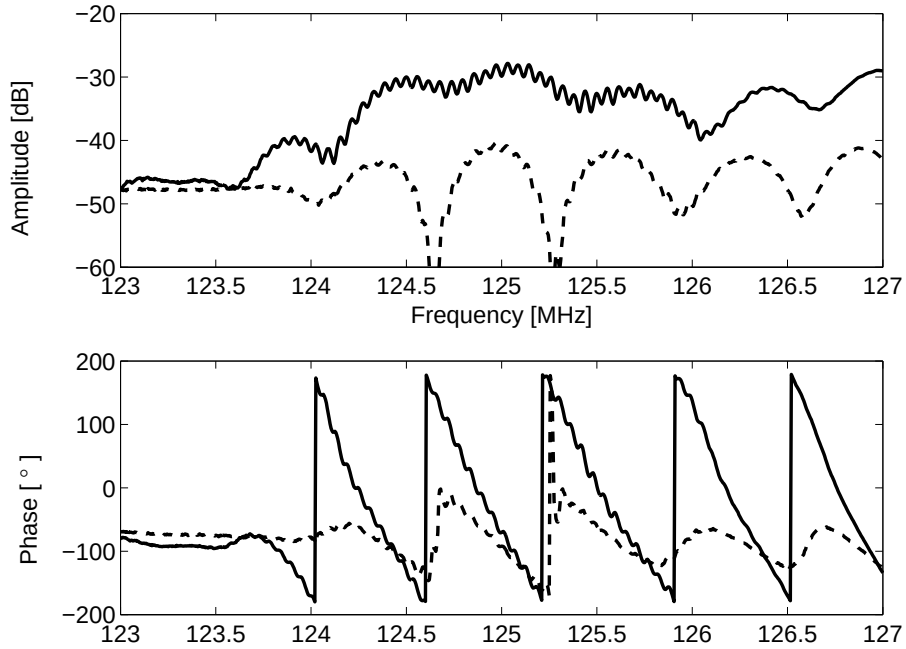


Fig. 3.10 – Experimental record of the transfer function of a quartz substrate SAW device showing the effect of water on the transducers. The top graph is the amplitude and the bottom graph is the phase of the electrical signal passing through the acoustic device as a function of the frequency. The solid line is the transfer function in air while the dashed line is the device loaded with water on one or on the two transducers, either partly or totally covering the electrodes of the transducers.

theoretically and experimentally the influence of such metalization extending on the transducers on their electrical parameters. Although the influence of the metal layer on the transfer function was not detailed, this method should be considered as an additional and efficient method to further eliminate any electrical interactions between the sensed media and the electrical transduction.

Although the fabrication of SAW biosensors is largely described in literature, the issue of their packaging is poorly documented. Only recent efforts address this issue, in particular the group of Länge emphet al. who developed a flow cell with a disposable polymer encapsulation of the SAW sensor, defined by stereolithography, and the electrical instrumentation of the device by capacitive coupling of the contact pads in order to reduce the volume of the flow cell to 60 nL while classical methods are practically limited to 50 μL [120, 121].

In this thesis, we address the design and the fabrication of a liquid cell that allows the packaging of SAW biosensors. The liquid cell aims at three characteristics:

- it prevents the presence of liquids on the IDTs;
- it has a small disturbance effect on the propagation of the surface acoustic wave;
- it does not interfere with the biochemical sensing event.

Our approach is based on the protection of the IDTs and of every area out of the acoustic sensing area by a vertical structure above them. The protecting structure is made of a polymer spacer defined between the sensor surface and a rigid capping layer atop of the spacer. Microfabrication techniques are required for the fabrication of the liquid cell. They allow to reduce the lateral dimensions of polymers that cause acoustic attenuation while in contact with the surface. Therefore, these techniques help to minimize interactions between polymers and the acoustic wave. In addition, they also allow the integration of the packaging at the wafer processing level with reproducible characteristics that address the micron-range scale of the sensor.

Four aspects have been taken in consideration in the design of the liquid cell: (1) the analyte solution must be correctly displayed on the sensing area; (2) the rigid capping layer above the IDTs must not come in contact with the electrodes to avoid a damping of the acoustic wave and their capacitive loading; (3) polymers as spacer cause an acoustic attenuation, consequently these materials must cover the smallest length of the acoustic path on the sensing area; and (4) the sensing area must be kept open for its cleaning prior to any biochemical recognition experiment, for instance with an UV-O_3 cleaning treatment.
Additionally, the packaging is required to withstand the cleaning procedure without contaminating the biochemical solutions. This involves the use of materials presenting good chemical resistance to organic solvents and to UV-O_3 surface treatment.

The SU-8 is a photodefinable epoxy selected to perform the spacer function [97]. Its selection is based on adequate properties:

- photosensitive that allows for a precise patterning of its structure around the IDTs by using standard photolithography techniques;
- high thicknesses attainable (up to 500 μm in one step, much thicker than other photosensitive encapsulant materials like benzocyclobutene –BCB– and polymethylmethacrylate – PMMA) with a high aspect ratio about 1:25;
- stiff epoxy leading to smaller absorption of the acoustic signal than soft polymers;
- good chemical resistance to a wide range of organic solvents and of surface treatments;
- low thermal budget and good adhesion on various materials.

The SU-8 spacer shaped as walls around the IDTs performs a continuous physical separation between the transducers and the sensing area. Because of its position above the acoustic path, this separating wall must be thin to minimize the acoustic damping and wide enough to assure a continuous and rigid physical contact with the sensor. In the present case, a compromise has been found with a 150 μm wide wall. Outside the acoustic path, the walls are larger to increase the adhesion

surface between the SU-8 and the sensor on one side, and with the capping layer on the other side. As capping material, quartz is selected because of its mechanical stiffness, its optical transparency that allows to visually check for the unwanted presence of liquids above the capped transducers, its electrical insulation to avoid interaction with the electromagnetic field emitted by the IDTs, and finally its resistance to a numerous amount of chemical products and surface treatments.

3.2.2 Liquid cell fabrication

We have used a two steps method to fabricate the liquid cell. The first step is achieved at the wafer level. It consists in the patterning of the SU-8 walls. The second step is achieved at the device level after the dicing of the wafer. It consists in the manual placement of the quartz capping. The fabrication methodology is schematically depicted in Figure 3.11 and described for a particular example here after. The fabrication method can be extended to various types of substrates and transducers designs without requiring extra developments.

The liquid cell was fabricated on a Love-mode SAW devices made on a 3 inches diameter and 500 μm thick ST-cut (42.5° Y-cut) quartz substrate (China National Scientific Instruments and Materials Corp., Hangzhou, P. R. of China) covered with a 1.2 μm thick silicon dioxide layer obtained by plasma-enhanced chemical vapor deposition (Plasmalab 100 from Oxford Plasma Technology, England). The IDTs have 100 finger pairs each with L=9 mm, W=3.2 mm and D=5 mm. The finger electrodes were made of 200 nm thick sputtered aluminum with split-finger geometry to minimize ripples in the passband of the device; each finger is 5 μm wide, and equally spaced such that the finger pairs periodicity corresponds to an acoustic wavelength λ of 40 μm.

For the first step, SU-8 walls with a thickness about 120 μm were obtained by using the following recipe. Photosensitive SU-8 type 2075 (Microchem Corp., MA) was spin coated with an acceleration of 100 RPM/s to reach 500 RPM that was held for 10 seconds, and followed by an acceleration of 300 RPM/s to reach 1500 RPM that was held during 30 seconds. After the spinning, the resist was baked for 3 hours at 95°C on a hotplate after a slow temperature ramp up in order to avoid stresses cracks in the epoxy layer. The SU-8 patterns were obtained by soft con-

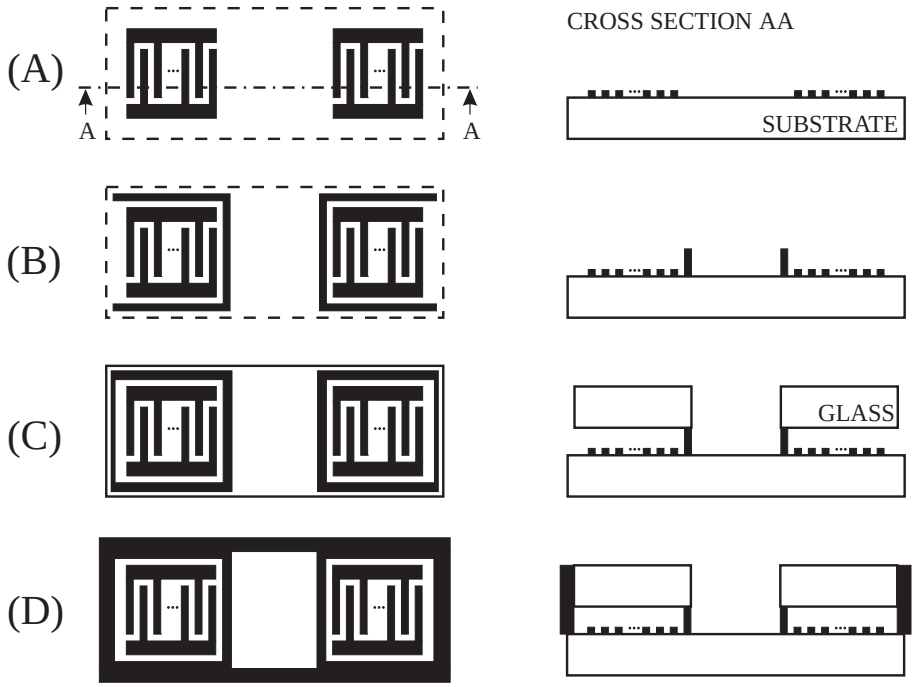


Fig. 3.11 – Schematic of the fabrication process. On each drawing, the left side is a top view of the device and the right side is the cross section AA. (A) Initial SAW device is a part of the wafer. (B) SU-8 walls are patterned partly around the transducers and the wafer is diced to release each sensor. (C) The sensor is attached to the printed circuit board and the contact pads are wire bonded to it (step not shown), the top part of the SU-8 walls is manually covered with an epoxy glue, immediately followed by the placement of the quartz glass capping and the curing of the epoxy. (D) The left parts are filled with the same epoxy glue to complete the protection and the packaging of the device. The liquid cell defines a well of precise dimensions above the sensing area of the packaged sensor.

tact lithography on a Karl-Süss MA6 mask aligner (SUSS MicroTech Inc., VT) for 5 cycles of 10 seconds and a rest time of 60 seconds between each exposure cycle. The exposure was followed by a baking of 15 minutes at 95°C on a hotplate after a slow temperature ramp up to finish the reticulation of the SU-8. The unexposed epoxy was then dissolved in propylene glycol monomethyl ether acetate (PGMEA) with ultrasonication for 10 minutes. Figures 3.12 and 3.13 show the resulting SU-8 structure patterned around the IDT. Following that step, the wafer was diced to release each sensors with the patterned SU-8 walls. The devices were subsequently wire bonded to a printed circuit board for electrical characterization.

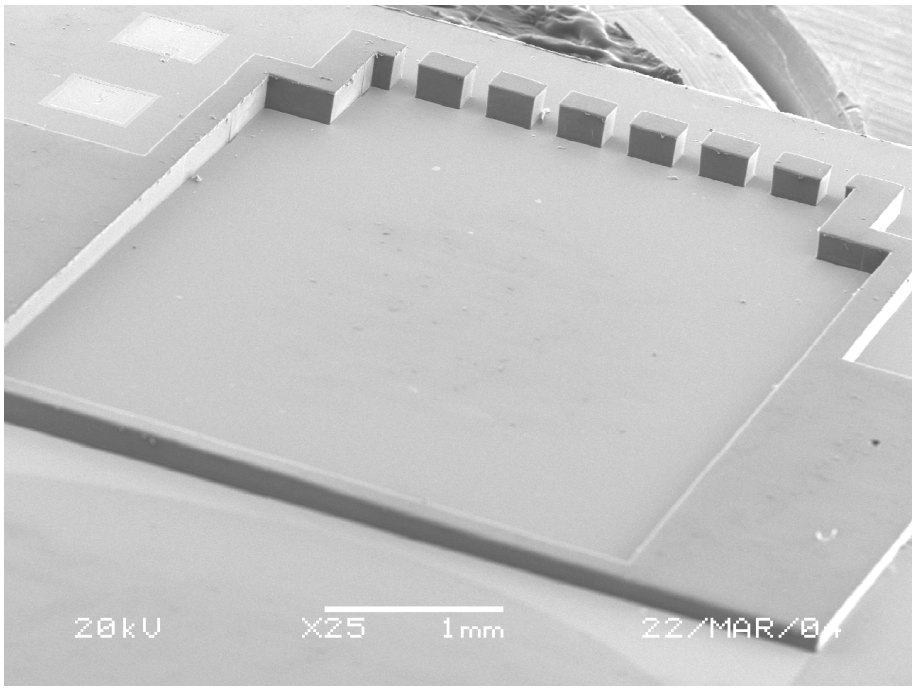


Fig. 3.12 – A scanning electron microscope (SEM) image of one SU-8 wall before glass capping. The sensing area is located in the bottom-left part of the picture.

For the second step, quartz glasses of 5 mm by 5 mm and 500 μm thick were placed and glued above the SU-8 structures. An epoxy glue (Epotek H54 from Epoxy Technology, MA, USA) was manually dispensed above the walls and followed by the placement of the glass. The

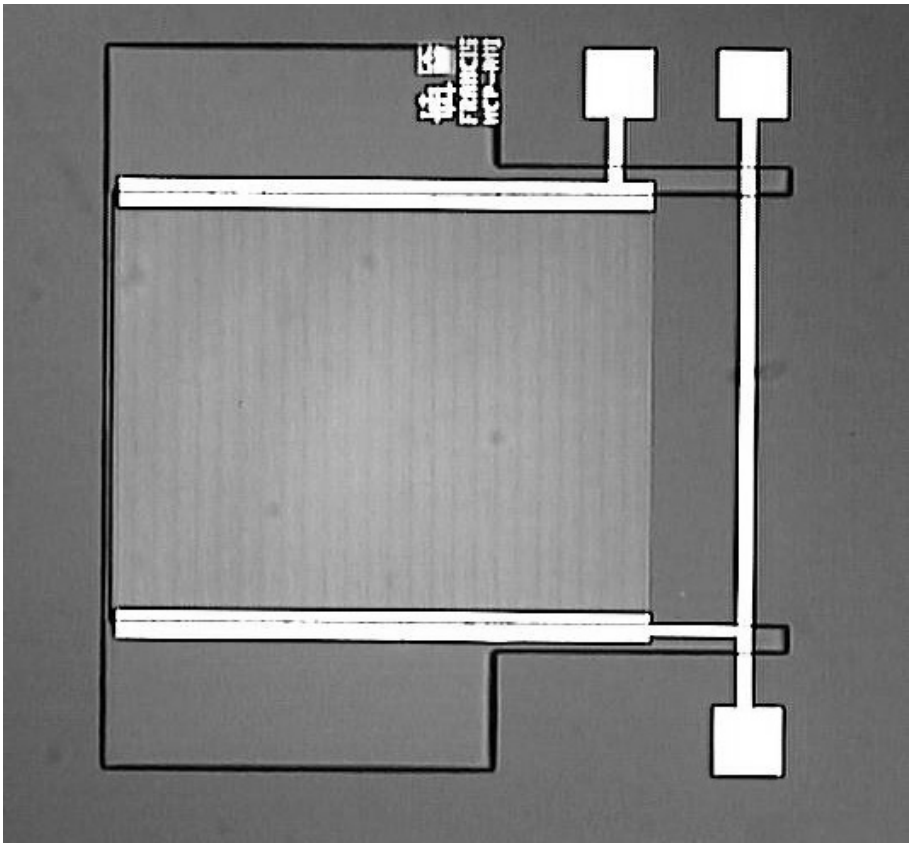


Fig. 3.13 – Optical top view picture of the SU-8 walls patterned around one interdigital transducer. The sensing area is located on the left and is separated from the aluminum electrodes of the transducer by a 150 μm wide on acoustic path, 120 μm high SU-8 wall.

final bonding between the SU-8 walls and the glass was obtained by a 15 minutes curing of the epoxy at 100°C. The flatness of the top surface of SU-8 helped for the perfect sealing between the walls and the capping. The same epoxy glue was used to make a 1 mm wide and 1-2 mm high well around the rest of the device and above the contact pads. This procedure defined an open liquid cell above the acoustic sensing surface with dimensions 4.7 mm ($= D$) by 3.5 mm ($> W$). Figure 3.14 shows a scanning electron microscope (SEM) image of the cross section of the packaged device. The fully packaged SAW biosensor itself is pictured in Figure 3.15.

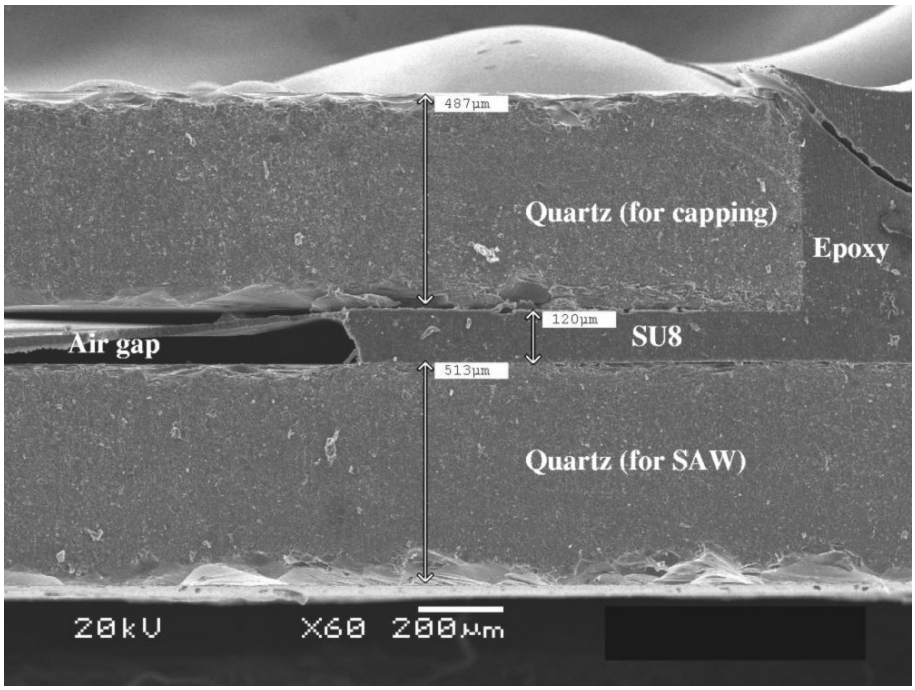


Fig. 3.14 – SEM image of the cross section of the SU-8 walls above the transducers and the quartz capping.

3.2.3 Performances of the packaging

In this section, the performance of the SU-8 liquid cell is evaluated and discussed. For the evaluation, we analyze the acoustic damping due to the liquid cell in a first place and we report a biochemical recognition experiment performed on the packaged SAW biosensor in a second place.

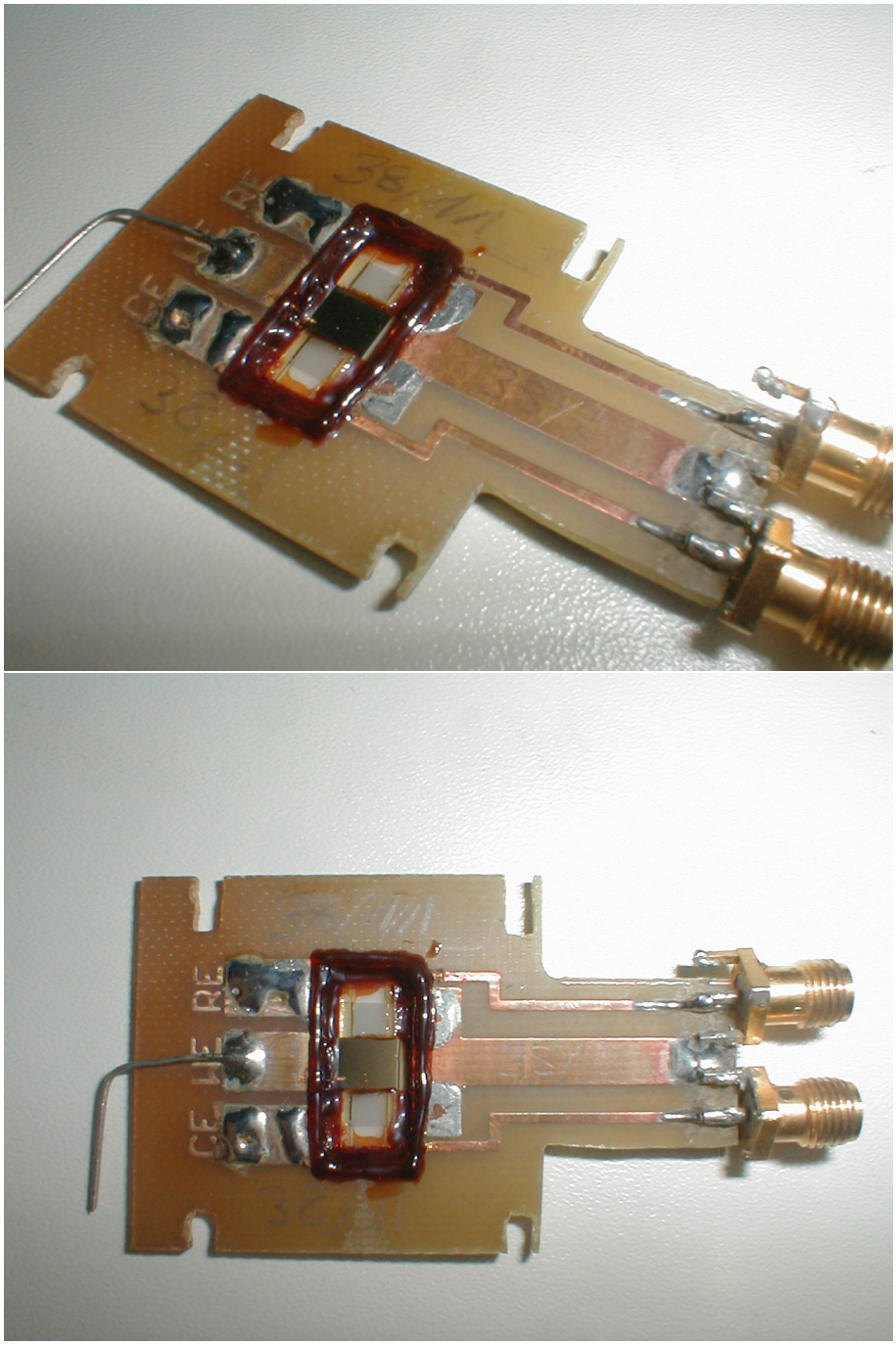


Fig. 3.15 – The fully packaged SAW biosensor on the printed circuit board.

The liquid cell prevents the presence of liquids on the IDTs and has a small disturbance effect on the propagation of the acoustic wave. The influence of the SU-8 walls on the acoustic performance of the device is shown in Figure 3.16 where the amplitude of the transfer function was measured in different situations on an identical device before the capping: with and without the SU-8 walls and with and without water loading.

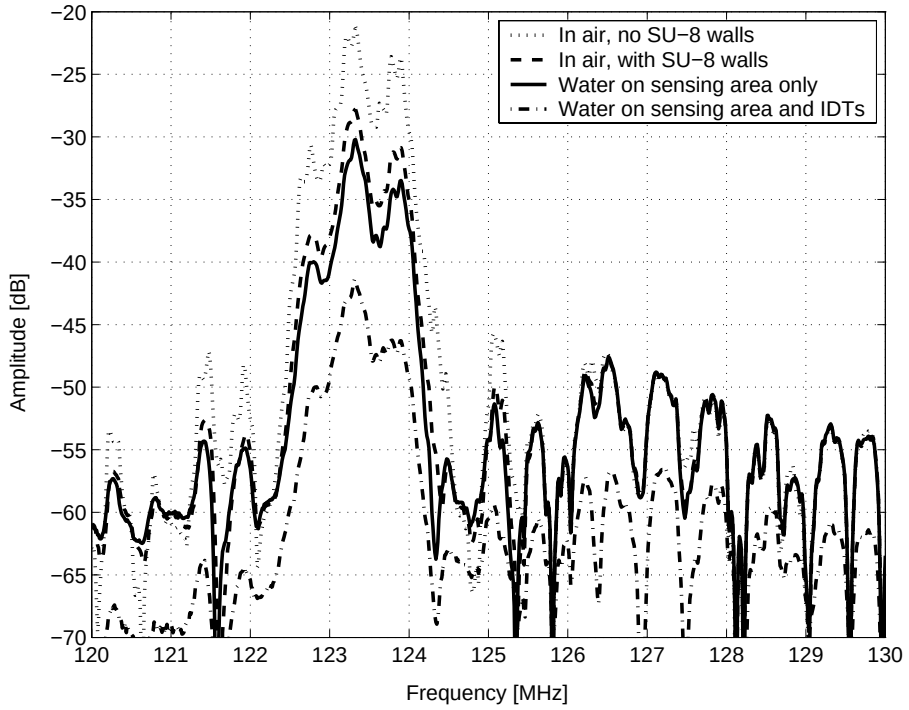


Fig. 3.16 – Effect of the SU-8 walls of the liquid cell on the amplitude of the transfer function. The figure displays the amplitude of the electrical signal as a function of the frequency in different situations indicated by the legend (the water loading is in addition to the SU-8 walls).

A loss of 7.7 dB is measured at the center frequency f_0=123.2 MHz, caused by the SU-8 walls on the acoustic path between the two transducers. Although designed with a 150 μm width, each wall covers an effective length of 160 μm caused by the aspect ratio of SU-8. Therefore, we estimate the attenuation of the shear acoustic wave by a factor of $\sim$1 dB per acoustic wavelength ($\sim$1 dB/λ). This figure helps to evaluate

the influence of the packaging on the acoustic characteristics of the sensor and serves as guideline for the miniaturization of the device. It can also be seen on Figure 3.16 that the SU-8 provides an efficient shielding against the negative influence of the water loading when it spreads over the entire sensor, including the IDTs.

In terms of the critical dimensions to attribute to the walls and to the acoustic wavelength, one is interested in smaller wavelengths to achieve SAW biosensors with higher operating frequencies. The attributed dimensions of the liquid cell is determined by the figure of 1 dB/λ. Different factors are involved in the design of the SU-8 liquid cell for the miniaturization of the device. Because of the precise patterning allowed with the photosensitive epoxy, minimum dimensions are mainly limited by the aspect ratio of the SU-8 and in our case by the manual alignment step of the glass capping that requires a relatively wide top surface. The height of the SU-8 walls must exceed one acoustic wavelength to avoid interactions between the electromagnetic field of the IDTs and the capping material. In the present case the SU-8 was three λ high; a carefully addressed investigation of the dimensions of the SU-8 walls would help to determine the impact of the liquid cell geometry on the performance of the SAW biosensor.

To illustrate the effectiveness of the SU-8 liquid cell, we report the monitoring of protein adsorption by the fully packaged Love-mode SAW biosensor described in section 3.2.2. The sensing area was covered by a 50 nm gold layer on a 10 nm titanium adhesion layer to interface the sensor with an hydrophobic self-assembled monolayer (SAM). The device was cleaned for 15 minutes in a UV-O_3 chamber, immediately followed by the coating of the sensing area with a drop of a 1mM stearyl mercaptan (Sigma-Aldrich) solution in ethanol. The deposition of the hydrophobic SAM took place during 3 hours after which the device was rinsed with ethanol and dried with a stream of nitrogen. As protein, type I fibrinogen from human plasma (Sigma-Aldrich) was diluted in PBS buffer (137 mM NaCl, 6.44 mM KH_2PO_4, 2.7 mM KCl and 8 mM Na_2HPO_4) to a concentration of 46 μg/ml. The adsorption of the protein on the sensing surface was monitored by the delay phase of the SAW biosensor at the central frequency f_0=123.2 MHz on a HP4396A Network Analyzer. The fibrinogen adsorption was preceded and followed

by a rinsing step with PBS buffer and water. Figure 3.17 reports the monitoring of the sensor as a function of time.

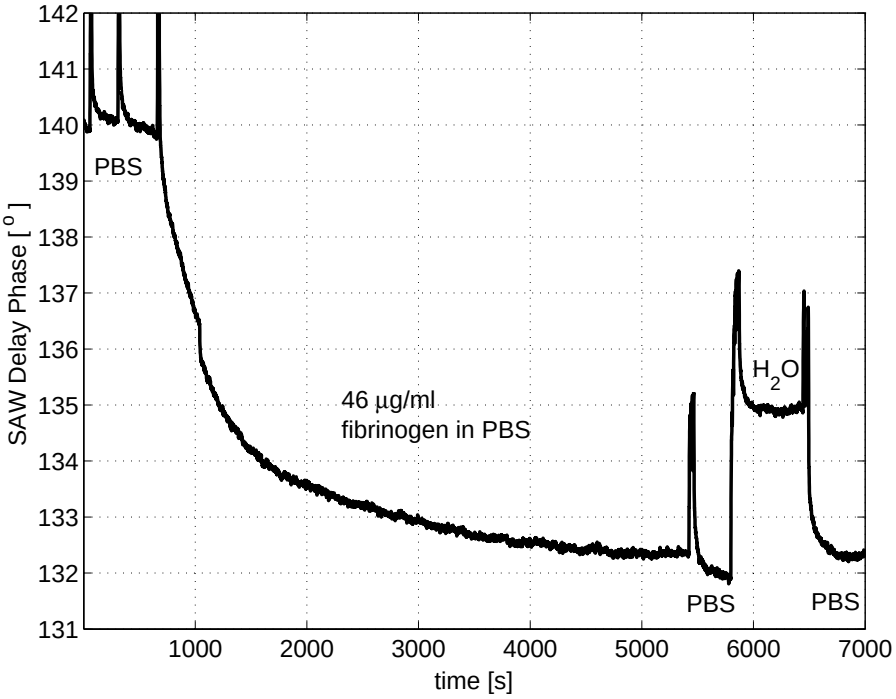


Fig. 3.17 – Fibrinogen adsorption experiment that shows no interference because of the presence of the liquid cell. The delay phase of a Love-mode SAW biosensor is monitored as a function of time. The fibrinogen adsorption on the sensing surface modifies the SAW velocity. This change appears as a delay phase shift because of the electrical transduction.

The packaging is not preventing the correct operation of the device and is apparently not interfering with the biochemical experiment. The adsorption of the protein on the sensing area causes a SAW velocity shift that appears as a delay phase shift through the IDTs. The adsorbed protein mass per surface unit $\Delta\sigma$ is related to the phase difference $\Delta\phi$ (in degrees) between starting and stopping points of the experience by [99]

$$\Delta\sigma = \frac{\lambda\Delta\phi}{360DS} \tag{3.1}$$

where D=4.7 mm is the effective sensing length, λ=40 μm and S the

mass sensitivity of this specific Love-mode SAW biosensor. The mass sensitivity has been calibrated to a value of 280 cm^2/g via copper electrodeposition [60]. In the present case, the observed phase shift of 8° in Figure 3.17 corresponds to a surface density of 675 ng/cm^2 that is a likely value for fibrinogen surface coverage. Based on this observation, we conclude to the absence of interaction between the liquid cell and the sensing performances.

A detailed comparison of our approach with other types of liquid cell is difficult to give because of a lack of data and studies with regards to its influence on the general performance of the SAW biosensor and partly because of the innovative aspect of the SU-8 liquid cell. One of the most difficult aspect related to a pre-molded liquid cell is the necessity to manually adjust its position above the sensing surface and to mechanically press the cell against the SAW device till a perfect sealing is reached so that no leaks can occur during the whole biochemical experiment. The position of the cell and the pressure are inevitably varying from experiments to experiments and may result in a lack of experimental reproducibility. In comparison, we claim that the precise patterning of the SU-8 associated to the rigidity and the stability of our whole packaging solution is an improvement that assures the experimental reproducibility of SAW biosensors.

3.3 Experimental calibration techniques

3.3.1 Experimental measurement of the dispersion curve

The dispersion curve is the relation between the Love mode velocity and the guiding layer thickness t normalized by the wavelength λ. Measuring the dispersion curve is a method to obtain an evaluation of the sensing properties of the device because the velocity variation caused by a modification of the guiding layer is interpreted as a surface density change. The entire dispersion curve can be obtained experimentally by recording the transfer function while depositing or removing the guiding layer. Since most deposition techniques of the guiding layers are not compatible with an *in situ* instrumentation of the device (e.g. spin coating, sputtering, chemical vapor deposition, ...), the acquisition of the dispersion curve is only allowed after deposition of the guiding layer

and with the help of one of the following possibilities:

- probing at different wavelengths with a constant guiding layer thickness (different periodicity of the interdigitated electrodes), which is a space consuming solution on the wafer and it requires an optimized IDT design;
- probing at constant wavelength different layer thicknesses, that solution dramatically increases the amount of tests that must be achieved before obtaining the entire dispersion curve;
- a combination of the two precedent possibilities to optimize processing and measurement times;
- in some specific cases when the deposition techniques allow it, the dispersion curve can be measured continuously during the guiding layer deposition [16].

The continuous monitoring of the transfer function during the etching of the guiding layer is an alternative possibility to establish the Love mode dispersion curve. For the present case of a silicon dioxide guiding layer, the device was immersed in fluorhydric acid while recording the transfer function thanks to a network analyzer connected to the packaged device. The solution was temperature controlled and mixed at a constant rate to ensure an homogeneous etching rate of the silicon dioxide. The result is displayed in Figure 3.18. This chemical wet etching can be extended to other types of guiding layer as long as an etching solution can be found. The conversion of the etching time to guiding layer thickness requires a pre-calibration of the material etching rate or an in-line optical measurement method.

Once obtained, the dispersion curve is interpolated by a polynomial expression. The derivation of the polynomial expression with regards to the silicon dioxide thickness gives the values of sensitivity as plotted in Figure 3.19 (we assumed a value of $\rho = 2200$ kg/m^3 for SiO_2).

3.3.2 Modification of the surface density

The technique described in the precedent section has the drawback to be destructive and to lack precision. It is generally more convenient to calibrate the mass sensitivity of a given SAW device by non-destructive means, with reproducible methods and in conditions close or similar

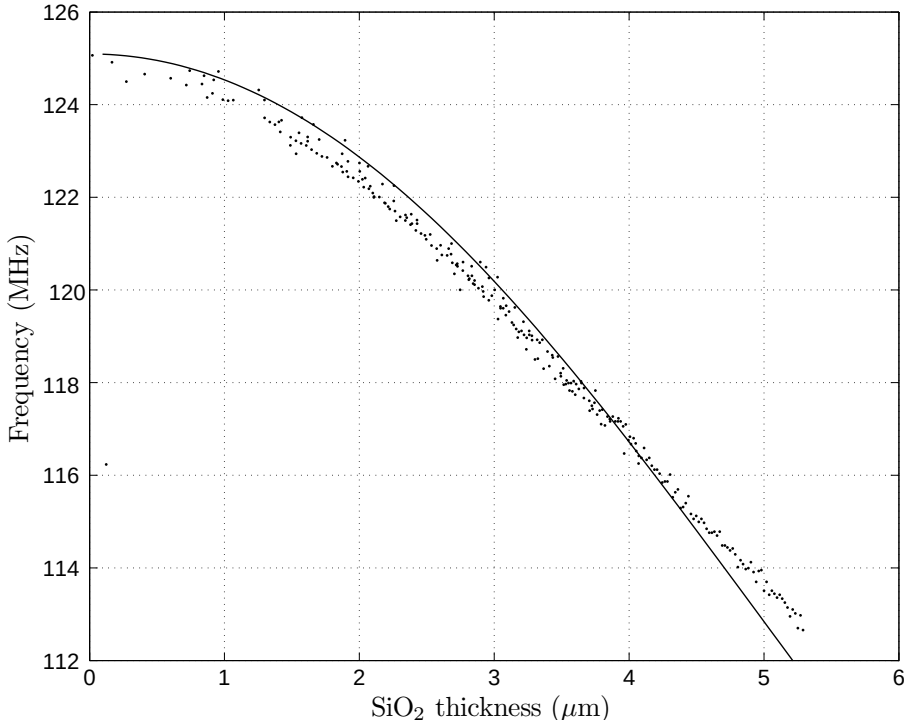


Fig. 3.18 – Record of the Love mode dispersion curve during the etching of the silicon dioxide guiding layer in a solution of fluorhydric acid: the dots are the experimental data while the solid line is the closest theoretical Love mode dispersion curve obtained by a fit of the experimental data.

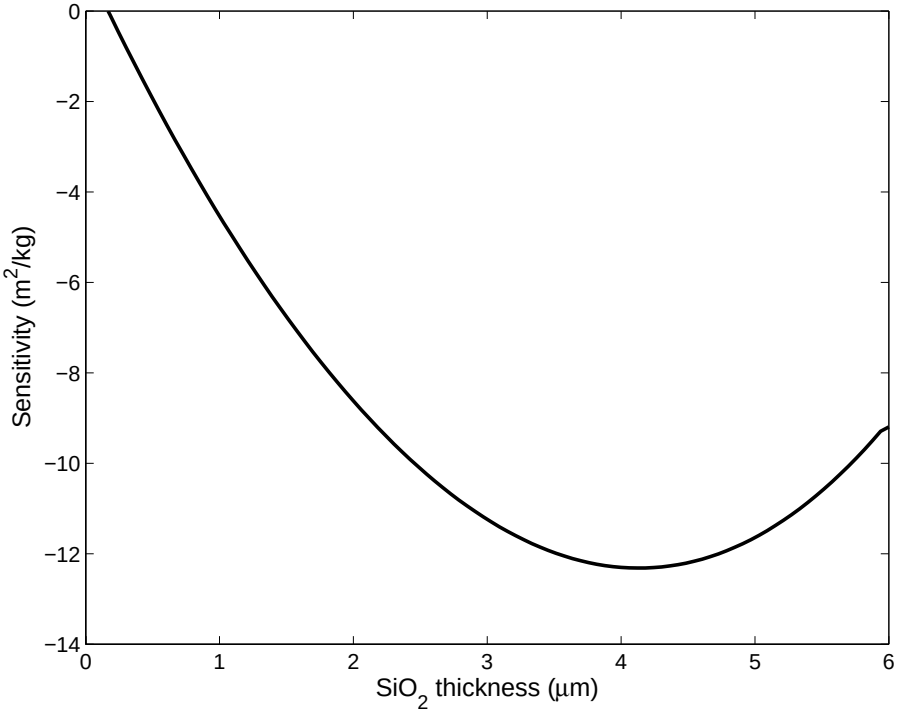


Fig. 3.19 – Sensitivity estimated by derivation for a 3^{rd} polynomial interpolation of the Love mode dispersion curve as a function of the guiding layer thickness.

to the actual operating conditions of the SAW device. In a second approach, we present three techniques to calibrate the mass sensitivity according to these criteria by modifying the surface density on the sensing area. Each techniques are presented by decreasing values of surface density modification: the etching of a gold thin film (5 μg/cm^2 to 100 μg/cm^2), the electrodeposition of copper (1 μg/cm^2 to 5 μg/cm^2), and the adsorption of a surfactant monolayer (0.14 μg/cm^2).

Metal thin film etching

The 50 nm gold layer deposited on the sensing area during the device fabrication is etched by a solution of KI/I_2 (4 g and 1 g respectively in 160 ml of water [196]). The phase angle was recorded during the etching of a 200 nm thick gold layer. The modification of the phase is plotted in Figure 3.20 *vs.* the gold thickness. Because of its electrical conductivity, the gold layer enhances the electromagnetic feedthrough between the transducers and results in interferences in the phase as the gold layer becomes thicker. This interference effect is described in details in Chapter 4.

To estimate the mass sensitivity, the phase variation based on the etching of 50 nm of gold served to plot the mass sensitivity versus the frequency in Figure 3.21. The interferences have an impact on this estimation by modifying the sensitivity with ripples that depends upon the measurement frequency. The mean value corresponds to the mass sensitivity of the sensor and is equal to -9.6 m^2/kg.

Metal electrochemical deposition

Electrochemical deposition, or *electrodeposition*, of thin metal films from electrolytic solutions has been proposed as a novel method to calibrate the mass sensitivity of SAW sensors. The methodology is employed to deposit and remove copper by electrodeposition [60]. The principle is based on a system of three electrodes dipped in a 0.01 M aqueous solution of $CuSO_4$. Copper is electrodeposited on a working electrode by applying a potential between this working electrode and a counter electrode while monitoring the current between the counter electrode and a reference electrode. In the present case, the working electrode is the gold coated sensing area of the SAW device, the counter electrode is a platinum wire and the reference electrode a copper wire, as seen

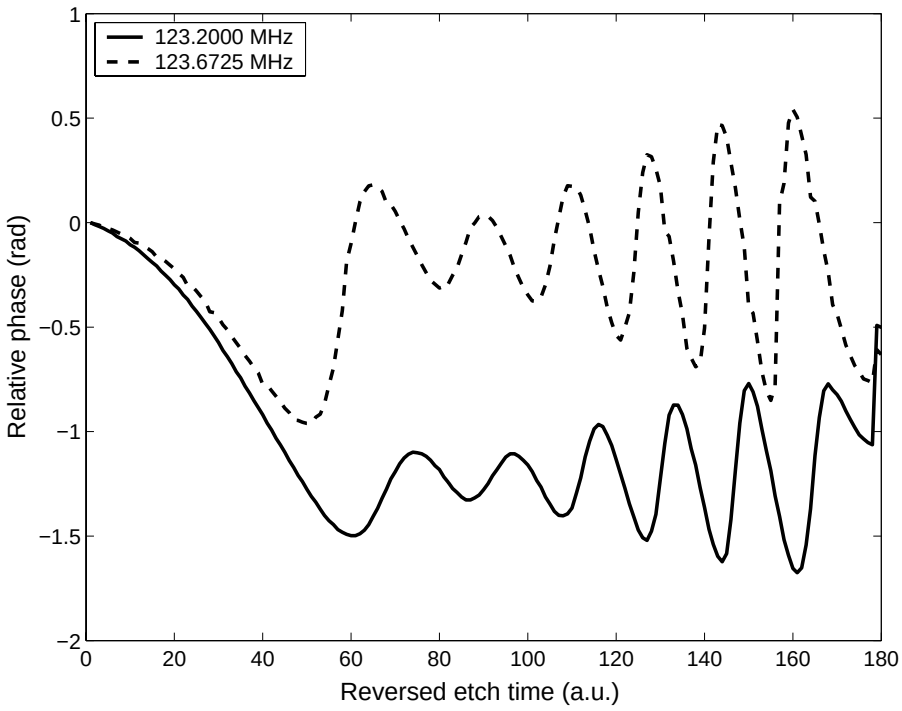


Fig. 3.20 – Relative phase at two frequencies (solid line 123.2 MHz and dashed line 123.6725 MHz) as a function of the gold layer thickness. The selected frequencies are in the designed passband of the SAW filter to indicate that a slight modification of the monitoring frequency results in variations of the measured electrical signal. Such difference results in different estimated values of the gravimetric sensitivity as a function of the frequency.

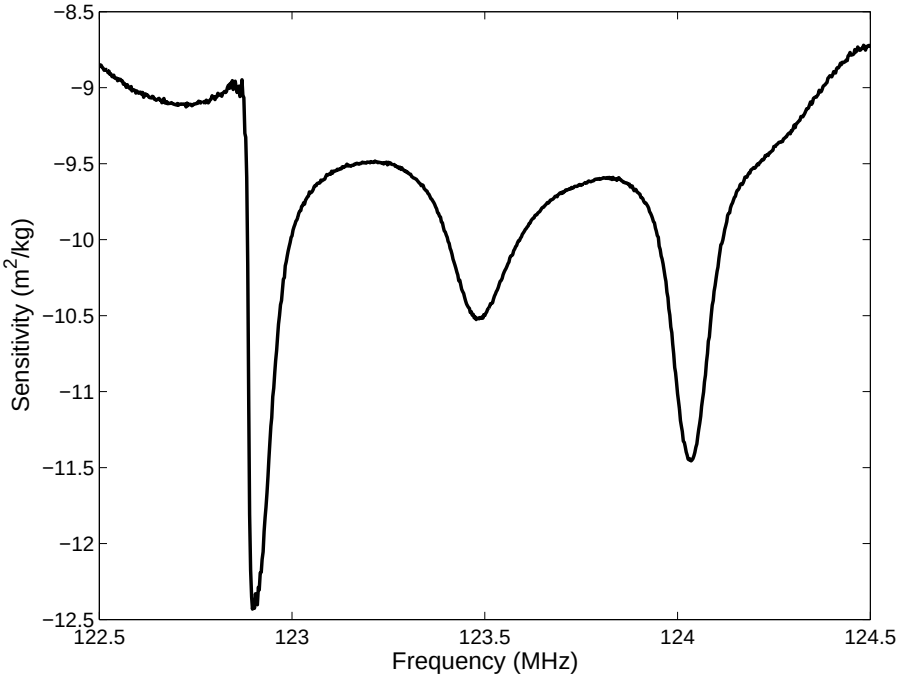


Fig. 3.21 – Sensitivity estimated by etching of 50 nm of gold as a function of the frequency.

in Figure 3.22. The tension between the working and the counter electrodes and the current between the counter and the reference electrodes are measured thanks to a potentiostat. An example of potentiostat is sketched in Figure 3.23. The electrodeposited mass is deduced from the current measurement I with a sampling period δt:

$$\Delta m = \frac{\sum_j I_j \delta t}{F} \frac{M}{n_e} \tag{3.2}$$

where $F = 96485$ C is the Faraday constant, M the molar weight of the electrodeposited metal and n_e the number of electrons exchanged for each metallic atom reduced.

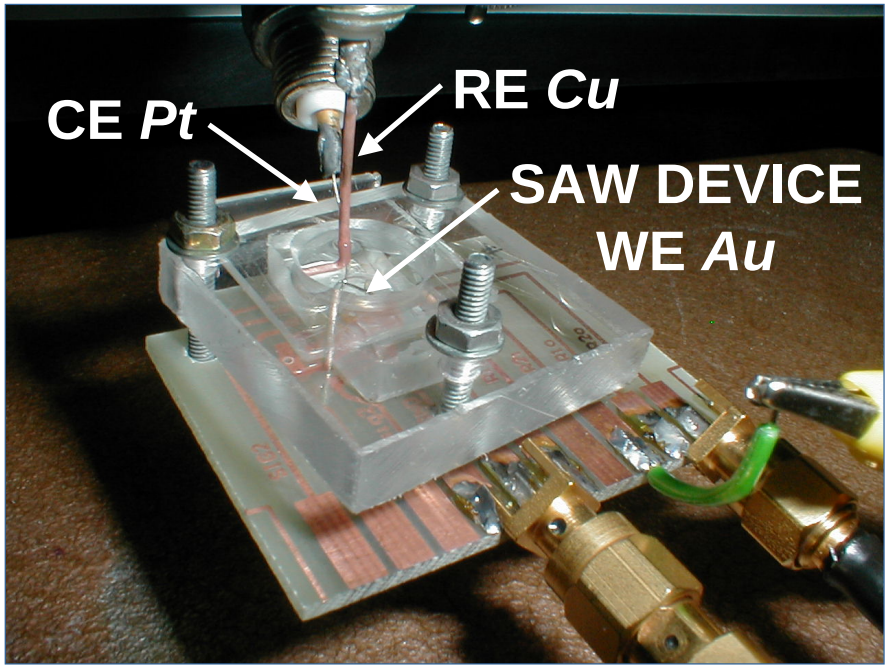


Fig. 3.22 – Picture of the setup for the electrodeposition of copper on the SAW gold sensing surface.

The electrodeposition of copper on the gold coated surface is forming a rough surface that traps the water and has an hydrodynamic drag effect on the acoustic measurement. The influence of surface roughening is a well-known effect observed initially in quartz crystal microbalance [188, 210]. The surface roughening has been observed by combined

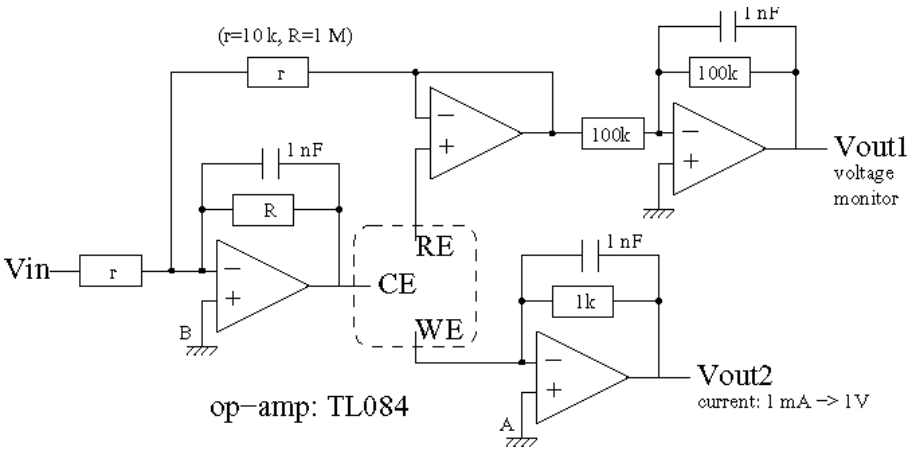


Fig. 3.23 – Electrical circuit of a potentiostat to measure the voltage and the current related to metal electrodeposition (RE: reference electrode, CE: counter electrode, WE: working electrode).

in situ measurement of surface roughness by atomic force microscopy (AFM) and electrochemical quartz crystal microbalance (EQCM) during a similar copper electrodeposition [27]. Considering the similarities of the operating principle of QCM and SAW, these effects are extended to our work by assuming that they influence the SAW measurement in a similar manner and result in an overestimation of the sensitivity. The consequence of the hydrodynamic drag effect is a high attenuation of the acoustic wave. To confirm this influence, Table 3.2 gives the measured phase and attenuation shifts recorded during the copper electrodeposition and Table 3.3 gives the calculated sensitivities $S_{\sigma,\phi}$ and $S_{\sigma,\alpha}$. As conclusion, one should notice that electrodeposition of a rough metal layer results in the overestimation of the sensitivity. We limit our contribution to the field to these measurements, no further correlation or modeling work have been attempted so far.

Organic layers adsorption

The etching of a metal film or the electrodeposition of metal are *in situ* characterization methods that are far from the biosensor application where biomaterials forming thin films are recognized by the sensing area. For instance, the surface density of a monolayer of IgG antibodies is about 400 ng/cm^2 [81] and is much lower than the surface density

Δm (ng)	$\Delta\phi$ (mrad)	$\Delta\alpha$ (dB)	$\Delta\alpha/\Delta\phi$ (dB/rad)
332.4 ± 19.5	-255.8 ± 16.6	0.562 ± 0.083	-2.20 ± 0.47
913.6 ± 13.8	-737.6 ± 5.5	1.303 ± 0.035	-1.77 ± 0.06
1015 ± 27.6	-785.8 ± 15.2	1.403 ± 0.066	-1.79 ± 0.12

Table 3.2 – Phase and attenuation changes as a function of the mass of copper electrodeposited

$\Delta\sigma$ $\left(\mathrm{ng/cm^2}\right)$	$S_{\phi,\sigma}$ $\left(\mathrm{m^2/kg}\right)$	$S_{\alpha,\sigma}$ $\left(10^6\mathrm{dB \cdot m/kg}\right)$
1286 ± 75	-26.95 ± 3.33	9.299 ± 1.919
3534 ± 53	-28.27 ± 0.64	7.844 ± 0.329
3928 ± 107	-27.09 ± 1.26	7.599 ± 0.564
Mean value	-27.43 ± 1.74	8.247 ± 0.937
Theoretical value	-17.9	0.378

Table 3.3 – Sensitivities of the device as a function of the amount of copper electrodeposited

changes resulting from metal thin film etching or electrodeposition. For the deposition of an organic thin film, we adsorbed a surfactant agent (CTAB, hexadecyltrimethylammonium bromide, Sigma-Aldrich) on the gold sensing area made hydrophobic by a self-assembled monolayer (octadecanethiol, Sigma-Aldrich). If we assume a densely packed monolayer, the CTAB induces a surface density shift of 137 ng/cm^2 [114]. The sensitivity obtained via the phase change recorded after adsorption is given in Figure 3.24. The presence of the gold induces interferences that modify the mass sensitivity that has a mean value about -14.9 m^2/kg.

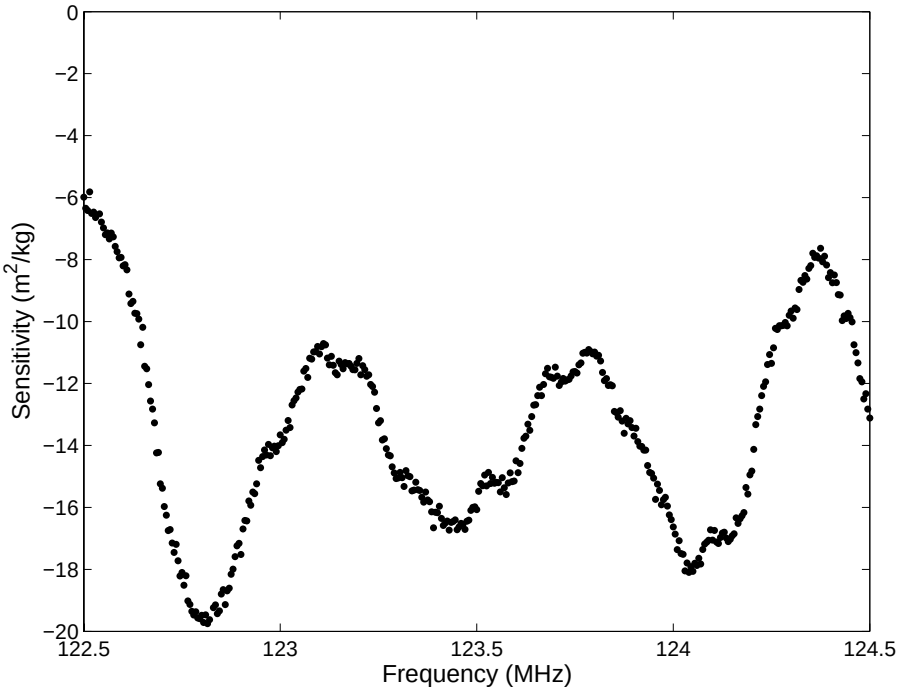


Fig. 3.24 – Mass sensitivity calculated from the CTAB adsorption as a function of the frequency.

3.3.3 Viscosity calibration

The modification of the surface density is related to the gravimetric sensitivity. The calibration of the viscosity must also be calibrated in order to extract the influence of viscosity changes in the bulk solution

during the biorecognition experiment. The attenuation shift to phase shift ratio evaluates the bulk viscosity sensitivity, corresponding to the use of the Love mode sensor as liquid sensor. For the calibration, a known technique is the display of different concentrations of glycerol-water solutions on the sensing area. The slope of the curves presented in Figure 3.25 is 11.6 dB/rad, 10.8 dB/rad, 12.2 dB/rad and 15.0 dB/rad for 0%, 20%, 40% and 60% of glycerol, respectively. The slope is more or less constant and corresponds to the theoretical value indicated in Figure 2.12 although discrepencies are observed for very viscous solutions. The water loading can be used as a rough estimation of the viscous sensitivity because its loading corresponds to approximately 1 $\mathrm{kg/m^2/s^{1/2}}$; the phase shift is -290 mrad corresponding to

$$S_{\phi,\rho\eta} = -3.9 \cdot 10^{-4}\ \mathrm{m^2 \cdot s^{1/2}/kg}, \tag{3.3}$$

and the attenuation shift is 3.2 dB corresponding to

$$S_{\alpha,\rho\eta} = 680\ \mathrm{dB \cdot m \cdot s^{1/2}/kg}. \tag{3.4}$$

These values are relatively close to the theoretical estimates given in (2.31) and (2.33).

Adsorbed biomolecules layers have a finite thickness that is much below the acoustic penetration depth (δ), which rises an issue about their mechanical behavior. The issue is related to the rigid or viscous behavior of adsorbed organic materials and, mainly, if a discrimination between the two extreme behavior is possible during the calibration with biomolecules. Thanks to the viscosity calibration, Table 3.4 gives a theoretical estimation of the phase and attenuation shifts expected if we consider the CTAB as pure rigid or pure viscous layer, and in the hypothetical case where the layer is thicker than 3 times the penetration depth. It can be seen that the difference between the two extreme cases (rigid and viscous) is not clearly differentiated by the experimental measurements, at least with our experimental device.

3.4 Conclusion

The fabrication of Love mode SAW device with H-rich silicon dioxide guiding layer is a stable and reproducible fabrication process. The

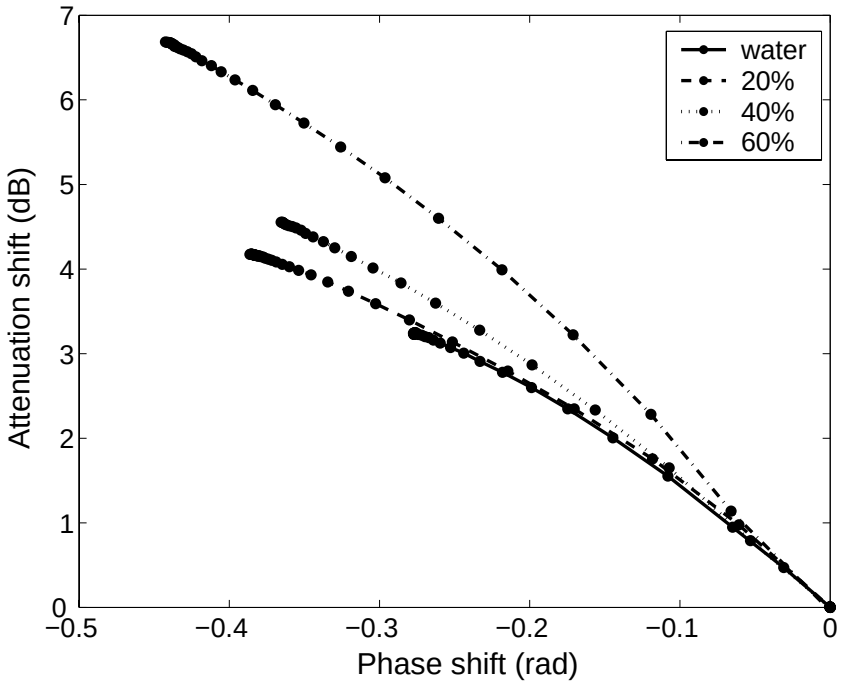


Fig. 3.25 – Experimental attenuation and phase shifts for solutions water-glycerol with varying proportion of glycerol.

	Rigid	Viscous $h = 1.5$nm	Viscous $h > 3\delta$
$\Delta\phi$ (mrad)	-17	-20	-254
$\Delta\alpha$ (dB)	0.01	0.005	2.35

Table 3.4 – Phase and attenuation shift calculated if CTAB is considered as a rigid or as a viscous layer.

enhancement of sensitivity due to a low density and a low is advantageous from the sensitivity point of view. The obtention of other guiding layers, zinc oxide and silicon germanium, is not entirely convincing from the fabrication aspect although the spray pyrolysis deposition of porous materials is possible, in order to obtain lower shear stiffness and higher mass sensitivity.

The packaging of surface acoustic wave biosensors is solved by the realization of a SU-8 based liquid cell. We have shown that the SU-8 assures the sealing of a capping layer above the transducers and prevents liquids to contact the electrodes of the transducers. The design of the liquid cell results in an attenuation factor about 1 dB per acoustic wavelength of SU-8 on the acoustic sensing path. The materials selected for the fabrication of the liquid cell have a good chemical resistance and are apparently not interfering with the biochemical sensing event. The presented SU-8 liquid cell is a basic step in the integration of the packaging of SAW biosensors at the wafer processing level but the influence of design parameters on the instrumentation and the sensing characteristics of the SAW biosensor is part of future developments.

For future developments, improvements are required to increase the integration of IC fabrication techniques in the realization of the packaging solution.
A first improvement to the presented solution resides in a microfluidic system for liquid flow above the sensing surface, an aspect that is missing in the developed liquid cell and although a static fluid display does not prevent the correct operation of the biosensor. An hybrid approach is based on the advantage provided by the SU-8 walls in term of integration, low acoustic attenuation and reproducibility, and by the flexibility of a pre-molded external cell. The SU-8 plays the role of a microfabricated O-ring precisely defining the sensing area; above this O-ring, the glass capping could be advantageously replaced by a removable PDMS molded microfluidic. This solution has the disadvantage of requiring a mechanical setup to apply a pressure for the sealing of the SU-8/PDMS interface. In terms of volume, the open air liquid cell can be filled with 180 to 200 μl of solution. This volume is reduced in to 2 μl, in a non-demonstrated flow cell arrangement, by the entire capping of the SU-8 O-ring.

A second improvement at the wafer level is the wafer bonding of the capping. The identification of two steps in the fabrication methodology let appear a clear break between batch and manual processes in the packaging of the SAW biosensor. The wafer bonding of a full glass wafer requires a glass with holed structures above the sensing area, for instance with sand blasted openings. The advantage is that SU-8 can be used as bonding material. This solution is an opportunity to have a full batch processing of the packaging, unless other packaging methods are developed.

The calibration of the gravimetric and the viscosity sensitivities of the Love mode device by different techniques is indicating differences in the estimated values of sensitivity. The etching of the guiding layer is a first destructive method which can give a rough estimation of the gravimetric sensitivity and is probably adapted to the prototyping of guiding layers.
The etching of a metal layer can be accompanied by electromagnetic interferences which modifies periodically the actual value of sensitivity. The electrodeposition of rough copper results in an overestimation of the mass sensitivity due to water trapping. Deposition or removal of metal layers is a large surface density change with respect to the adsorption of organic materials but the calibration with organic materials forming self-assembled layers of well defined surface density is not sufficient because of the viscous behavior of organic materials.
The experimental values for the mass sensitivity $S_{\phi,\sigma}$ are close to the theoretical value. Discrepancies are attributed to varying properties in the mechanical values of the materials and to the specificity of each experimental technique used for the determination of the sensitivity.

Chapter 4

Effect of interferences on the sensitivity

> As far as the laws of mathematics refer to reality, they are not certain; and as far as they are certain, they do not refer to reality.
>
> *Albert Einstein*

The acoustic signal launched and detected in surface acoustic waveguides by electrical transducers is accompanied by an electromagnetic wave; the interaction of the acoustic and the electromagnetic signals, easily enhanced by the open structure of the sensor, creates interference patterns in the transfer function of the sensor. In this chapter, we use the interference peaks to determine the sensitivity of the acoustic device. We show that electromagnetic interferences generate a distortion in the experimental value of the sensitivity. This distortion is not identical for the two classical instrumentation of the sensor that are the open and the closed loop configurations. A formalized approach is completed by the experimentation of an actual Love mode sensor operated in open loop configuration under liquid conditions. The experiment indicates that the interaction depends on frequency and mass modifications.

4.1 Introduction

Acoustic waves guided by the surface of solid structures form waveguides used as delay lines and filters in telecommunications [29]. Waveguides support different modes with specific strain and stress fields [4]. The acoustic velocity of each mode depends on different intrinsic and extrinsic parameters such as the mechanical properties of the materials, the temperature or the applied pressure. Waveguides are used as sensors when the velocity change is linked to environmental changes. For gravimetric sensors, the outer surface of the waveguide is exposed to mass changes. Due to the confinement of the acoustic wave energy close to the surface, these sensors are well suited for (bio)chemical sensors operating in gas or liquid media. Among a wide variety of waveguides used for that purpose, Love mode sensors have attracted an increasing interest during the last decade as described in the previous chapter [63, 82].

A Love mode is guided by a solid overlayer deposited on top of a substrate material. The usual substrates are piezoelectric materials like quartz, lithium tantalate and lithium niobate [88]. Associated to specific crystal cut of these substrates, the Love mode presents a shear-horizontal polarization that makes it suitable for sensing in liquid media.

Current research in Love mode sensors concerns the guiding materials in order to optimize the sensitivity, that is the variation of the acoustic signal under surface modifications. Typical materials under investigations are dielectrics like silicon dioxide and polymers, and more recently semiconductors with piezoelectric properties like zinc oxide [81,107,156]. Although the dispersion relation for Love mode is well set and the dependence of the sensitivity of the liquid loaded sensor to the overlayer thickness has been thoroughly investigated [99, 137, 197], little has been devoted to study the role played by the structure of the sensor and their transducers.

In this chapter, we investigate the role played by the structure of the sensor and by the interferences between the acoustic and the electromagnetic waves on the sensitivity. In the first part, we present a general model of the transfer function including the influence of electromagnetic interferences. In the second part, we show how these interferences modify the sensitivity in open and closed loop configurations of the sensor. Finally, these effects are illustrated experimentally on a Love mode sensor.

4.2 Modeling

Waveguide sensors consist of a transducing part and a sensing part. The transducing part includes the generation and the reception of acoustic signals and their interfacing to an electrical instrumentation. The most common transducers are the widespread interdigital transducers (IDTs) on piezoelectric substrates introduced by White and Voltmer in 1965 [202]. Although the transducing part can be involved in the sensing part, practical sensing is confined to the spacing between the transducers. This confinement takes especially place when liquids are involved since these produce large and unwanted capacitive coupling between input and output electrical transducers. This coupling dramatically deteriorates the transfer function and is an important issue for the instrumentation and the packaging of the sensors [128].

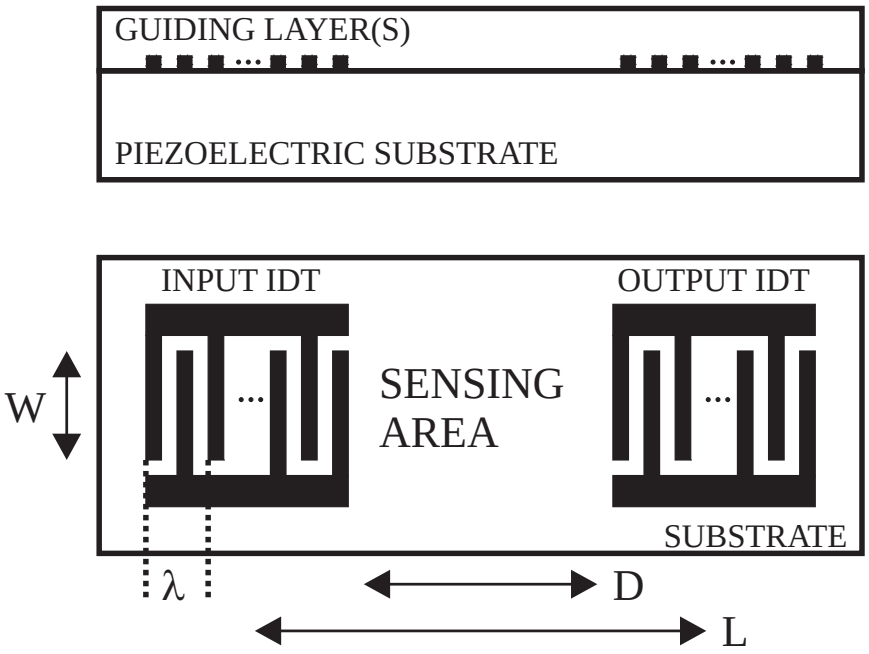


Fig. 4.1 – Structure of the acoustic device.

The sensor itself is configured as a delay line formed by two transducers separated by a certain distance. The sensor can also be configured as a resonator but we will restrict our approach to the delay line configu-

ration because the operation principle in these two configurations is not similar. The Love mode sensor is sketched in Figure 4.1. Transducers with a constant apodization are identified to their midpoint; the distance between the midpoints is L and the interdigitated electrodes have a periodicity λ_T. The sensing part is located between the transducers and covers a total length D so that $D \leq L$. The guided mode propagates with a phase velocity $V = \omega/k$, where $\omega = 2\pi f$ is the angular frequency and $k = 2\pi/\lambda$ is the wavenumber. The waveguide is dispersive when the group velocity ($V_g = \mathrm{d}\omega/\mathrm{d}k$) differs from the phase velocity.

The velocity is a function of the frequency and of the surface density $\sigma = M/A$ for a rigidly bound and non viscous mass M per surface area A. For an uniformly distributed mass, the surface density is rewritten in terms of material density ρ and thickness d by $\sigma = \rho d$. The phase velocity for an initial and constant mass σ_0 is denoted V_0, and the group velocity V_{g0}. In the sensing part, the phase velocity is V and the group velocity V_g. According to this model, the transit time τ on the delay line is given by

$$\tau = \frac{D}{V} + \frac{L - D}{V_0}. \tag{4.1}$$

At the output transducer, the two kinds of waves interact with an amplitude ratio, denoted by α, that creates interference patterns in the transfer function $H(\omega)$ of the delay line. The transfer function itself is given by the ratio of the output to the input voltages. A general expression of the interferences is given by:

$$H(\omega) = \underbrace{H_T(\omega)\exp(-\mathrm{i}\omega\tau)}_{\text{delay line}} \left(1 + \underbrace{\alpha(\omega)\exp(-\mathrm{i}\omega\tau_D)}_{\text{interference}}\right) \tag{4.2}$$

where τ_D is the delayed signal that causes interference by its interaction with the main delay line signal. By developing the expression, the interferences are known to create ripples in the passband of the acoustic signal; if we rewrite the transfer function as

$$H(\omega) = \|H(\omega)\| \exp(\mathrm{i}\phi)$$

where expressions for the amplitude $\|H(\omega)\|$ and the phase ϕ are given

by:

$$\|H(\omega)\| = \|H_T(\omega)\| \left\| \sqrt{1 + 2\alpha\cos(\omega\tau_D) + \alpha^2} \right\|; \quad (4.3)$$

$$\phi = \phi_0 - \arctan\left(\frac{\sin(\omega\tau) + \alpha\sin(\omega\left[\tau + \tau_D\right])}{\cos(\omega\tau) + \alpha\cos\left(\omega\left[\tau + \tau_D\right]\right)} \right). \quad (4.4)$$

Two main kind of interferences arise in surface acoustic waves: the triple transit echo (TTE) and the electromagnetic feedthrough (EM). The TTE is due to the regeneration of the incoming acoustic wave by the output transducer, that get reflected once again by the input transducer before being finally detected at the output transducer. The triple transit echo has a delay time twice the main transit time, i.e. $\tau_D = 2\tau$. The amplitude of the TTE depends of the geometry of the fingers and the mechanical loading they provide through the mechanical and electrical mismatch at their edges. The amplitude of the TTE is strongly reduced by using split-fingers geometry [29].
Electromagnetic interferences are due to the cross-talk between the IDTs [53]. The electromagnetic wave (EM) emitted by the input transducer travels much faster than the acoustic wave and therefore is detected at the output transducer without noticeable delay, i.e. $\tau_D = -\tau$. The EM is modeled by an additional shunt capacitance between the input and the output IDTs of value C_{EM}.

4.3 Electromagnetic interferences

The transfer function with electromagnetic interferences is modeled by the following equation:

$$H(\omega) = \underbrace{H_T(\omega)\exp(-\mathrm{i}\omega\tau)}_{\text{delay line}} + \underbrace{\alpha H_T(\omega)}_{\text{EM coupling}} . \quad (4.5)$$

The transfer function $H_T(\omega)$ is associated to the design of the transducers. The total transfer function can be rewritten as $H(\omega) = \|H(\omega)\|\exp(\mathrm{i}\phi)$ where expressions for the amplitude $\|H(\omega)\|$ and the phase ϕ are obtained with help of complex algebra:

$$\|H(\omega)\| = \|H_T(\omega)\| \left\| \sqrt{1 + 2\alpha\cos(\omega\tau) + \alpha^2} \right\|; \quad (4.6)$$

$$\phi = \phi_0 - \arctan\left(\frac{\sin(\omega\tau)}{\alpha + \cos(\omega\tau)} \right). \quad (4.7)$$

The phase ϕ_0 corresponds to the packaging of the sensor and is due to different aspects linked to the instrumentation. It will be assumed independent of the frequency and of the sensing event. The synchronous frequency $\omega_T = 2\pi f_T$ is determined by the design of the IDTs and is generally equal to the maximum amplitude of $\|H_T(\omega)\|$ when the wavelength of the acoustic wave λ_0 matches the transducers periodicity λ_T.

The relations (4.6) and (4.7) are the sources of ripples in the transfer function at the ripple frequency $\Delta\omega \simeq 2\pi/\tau$, its exact expression depends also of the dispersion on the line. Interference peaks corresponding to the maximum effect are observed at quantified frequencies f_n when $\cos(2\pi f_n \tau) = -1$, that is for frequencies such that

$$f_n = \frac{2n+1}{2\tau} \tag{4.8}$$

where $n \in \mathbb{N}$ is the interference mode number. A direct relation to the velocity in the sensing area is obtained from this latter equation as seen by replacing the transit time τ by its definition:

$$\boxed{V = \frac{2DV_0 f_n}{(2n+1)V_0 + 2(D-L)f_n}.} \tag{4.9}$$

The interference mode numbers are determined by considering the uncovered delay line; in such case $V = V_0$ and $D = L$, and n for the interference peak located below the synchronous frequency (i.e. for $f_n \leq f_T$) is given by

$$n = \left\lfloor \frac{L}{\lambda_T} - \frac{1}{2} \right\rfloor \tag{4.10}$$

while the other peaks are labeled subsequently to their position with respect to the peak referenced by Eq. (4.10).

The relative amplitude peak to peak of the perturbation on the amplitude has a maximum effect (in dB) equals to $40\log[(1+\alpha)/(1-\alpha)]$. The amplitude (in dB and normalized to have $\|H_T(\omega)\| = 1$) and the phase (in radians) as a function of the frequency are simulated in Figures 4.2(a) to 4.2(d) for different values of α.
Under the influence of the interferences, the phase has different behaviors function of α:

1. when $\alpha = 0$ (no interferences), the phase is linear with the frequency and has a periodicity equal to 2π (Figure 4.2(a));

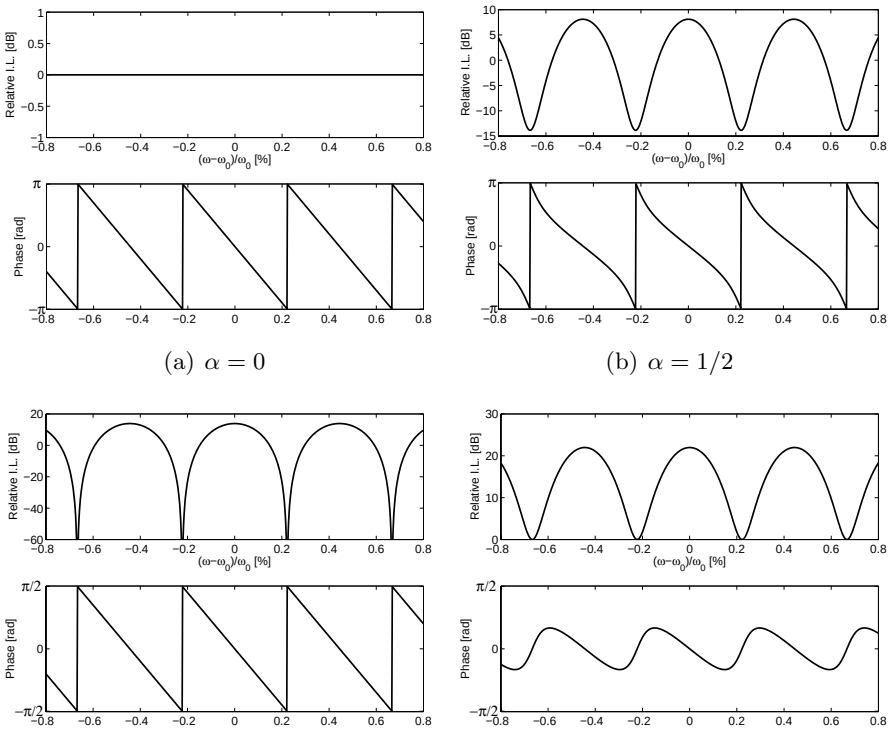
2. when $\alpha < 1$, the phase is deformed but has still a periodicity equal to 2π (Figure 4.2(b));

3. when $\alpha = 1$, the phase has a periodicity equal to π (Figure 4.2(c));

4. when $\alpha > 1$, the periodicity is lower than π (Figure 4.2(d));

5. when $\alpha \to \infty$, the phase is not periodic anymore and its value tends to ϕ_0.

This specific behavior of the phase under the influence of the electromagnetic interferences has to be considered while evaluating the sensitivity.



(a) $\alpha = 0$ (b) $\alpha = 1/2$

(c) $\alpha = 1$ (d) $\alpha = 2$

Fig. 4.2 – Relative insertion loss and phase of the transfer function for different values of the interaction parameter α. When $\alpha \geq 1$, the phase spans at maximum between $-\pi$ and π.

4.4 Sensitivity

Changes in the boundary condition of the waveguide due to the sensing event modify phase and group velocities. As consequence, the transit time of the delay line and the phase of the transfer function are modified. The sensing event is quantified by recording the phase shift at a fixed frequency (open loop configuration) or the frequency shift at a fixed phase (closed loop configuration). This quantification gives rise to the concept of sensitivity. The sensitivity is not an unique concept for acoustic sensors because various parameters influence the acoustic velocity. As example of such parameters, there is the density and the viscosity of liquid solutions and adsorbed biomolecules film when the device is used as biosensor, as discussed in the previous chapter. The sensitivity is the most important parameter in design, calibration and applications of acoustic waveguide sensors. Its measurement must be carefully addressed in order to extract the intrinsic properties of the sensor.

4.4.1 Definitions of the sensitivity

The *velocity sensitivity* S_V is defined by the change of phase velocity as a function of the surface density change at a constant frequency. Its mathematical expression is given by Ref. [99]:

$$S_V = \frac{1}{V}\frac{\partial V}{\partial \sigma}\bigg|_{\omega}. \tag{4.11}$$

The definition reflects the velocity change in the sensing area only while outside this area the velocity remains unmodified. The expression is general because the initial velocity V of the sensing part does not need to be equal to V_0; this situation occurs in practical situations where the sensing part has a selective coating with its own mechanical properties, leading to an initial difference between V and V_0.

To link the sensitivity (caused by the unknown velocity shift) to the experimental values of phase and frequency shifts, we introduce two additional definitions related to the open and the close loop configurations, respectively. The *phase sensitivity* S_ϕ is defined by

$$S_\phi = \frac{1}{kD}\frac{\mathrm{d}\phi}{\mathrm{d}\sigma}, \tag{4.12}$$

and the *frequency sensitivity* S_ω is defined by

$$S_\omega = \frac{1}{\omega}\frac{\mathrm{d}\omega}{\mathrm{d}\sigma}. \tag{4.13}$$

4.4.2 Phase differentials without interferences

In order to point clearly the effects of the electromagnetic interferences on the different sensitivities presented in the previous section, we calculate the phase differentials in the ideal case of no interferences. For that case, the phase of the transfer function is a function of the frequency and of the velocities in the different parts of the sensor, themselves function of the frequency and of the surface density:

$$\begin{aligned} \phi(\omega, V(\omega,\sigma), V_0(\omega)) &= -\omega\tau & (4.14)\\ &= -\omega\left(\frac{D}{V} + \frac{L-D}{V_0}\right). & (4.15) \end{aligned}$$

Therefore, the total differential of the phase is

$$\begin{aligned} \mathrm{d}\phi &= \left(\left.\frac{\partial\phi}{\partial\omega}\right|_{V,V_0} + \left.\frac{\partial\phi}{\partial V}\right|_{\omega,V_0}\left.\frac{\partial V}{\partial\omega}\right|_{\sigma} + \left.\frac{\partial\phi}{\partial V_0}\right|_{\omega,V}\frac{\mathrm{d}V_0}{\mathrm{d}\omega}\right)\mathrm{d}\omega \\ &\quad + \left.\frac{\partial\phi}{\partial V}\right|_{\omega,V_0}\left.\frac{\partial V}{\partial\sigma}\right|_{\omega}\mathrm{d}\sigma & (4.16)\\ &= \left.\frac{\partial\phi}{\partial\omega}\right|_{\sigma}\mathrm{d}\omega + \left.\frac{\partial\phi}{\partial\sigma}\right|_{\omega}\mathrm{d}\sigma. & (4.17) \end{aligned}$$

The derivative of the phase velocity as a function of the frequency comes from the definitions of phase and group velocities; at constant surface density we have from Ref. [137]:

$$\begin{aligned} \left.\frac{\partial V}{\partial\omega}\right|_{\sigma} &= k^{-1}\left(1 - \frac{V}{V_g}\right); & (4.18)\\ \frac{\mathrm{d}V_0}{\mathrm{d}\omega} &= k_0^{-1}\left(1 - \frac{V_0}{V_{g0}}\right). & (4.19) \end{aligned}$$

The other partial differentials are obtained by differentiation of Eq. (4.14):

$$\left.\frac{\partial\phi}{\partial\omega}\right|_{V,V_0} = -\tau; \tag{4.20}$$

$$\left.\frac{\partial\phi}{\partial\omega}\right|_{\sigma} = -\tau - \omega \left.\frac{\tau}{\omega}\right|_{\sigma} \tag{4.21}$$

$$= -\tau_g; \tag{4.22}$$

$$\left.\frac{\partial\phi}{\partial V}\right|_{\omega,V_0} = \frac{\omega D}{V^2}; \tag{4.23}$$

$$\left.\frac{\partial\phi}{\partial V_0}\right|_{\omega,V} = \frac{\omega(L-D)}{V_0^2}. \tag{4.24}$$

The *time of flight* (or *group delay*) τ_g introduced in Eq. (4.22) is calculated as

$$\tau_g = \frac{D}{V_g} + \frac{L-D}{V_{g0}}. \tag{4.25}$$

4.4.3 Open loop configuration

In the open loop configuration, the input transducer is excited at a given frequency while the phase difference between output and input transducers is recorded. This configuration with a constant frequency has $d\omega = 0$ in Eq. (4.16); related phase variations caused by surface density variations are obtained by

$$\frac{\mathrm{d}\phi}{\mathrm{d}\sigma} = \left.\frac{\partial\phi}{\partial V}\right|_{\omega,V_0} \left.\frac{\partial V}{\partial\sigma}\right|_{\omega} \tag{4.26}$$

$$= \left.\frac{\partial\phi}{\partial V}\right|_{\omega,V_0} V S_V. \tag{4.27}$$

In the absence of interferences, phase variations obtained experimentally are directly linked to velocity changes by the product kD involving the geometry of the sensor as seen by replacing Eq. (4.23) in Eq. (4.27):

$$\boxed{\frac{\mathrm{d}\phi}{\mathrm{d}\sigma} = kDS_V.} \tag{4.28}$$

In other words: $S_\phi = S_V$ when there are no interferences. In a first approximation k is assumed equal to k_T, an assumption valid as long as the phase shift is evaluated close to the synchronous frequency and for

waveguides with low dispersion. The wavelength is only known when the sensing part extends over the transducers ($D = L$). In that case, the transfer function of the IDTs is modified accordingly to the velocity changes. In practice, the value of the sensitivity is slightly underestimated to its exact value since $k \leq k_T$, the error being less than 5%.

In the case where interferences occur, the partial differential of ϕ with respect to the velocity is obtained by differentiation of Eq. (4.7):

$$\left.\frac{\partial \phi}{\partial V}\right|_{\omega,V_0} = \left(\frac{1+\alpha\cos(\omega\tau)}{1+2\alpha\cos(\omega\tau)+\alpha^2}\right)\frac{\omega D}{V^2}, \tag{4.29}$$

and the phase sensitivity is obtained by combining the latter equation with Eq. (4.27):

$$\boxed{S_\phi = \left(\frac{1+\alpha\cos(\omega\tau)}{1+2\alpha\cos(\omega\tau)+\alpha^2}\right) S_V.} \tag{4.30}$$

The influence of electromagnetic interferences on the phase sensitivity is simulated in Figure 4.3 versus the relative frequency for different values of α. The phase sensitivity is always different compared to the velocity sensitivity. For the threshold value $\alpha = 1$, the phase sensitivity present a singularity and is undefined; for higher values of α, the phase sensitivity is always underestimated to the velocity sensitivity.

The interference peaks permit a direct evaluation of α because at these points $\cos(\omega\tau) = -1$ and Eq. (4.30) becomes linear with α:

$$\alpha = 1 - \frac{V^2}{\omega D}\left.\frac{\partial \phi}{\partial V}\right|_{\omega,V_0} \tag{4.31}$$

$$= 1 - \frac{S_V}{S_\phi}. \tag{4.32}$$

4.4.4 Closed loop configuration

In the closed loop configuration, the frequency is recorded while a feedback loop keeps the phase difference between output and input transducers constant. The configuration at constant phase has $d\phi = 0$, the variation of the frequency as a function of the mass change is given by

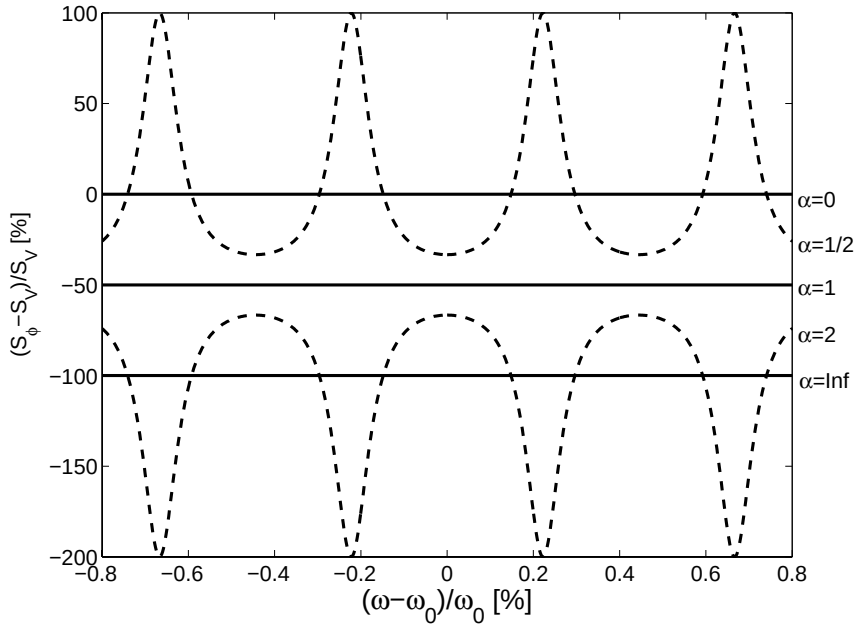


Fig. 4.3 – Phase sensitivity at constant frequency as a function of the relative frequency for different values of simulated interferences obtained by Eq. (4.30).

introducing this condition in Eq. (4.17):

$$\frac{\mathrm{d}\omega}{\mathrm{d}\sigma} = -\left(\left.\frac{\partial\phi}{\partial\sigma}\right|_{\omega}\right)\left(\left.\frac{\partial\phi}{\partial\omega}\right|_{\sigma}\right)^{-1}. \tag{4.33}$$

The upper term is replaced by Eq. (4.27). The phase slope as a function of the frequency at constant mass is obtained by differentiation of Eq. (4.7):

$$\left.\frac{\partial\phi}{\partial\omega}\right|_{\sigma} = -\left(\frac{1+\alpha\cos(\omega\tau)}{1+2\alpha\cos(\omega\tau)+\alpha^2}\right)\tau_g. \tag{4.34}$$

We can establish a finalized equation taking into account the electromagnetic interferences by combining Eqs. (4.27),(4.29) and (4.34) in Eq. (4.33):

$$\boxed{S_\omega = \tfrac{DS_V}{V\tau_g}.} \tag{4.35}$$

If the waveguide is not dispersive and $V = V_0$, frequency variations obtained experimentally are directly linked to the velocity sensitivity by the ratio D/L as seen by replacing the transit time in Eq. (4.35):

$$S_\omega = \frac{D}{L}S_V. \tag{4.36}$$

If the waveguide is dispersive, the transit time τ contains the combined information of the group velocities in the transducing and sensing part and the phase velocity in the sensing part. If the sensing part extends to the entire delay line ($D = L$), we obtain an expression corresponding to a well-known result, for instance [99]:

$$S_\omega = \frac{V_g}{V}S_V. \tag{4.37}$$

At the opposite of the open loop configuration, the frequency sensitivity is not influenced by the interferences. However, as indicated by Eq. (4.35), the frequency sensitivity is strongly dependent of the structure of the sensor and the dispersion characteristics of the delay line. As result, the link between the frequency sensitivity and the velocity sensitivity is difficult to exploit although it can be noticed that $S_\omega \leq S_V$ since $V_g \leq V$ for Love mode devices.

4.5 Experimental results

For the practical consideration of the described and modeled behavior, we investigated a Love mode sensor. It was fabricated and tested under liquid condition in the open loop configuration to evaluate the influence of the electromagnetic interferences. In a first part, the sensor fabrication and instrumentation is described, followed in a second part by the application of the model to these results to demonstrate the influence of the interferences on the sensitivity of the sensor.

4.5.1 Sensor fabrication and instrumentation

The Love mode was obtained by conversion of a surface skimming bulk wave (SSBW) launched in the direction perpendicular to the crystalline X axis of a 500 μm thick ST-cut (42.5° Y-cut) quartz substrate. The conversion was achieved by a 1.2 μm thick overlayer of silicon dioxide deposited on the top side of the substrate by plasma enhanced chemical vapor deposition (Plasmalab 100 from Oxford Plasma Technology, England). Via were etched in the silicon dioxide layer using a standard SF_6/O_2 plasma etch recipe. This process stopped automatically on the aluminum contact pads of the transducers.

The transducers consist of split fingers electrodes etched in 200 nm thick sputtered aluminum. The fingers are 5 μm wide and equally spaced by 5 μm. This defines a periodicity λ_T of 40 μm. The acoustic aperture defined by the overlap of the fingers is equal to $80\lambda_T$ (= 3.2 mm), the total length of each IDT is $100\lambda_T$ (= 4 mm) and the distance center to center of the IDTs is $225\lambda_T$ (L= 9 mm, D= 5 mm).

The sensing area was defined by covering the space left between the edges of the IDTs by successive evaporation and lift-off of 10 nm of titanium and 50 nm of gold in a first experiment, and 200 nm of gold in a second experiment. The fingers were protected against liquid by patterning photosensitive epoxy SU-8 2075 (Microchem Corp., MA) defining 120 μm thick and 80 μm wide walls around the IDTs. Quartz glasses of 5 by 5 mm^2 were glued on top of the walls to finalize the protection of the IDTs [56].

The device was mounted and wire-bonded to an epoxy printed circuit board and its transfer function was recorded on a HP4396A Network Analyzer. This setup corresponds to the open loop configuration. Epoxy around the device covered and protected it and defined a leak-free liquid cell. The sensing area was immersed in a solution of KI/I_2 (4 g and 1 g respectively in 160 ml of water) that etched the gold away of the surface [196]. The transfer function of the device was recorded every 4 seconds (limited by the GPIB transfer speed) during the etching of the gold with a resolution of 801 points over a span of 2 MHz centered around 123.5 MHz. The initial transfer function of the device is presented in Figure 4.4 with and without gold. The transfer function during etching of the 200 nm is shown at two moments (44 seconds and 356 seconds after etching start) in Figure 4.5. The total time for this etching was approximately 620 seconds.

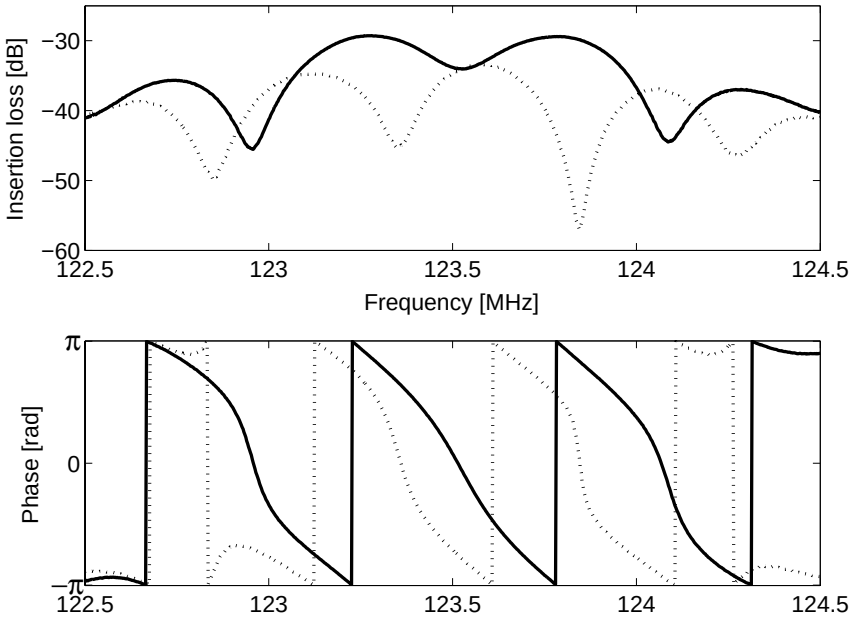


Fig. 4.4 – Initial aspect of the experimentally recorded transfer function of the Love mode sensor with (dashed line) and without (solid line) an overlayer of 200 nm of gold. This device presents an initial phase $\phi_0 = \pi$, leading to a vertical offset by π compared to the simulated phase curve represented in Figure 4.2(b).

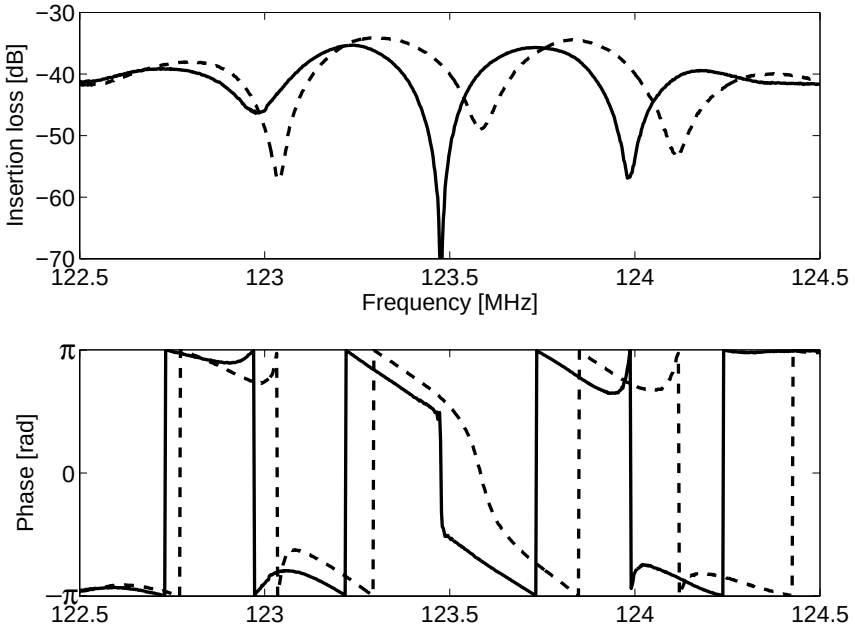


Fig. 4.5 – Aspect of the experimentally recorded transfer function at two different moments of the etching of 200 nm of gold (solid line after 44 seconds and dashed line after 356 seconds). The solid line shows a value of α close to 1 around 123.5 MHz.

4.5.2 Correlation of the results with the model

The correlation of the experimental results with the model is presented in two steps. In the first step, we show the calculation of the phase velocity from the interference peaks; and in the second step, we evaluate the mass sensitivity in the open loop configuration by the delay phase angle and the phase velocity variations recorded during the gold etching .

The record of the interference peaks frequency f_n during a sensing event permits to follow the evolution of the phase velocity in the sensing area either for constant and integer values of the interference mode numbers n as given by Eq. (4.9), either by sampling the mode numbers at a constant frequency.
Figure 4.6 plots the interference peaks versus time and frequency for the

etching of the 200 nm thick gold layer; the interference mode numbers n were attributed according to Eqs. (4.9) and (4.10) with $V_0 = 4940$ m/s (given by the synchronous frequency of f_T=123.5 MHz times the transducers periodicity λ_T).
The evolution of the velocity in the sensing area with time is representative of the etching rate of the gold layer and is plotted for three different frequencies (123.5 MHz, 123.75 MHz and 124 MHz) in Figure 4.7. At three different frequencies, the values of velocity should differ as a function of the group velocity. This effect is seen better when the probing frequencies are taken far away from each others and for a strongly dispersive delay line, which is not the case for the experimental device presently used.

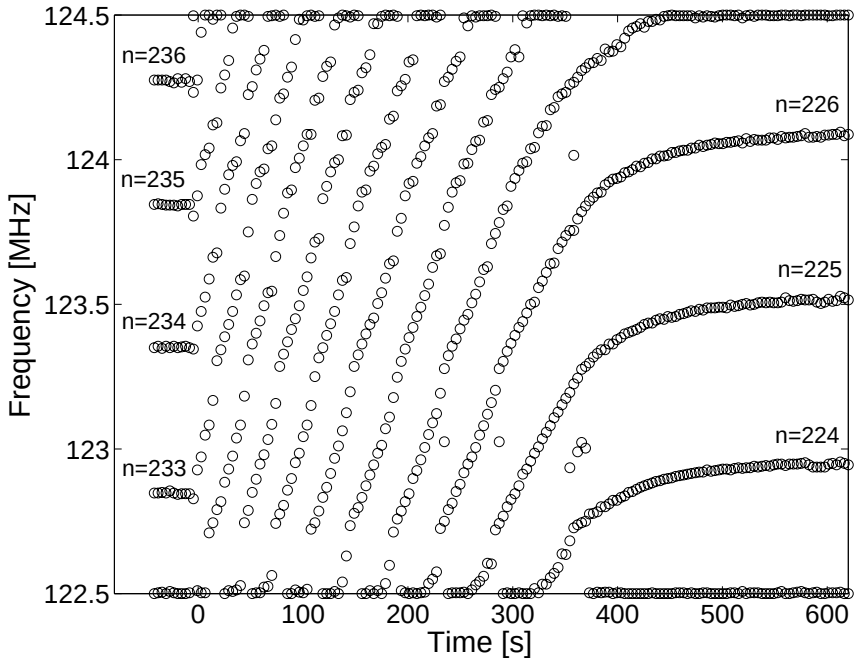


Fig. 4.6 – Interference modes in the amplitude of the transfer function as a function of time and frequency recorded during the etching of 200 nm of gold. The modes are labeled in the figure; at a given frequency, the mode numbers are decreasing as the mass decreases in the sensing area, reflecting the acoustic velocity increase.

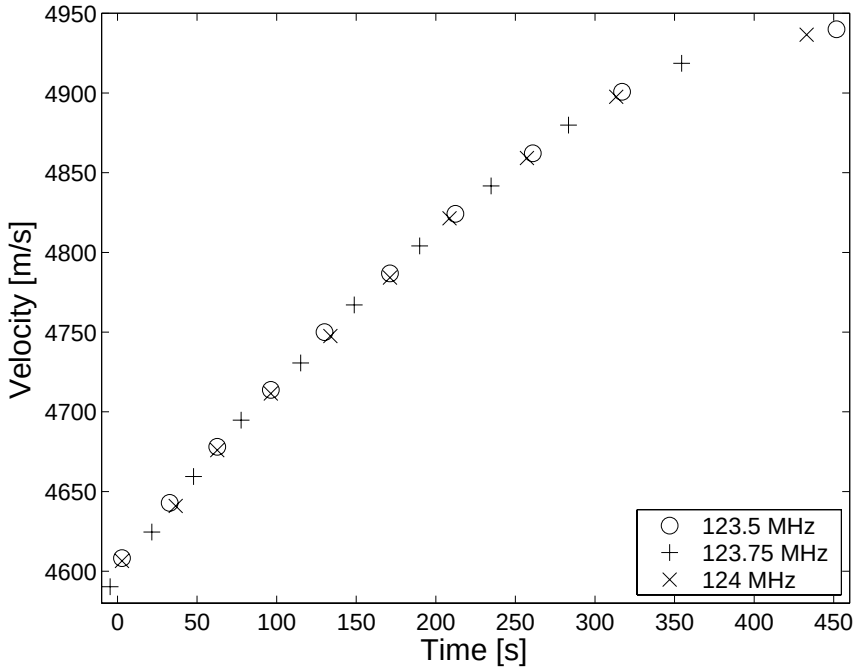


Fig. 4.7 – Evaluation of the acoustic velocity on the sensing area during the etching of the gold as a function of time for different values of frequency.

At constant frequency, the peaks are spaced by an unit variation of n, therefore the velocity difference measured between two peaks is obtained by differentiation of Eq. (4.9) with respect to n:

$$\boxed{\frac{\partial V}{\partial n}\Big|_{f_n,V_0} = -\frac{4DV_0^2 f_n}{[(2n+1)V_0+2(D-L)f_n]^2}} \tag{4.38}$$

which gives a variation roughly equals to -40 m/s between two peaks at the three sampling frequencies. From the acoustic velocity variation (4610 m/s for 200 nm gold to 4940 m/s when all the gold is etched) and by assuming that gold has a density of $\rho = 19.3$ g/cm^3, we have an evaluation of S_V equals to -173 cm^2/g. Because the phase loses its periodicity for the thick gold layer, we were not able to determine a value for the phase variation and consequently we have no value for S_ϕ. The Eq. (4.31) was employed to estimate the value of α at the interference peak; the result is displayed in Figure 4.8 that demonstrates a variation of α with the frequency. Around the synchronous frequency, α equals 0.33 and the phase has a periodicity of 2π; but as the frequency is far from the synchronous frequency, α clearly change above the critical value of 1 (in the present case $\alpha = 5.7$). The consequence is seen in the phase that presents at this point of calculation a positive slope and a periodicity below π.

We applied the same procedure to the thinner gold layer of 50 nm. Figure 4.9 shows the transfer function recorded before and after the gold etching; the interference mode number 225 has been followed and give a velocity varying from 4876.5 m/s to 4940 m/s. The resulting velocity sensitivity is $S_V = -96$ cm^2/g. This value is lower than the one obtained by etching of the thick gold layer since a thicker layer enhances the sensitivity due to a better entrapment of the acoustic energy in the top guiding layer.

The phase sensitivity S_ϕ could be calculated for frequencies where α remained inferior to the critical value of 1, that is close to the synchronous frequency. The result is plotted versus the frequency in Figure 4.10 and compared with the estimated value of S_V while the values of α indicated on the graph have been estimated at the interference peaks thanks to Eq. (4.32). The graphs shows that the interferences modify the value of the sensitivity as given by Eq. (4.30). A comparison of the Figures 4.3

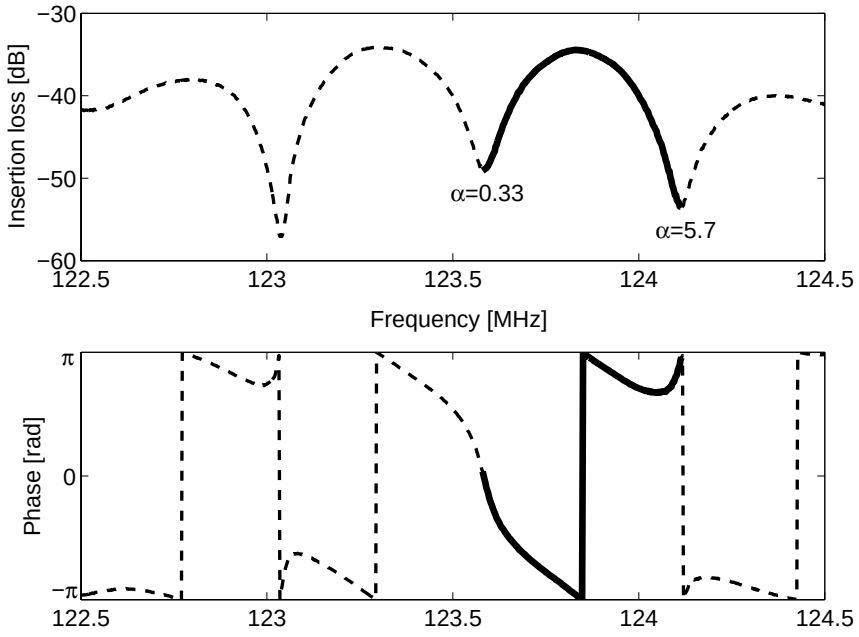


Fig. 4.8 – Evaluation of α at the position of the interference peak.

and 4.10 shows the correlation between the theoretical modeling of the effects of electromagnetic interferences on the sensitivity of the surface acoustic waveguide sensor and the experimental results.

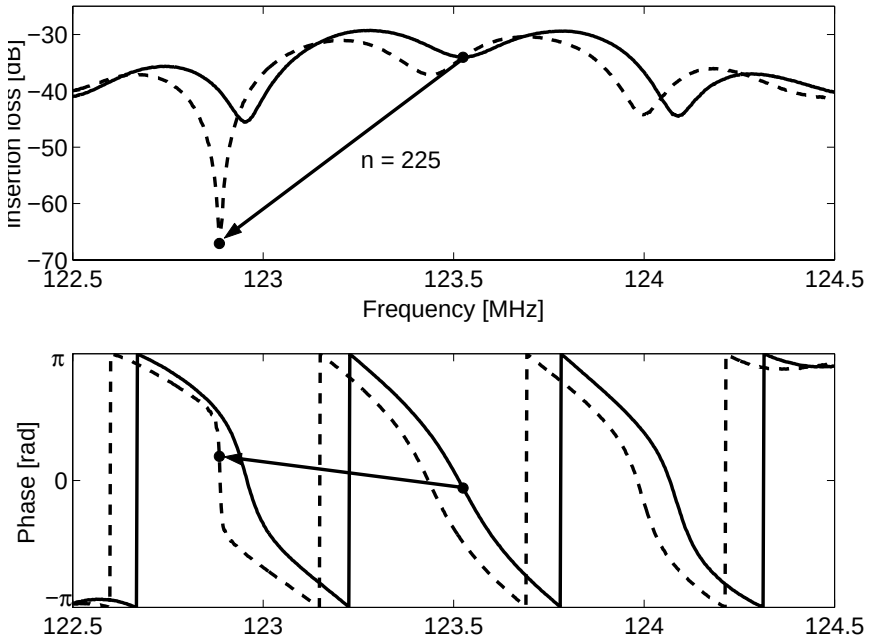


Fig. 4.9 – Transfer function before and after the etching of 50 nm of gold. The arrows indicate the interference mode 225 followed to estimate the velocity sensitivity.

Figure 4.11 shows a simulation of the frequency sensitivity S_ω obtained by interpolating the data recorded in the open loop to obtain an equal span of the points before and after the etching. The frequency sensitivity varies around a mean value of -52.8 cm^2/g (measured at a phase of 0 radian) and this variation is attributed to the variation of α with the frequency while the model assumes a constant value for the interaction parameter.

4.6 Discussion

Electromagnetic interferences have a clear effect on the transfer function of the acoustic device because of the ripples they cause. The interaction modeled as a constant factor α is specific to each device and must

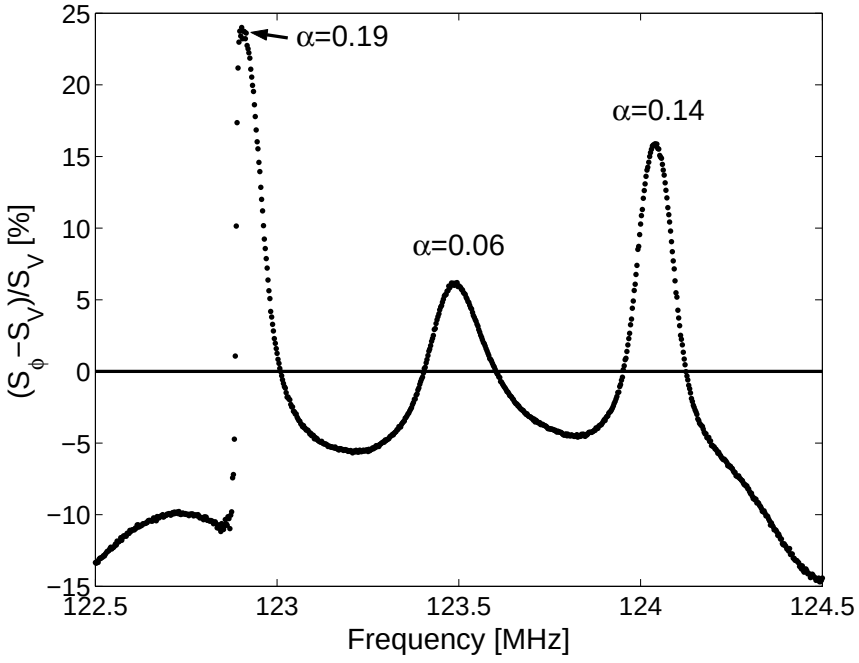


Fig. 4.10 – Phase sensitivity relative to the velocity sensitivity as a function of the frequency and computed from the experimental data obtained by etching 50 nm of gold. Oscillations are attributed to the electromagnetic interferences.

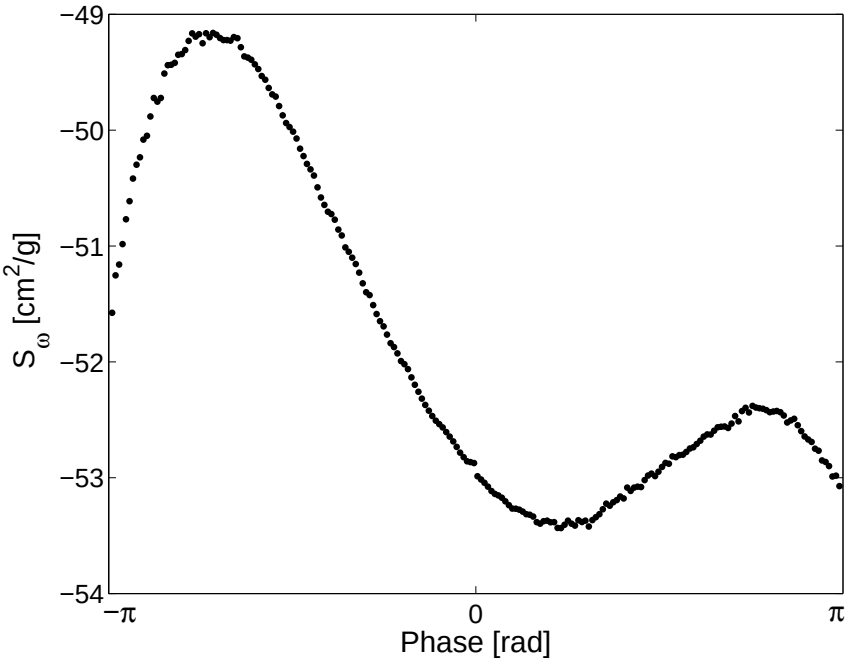


Fig. 4.11 – Simulated closed loop frequency sensitivity.

be identified by a careful inspection of the transfer function. The amplitude of the transfer function peak to peak is supposed to be the product between the transfer function of the transducers and the interference, and therefore an evaluation of α is possible if the transfer function of the transducers only is known. However, the experiment shows that α is a function of the frequency and the surface density, indicating that finding its exact value is not straightforward. Only the phase indicates whether α is higher or lower than one.

4.6.1 Expression of the EM interaction term

A simple evaluation of the EM interaction term α is obtained by considering Eq. (4.5):

$$\alpha = \frac{H(\omega) - H_T(\omega)}{\|H_T(\omega)\|} \tag{4.39}$$

where $H_T(\omega)$ is assumed to be given by its expression given in Appendix B (Eq. (B.3)) while neglecting the triple transit term (e.g. the term

$Y_{IDT}R$ at the denominator):

$$\alpha = \frac{\mathrm{i}\omega C_{EM} R}{(1 + Y_{IDT}R)^2 \left\| \frac{Y_{DL}R}{(1+Y_{IDT}R)^2} \right\|} \tag{4.40}$$

with expressions of the admittances Y_{IDT} and Y_{DL} given by Eqs. (B.1) and (B.4), respectively. The expression can be simplified further when the radiation conductance of the IDT is small with respect to the static capacitance ($G_a(\omega) < \omega C_T$), then we obtain a term with a phase almost equal to zero:

$$\boxed{\alpha \simeq \frac{\omega C_{EM}}{G_a(\omega)}} \tag{4.41}$$

or, equivalently, in a finalized form:

$$\boxed{\alpha \simeq \frac{\omega C_{EM}}{8K^2 f_0 N C_T \mathrm{sinc}^2(N\pi(f-f_0)/f_0)}} \tag{4.42}$$

The latter expression can be used advantageously in the design of SAW sensor to determine rules to decrease as much as possible the influence of the interaction parameter. The term α is made the smallest by:

decreasing the operating frequency ω operation at low frequencies is reducing the magnitude of the parasitic capacitance;

decreasing the electromagnetic capacitance C_{EM} obtained by separating electrically input and output transducers, by a grounded metal pad between both transducers and by avoiding liquids (in general) or highly ionic liquids;

increasing the electromechanical coupling coefficient K^2 piezoelectric substrates with a high coupling coefficient should be preferred, such as lithium compounds instead of quartz;

increasing the amount of fingers N which might result however in a larger value of C_{EM} and is also negatively increasing the sine cardinal term, a trade-off must be calculated from that aspect;

increasing the acoustic aperture W with an increasing size of the sensing area;

increasing the static capacitance of the IDTs $C_T = NWC_0$ which require to use materials with a high dielectric constant such as

lithium compounds; for layer coated devices, with the thickest coating possible; and by increasing the amount of finger pairs in the IDTs.

4.6.2 Sensitivity gain bandwidth

As indicated by Eq. (4.30), the factor of proportionality between the velocity sensitivity and the open loop sensitivity can be higher than unity for given values of α and frequencies, thus resulting in a type of amplification. We suggest to use this mechanism to enhance the detection limit of the mass sensor; the maximum effect occurs at interference peaks and is effectively enhancing the sensitivity when α is lying between 0 and 2. A major enhancement is reached for values of the interference parameter the closest possible to 1. Since the position of an interference peak is modified by the change in acoustic velocity, this gain exists only on a frequency interval centered around an interference peak. We introduce the *sensitivity gain bandwidth* SGBW defined by this interval such that the phase sensitivity is higher than the velocity sensitivity. This bandwidth is given by:

$$\boxed{\mathrm{SGBW} = \frac{1}{\tau}\left(1 - \frac{\arccos\left(-\alpha/2\right)}{\pi}\right)} \tag{4.43}$$

which has sense for $\alpha \in [0, 1]$. The SGBW is comprised in the interval $[1/3\tau, 1/2\tau]$ as α decreases from 1 to 0. As example, in Figure 4.10, the three values of α are 0.19, 0.06 and 0.14. The maximum enhancement is given by $1/(1-\alpha)$ and is therefore equals to 24%, 6% and 16%, respectively. For these values of α, the SGBW is theoretically equal to 258, 270 and 262 kHz, respectively. These results are correlated by the figure although they differ in reason of the variation of α: the measured values are 198 kHz and 173 kHz for α equals to 0.06 and 0.14 (which give τ=2.48 and 2.76 μs, respectively). The theoretical evolution of the SGBW as a function of the parasitic electromagnetic capacitance is obtained after replacement of the estimation of α, given by Eq. 4.42, in Eq. 4.43 and sketched in Figure 4.12. It can be deduced from the graph that, as the value of α is kept constant, and thus a constant gain is achieved, variations of the electromagnetic capacitance C_{EM} can be compensated by varying the frequency while keeping a constant SGBW.

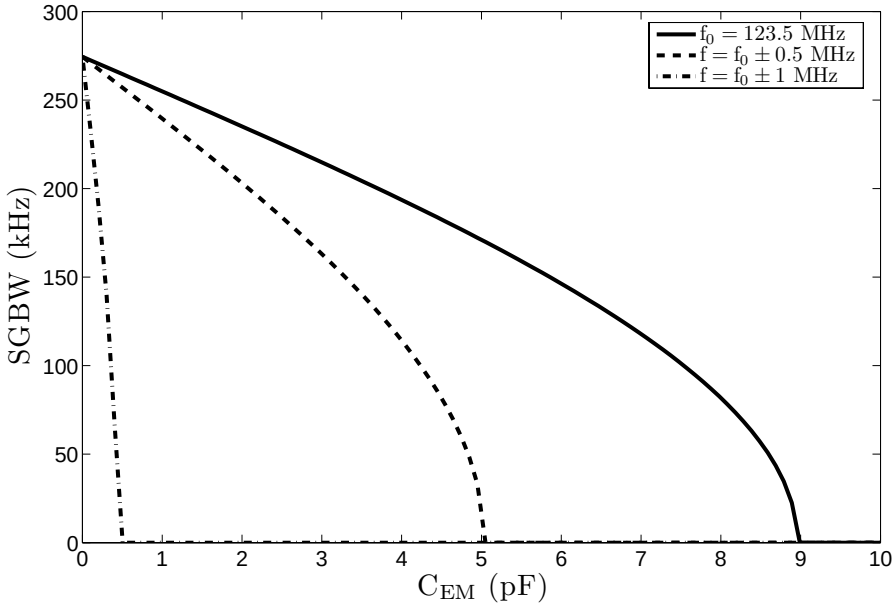


Fig. 4.12 – Theoretical evolution of the sensitivity gain bandwidth as a function of the electromagnetic capacitance C_{EM} for different frequencies.

4.6.3 Periodicity

In term of sensitivity, when $\alpha \geq 1$ the phase has a periodicity P in the range 0 to π. We suggest the following correction to the experimental phase sensitivity:

$$S_\phi = \frac{2\pi}{P}\frac{1}{kD}\frac{d\phi}{d\sigma}. \tag{4.44}$$

This modification gives a better evaluation of the velocity sensitivity by stretching the phase of the transfer function to 2π. Only the extraction of P is not immediate since it depends upon α. From a physical point of view, α indicates the strength of the electromagnetic wave in comparison with the acoustic wave. For a constant amplitude of the EM wave, a higher α stands for a larger attenuation of the acoustic wave; its precise value is an indication of the actual attenuation of the acoustic wave along the delay line.

The observation of the interference peaks in the experimental part was facilitated by the large velocity change induced by the gold coating. Indeed, 50 nm of gold corresponds to a surface density of 96.5 μg/cm^2, a relatively large shift in comparison to the targeted (bio)chemical recognition application where molecules films surface density are in the order of hundreds of ng/cm^2 and even lower. The calibration of the sensitivity is best recorded by adding or etching thin layers of materials and that under the operating conditions of the sensor, especially if liquids are involved [60]. In (bio)chemical measurements, the precision on the velocity measurement depends upon the assessments on the initial conditions (i.e. V_0 and n) but also on the induced variation of velocity, which is function of the velocity sensitivity of the waveguide. The evaluation of the mass sensitivity by the frequency variation of an interference peak is identical to a closed loop measurement locked on the interference peak instead on a constant value of the phase. For the detection of a minimum value of the surface density $\Delta\sigma$, the frequency shift of an interference peak must be measured with a precision estimated from Eq. (4.35):

$$\boxed{\Delta f_n = \frac{DS_V f_n}{V\tau_g}\Delta\sigma} \tag{4.45}$$

that gives $\Delta f_n/\Delta\sigma \simeq -6.5$ cm^{2}Hz/ng in the present case. The detection of a monolayer of proteins, about 400 ng/cm^2, requires to detect a frequency variation of 2.6 kHz, which is compatible with the instrumentation of surface acoustic waveguide sensors.

One benefit of our calculation method resides in the possibility to still measure the acoustic velocity in the sensing area even when the electromagnetic and the acoustic waves are strongly interfering, in particular for α greater than one. Strong interferences are unwanted in an experimental setup because they prevent the correct electrical measurement of the sensor. It must be noticed that for these high values of interference, the electromagnetic wave amplifies the acoustic signal as seen in Figure 4.2(d), which could be of interest for the operation of the device even in conditions where the acoustic signal is weak. Finally, the presented method operates directly on the raw signal of the acoustic device thus avoiding a lost or a modification of the physical information it carries.

4.7 Conclusion

We have proposed a model for surface acoustic waveguides used as sensors. The model shows the influence of electromagnetic interferences caused by interdigital transducers on the velocity sensitivity in open and closed loop configurations. In both cases, the dimensions of the delay line and the sensing part influence the experimental value of phase or frequency shifts.

The interference peaks in the transfer function offer an unique possibility to access the information about the acoustic phase velocity in the sensing area. The velocity sensitivity was calculated directly from these peaks.

In an open loop configuration and with interferences, the *phase* shift is disturbed and the sensitivity is over- or under-estimated to the value of the velocity sensitivity. For strong interferences, the phase has a periodicity lower than 2π that must be considered when normalizing the phase shift to obtain a correct figure of the sensitivity.

In a closed loop configuration and with interferences, the *frequency* shift is not disturbed. The frequency shift is proportional to the sensitivity by the ratio between the length of the sensing area and the distance separating the transducers. In addition, the frequency shift is influenced by the dispersive properties of the waveguide.

The influence of the electromagnetic interferences on the transfer function of a Love mode sensor operating in liquid conditions was presented for a comparison. From the experiment it appears that the interferences are function of both the frequency and the surface density.

An analytical expression of the electromagnetic-acoustic interaction and the parameters acting on it have been identified in order to reduce the influence or, on the opposite, to enhance the velocity sensitivity of surface acoustic waveguides. This analysis introduced the concept of Sensitivity Gain Bandwidth (SGBW). The SGBW corresponds to a frequency interval in which the phase shift is higher than the phase velocity shift according to the importance of the interaction between the electromagnetic and the acoustic waves, and resulting in a mechanism that can be used at profit to enhance the sensitivity of the device.

Chapter 5

Combining acoustic and optical biosensors

> Menschen des Zufalls. – Das Wesentliche an jeder Erfindung thut der Zufall, aber den meisten Menschen begegnet dieser Zufall nicht.
>
> *Friedrich Nietzsche*
> Morgenröthe

We present results from a novel instrument combining a Love mode SAW sensor with surface plasmon resonance (SPR) measurements. This is a new technique with the objective to use two independent methods, the former based on adsorbed mass or viscosity change measurements and the latter on surface dielectric properties variations, to identify physical properties of viscoelastic layers such as proteins, and more specifically their water content. Methodologies are presented for the extraction of quantitative information related to the thickness and the density of rigid layers and to the thickness, the density and the viscosity of viscous layers. For rigid layers, the methodology is applied to the electrodeposition of copper and to extract the thickness and the water content of S-layer proteins, where we obtained 4.7±0.7 nm and 75±15%; while for viscous layers, the methodology is applied to study the thermal behavior of physisorbed PNIPAAm, a polymer whose conformation is sensitive to temperature, under a cycling variation of temperature between 20 and 40 °C. Under the assumption of the bulk density and the bulk refractive

index of PNIPAAm, thickness and viscosity of the film are obtained from simulations; the viscosity is correlated to the solvent content of the physisorbed layer.

5.1 Introduction

Sorption processes at the solid/liquid interface by which (bio)molecules bound to material surfaces are of interest for biosensors, biomaterials, materials characterization and surface science. Understanding the three-dimensional organization (including density, water content and thickness) of the resulting sorbed film and its evolution during the process is crucial for many applications in these domains. For biosensors, more specifically, there is a need to monitor the response in real-time and to be able to distinguish contributions coming from the dry sorbed mass, which is the physical criterion for estimating sensitivity, and those that should be attributed to effects intimately associated to the film organization, like sorbent-bound water and viscosity for example. While a wide variety of methods can qualitatively detect the formation of sorbed films, almost none of them, alone, is quantitative and able to reveal the film organization. Furthermore, only a few techniques can monitor the sorption process in real-time. Scanning probe microscopies might fulfill all these requirements, mainly for submonolayers sorbed on ultra smooth surfaces [110]. Neutron reflectivity [132], XPS [152], mass spectroscopy [80] and radiolabeling [50] are quantitative techniques able to directly measure the dry sorbed amount, nevertheless compatible to very different film organizations. Of all the direct detection (i.e. label-less) techniques, we have identified acoustic and optical methods as being the only ones fulfilling two fundamental criteria of our measurements: time resolved and *in situ* (liquid phase) measurement of the physical properties of the adsorbed layer.

Various methods of direct detection of biochemical layers have been developed, either based on the disturbance of an acoustic wave [34] (quartz crystal microbalance [158] – QCM – and surface acoustic wave devices [65] – SAW) or of an evanescent electromagnetic wave (optical waveguide sensors [39, 195] and surface plasmon resonance [96, 130] – SPR). While each one of these transducers provides reliable qualitative curves during the adsorption of a soft layer on their functionalized sur-

face, such as proteins for example, extraction of quantitative physical parameters such as optical index, density, viscosity or water content requires modeling of the adsorbed layers [91]. The modeling includes multiple parameters which must be identified simultaneously: hence the need for the combination of acoustic and optical detection methods in a single instrument [7, 26, 122, 153].

We here use a combination of Love mode surface acoustic wave (SAW) device and surface plasmon resonance (SPR) and present a methodology to extract out of experimental data and simulations a quantitative value for the density and for the thickness of rigid layers and a quantitative value for the density, for the viscosity and for the thickness of adsorbed soft layers from a liquid phase. The viscosity and the density are correlated further to the water content in the adsorbed layer.

5.2 Operation principle of surface plasmon resonance

Surface plasmon resonance (SPR) is a well accepted direct detection technique for monitoring biological processes [90, 96, 130]. Surface plasmon resonance is based on the modification of the resonance of plasmon surface polaritons (PSP) upon a modification of the thickness and/or of the dielectric constant of a dielectric slab contacting a thin film metal.

5.2.1 Plasmon surface polaritons

Plasmon surface polaritons are the collective electromagnetic resonance modes of the interface between a metal and a dielectric [183]. PSP are obtained by the coupling of photons with the free electric charges at the surface of the metal. The surface modes are $p-$polarized, also named *transverse magnetic* (TM), which means that the electric field vector is contained in the plane defined by the normal to the surface and the wavevector $\vec{k_p}$ of the PSP. The wavevector $\vec{k_p}$ is contained in the surface. The PSP modes are allowed at resonance frequencies ω where the real part of the dielectric function of the metal $\Re\varepsilon_m(\omega)$ is less than $-\varepsilon_d$, where ε_d is the dielectric constant of the dielectric material. Because of its confinement at the interface, the field amplitude decays exponentially in directions perpendicular to the surface with a decay

length of the order of the wavelength of freely propagating light at the same frequency ω.

At the metal-dielectric interface, the relation of dispersion is given by

$$\omega = ck_p \sqrt{\frac{1}{\varepsilon_m(\omega)} + \frac{1}{\varepsilon_d}} \tag{5.1}$$

where c is the speed of light in vacuum. The dielectric function of the metal is based on the free electron gas model that states

$$\varepsilon_m(\omega) = 1 - \left(\frac{\omega_p}{\omega}\right)^2 \tag{5.2}$$

where ω_p is the plasma frequency defined by $\omega_p^2 = 4\pi e^2 \rho / m_e$ (with e the charge of the electron, ρ the conduction electron number density and m_e the mass of the electron). The plasma frequency corresponds to the vibration mode of bulk plasmons. The PSP dispersion relation follows the asymptotic value $\omega = ck/\sqrt{\varepsilon_d}$ for small wavenumbers k_p and, for high wavenumbers, to the surface plasmon cut-off frequency given by $\omega_{sp} = \omega_p/\sqrt{1+\varepsilon_d}$. Due to this aspect of the dispersion relation, PSP can not be directly excited from photons propagating in the dielectric since the wavenumber and the frequency of such photons will never correspond to a point of the PSP dispersion relation. Therefore, the excitation of the surface polaritons is obtained thanks to a coupling prism in the so-called *Kretschmann configuration*.

In the Kretschmann configuration, the metal film is placed in close contact with a prism such that a coupling of an incident beam of light with the PSP occurs. The wavenumber of the light in the prism is given by $k_{prism} = n_{prism}\omega/c$, where n_{prism} is the refractive index of the prism material. If the relation $n_{prism} > \sqrt{\varepsilon_d}$ is observed then the asymptotic relation for small wavenumbers of the PSP is rotated and therefore crosses the PSP dispersion relation. Actually, the wavevector of the light in the prism has a component parallel to the surface $k_{\|}$ that must correspond to k_p for an effective coupling of the incident photons with the surface polaritons:

$$k_{\|} = \frac{n_{prism}\omega \sin\theta}{c} \tag{5.3}$$

where θ is the incidence angle in the prism. Therefore, the coupling wavevector is comprised between 0 and $n_{prism}\omega/c$ by swapping the incidence angle θ on the prism at constant wavelength. At the coupling angle, a part of the energy of the incident light is transfered to and results in a dip observed in the intensity of the reflected light beam as the angle θ is varied.

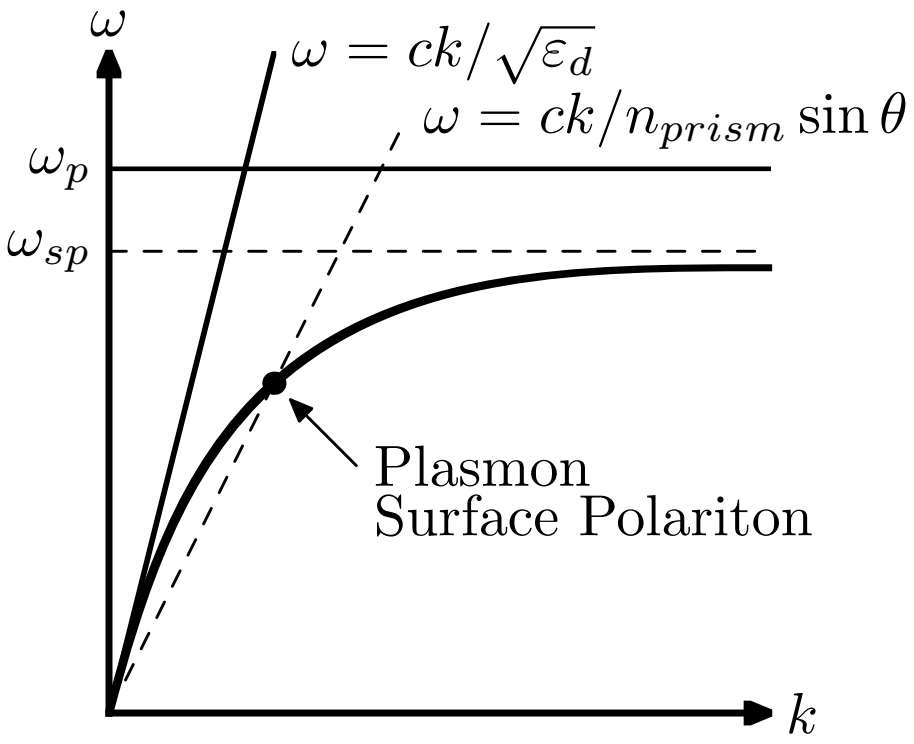


Fig. 5.1 – Relation of dispersion for plasmon surface polaritons (frequency ω *vs.* wavenumber k) and the coupling of energy obtained with a prism of refractive index n_{prism} with an incident light beam at an angle θ.

5.2.2 Surface plasmon resonance biosensor

The operation principle of an SPR biosensor (sketched in Figure 5.2) is based on the monitoring of the position of the dip angle as a function of the amount of biomolecules adsorbed on the surface (see Figure 5.3). For simulations the adsorbed layer is modeled by a thin, flat and infinitely

extended dielectric slab above the metal surface. In practical application with UV-Vis and IR light sources, the choice of metal is restricted to gold, silver, copper and aluminum [155]. Because of its chemical stability and the allowed formation of engineered surface based on alkanethiols self-assembled monolayers, gold is the most commonly used metal in SPR biosensors. Nevertheless, gold has a broad PSP resonance, is mechanically soft and is restricted to wavelengths in the red and infra-red, those drawbacks can be eliminated through the use of photonic band-gap materials as recently suggested by Shinn and Robertson [173].

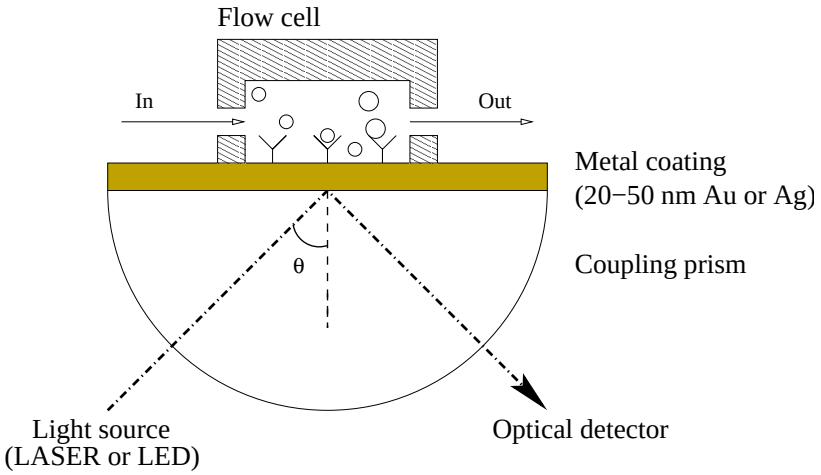


Fig. 5.2 – Surface plasmon resonance (SPR) biosensor in the Kretschmann configuration. A change of the refractive index at the top surface of the metal is monitored through a shift of θ at which the SPR signal presents a minimum.

While ellipsometry is another well known method for analyzing thin film properties [91], its use in liquid medium for monitoring biochemical reactions is made difficult by the varying environment through which the probing light beam has to propagate. In the Kretschmann configuration, the laser generating the SPR evanescent wave is only propagating through the substrate, leading to a better control over the influence of the various buffer solutions used during biomolecules adsorption experiment. The SPR biosensor is conventionally limited to a mass detection of 0.1 ng/cm^2; recently, it has been demonstrated that a coating of the sensing surface with gold nanoclusters embedded in a dielectric film,

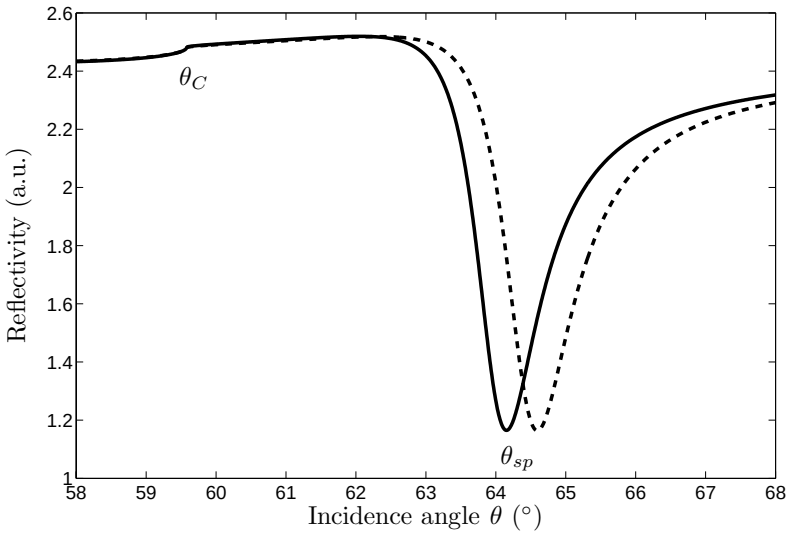


Fig. 5.3 – Reflectivity curve of the SPR biosensor during a biorecognition experiment. The dip angle θ_{sp} is observed at an incidence angle where surface plasmon polaritons are excited. The induced change of resonance due to the adsorption of biomolecules results in a shift of the dip angle (solid line to dashed line). At the left, the break in the curve is the onset of the total internal reflection inside the prism, at the critical angle θ_C.

such as SiO_2, results in a 10-fold increase of the mass sensitivity [93]. The enhancement is linked to the dielectric constant ε_e of the compound layer with metal nanoclusters embedded in a dielectric layer, which is given by [93]:

$$\varepsilon_e = \varepsilon_m \frac{\varepsilon_i (1 + 2\varphi) + 2\varepsilon_m (1 - \varphi)}{\varepsilon_i (1 - \varphi) + \varepsilon_m (2 + \varphi)} \tag{5.4}$$

where φ is the concentration of metal nanoclusters, ε_i the dielectric constant of the dielectric and ε_m the one of the metal. The formula applies for nanocluster concentration lower than 1/3. Finally, the coupling of the surface plasmon with multimode optical waveguides has been recently introduced [180], thus eliminates the need of a coupling prism.

5.2.3 Combining SPR and SAW methods

In the present study, Love mode SAW devices were chosen for a high mass sensitivity and a compatibility with measurements in liquid media [49,63,137,197]. Being based on the propagation of a shear-horizontal acoustic wave, their interaction with the surrounding liquid is minimal although the bulk properties of the solvent influence the acoustic wave propagation and must be considered in the analysis of the sensing device [87, 98] and a model for the analysis of the structure, including the adsorbed layer and the liquid, is presented in the theoretical developments about Love mode devices (see Chapter 2). While both SAW and SPR sensors display theoretically similar sensitivities and detection limits, acoustic sensors are typically sensitive to temperature fluctuations unless optimized to achieve a zero temperature coefficient of frequency (TCF) by finding an appropriate crystal cut of the substrate and an adequate thickness of the PECVD silicon dioxide guiding layer, although this latter may present a non-linear thermal behavior complicating the experimental determination of the optimum parameters [86, 101]. To avoid this issue, care must be taken to properly control the environment around the instrument to keep a stable temperature.

We take advantage of the unique geometrical setup of the surface acoustic wave (SAW) device which leaves the backside of the quartz wafer free of electrodes to inject a laser in order to generate an evanescent surface plasmon on the gold coated sensing area. Such a setup enables simultaneous estimates of the bound mass and dielectric surface

properties changes during electrochemical and biochemical reactions occurring on the sensing electrode [7, 122].

5.3 Experimental method

We use a modified commercial SPR instrument (IBIS II, IBIS Technologies BV, The Netherlands) to detect the surface plasmon resonance angle after replacing the gold coated glass slide by a Love mode SAW device (Figure 5.4). The excitation laser in this instrument has a wavelength of 670 nm. All reflected intensity *vs.* angle curves (6 ° angle span recorded on a 200 pixels CCD array) were recorded and later fitted by a polynomial to extract with high accuracy the position of the resonance dip. The acoustic wave device is made of a 500 μm thick ST-cut quartz wafer on which 200 nm thick sputtered Al interdigitated electrodes are patterned. The surface is coated by a 1.2 μm PECVD silicon dioxide layer acting as a guiding layer, and the 4.9×5.4 mm^2 sensing area is coated with 10 nm Ti and 50 nm Au. This area acts both as a working electrode for electrochemistry or a grounded electrode during biochemical experiments, as well as a supporting layer for the surface plasmon resonance generation.

The combination of two instruments rise the issue of their interaction and their mutual influence on experimental results. On one hand, Sun *et al.* have studied the interaction of surface plasmons with surface acoustic wave devices [182], where the SAW was used as a dynamic grating. They concluded for low frequencies and small amplitude of the acoustic wave to a negligible interchange of energy between the surface plasmon and the acoustic wave. On the other hand, the influence of the SAW device substrate over the detection of the SPR is seen in our experiments through interference patterns due to the birefringence of the quartz and to the optical index mismatch between the quartz and the deposited silicon dioxide layer. The former effect is reduced by orienting the optical axis of quartz so that it is in the plane defined by the normal to the sensing surface and the wavevector of the laser, thus minimizing the optical index difference between the ordinary and the extraordinary axis. The remaining interference patterns lead to fringes with a contrast low enough so that the surface plasmon peak is easily identified and tracked during the experiments.

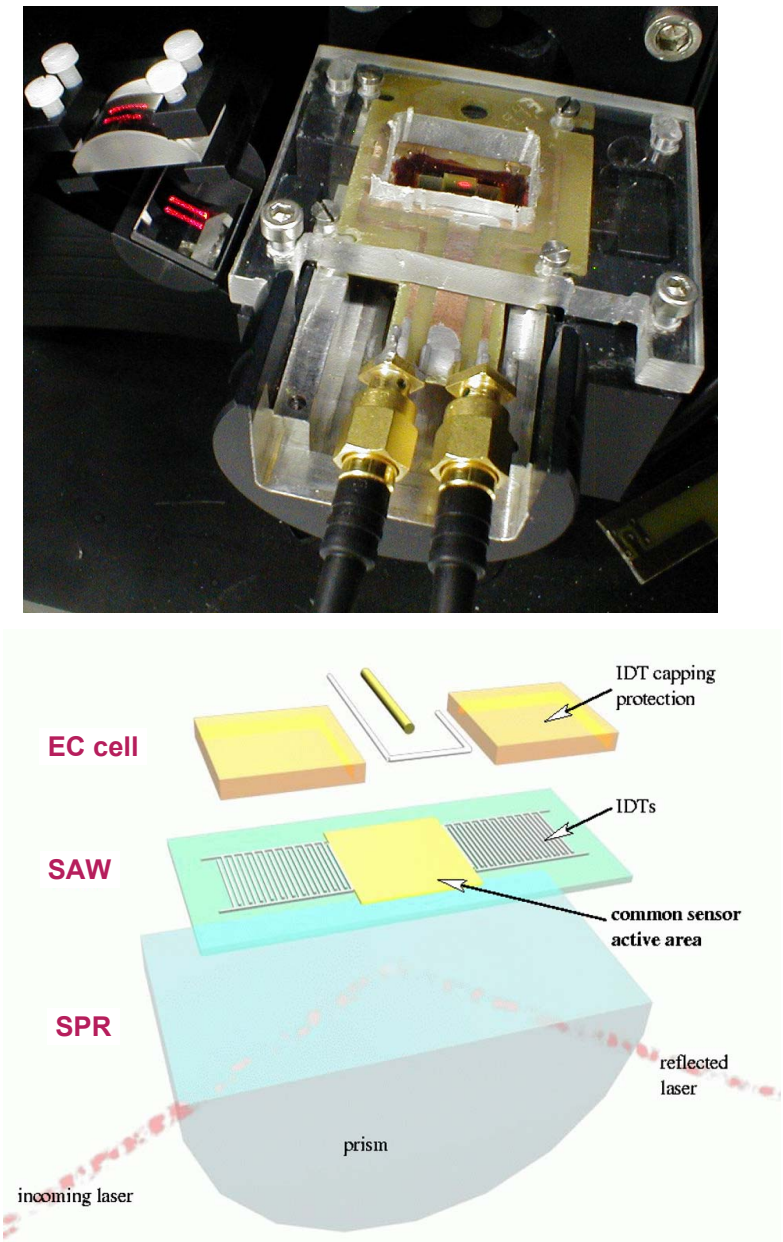


Fig. 5.4 – Experimental setup including, from bottom to top: the cylindrical glass prism for injecting the laser, the quartz wafer patterned with interdigital transducers for generating the acoustic waves and coated with a thin (1.2 μm) SiO_2 layer, and the SU-8 walls supporting the glass slides capping preventing the contact of the liquid over the transducers area.

5.4 Data mining for rigid layers

This section presents the methodology to extract the thickness and the density of a rigid layer. The methodology is applied to identify the amount of solvent dissolved in an organic self-assembled monolayer of S-layer after calibration of the SAW device by copper electrodeposition.

5.4.1 Methodology

The parameters required for analyzing the SAW data resulting from the surface adsorption of the rigid layer are its thickness h and its density ρ_C. The parameters required for analyzing the SPR data are the common layer thickness h and the optical index n_C of the adsorbed layer. We have three free parameters and only two measurements, namely the adsorbed mass per unit area and an SPR resonance angle shift which is a function of both the refractive index n_C and the film thickness h.

Two options are possible to resolve the missing link: the first one is to add one more measurement parameter, such as an SPR dip position as a function of wavelength which would lead to a unique identification of h and n_C [142]; the second one is to reduce the number of variables by adding the assumption that the layer is made of a homogeneous mixture of a proportion x of proteins and $(1-x)$ of solvent. Under this assumption, the layer density ρ_C is given by

$$\rho_C = x\rho_L + (1-x)\rho_F \tag{5.5}$$

where ρ_L is the bulk density of the material deposited in the composite layer. Similarly, we use then the optical index of the layer

$$n_C = xn_L + (1-x)n_F. \tag{5.6}$$

The remaining unknown parameters are then the layer thickness h and the proportion of solvent content $(1-x)$. By simulating a stack of planar multilayers for the angle shift as a function of water content and layer thickness, one obtains a set of pairs of values for these two parameters compatible with the observed angle shift .

Then, by calculating the mass per unit area $\Delta\sigma = \rho h$, a comparison with the experimentally observed adsorbed mass as seen from the

phase shift of the SAW device leads to a unique set of parameters both compatible with the optical index change and the adsorbed mass. The methodology to extract the thickness and composition of the rigid composite layer is summarized in Figure 5.5.

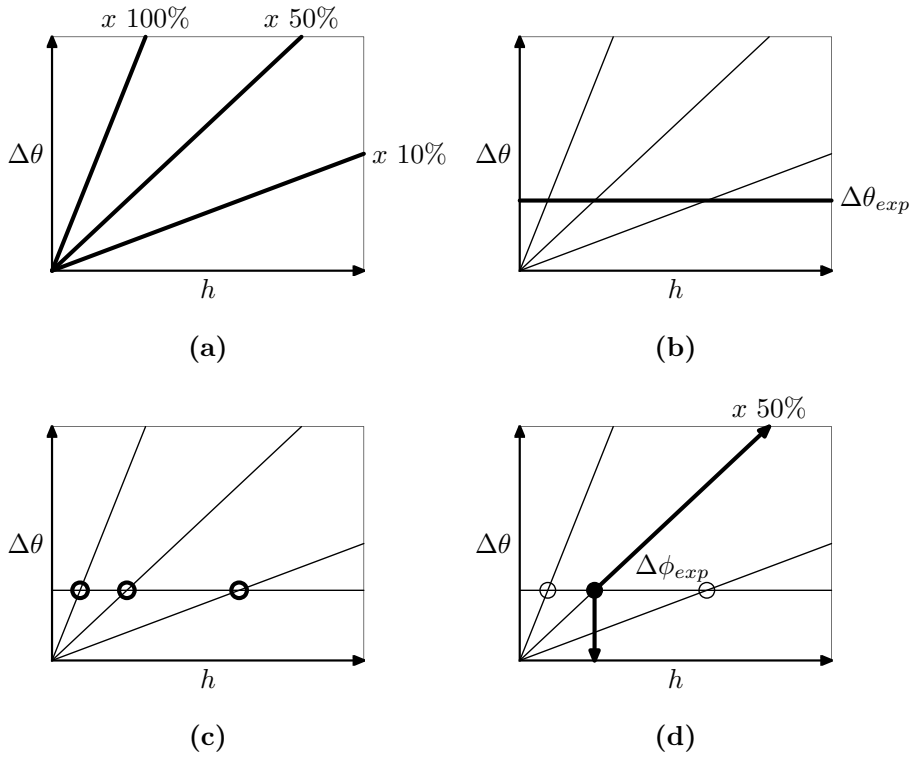


Fig. 5.5 – Graphical method to retrieve information of film thickness and composition from SAW and SPR data. A graph of the SPR shift $\Delta\theta$ is set *vs.* film thickness h. (a) Abacus of SPR shifts for isoconcentrations x are computed and plotted from SPR simulations. (b) The experimental SPR shift, $\Delta\theta_{exp}$ is reported in the abacus. (c) The points of intersection between the abacus and the experimental shift have an unique value of film thickness and composition that is translated into possible values of SAW shifts. (d) The experimental SAW shift gives an unique thickness and composition of the film probed by both techniques.

5.4.2 Application to S-layers

As seen in Figure 5.6, the electrodeposition of copper for the calibration of the mass sensitivity is followed simultaneously by the acoustic and the optical methods. Optical measurement displayed resonance angle shifts due to the varying potential [118]. When the voltage applied by the potentiostat is above 0.2 V with respect to the Cu pseudo reference electrode, the SPR angle slightly shifts due to the electroreflectance effect described by Kötz *et al.* [118]. Below 0.2 V, underpotential deposition starts depositing a monolayer of Cu atoms on the gold surface as visible both in the phase shift of the SAW device and as a reversal of the trend of the angle shift of the SPR. Below 0 V, a rough Cu layer is deposited, leading to a loss of the SPR peak and a large phase shift of the SAW device due to the large added mass. The rough, discontinuous film of copper clusters a few tens to hundreds of nanometers high was observed by *in situ* AFM imaging. Simulating the influence of sub-wavelength metallic structures on the surface plasmon resonance is a difficult task [51, 78] which we have not attempted to solve.

Once the mass sensitivity of the SAW is calibrated, we adsorbed on the same device a crystalline monolayer of S-layer proteins (100 μg/ml of the protein SbpA of *Bacillus sphaericus* CCM 2177 in 0.5 mM tris, 10 mM $CaCl_2$, pH=9 buffer) [77, 166] while monitoring simultaneously with the SAW device the mass variation and with SPR the surface dielectric change. The adsorption and desorption steps, the latter being possible with the use of 2 % NaOCl, was repeated several times (Figure 5.7). A property of this protein which makes it suitable for calibration of a new instrument is that it only forms a monolayer and will not stack to multiple layers even at high concentrations.

For the simulation, ρ_L is assumed to be equal in the 1.2 g/cm^3 to 1.4 g/cm^3 range [32, 91, 92, 135], and $\rho_F = 1$ g/cm^3 is the density of the water solvent. For the optical data, the optical index of the protein layer assumed to be in the $n_L = 1.45$ to 1.465 range [92, 130, 135], and that of water $n_F = 1.33$. The SPR simulation of the stack has been done with the following parameters: glass $n_{glass} = 1.518$, 1200 nm silicon dioxide $n_{SiO_2} = 1.45$, 2 nm titanium $n_{Ti} = 2.76 + i3.84$ [147], 50 nm gold $n_{Au} = 0.14 + i3.697$ [147], proteins, water $n = 1.33$.

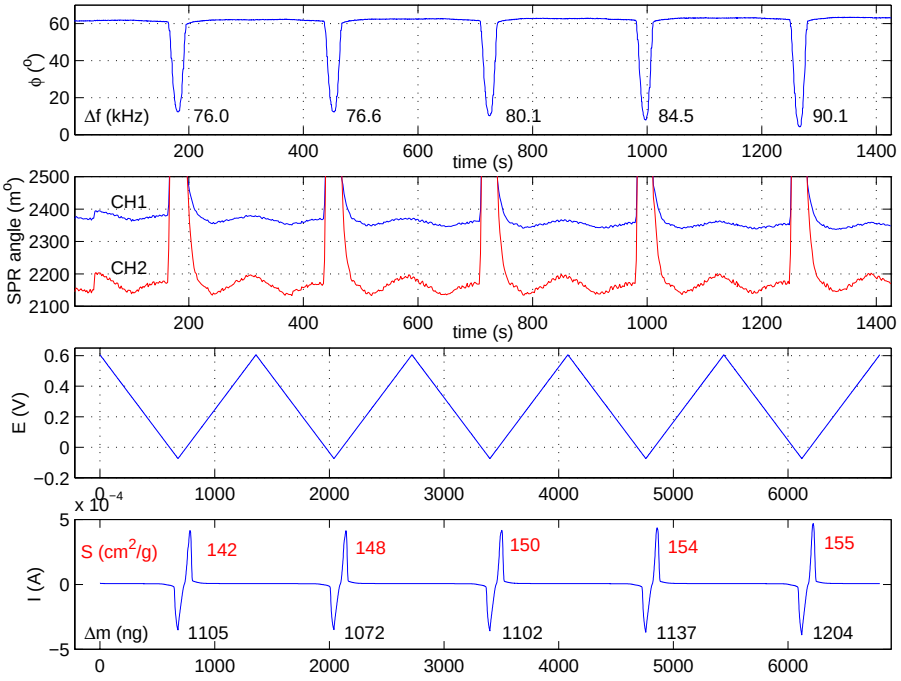


Fig. 5.6 – SAW sensitivity calibration curves using copper electrodeposition. From bottom to top: potentiostat current and potential *vs.* a copper wire acting as a pseudo reference electrode with the Cu^{2+} ions in solution ; SPR angle shift (channel 1 and 2 are separated by about 2 mm) ; and surface acoustic wave phase monitored at a fixed frequency (123.2 MHz) and converted to a frequency shift thanks to the linear phase to frequency relationship (data not shown). We indicate for clarity on the top graph the equivalent frequency shift (in kHz) and on the bottom graph the equivalent mass and calculated sensitivity.

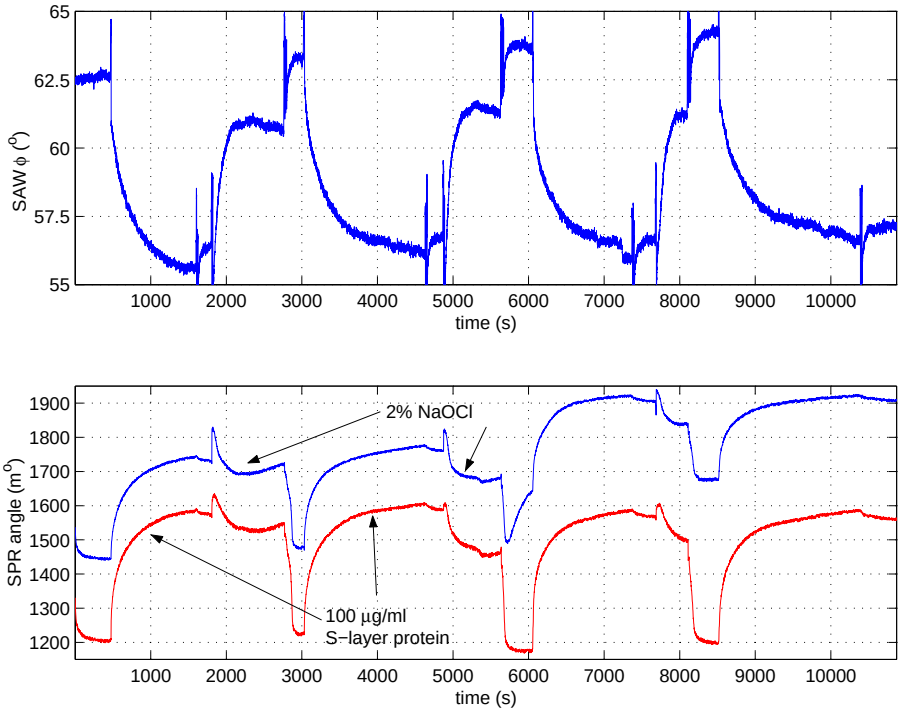


Fig. 5.7 – Simultaneous measurement of the SAW phase at 123.200 MHz and the SPR angle shift during similar experiments: injection of buffer solution, injection of S-layer protein (100 μg/ml), injection of buffer and removal of the proteins by injecting 2% NaOCl.

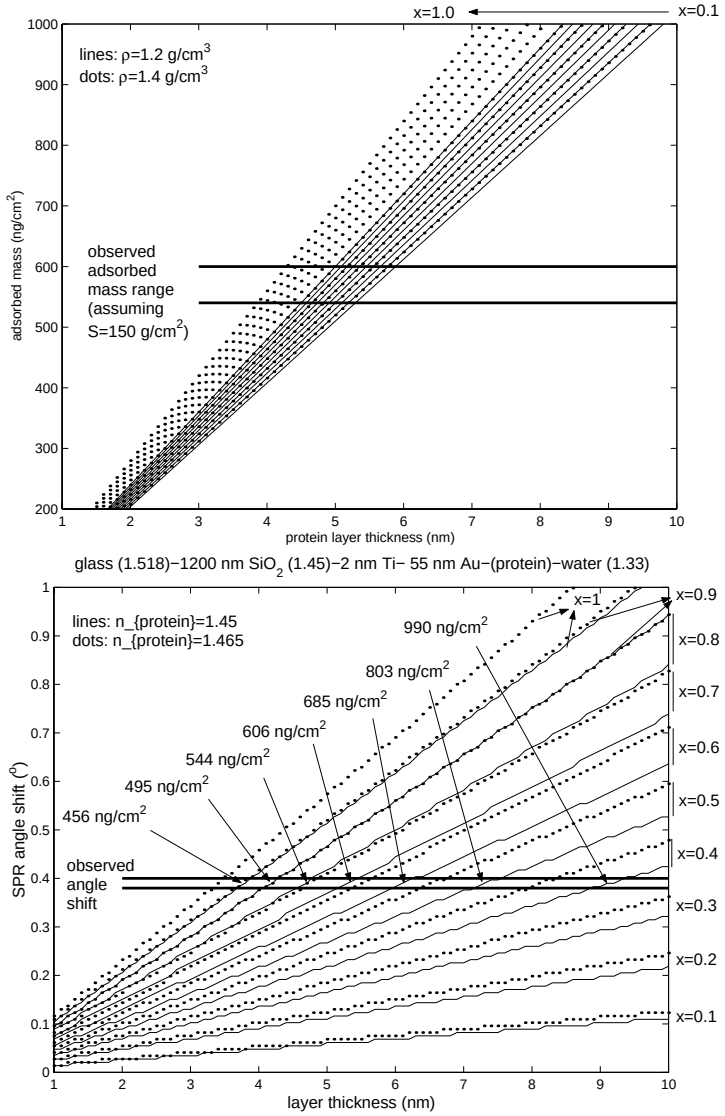


Fig. 5.8 – Top graph: simulation of the SAW frequency shift for varying protein layer thickness (abscissa) and proportion of proteins in the layer (from $x = 10\%$ to $x = 100\%$ from right to left), and varying the density of the protein layer within the values found in the literature (from 1.2 g/cm^3 as solid lines to 1.4 g/cm^3 as dots). Bottom graph: simulation of the SPR angle shift for varying protein layer thickness (abscissa) and proportion of proteins in the layer (from $x = 10\%$ to $x = 100\%$ from bottom to top), and varying the optical index of the protein layer within the values found in the literature (from 1.45 as solid lines to 1.465 as dots). The mass density of the points lying in the region of experimentally observed angle shift have been indicated for added clarity.

The calculation result is explained in Figure 5.8. In the case under consideration here, an observed angle shift of 380 to 400 m° and an adsorbed mass of 540 to 580 ng/cm^2 is only compatible with $x = 0.75 \pm 0.15$ and $h = 4.7 \pm 0.7$ nm. The thickness result is compatible with atomic force microscope (AFM) measurements in liquid [77] while the mass per unit area is compatible with morphological data obtained by electronic microscopy [166]. While the main source of uncertainty is due to the wide possible values of the density and optical index reported in the literature, the experimental results display good reproducibility. The water content is lower than that observed by other authors for different kinds of proteins [91,135] but compatible with the 30 to 78% value cited in Ref. [178]. The dense packing of protein is explained by the regular arrangement of identical S-layer subunits in the p4 lattice [199, 200].

5.5 Data mining for soft layers

In this section, we show the theoretical and experimental combination of acoustic and optical methods for the *in situ* quantitative evaluation of the density, the viscosity and the thickness of soft layers adsorbed on chemically tailored metal surfaces. For the highest sensitivity and an operation in liquids, a Love mode surface acoustic wave (SAW) sensor with a hydrophobized gold coated sensing area is the acoustic method while surface plasmon resonance (SPR) on the same gold surface as the optical method is monitored simultaneously in a single setup for the real-time and label-free measurement of the parameters of adsorbed soft layers, which means for layers with a predominant viscous behavior. A methodology is presented to identify from SAW and SPR simulations the parameters representatives of the soft layer. During the absorption of a soft layer, thickness or viscosity changes are observed in the experimental ratio of the SAW signal attenuation to the SAW signal phase and are correlated with the theoretical model.

5.5.1 PNIPAAm and notation conventions

As a showcase of the analysis of soft layers, the detection of the physisorption of poly(N-isopropyl acrylamide) – PNIPAAm – is presented. PNIPAAm is a thermally sensitive polymer with a conformal transition

investigated previously by SPR and QCM techniques [9, 153]. Our approach is presented as a sequel to the study by Plunkett *et al.* [153] where the properties of PNIPAAm physisorbtion to a hydrophobic surface was monitored by a combination of SPR and QCM, and the subsequent temperature-dependent conformation transition was monitored by QCM alone by measuring both the resonance frequency and the quality factor of the resonator.

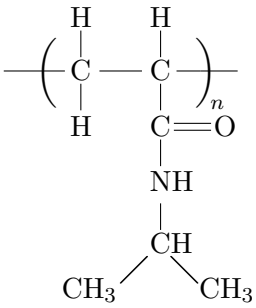


Fig. 5.9 – Schematic of the PNIPAAm structure for a degree of polymerization n.

In general, acoustic sensors display an unwanted thermal drift. However, in the present case, the temperature will be voluntary modified and monitored to modify the characteristics of the adsorbed PNIPAAm thus requiring a preliminary calibration curve of the acoustic response as a function of the temperature. The analysis of the layer will assume that a certain amount of the solvent – water in the present case – is contained in the layer. A schematic representation of the experimental combined setup used for this study is given in Figure 5.10.

In the combined SAW/SPR technique, the SPR signal is a measurement of the coupling plasmon angle as a function of variations in refractive index n and thickness h of the adsorbed layer. A single SPR measurement is therefore not sufficient to determine independently these two parameters. Our previous analysis applied to rigid layers, therefore the SAW shift was assumed to be proportional to the density and thickness of the layer with respect to a mass sensitivity calibration of the SAW device by copper electrodeposition. In the rigid layer assumption, the

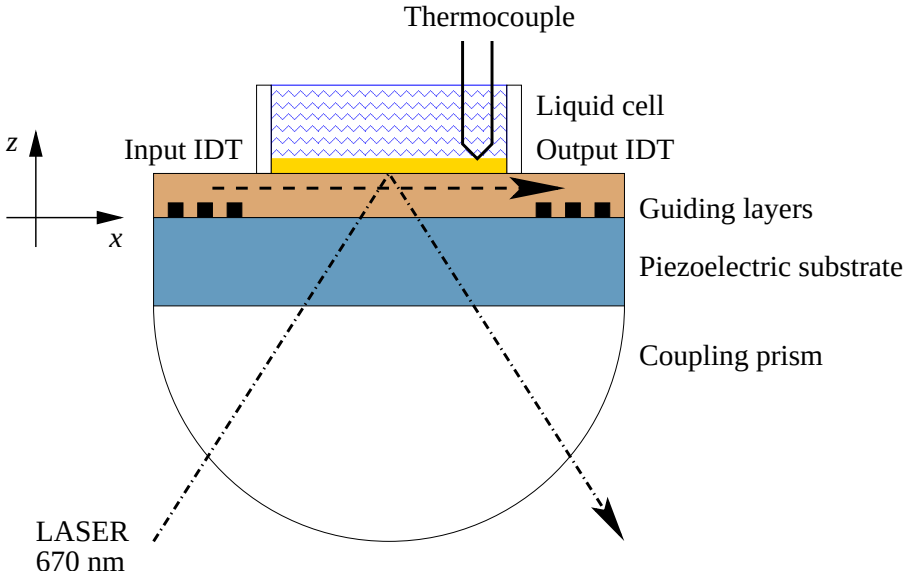


Fig. 5.10 – Schematic cross-section of the combined SAW/SPR setup: a SAW device is attached with optical index matching oil to a prism for the coupling of a LASER light with the gold coated surface of the acoustic device to generate the surface plasmon resonance. The arrows indicate the propagation of the acoustic wave (dashed line) and the collimated LASER beam (dot-dashed line).

acoustic phase difference combined to the SPR signal is sufficient to estimate independently the density and the thickness of the layer under the assumption of a linear relationship between the variation of the density of the layer and its refractive index variation. Generally, for any added layer on the sensing surface, four parameters must be evaluated from the measurement (density, shear stiffness, viscosity and thickness) while the SAW device gives only two independent measurements linked to the real and the imaginary part of the acoustic wavevector measured electrically by the transducers (insertion loss and phase); therefore, an assumption must be made to solve some complexity of the analysis to evaluate the unknown parameters. To that purpose, we assume in this section that the composite layer and the surrounding liquid are Newtonian fluids, meaning that the shear stiffness in both layers, μ_C and μ_F, is discarded in regard to the viscous components $\omega\eta_C$ and $\omega\eta_F$. This working hypothesis has been previously described in the literature [163] through the *relaxation time* $\tau = \eta/\mu$, and a comparison of the relaxation time to the excitation frequency ω driving the mechanical motion of the waveguide surface. The SAW and SPR data are linked by a similar relation than the one established in the case of a rigid layer which will still be assumed to hold under the form:

$$\frac{\rho_C - \rho_F}{\rho_L - \rho_F} = \frac{n_C - n_F}{n_L - n_F} \tag{5.7}$$

where ρ is the density and n the refractive index while the subscript F refers to the semi-infinite fluid layer, C to the composite surface adsorbed layer, and L to the bulk characteristics of the component segregating from the fluid on the sensing surface.

5.5.2 Methodology

The methodology to obtain an estimate of the density, viscosity and thickness of the soft layer is based on the principle described here after. For a possible value of the film thickness, the acoustic attenuation ΔA and the acoustic phase shift $\Delta\phi$ correspond, each of them, to a set of values for the density and the viscosity as obtained from the model described in Chapter 2. Considered together, the two sets present a common point, thus resulting in a couple values $[\rho_C(h), \eta_C(h)]$ as shown in Figure 5.11 where the lines of expected amplitude and phase shifts are plotted at a given thickness for a given value of the amplitude and

phase shifts versus density and viscosity.

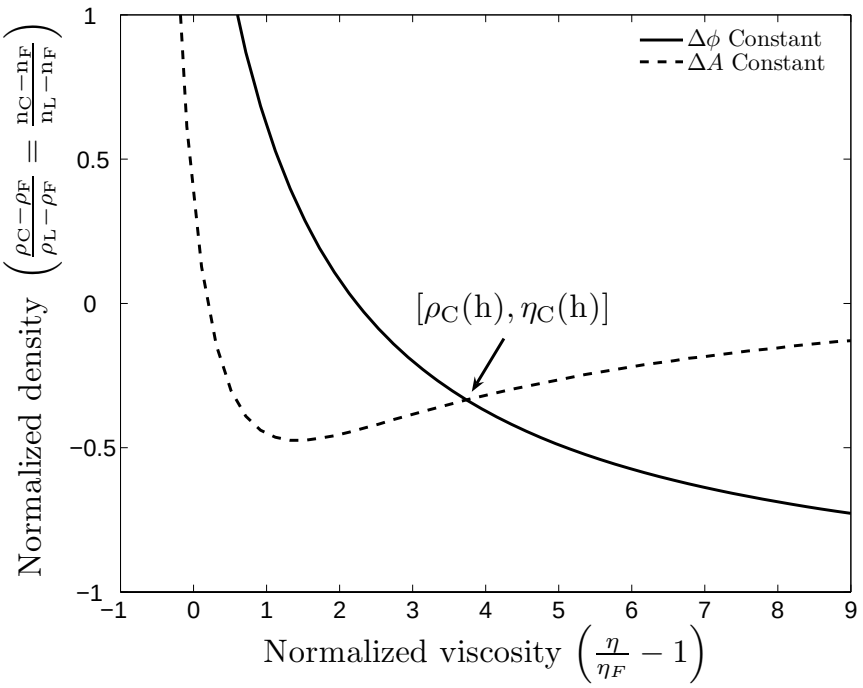


Fig. 5.11 – Plot for a given film thickness of the values of normalized density and normalized viscosity for a given and constant value of the SAW phase shift $\Delta\phi$ (solid line) and a constant value of the SAW insertion loss shift ΔA (dashed line). The values of density are normalized to obtain the direct correlation with SPR data. The intersection point of the two curves gives for that thickness the density and viscosity of the film. The procedure must be repeated for all possible values of the film thickness.

For a set of values for the thickness, a curve of possible values of viscosity and density are obtained. An unique solution $[h, \rho_C, \eta_C]$ is obtained thanks to the SPR data: for each value of thickness at a given SPR angle shift $\Delta\theta$ corresponds an unique value of the refractive index [73] that is further related to the density of the layer thanks to Eq. 5.7, which assumes an identical evolution of the refractive index and of the density of the composite layer. The methodology is schematically depicted in

the following diagram:

$$\left.\begin{array}{l}\Delta\phi\\ \Delta A\end{array}\right\} \rightarrow [\rho_C(h), \eta_C(h)] \left.\begin{array}{r}\\ \\ \Delta\theta\end{array}\right\} \overset{Eq.5.7}{\rightarrow} [h, \rho_C, \eta_C]$$

Our method has the unique characteristics to provide the thickness, the density and the viscosity of the adsorbed layer out of three independent experimental measurements (phase and insertion loss of the SAW and coupling angle of the SPR), under assumed values for the density ρ_L and the refractive index n_L of the component and under the further assumption of an entirely viscous interaction between the composite layer and the acoustic wave (i.e. $\omega\eta_C \gg \mu_C$). At this stage, it is reminded that the ratio $\Delta A/\Delta\phi$ can be used to determine the viscous behavior of the composite layer as a function of its thickness with respect to the penetration depth δ (cfr. Figure 5.12), as discussed in Chapter 2.

5.5.3 Materials and Methods

Acoustic waveguide sensor. We used a Love mode SAW sensor obtained by coating a 0.5 mm thick ST-cut quartz substrate with a 1.2 μm thick layer of silicon dioxide by plasma enhanced chemical vapor deposition (Plasmalab 100, Oxford Plasma Technology, UK). The interdigital transducers (IDTs) were etched in a 200 nm thick aluminum layer sputtered on the substrate consisting of 100 pairs of split fingers with a periodicity of 40 μm and an acoustic aperture of 3.2 mm. The acoustic filter had its central frequency at 123.5 MHz. The sensing area between the transducers was covered with a 10 nm titanium, 50 nm gold coating that was electrically grounded to shield the acoustic waveguide. The sensor was packaged using a technique described elsewhere [56] that defined a 180 to 200 μl open well above the sensing area of $D = 4.7$ mm length and isolated the sensing area from the electrode area in order to reduce electrical interactions between the IDTs and the liquid. The open well formed a static liquid cell in which the solution was manually injected using a micropipette. The SAW phase and insertion loss were continuously monitored in an open loop configuration with an HP4396A Network Analyzer and logged on a PC through the GPIB interface.

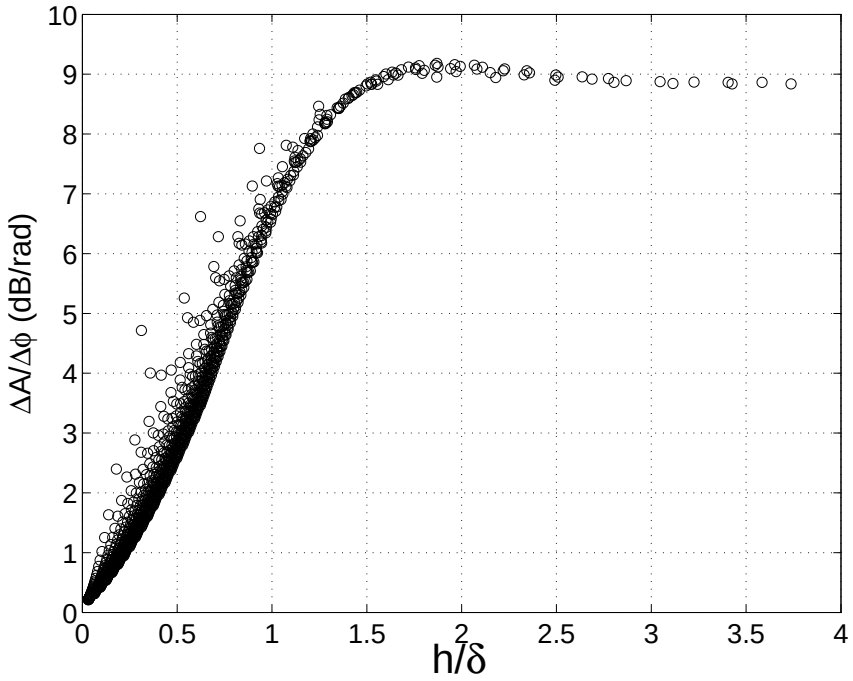


Fig. 5.12 – Simulated values for the ratio of the SAW attenuation shift to the SAW phase shift $\Delta A/\Delta\phi$ as a function of the composite film thickness normalized to the penetration depth in this film $\delta = \sqrt{2\eta_C/(\rho_C\omega)}$.

Combined SAW/SPR setup. The setup has been described elsewhere [61]. Briefly, a commercial IBIS II SPR instrument (IBIS Technologies BV, Hengelo, The Netherlands) based on a 670 nm laser diode has been modified in order to replace the usual gold-coated glass slide with the packaged Love mode SAW sensor.

Temperature monitoring. A type K thermocouple (Chromel-Alumel) junction was made by wire-bonding two 100 μm-diameter wires (Filotex, France) and was monitored by an AD595AD chip connected to an HP3478A multimeter. The temperature of the solution right above the sensing area was continuously monitored during the experiment and synchronously with the SAW and SPR measurements.

Surface preparation. The device was cleaned in UV-O_3 for 30 minutes and followed by a 3 hours contact coating with octadecanethiol hydrophobic self-assembled monolayer obtained from Sigma-Aldrich.

poly(N-isopropyl acrylamide) (PNIPAAm) from Polysciences Inc. (Warrington, PA, USA) was obtained with an average molecular weight $M_w = 40$ kD and a polydispersity index (M_w/M_n) of 2 as characterized by the manufacturer. A solution of 500 ppm polymer in deionized (DI) water (clean room grade, 18 MΩ.cm) was prepared, dialyzed to cut-off molecular weight of 12-14 kD (dialysis tubing DTV1200 from Medicell International Ltd, UK) over night and stored at 4 °C.

Experimental method. The temperature dependence of the thiol coated SAW sensor was first calibrated in DI water by cycling from 20 °C to 40 °C (rising temperature rate: 85 ± 2 K/h, decreasing rate: 49 ± 2 K/h). After calibration, the 500 ppm polymer solution was injected while the temperature was set at 29 ± 1 °C. Following the procedure described by Plunkett *et al.* [153], the sensing area was washed with twice the volume of DI water after 3 hours at a constant temperature of 29 ± 1 °C. A third volume of DI water was then injected for the measurement. The temperature was then cycled several times from $\sim$ 20 °C to $\sim$ 40 °C to monitor the influence of the temperature induced conformation changes of the polymer on the acoustic and optical signals.

5.5.4 Results

The experimental results of SAW and SPR data are given after subtraction of the temperature calibration in Figure 5.13 that provides the thermal cycle for the SAW insertion loss I.L., the SAW phase variation $\Delta\phi$ and the SPR coupling angle variation $\Delta\theta$ for the thermal cycling during the calibration step and after the polymer adsorption. The temperature calibrations were fitted by polynomial interpolations and subtracted from the raw data with expressions as a function of the temperature T, in °C, as following:

- SAW insertion loss I.L. (dB) $= 1.27 \cdot 10^{-4}T^3 - 1.29 \cdot 10^{-2}T^2 + 0.422T - 25.8$;
- SAW phase ϕ (°) $= 2.57T + 45.1$ (corresponding to a temperature coefficient of frequency - TCF - of 32 ppm/°C);
- SPR angle shift $\Delta\theta$ (m°) $= -22.7T + 1797$.

The observed average shift with temperature is compatible with the tabulated variation of bulk water refraction index [1] while the average shifts of the SAW data are following more complicated patterns that involve the effect of the transducers and the thermal shift of the acoustic propagation, not linearly correlated with temperature as in the SPR case. The mechanical and optical constants used for the SAW and SPR models are given in Table 5.1 [1, 25, 147].

Material	ρ g/cm^3	μ GPa	η cP	n
Quartz	2.648	66.3		1.518
SiO_2	2.61	8.31		1.5
Ti	4.51	46.7		2.76 + 3.84i
Au	19.3	28.5		0.14 + 3.697i
Water	1		1	1.33
PNIPAAm	1.4			1.47

Table 5.1 – Mechanical and optical constants used for SAW and SPR simulations

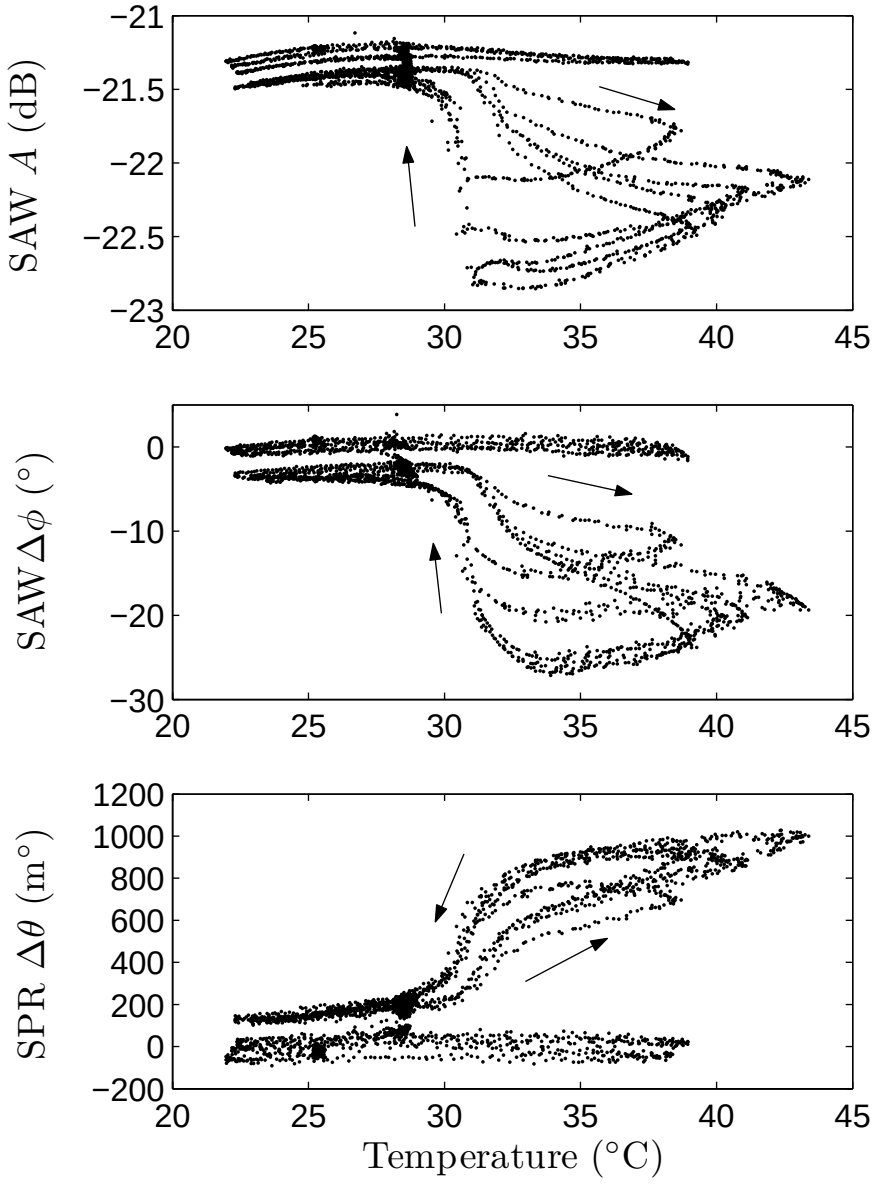


Fig. 5.13 – Raw SAW and SPR data temperature calibration and temperature cycling effect as a function of the temperature for 5 cycles after removal of the temperature effect. The arrows indicate the direction of the temperature cycling. Top graph: SAW insertion loss, middle graph: SAW phase, and bottom graph: SPR angle.

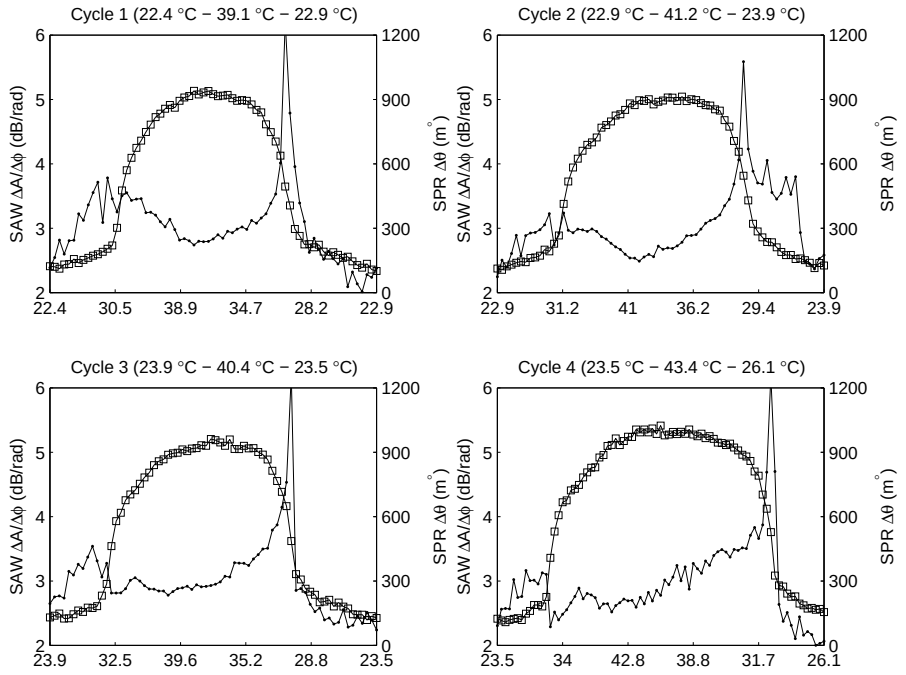


Fig. 5.14 – Evolution of the SAW attenuation shift to phase shift ratio (dots, left axis) and SPR shift (squares, right axis) for the 4 first temperature cycles.

The evolution of the acoustic and optical data per thermal cycle is given in Figure 5.14. One temperature cycle starts for the lowest temperature and ends at the next temperature minimum. It shows the evolution of the ratio of the SAW attenuation to the SAW phase $\Delta A/\Delta\phi$ (left axis) and the SPR angle $\Delta\theta$ (right axis) for the first 4 cycles. The SAW/SPR data measured at 5 different points on each cycle (25.0 °C and 35.1 °C during heating up, and 34.9 °C, 30.8 °C and 25.0 °C during cooling down) are reported in Table 5.2; the point of 30.8 °C with decreasing temperature corresponds to the peak value of $\Delta A/\Delta\phi$. The simulated values obtained with the methodology presented in the theoretical section are reported in Table 5.3. The evolution of the polymer weight concentration and the viscosity of the PNIPAAm-water layer is plotted in Figure 5.15, respectively, as a function of the layer thickness.

Thermocouple	**SAW**		**SPR**
Temp. (°C)	ΔA (dB)	$\Delta\phi$ (°)	$\Delta\theta$ (m°)
$25.0 \pm 0.1 \searrow$	-0.17 ± 0.04	-3.60 ± 0.38	146 ± 17
$25.0 \pm 0.1 \nearrow$	-0.14 ± 0.02	-2.72 ± 0.74	142 ± 13
$30.8 \pm 0.3 \searrow$	-1.05 ± 0.43	-10.0 ± 2.4	501 ± 21
$34.9 \pm 0.3 \searrow$	-1.35 ± 0.22	-24.0 ± 5.2	902 ± 52
$35.1 \pm 0.1 \nearrow$	-0.66 ± 0.45	-13.2 ± 5.4	681 ± 127

Table 5.2 – Experimental mean values observed during the 4 first temperature cycles probed at 5 different points for the thermocouple, the SAW and the SPR. The arrows indicate the direction of the temperature cycle.

5.5.5 Discussion

The ratio of the SAW attenuation shift to the phase angle shift is a good indicator of the variation of viscosity or thickness of the film and of conformational changes that occur in the film, this analysis can be extended to films evolving at constant temperature such as during

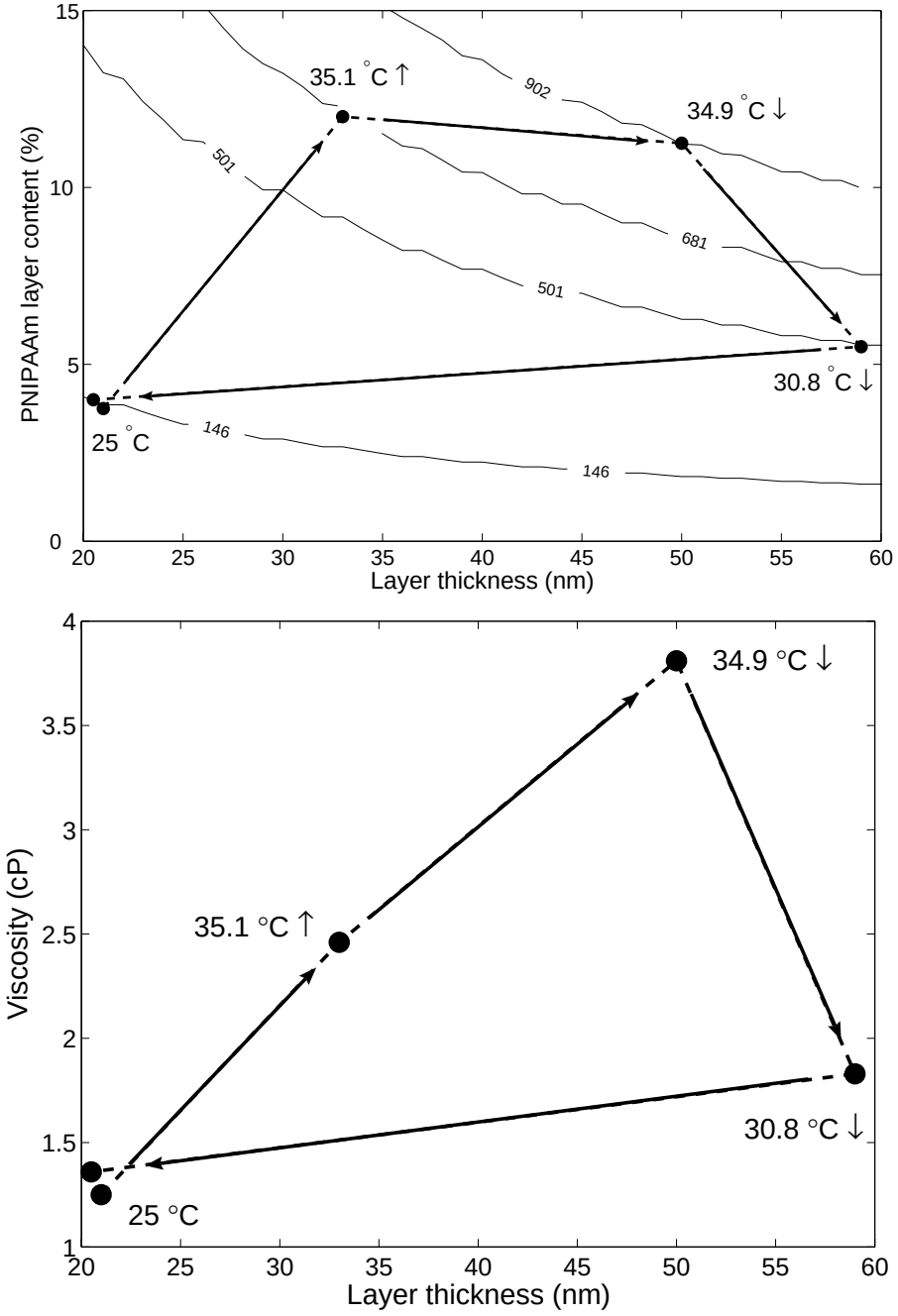


Fig. 5.15 – Summarizing graph of the evolution of (top graph) the estimated PNIPAAm weight concentration and of (bottom graph) the estimated viscosity of the adsorbed layer in the adsorbed layer *vs.* thickness for the 5 probed temperatures. The background lines in the top graph are the measured SPR angle shifts.

Temp. (°C)	$\rho_{\mathbf{C}}$ (g/cm^3)	$\eta_{\mathbf{C}}$ (cP)	**h** (nm)	δ (nm)	$\mathbf{h}/\delta$	$\Delta A/\Delta\phi$ (dB/rad)
25.0 ↘	1.016	1.36	20.5	59	0.35	2.6 ± 0.6
25.0 ↗	1.015	1.25	21	56	0.37	3.0 ± 0.5
30.8 ↘	1.022	1.83	59	68	0.87	5.9 ± 1.3
34.9 ↘	1.045	3.81	50	97	0.51	3.2 ± 0.3
35.1 ↗	1.048	2.46	33	78	0.42	2.8 ± 0.9

Table 5.3 – Evaluation of the density ρ, viscosity η, thickness h, penetration depth in the film δ simulated with the results indicated in Table 5.2. The simulated thickness to penetration depth ratio h/δ and the experimental SAW amplitude shift to SAW phase shift $\Delta A/\Delta\phi$ are given for a comparison with Figure 5.12.

immunoassay reactions. Taken separately, the increase of the amplitude ΔA and the phase $\Delta\phi$ indicate that the film is getting more viscous and thicker, while their ratio determines which factor is predominant. As given in Figure 5.12, a proportionality exists between this ratio and $h\sqrt{\rho_C}/\sqrt{\eta_C}$; consequently, if density variations are small in comparison to fluctuations of the film thickness and viscosity, an increasing ratio denotes a decrease of the viscosity or a thickening of the layer while a decreasing ratio indicates the opposite, i.e. an increasing viscosity or a thinning layer.

As the film thickness gets over the penetration depth, the SAW signal ratio saturates and the acoustic wave sees the deposited film as a semi-infinite bulk fluid. In such case, viscosity variations are probed through the individual variation of phase or insertion loss of the device. Hence, measuring the SAW signal ratio for viscous fluids is meaningless since its value is constant and equals a saturation value specific to each particular SAW sensor. In the same order of idea, a direct comparison of the SAW phase shift with the one obtained from a standard calibration of the sensor with a bulk viscous solution is not adequately fitted to the actual event that takes place on the sensing surface during the

segregation of a soft layer: at each time that the film is smaller than the penetration depth, the film thickness plays a crucial role and must be determined independently to estimate correctly the relevant characteristics of the adsorbed film, as presently for the PNIPAAm case.

PNIPAAm presents a conformational transition temperature, also called Lower Critical Solution Temperature (LCST), that identifies a clear separation of the physical characteristics of the polymer as seen qualitatively by acoustic and optical techniques. The transition corresponds to a switch from hydrophilic to hydrophobic because of the unshielded isopropyl group [109, 131, 167]. The LCST noticed by the abrupt change of SAW and SPR signals as seen in Figure 5.14 is located at 30.8 ± 0.3 °C for both rising up and cooling down. The transition is accompanied by a modification of the solubility of the polymer in solution and therefore by a gradient of concentration from the surface to the volume. Through this thesis, it is assumed that the composite layer is PNIPAAm with water as solvent and a step gradient in concentrations defines a clear interface between the adsorbed layer and the bulk fluid. Practically, it is more likely that the layer-fluid interface displays a smoother gradient due to dangling polymer strands and polymer diffusion. According to the same principle, surface roughness effects known to influence the acoustic signal are disregarded at the moment as the surface roughness has been measured with a value in the order of 3-5 $\mathrm{nm_{pp}}$ [60], which is much smaller than the acoustic penetration depth and the film thickness. These specific effects, gradient of concentration and surface roughness, were not considered since the presented methodology is not complete enough to address such interfaces yet. To that end, further assumptions on the concentration distribution as a function of the depth are needed and must be implemented in the model as, for instance, a multilayered composite layer with varying mechanical characteristics following a diffusion law. This type of implementation requires additional theoretical and experimental work to establish and measure concentration gradients and surface roughness in order to determine their exact incidence on the quantitative results presented here. Such developments are far beyond the scope of this thesis.

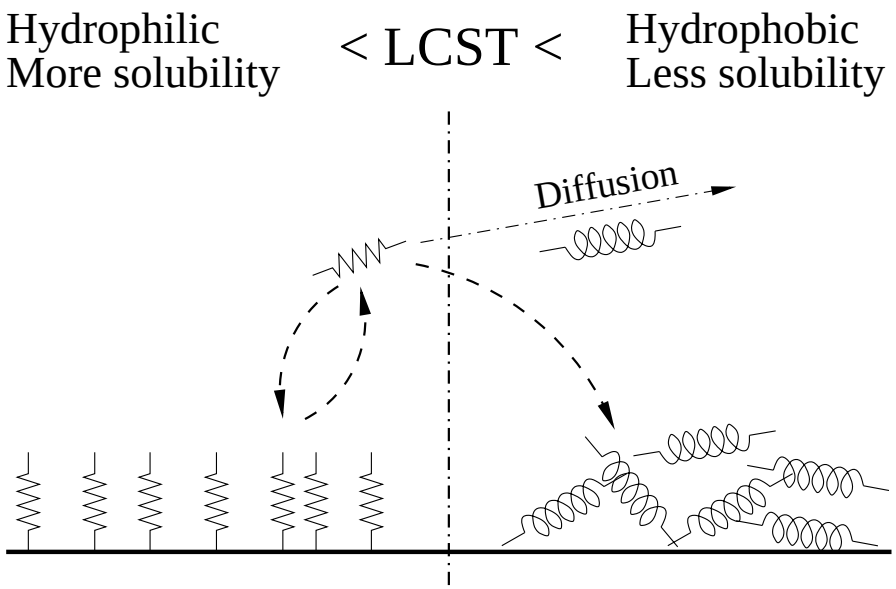


Fig. 5.16 – Pictorial representation of the mechanisms probed by the SAW/SPR for the investigation of PNIPAAm. Below LCST, the layer contains a large amount of water and because of the solubility of the physisorbed PNIPAAm, there is an equilibrium between surface and bulk concentrations. As the temperature increases above LCST, the conformation changes and results in an hydrophobic material collapsing on the surface, in addition to a segregation: as a result, a denser and thicker layer builds above the surface. As diffusion drives part of the material away from the surface, SAW and SPR signals are getting different as the number of thermal cycles increases.

Qualitatively and quantitatively, several variations are detected for each thermal cycle, with consistency from cycle to cycle. Variations occur in all observed parameters - density, viscosity and film thickness - through the cycle. The discussion is facilitated by distinguishing 3 regions per thermal cycle: (I) from 25 °C to the LCST; (II) from LCST with temperature increasing to LCST with temperature decreasing; (III) from LCST to 25 °C. Figure 5.16 is a pictorial representation of the assumed mechanisms probed by the combined SAW/SPR technique and discussed here after.

In region (I), a 4 wt % PNIPAAm hydrophilic layer absorbed on the surface is at equilibrium with the bulk solution. As the LCST is reached, the conformational transition of the polymer results, in region (II), in a radical and direct modification of the concentration that jumps almost immediately to a denser layer (12 wt %), thus a high viscosity resulting from stronger chains interactions. During the same time, the polymer in solution has a lower solubility and is segregating to the layer that continuously grows till a novel equilibrium is reached between surface and bulk concentrations. Meanwhile and as seen in the bottom graph of Figure 5.15, the viscosity increases as more chains interactions are taking place. This explanation is correlated with the SPR signal that presents a sudden variation after the LCST is reached, reflecting the conformational change of the layer. On the other hand, the abrupt transition is seen in the SAW ratio that presents a slow ramp up in region (I) followed by a slight decrease in region (II). As mentionned before, a decreasing ratio $\Delta A/\Delta\phi$ indicates that the viscosity increases or the thickness decreases, the situation that prevails here is an increasing viscosity.

The situation that occurs during cooling is different as observed at the transition between regions (II) and (III). As the temperature reaches again the LCST, the polymer is back to a hydrophilic behavior and start to swell in water. Because of the swelling, the layer thickness slightly increases but the PNIPAAm concentration and the viscosity are dropping fast. The effect is seen in the SAW signal ratio that is ramping up since a decrease of viscosity increases the ratio. Immediately after, in the early stage of region (III), the layer is effectively swelling and gets thinner while the viscosity remains constant, therefore the ratio is coming back to the initial value it presented in region (I). The estimation of the viscosity of organic monolayers is a specific feature displayed by the combined technique while few methods are able to tackle this type of measurement [11], so an exact comparison of our results with literature values is not directly possible although the estimated values determined by simulations are reasonable and of the same order of magnitude as the ones reported by Milewska *et al.* [139] for bulk solutions of PNIPAAm although they characterized PNIPAAm solutions with a larger molecular weight of 525 kD.

The asymmetry seen in the intensity of the SAW signal ratio peaks at LCST is possibly linked to the large difference in rising and decreasing temperature rates. It has been reported by Boutris *et al.* [23] from optical density measurements that the scanning rate influences the temperature transition because the system is not at equilibrium for large scanning rates; in our measurement, the scanning rate is moderate and the LCST is seen at the same temperature for both directions of the thermal cycling, indicating that the system is at equilibrium at any moment of the cycle otherwise we would observe a shift in the location of the LCST as a function of the temperature direction. Boutris *et. al* equally reported that the dissolution of the PNIPAAm during cooling is a much slower process for an identical temperature scanning rate than the abrupt transition noticed during the heating up, which might account for the intensity difference of the SAW signal ratio seen upon heating up and cooling down. Finally, as the number of cycles increases, a part of the polymer is diffusing away from the surface and will not re-enter the surface-volume equilibrium process of the following thermal cycle, explaining for the cycle degradation.

The temperature change might also cause modification to the interpretation of the data and are important for the calibration. The SPR sees the refractive index modification quite clearly and is linearly dependent upon the change with a given slope. The SAW situation differs from the SPR: with temperature, the water viscosity drops from $\simeq$1 cP to 0.6 cP from 20 °C to 35 °C as tabulated [1], corresponding theoretically to lower value of the insertion loss and a phase shift but in the same time the propagation characteristics of the Love mode device are modified by the temperature shift, the net result is the 3^{rd} order polynomial expression for the temperature on the insertion loss of the device while it is included in a linear relation for the phase. The effects compensate for each other.

Our observations are in agreement with the results reported by Plunkett *et al.* of a dense wetting layer that grows in thickness above the LCST. Our method provides an additional quantitative evaluation of the layer viscosity below and above the transition temperature, and quantitative information determining the amount of solvent and the thickness of the adsorbed soft layer.

5.6 Conclusion

We have shown here how the combination of Love mode SAW device with SPR provides advantageous combinations of information on the bound mass as well as on the dielectric changes when monitoring protein adsorption. The resulting protein layer thickness and protein content percentage, respectively $h = 4.7 \pm 0.7$ nm and $x = 75 \pm 15$ % for S-layer presently measured, is in agreement with independent AFM estimates.

The combination of surface acoustic wave and surface plasmon resonance measurements delivers useful information to estimate the *in situ* properties of surface adsorbed layers. A general method of data extraction has been presented that can be applied to layers adsorbed from liquid environments, such as in biosensors. The experimental ratio of amplitude shift to phase shift of the SAW signal correlated to simulations is an indicator of a rigid or a viscous interaction between the layer and the acoustic wave. A soft layer is characterized by a viscous behavior that results in a high damping of the acoustic wave, thus to a high ratio of the attenuation to the phase shift. The ratio is not a sufficient criterion to discriminate between soft and rigid layers since for very thin adsorbed layers, the two possible behaviors have a similar effect on the acoustic signal. Without data analysis, the experimental ratio is an indicator of the evolution of the thickness or of the viscosity of the layer: an increasing ratio is related to a growing film or to a viscosity decrease, while a decreasing ratio is related to a thinning film or to a viscosity increase.

With simulations of an equivalent viscoelastic transmission lines model, SAW and SPR data are used to assess quantitatively the density, the viscosity and the thickness of soft layers. The potential of the method has been demonstrated with the example of PNIPAAm, a thermally sensitive polymer. The record of SAW and SPR data during a thermal cycle clearly shows a conformational transition at the LCST point measured at 30.8 °C. The LCST transition is seen in the SAW signal ratio by a peak value and in the same time by an abrupt variation of the SPR signal. Graphs showing the evolution of the PNIPAAm weight concentration and viscosity versus the layer thickness were built that indicate

first a thickening of the layer followed by an increase of viscosity then the collapse of the layer. We also conclude from this study that the analysis of the adsorbed layer of PNIPAAm can be considered under the assumption of a soft layer as determined by the high value of the experimental SAW signal ratio $\Delta A/\Delta\phi$ ratio which is in agreement with a viscous interaction between the layer and the acoustic wave. Simulation results validate the soft layer hypothesis as seen by a high water content in the layer (between 88 wt % and 96 wt %).

5.7 Additional resources

Matlab M-files for the quantitative analysis of combined measurements from surface acoustic wave device and surface plasmon resonance are archived and documented on the website `http://jmfriedt.free.fr` or available on simple request by e-mail to francisl@ieee.org.

Part II

Thin Film Nanocrystalline Diamond Membranes

Chapter 6

Characterization method with flexural plate waves

> Toutefois il se peut faire que je me trompe, et ce n'est peut-être qu'un peu de cuivre et de verre que je prends pour de l'or et des diamants.
>
> *René Descartes*
> Discours de la Méthode

Nanocrystalline diamond (NCD) is a promising material for the fabrication of highly sensitive flexural plate wave (FPW) sensors. The design of FPW sensors requires the determination of the mechanical properties of a vibrating thin film membrane. In this thesis, we present a method to investigate the mechanical resonance of NCD membranes. Membranes with lateral dimensions in the millimeter range and 1.2 μm thick were excited in air by a loudspeaker and the resonance mode shapes were recorded optically with a stroboscopic interferometer. The resonance frequencies helped to determine directly the mechanical parameter of interest for the design of diamond-based FPW devices and the residual stress in the NCD layer. Our method allows the rapid investigation of prototype materials without requiring an integrated transduction system and can be applied to analyze structures with the actual dimensions of FPW sensors. The experimental results are used to assess the sensing properties of FPW devices with NCD membranes, which are enhanced with respect to classical materials such as silicon-based materials.

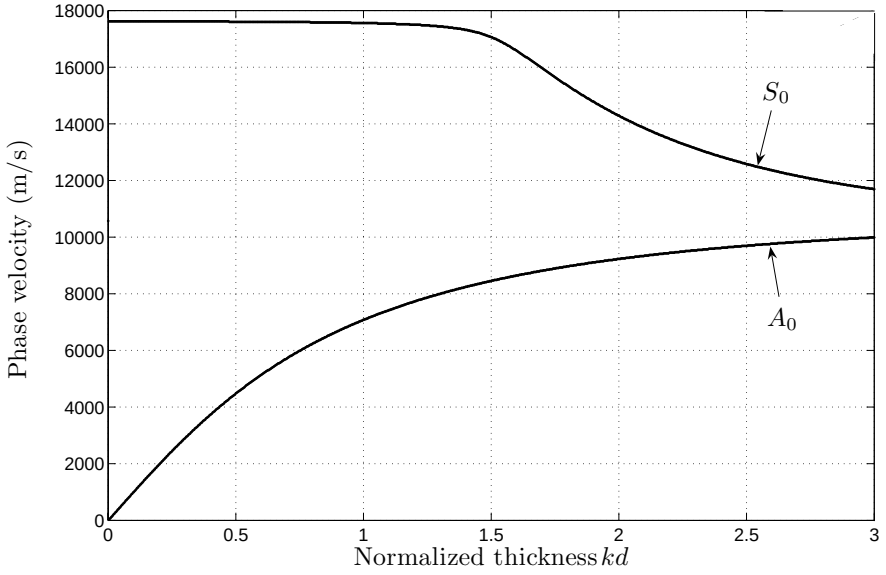


Fig. 6.1 – Phase velocity of the first symmetric (S_0) and anti-symmetric (A_0) Lamb mode for diamond as a function of the normalized thickness kd for a film of thickness d and a wavenumber k.

6.1 Introduction

Flexural plate wave (FPW) devices have found various applications as sensors and actuators: gas chromatography detector, (bio)chemical or mechanical sensors, fluid pumping, and particles filtering [10, 21, 28, 33, 126, 143]. The FPW is formed by a suspended thin film membrane vibrating on the lowest-order antisymmetric Lamb mode for which a wide variety of actuation and sensing methods have been reported (piezoelectric, capacitive, optical, magnetic, ...) [205]. For gas and liquid (bio)chemical sensing, the lowest mass detection is obtained for the thinnest membrane and the best quality factor, a condition requiring membrane materials with high mechanical qualities. To this end, nanocrystalline diamond (NCD) is a promising material from mechanical and chemical points of view [151, 203]. From a mechanical aspect, its high Young's modulus allows high operating frequencies with an expected high quality factor and its high tensile strength allows less fragile and thinner membranes than any other materials. Thanks to these unique mechanical properties, nanocrystalline diamond based FPW sen-

sors are expected to achieve mass sensitivities several times higher than silicon-based ones reported so far. From a chemical aspect, its high chemical resistance makes it attractive for devices operating in harsh environments while its surface functionalization for biosensor applications has been recently demonstrated [84].

Since the mechanical properties of diamond can be tuned by varying the deposition parameters, the design of optimized diamond-based FPW devices requires the investigation of NCD thin film membranes. For the mechanical characterization of diamond, non-destructive probing techniques have been reported such as Brillouin light scattering [105] or laser ultrasonics [55, 189, 203]. For the characterization of micromachined membranes, other specific methods like Resonant Ultrasound Spectroscopy (RUS) [75] or load-deflection [184] have been suggested. However, none of these methods are directly aimed at measuring the dynamic parameters required for the design of FPW devices. Therefore, in complement to these various approaches, we report in this thesis a fast and non-destructive method for the experimental measurement of the mechanical properties of nanocrystalline diamond membranes. The method is directly aimed at flexural plate wave applications [57].

Our analytical method is based on the contactless excitation in the low frequencies regime, with a mid-range loudspeaker, of the flexural resonance frequencies of nanocrystalline diamond membranes. The resonance frequencies and their mode shapes are optically recorded with a stroboscopic interferometer. Out of the experimental data, the mechanical parameter of interest for the design of FPW sensors and the biaxial stress in the thin film are extracted.

6.2 Modeling

In this section, we address the theoretical aspects necessitated for the analysis of the flexural resonance of stressed membranes. Based on these aspects, a mathematical method is given to extract the mechanical information from vibrating thin films.

6.2.1 Flexural frequencies and mode shapes

From a theoretical point of view, a membrane clamped to a supporting and rigid frame is modeled by a fixed edges plate (length a, width b, thickness h) with natural flexural vibration frequencies f_{ij} described by mode numbers i and j, respectively along the length and the width of the membrane. The single layer of the membrane is made of a material with a Young's modulus E, a density ρ, a Poisson's ratio ν and a biaxial stress σ.

For a plate with pinned ends and without axial tension (i.e. $\sigma = 0$), the frequencies are approximated by the product of two terms, a material constant $\alpha = \alpha(E, \rho, \nu)$ and a structural term $\beta_{ij} = \beta_{ij}(a, b, h)$, such that [22, 44, 198]:

$$f_{ij} = \alpha\beta_{ij} \tag{6.1}$$

$$\alpha = \frac{\pi}{4}\sqrt{\frac{E}{3\rho\,(1-\nu^2)}} \tag{6.2}$$

$$\beta_{ij} = h\sqrt{\frac{G_i^4}{a^4} + \frac{G_j^4}{b^4} + \frac{2J_iJ_j}{a^2b^2}} \tag{6.3}$$

with

$$G_n = \begin{cases} 1.506 & \text{for } n = 1 \\ n + \frac{1}{2} & \text{for } n > 1 \\ n & \text{for } n \gg 1 \end{cases} \tag{6.4}$$

and

$$J_n = \begin{cases} 1.248 & \text{for } n = 1 \\ \left(n + \frac{1}{2}\right)^2 \left[1 - \frac{2}{\left(n+\frac{1}{2}\right)\pi}\right] & \text{for } n > 1 \\ n^2 & \text{for } n \gg 1 \end{cases} \tag{6.5}$$

The mode shapes are given by

$$z_{ij}(x, y) = \sin\frac{i\pi x}{a}\sin\frac{j\pi y}{b} \tag{6.6}$$

with $x \in [0, a]$ and $y \in [0, b]$. For square membranes, $f_{ij} = f_{ji}$ and the corresponding shape results from a linear combination of the modes ij and ji:

$$z_{ij}(x, y) = \sin\frac{i\pi x}{a}\sin\frac{j\pi y}{a} + \sin\frac{j\pi x}{a}\sin\frac{i\pi y}{a}\cos\phi \tag{6.7}$$

with $(x, y) \in [0, a]$ and where $\phi \in [0, 2\pi]$ is a phase difference that depends of the exact boundary conditions applied to the membrane and the excitation method.

A biaxial stress σ in the thin film modifies the resonance frequencies, written $\tilde{f}_{ij}$, as given by the following expression (derived from Ref. [22]):

$$\tilde{f}_{ij}^2 = f_{ij}^2 + \frac{\sigma}{4\rho}\left(\frac{J_i}{a^2} + \frac{J_j}{b^2}\right) \tag{6.8}$$

A tensile stress ($\sigma > 0$) increases the resonance frequencies while a compressive stress ($\sigma < 0$) reduces them. The mode shapes are almost unaffected by the residual stress.

6.2.2 Extraction of the material constant and the stress

The material constant α and the residual stress σ are extracted from experimental measurements of membranes with given dimensions that are excited on different resonance frequencies. For each observed resonance frequency $\tilde{f}_{ij}$, if one captures the shape of the dynamic deformation then the mode numbers i and j are attributed. Hence, the geometry dependent parameters G_n, J_n, and β_{ij} are determined.

For stress-free membranes, $\tilde{f}_{ij} = f_{ij}$ and α is directly obtained by a linear fit of the frequencies as a function of the values of the structural parameter β_{ij}. However, a residual stress is unavoidable in thin film materials, resulting in the offset of the experimental resonance frequencies. This offset is function of the stress and the resonance modes. Therefore, a linear regression applied like for stress-free membranes is not providing the intrinsic value of α.

For stressed membranes, the material constant is obtained by a linear regression applied on values calculated by combining Eq. (6.1) with Eq. (6.8):

$$\boxed{\alpha = \frac{1}{\beta_{ij}}\sqrt{\tilde{f}_{ij}^2 - \frac{\sigma}{4\rho}\left(\frac{J_i}{a^2} + \frac{J_j}{b^2}\right)}} \tag{6.9}$$

If the density is assumed, the only unknown variable left is the residual stress. The stress is resolved by finding its value that gives a zero slope to the linear regression of the material constant calculated by Eq. (6.9)

as a function of the structural parameter β_{ij}. By applying this method, the material constant α (equals to the intercept of the linear fit) and the residual stress σ are extracted from experimental measurements, under the assumption of the density, and without requiring sophisticated calculations.

6.3 Experimental methodology

The experimental methodology required for the application of the theoretical principle is described in this section. In a first part, the fabrication of nanocrystalline diamond membranes is given, followed in a second part by the experimental setup used to excite and detect the vibration of these membranes. The flexural resonances are acoustically driven with a loudspeaker and optically detected with a stroboscopic interferometer.

6.3.1 Fabrication of nanocrystalline diamond membranes

Nanocrystalline diamond thin films are grown on silicon substrates by hot-wire chemical vapor deposition from a CH_4 (1-5%)/H_2 (99-95%) mixture (films deposited by ρ–BeSt coating GmbH, Austria). Prior to deposition, the silicon wafers are cleaned by wet chemistry and nucleated by ultrasonic seeding technique using a nano-sized diamond powder. On the basis of X-ray photoelectron spectroscopy (XPS) we estimated the contribution from $sp2$–hybridized carbon atoms to less than 5 at.%. In addition, Raman spectroscopy has been used to assess the quality of the nanocrystalline diamond films obtained with this technique. The Raman analysis confirmed that our NCD films have comparable quality to that of state-of-the-art NCD films deposited on silicon [20]. In this experiment, the thickness of the diamond film measured by SEM imaging of the cross-section is about 1.2 ± 0.1 μm, with an average grain size about 20 nm evaluated from X-ray diffraction measurements.

Square and rectangular NCD membranes with dimensions comprised between 800 μm and 6 mm were fabricated with the process schematically described in Figure 6.2. The membranes are micromachined by subsequent back-side deposition of a masking layer (200 nm Al) with photo-defined patterns of the membranes followed by a silicon deep re-

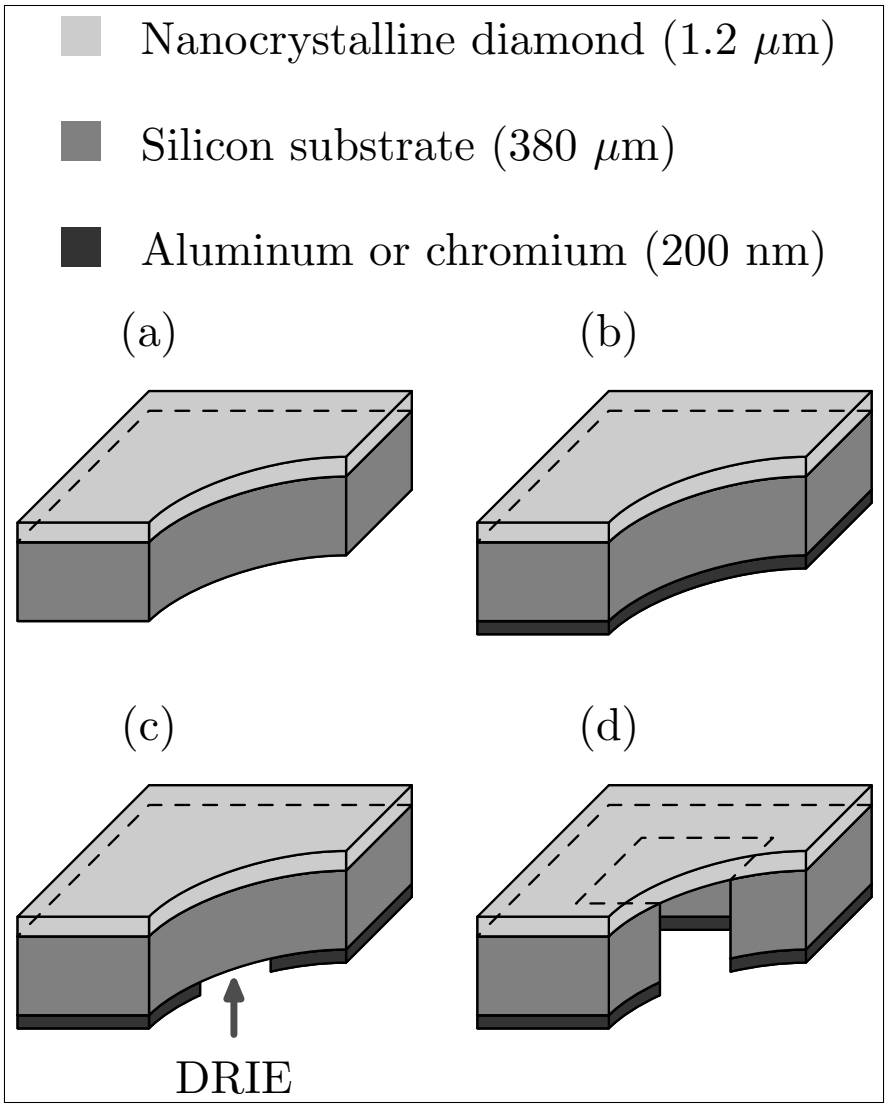


Fig. 6.2 – Membrane fabrication: (a) nanocrystalline diamond deposition on a silicon substrate; (b) backside deposition and patterning of a masking layer; (c) silicon DRIE; (d) final result: diamond membrane supported by a silicon frame.

active ion etching (DRIE, Bosch Process). Diamond is an automatic etch stop material for this process. The resulting membranes are photographed in Figure 6.3.

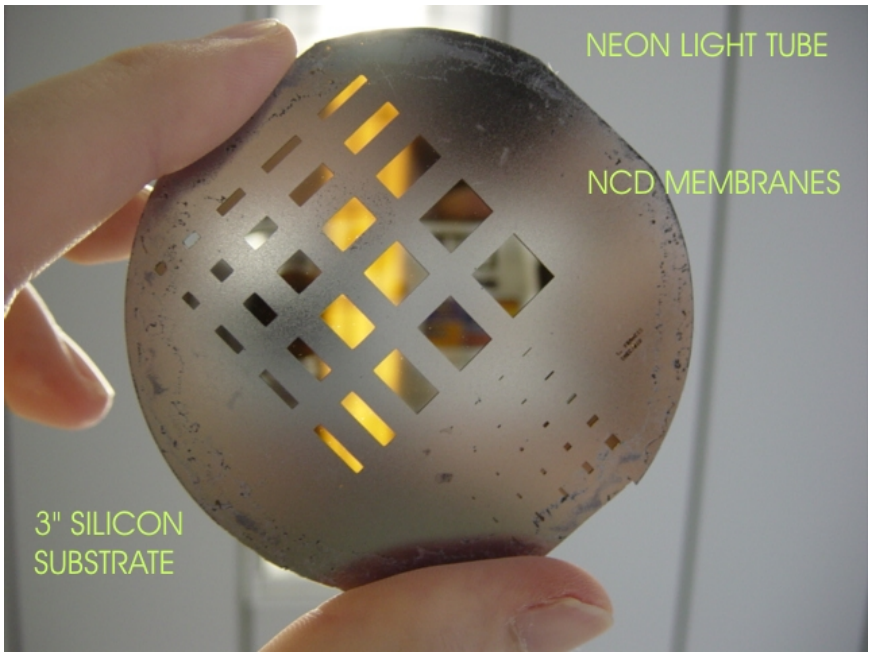


Fig. 6.3 – Nanocrystalline diamond membranes of various dimensions supported by a 3 inches silicon substrate. Although the membranes are not optically transparent, probably because of the presence of $sp2-$hybridized forms of carbon in the film, the neon light tube in the back is partly visible through them.

6.3.2 Actuation and detection methods

For the excitation of the membranes, the sample is clamped between two 5 mm-thick PVC plates with a 2 cm diameter hole in the middle. The plates are then rigidly attached to the outer frame of a mid-range loudspeaker (model PS 100M, Conrad Electronic, Germany) to actuate the membranes in air. At resonance, the coupling of energy between the air pressure and a membrane results in a small amplitude (nanometer range) vibration on a mode that must be identified.

For the detection and the analysis of the resonance mode, non-destructive optical imagery of vibrating structures based on interferometric principles have been demonstrated previously [31, 70, 71]. Most of these methods are based on point analysis and require to scan the probing point on the entire vibrating area to obtain an image of the dynamic deformation. To scan at once the largest part of the membrane, we used a stroboscopic interferometer to record the motion of the NCD membranes with a nanometer resolution [83, 150, 190].

The experimental data were recorded with a dedicated interferometer (Optonor MicroMap 5000 laser TV holography system, Norway). Its operation principle, schematically depicted in Figure 6.4, is based on the projection of an interferometric image on the CCD camera obtained by combining in the beam splitter a sample beam and a reference beam. Only significant out-of-plane deformations, associated to flexural modes, modify the fringes interferences and are recorded. An heterodyne measurement of the pattern deformation under the excitation of the membranes is obtained by a reference beam modulated at a slightly different frequency than the sample beam, resulting in a low frequency beating of the image recorded by the CCD. A software post-treatment of the fringes intensity allows for the determination of the displacement. As example, Figure 6.5 shows a part of the 4 by 4 mm^2 membrane vibrating at f_{21}. For practical reasons, only a quarter of the membrane is visible since the aperture of the microscope lens covers an approximate 2 by 2 mm^2 area.

The flexural resonance frequencies are mapped by the maximum in the displacement amplitude while sweeping the loudspeaker excitation frequency between 500 Hz and 20 kHz with a resolution of 100 Hz. The shape of a vibrating membrane is associated to a resonance mode ij according to Eqs. (6.6) and (6.7). This method allows the rapid and non-destructive investigation of the material without requiring an integrated transduction system and can be applied to structures with the large dimensions of FPW devices.

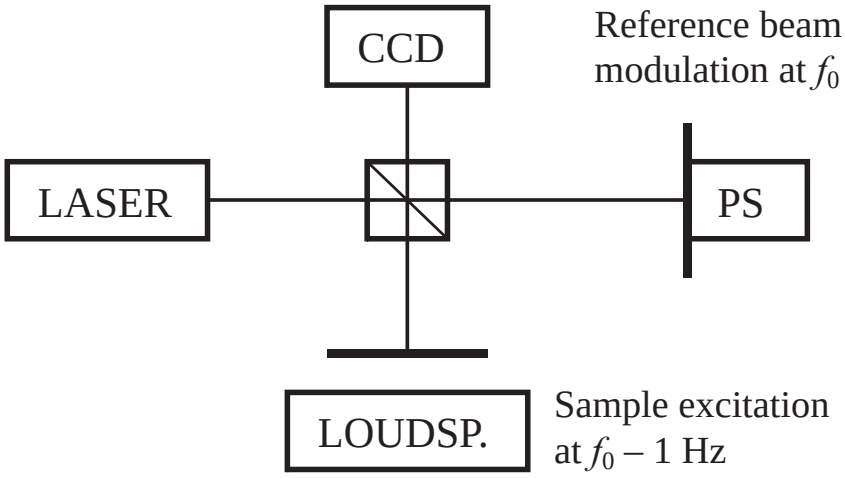


Fig. 6.4 – Schematic of the experimental setup. The operating principle is based on an interferometer with beat frequency imaging (LASER: laser source, PS: piezoelectric stage, CCD: camera), the sample is actuated by a loudspeaker (LOUDSP.).

6.4 Results

This section reports the measured frequencies and the calculation results. The material constant obtained by the dynamic characterization is compared with a theoretical estimate. The influence of the biaxial stress is discussed and correlated with static measurements of the residual stress in the diamond film.

6.4.1 Dynamic characterization

In the dynamic mode of the interferometer, the measured vibrating membranes presented resonance frequencies reported in Table 6.1. A linear fit on the raw data gives the relation $\tilde{f}_{ij} = 8392\beta_{ij} - 41$ with a coefficient of determination $R^2 = 0.98$, indicating a nearly perfect fit. The procedure of regression applied for different values of the residual stress, assuming that NCD has a density ρ of 3500 kg/m^3, leads to a zeroed regression slope for $\sigma = -120$ kPa as shown in Figure 6.6. At this point, the intercept of the linear fit gives $\alpha = 8.67$ km/s, and $R^2 = 1$.

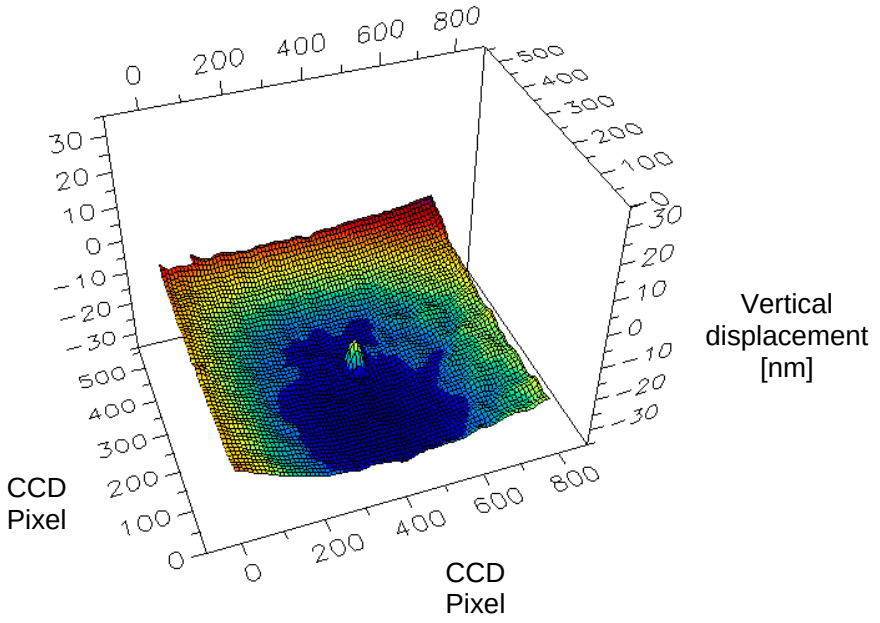


Fig. 6.5 – Capture of the deformation shape during the dynamic characterization of a 4 by 4 mm^2 diamond membrane (the image displayed is 2 by 2 mm^2). The membrane resonates on the mode (2,1).

$a \times b$	mode		β_{ij}	$\tilde{f}_{ij}$	f_{ij}
(mm × mm)	i	j	(1/m)	(kHz)	(kHz)
4 × 2	1	1	0.75	4.6	6.5
	2	1	0.97	5.7	8.4
	3	1	1.4	12.8	11.8
	2	2	2.2	17.8	18.8
4 × 4	2	1	0.56	4.6	4.9
	4	1	1.6	12.6	13.9
6 × 6	1	1	0.12	0.67	1.1

Table 6.1 – Modes of resonance along the length (i) and the width (j), structural parameter β_{ij}, recorded ($\tilde{f}_{ij}$) and corrected (f_{ij}) resonance frequencies of the 1.2 μm nanocrystalline diamond membranes with different lateral dimensions (length a, width b).

For a comparison, the experimental frequencies $\tilde{f}_{ij}$ and their corrected values f_{ij} are plotted in Figure 6.7. Without the appropriated correction brought by the regression technique, a compressive (respectively tensile) stress in the film results in a under– (respectively over–) estimation of the material constant α. In the initial fit done on the uncorrected frequencies, α differs by 3% from its corrected value. This small error is due to a low stress in the tested film. Higher stresses would result in a larger error on the uncorrected estimation of α.

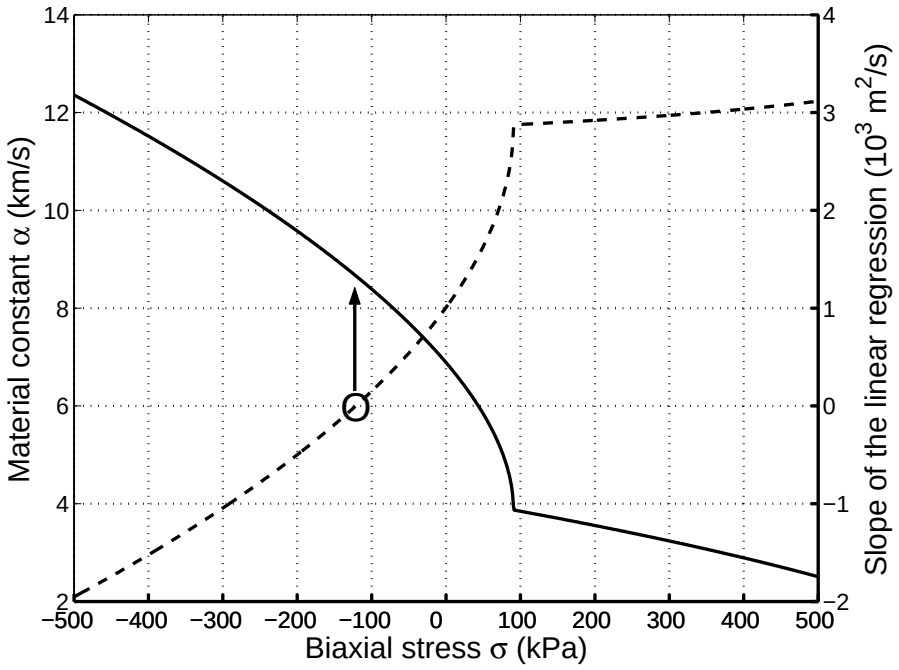


Fig. 6.6 – Evolution of the fitting parameters (solid line: intercept, dashed line: slope) versus the residual stress in the diamond membrane. The slope is equal to 0 for a stress value of −120 kPa, giving a value of the material constant α of 8.67 km/s as indicated by the arrow.

The experimental value of the material constant is comparable with a theoretical estimation of $\alpha = 8.10$ km/s calculated with $E = 1100$ GPa, $\rho = 3500$ kg/m^3 and $\nu = 0.12$ (literature data [151]). Whatsoever, the density and the Poisson's ratio are likely to vary; for instance, the density of different varieties of diamond are reported between 3150 and 3530 kg/m^3. With the regression technique, the difference between as-

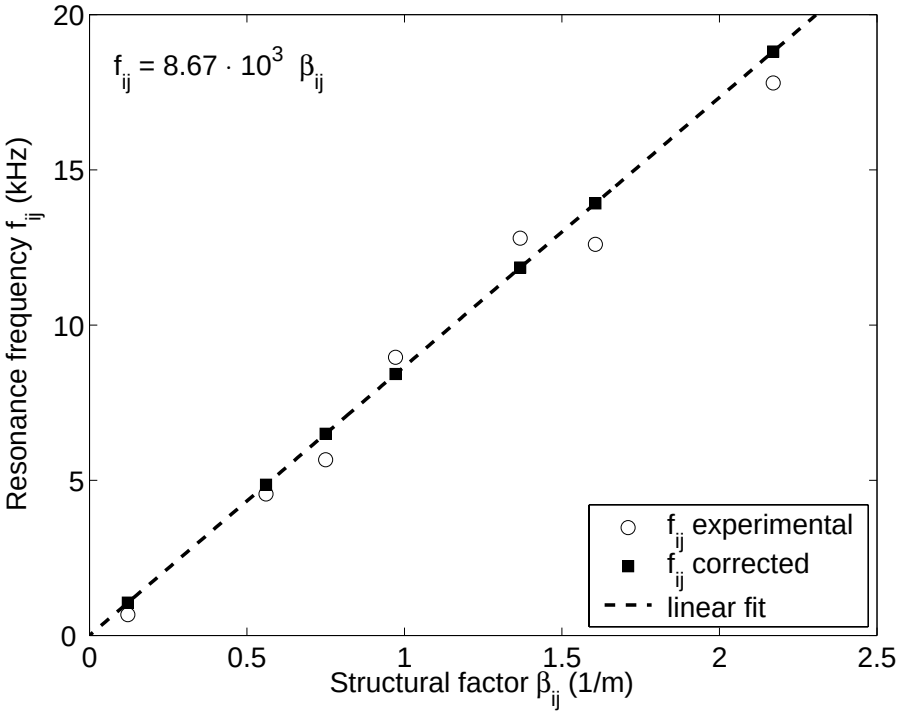


Fig. 6.7 – Recorded and corrected flexural resonance frequencies f_{ij} for different membrane sizes versus the structural parameter β_{ij}.

sumed and actual material density influences the estimation of the residual stress but has a negligible impact on the evaluation of the material constant provided that the amount of experimental data is sufficiently large as explained here after: a variation of the assumed density shifts laterally the regression parameters plotted in Figure 6.6 while the shape of the curves is unchanged. Consequently, the position of the zeroed value of the regression slope (determining σ) is modified while the value of the intercept (determining α) stays the same.

The relative error on the estimation of the residual stress is equal to the one on the density while the relative error on the material constant is independent of this variation but is linked to the experimental measurement error and is reduced by a larger amount of experimental data. For example, a NCD density of 3500 kg/m^3 was assumed for the regression, a variation of the density by 10% to $\rho = 3150$ kg/m^3 results in a 10% change of the estimated residual stress, from -120 kPa to -109 kPa, while α keeps an identical value of 8.67 km/s. It can be concluded that a lower (respectively higher) assumed density of the film material than the actual one results in an under– (respectively over–) estimation of the actual residual stress σ.

6.4.2 Correlation with static measurements of the residual stress

In the semi-static deflection mode of the interferometer, the deformed fringes pattern indicates an initial buckling of the NCD membranes as seen in Figure 6.8. The bulge of a square membrane due to a compressive stress is derived from a formula cited in Ref. [148]:

$$\sigma = \frac{4C_2 f(\nu) E d^2}{C_1 a^2 (\nu - 1)} \tag{6.10}$$

with $C_1 = 3.04$, $C_2 = 1.37$, $f(\nu) = 1.075 - 0.292\nu$ and d the center deflection.

The static bulge of the smallest square membrane (side length $a = 800$ μm) was measured with an optical 3D profiling system (Veeco Wyko NT3000). The deflection, measured along the diagonal, is plotted in Figure 6.9. The center deflection is roughly equal to 100 nm, a small

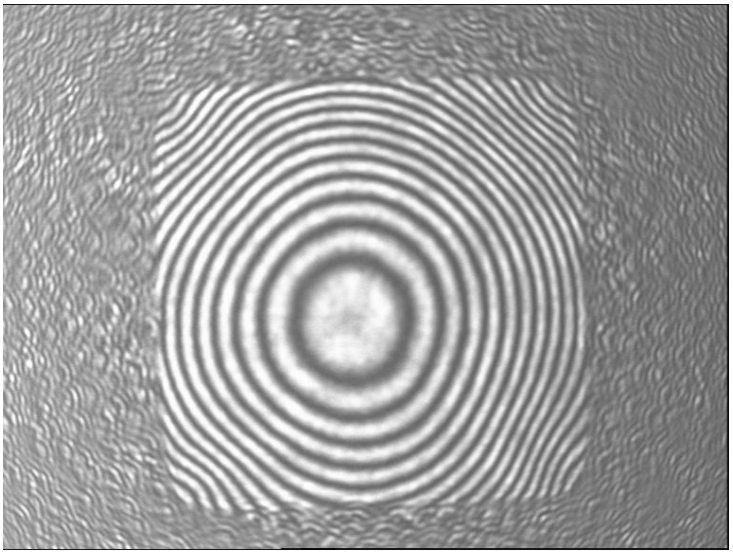


Fig. 6.8 – CCD capture of the circular fringes pattern projected on a 800 by 800 μm^2 membrane. The deformed pattern on the membrane is due to a small compressive stress that buckles the membrane.

deformation caused by a low compressive stress in this sample. According to Eq. (6.10), $\sigma = -37$ kPa. The static measurement of the residual stress in this membrane is in the same range as the one obtained by the dynamic characterization ($\sigma = -120$ kPa).

In any cases, the stress is a variable factor that depends of the material deposition conditions. The wafer bow curvature of silicon substrates was measured with a contactless wafer geometry gauge (MX203 from Eichhorn-Hausmann GmbH, Germany) before and after the deposition of NCD layers 700 nm to 2.3 μm thick grown in different conditions than the sample presently used, and given in Figure 6.10. The results indicated residual stresses varying from -60 to 60 MPa at increasing thickness. At this stage, an in-depth understanding of the mechanisms resulting in this evolution of the stress is ongoing and likely explanations to resolve are

- a faster relaxation of the stress in NCD films due to more area at the grain surface with increasing thickness,
- more hydrogen incorporated in the grain boundaries with increasing thickness,

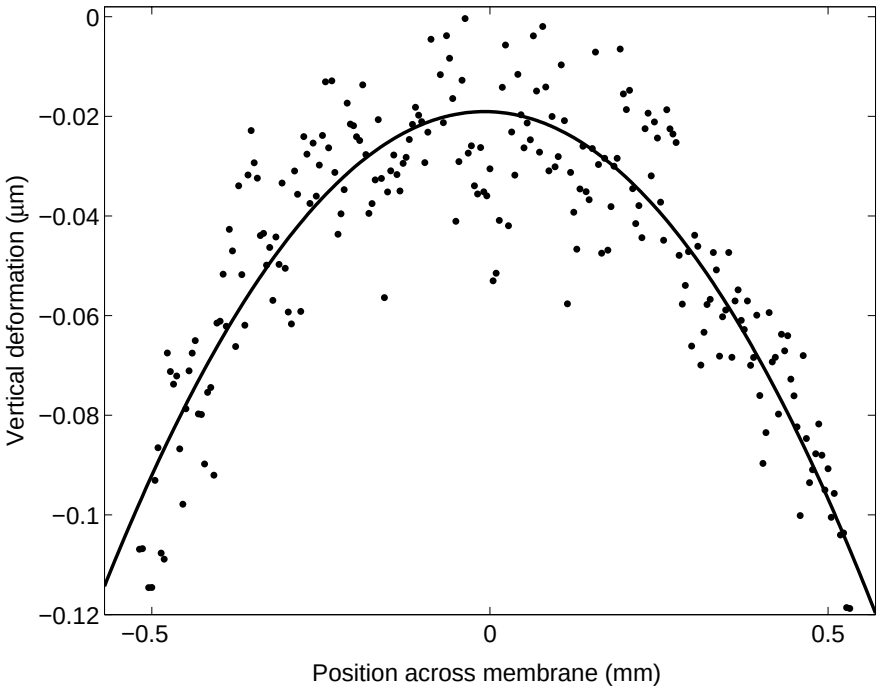


Fig. 6.9 – Static bulge measured with an optical profiling system across the diagonal of the membrane pictured in Figure 6.8 (dots: experimental measurement, solid line: parabolic fitting curve). The maximum deflection of 100 nm reveals a compressive residual stress in the diamond film.

- more non-sp^3 phases of carbon incorporated in the film during its growth.

Optimization and reproducibility of the residual stress form an important challenge in the development of NCD membranes for FPW applications, whereas our method advantageously dissociates the material characteristics from the mean value of the residual stress.

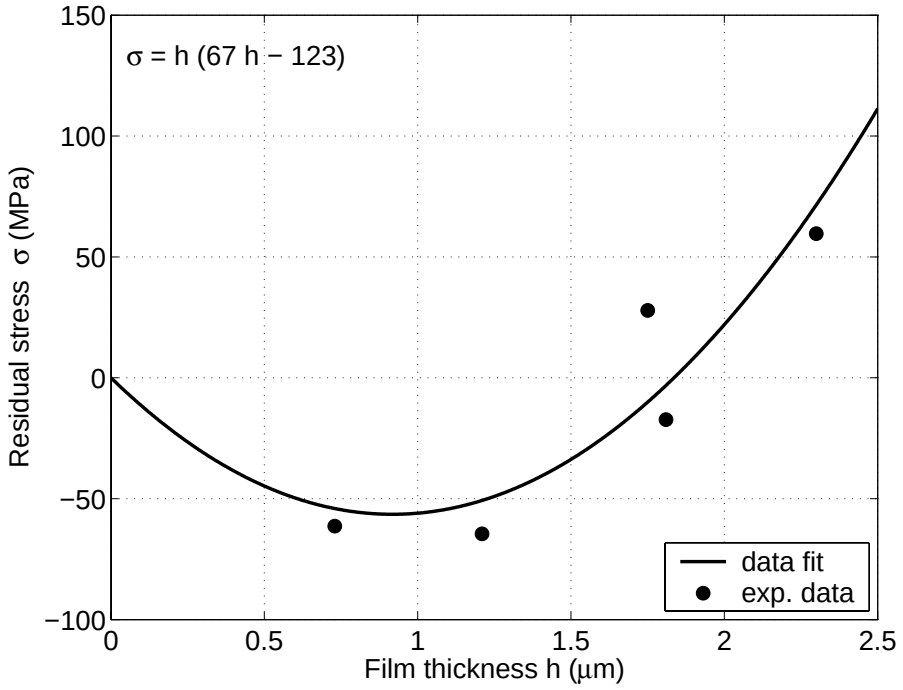


Fig. 6.10 – Static stress extracted from bow curvature measurements of nanocrystalline diamond thin films deposited on Si substrates (dots: measured values, solid line: parabolic fitting curve).

6.5 Discussion

This part applies the results of the characterization method to assess the theoretical operating frequency and mass sensitivity of diamond-based FPW devices. The mass sensitivity in NCD membranes is theoretically compared with silicon-based membranes at identical film thickness and acoustic wavelength. In a final point, the drawbacks of the dynamic characterization technique are discussed.

6.5.1 Critical stress and FPW frequencies

Flexural plate wave devices are described by flexural modes $(n, 1)$ with $n \gg 1$. For convenience and comparison with conventional notations, the material constant α is linked to the flexural rigidity of the plate $D = Eh^3/12(1-\nu^2)$ by the relation

$$D = \frac{4\rho h^3 \alpha^2}{\pi^2} \tag{6.11}$$

and the stress-free acoustic phase velocity is approximated by [10]

$$v_p = \frac{2\pi}{\lambda}\sqrt{\frac{D}{\rho h}} \tag{6.12}$$

$$= \frac{4h\alpha}{\lambda} \tag{6.13}$$

where $\lambda = 2a/n$ is the acoustic wavelength.

Under these considerations and from Eq. (6.9), the stressed resonance frequencies are approximated by

$$\tilde{f}_{n1} = \frac{2}{\lambda}\sqrt{\left(\frac{2h\alpha}{\lambda}\right)^2 + \frac{\sigma}{4\rho}}. \tag{6.14}$$

The residual stress can be ignored if it satisfies the relation $|\sigma| \ll \sigma_C$ where the *critical stress* σ_C is given by

$$\boxed{\sigma_C = \rho v_p^2.} \tag{6.15}$$

By then, the stress-free FPW frequencies are expressed by

$$f_{n1} = \frac{v_p}{\lambda}. \tag{6.16}$$

6.5.2 Minimum mass per area detection of diamond FPW sensors

Because FPW devices find several sensing application, we will consider only the gravimetric sensor applications. Expressions of the mass sensitivity in gas or fluid loading conditions (e.g. biosensors) are found in Ref. [10].

For a FPW sensor placed in an oscillation loop, the minimum detected mass per area Δm depends of the noise on the frequency measurement Δf. In practice, it is considered that the frequency shift must exceed by three times the noise frequency to be significant.

For mass sensing in air, the minimum detected mass per area is given by

$$\boxed{\Delta m = \frac{-\rho\lambda^2}{2\alpha}\left(3\Delta f\right).} \tag{6.17}$$

For mass sensing in fluids (sound velocity v_F, density ρ_F), the minimum detected mass per area is given by

$$\boxed{\Delta m_F = \Delta m + \frac{\delta}{h}\left[\frac{-\rho_F\lambda^2}{2\alpha}\left(3\Delta f\right)\right]} \tag{6.18}$$

where δ is the penetration depth of an evanescent wave in the fluid, which is given by

$$\delta = \frac{\lambda}{2\pi}\left[1 - \left(\frac{v_p}{v_F}\right)^2\right]^{-1/2}. \tag{6.19}$$

When $v_p \ll v_F$, $\delta \to \lambda/2\pi$. Eq. (6.19) imposes the energy trapping condition $v_p < v_F$ that involves $\lambda > \lambda_F$, with the minimum wavelength for fluids λ_F given by

$$\boxed{\lambda_F = \frac{4h\alpha}{v_F}.} \tag{6.20}$$

All the expressions are summarized in Table 6.2 and used to compare the expected characteristics of FPW sensors comprising silicon-based (SiO_2, Si and Si_3N_4) or NCD membranes. For numerical values, we took the most likely values such that $h = 1$ μm, $\lambda = 100$ μm, $\sigma = -50$ MPa and a noise frequency Δf of 1 Hz. The influence of the residual stress is clearly visible on the frequency: when the condition $|\sigma| \ll \sigma_C$ is not met, stressed and stress-free frequencies are clearly diverging. For the mass sensitivity, the influence of the stress has not been considered and the minimum detected mass per area in the Table is calculated for stress-free conditions.

Parameter		Symbol	Expression	Eq.	Units	SiO_2	Si	Si_3N_4	**NCD**
Material	density	ρ			kg/m^3	2200	2330	3100	**3500**
	constant	α	$\frac{\pi}{4}\sqrt{\frac{E}{3\rho(1-\nu^2)}}$	(6.2)	km/s	2.60	3.87	5.15	**8.67**
Ratio material constant to density			$\frac{\alpha}{\rho}$		$m^4/kg/s$	1.18	1.66	1.66	**2.48**
Stress-free phase velocity		v_p	$\frac{4h\alpha}{\lambda}$	(6.13)	m/s	104	155	206	**347**
Critical stress		σ_C	ρv_p^2	(6.15)	MPa	24	56	131	**421**
Frequency	stressed	$\tilde{f}_{n1}$	$\frac{2}{\lambda}\sqrt{\left(\frac{2h\alpha}{\lambda}\right)^2+\frac{\sigma}{4\rho}}$	(6.14)	MHz	$--$	0.50	1.62	**3.26**
	stress-free	f_{n1}	$\frac{v_p}{\lambda}$	(6.16)	MHz	1.04	1.55	2.06	**3.47**
Minimum wavelength for fluids		λ_F	$\lambda\left(\frac{v_p}{v_F}\right)$	(6.20)	μm	8	12	16	**27**
Penetration depth		δ	$\frac{\lambda}{2\pi}\left[1-\left(\frac{v_p}{v_F}\right)^2\right]^{-1/2}$	(6.19)	μm	16	16	16	**16.5**
Minimum detected mass per area	in a gas	Δm	$\frac{-\rho\lambda^2}{2\alpha}(3\Delta f)$	(6.17)	pg/mm^2	13	9	9	**6**
	in a fluid	Δm_F	$\Delta m+\frac{\delta}{h}\left[\frac{-\rho_F\lambda^2}{2\alpha}(3\Delta f)\right]$	(6.18)	pg/mm^2	105	71	56	**34**

Table 6.2 – Summary of the theoretical properties of flexural plate wave sensors with a thickness $h = 1$ μm, a wavelength $\lambda = 100$ μm, a residual stress $\sigma = -50$ MPa (compressive), and a noise frequency of $\Delta f = -1$ Hz. In water, the acoustic speed is $v_F = 1300$ m/s and $\rho_F = 1000$ kg/m^3.

The results of Table 6.2 indicate that, for same thickness and same acoustic wavelength, the NCD sensor has a greater mass sensitivity than silicon-based devices for both gases and fluids loading. As seen in Eq. (6.17), the highest mass sensitivity is achieved for materials that have the highest ratio of the material constant to the density α/ρ, which is linked to a high Young's modulus and a low density. With a fluid loading, a high material constant results in a lower detection limit by trapping the acoustic energy closer to the solid-fluid interface, as given by the right-hand term of Eq. (6.18). Despite a high density, NCD is a material of choice for the achievement of sensors with a low limit of detection since its Young's modulus increases faster than its density when compared to silicon-based materials. An additional advantage of NCD is a high tensile strength; therefore the sensitivity can be enhanced further by decreasing the film thickness while keeping the same membrane size. Experimental investigations of the lowest limit of detection are in the scope of future developments.

6.5.3 Drawbacks of the method

Although convenient and attractive because of its simplicity of use, the actuation helped by a loudspeaker introduces two main limitations in the measurement. A first limitation is a complex analysis of the motion when the mode numbers become greater than 5, leading to potential errors in the attribution of the mode numbers.

A second limitation is the range of frequency limited to 20 kHz, that might be sufficient in most cases because materials present a low value of α and thus low first-orders modes frequencies. For higher frequencies or smaller membranes, a direct piezoelectric excitation of the membranes is required in a method similar to Resonant Ultrasound Spectroscopy [75], where the excitation is done by a broadband piezoelectric transducer, while the vibration modes could be determined optically.

6.6 Conclusion

The analysis of nanocrystalline diamond vibrating thin films provides a rapid and non-destructive dynamic characterization of mechanical properties used to assess the characteristics of diamond-based flexural plate wave sensors.

The membranes are excited in air with a loudspeaker while the flexural resonance frequencies and the corresponding mode shapes are recorded optically with a stroboscopic interferometer. Under the simple assumption of the material density, the theoretical and experimental method dissociates the intrinsic mechanical characteristics of the material from the residual stress without requiring sophisticated calculations or modeling work.

Experimental results were used to theoretically assume the mass sensitivity of diamond-based FPW devices. At equivalent thickness and acoustic wavelength, nanocrystalline diamond FPW sensors present a lower detection limit in gases and fluids than silicon-based sensors and have significant potential for the development of highly sensitive gravimetric biosensors.

Chapter 7

Composite thin film bulk acoustic resonators

> No problem is too small or too trivial if we can really do something about it.
>
> *Richard Feynman*

Nanocrystalline diamond (NCD) is an emerging material with unique mechanical and chemical properties that can be used for the development of thin film micromachined sensors. This study comes as a preliminary step towards the integration of NCD thin film membranes in gravimetric sensors with low detection limits. We investigate theoretically the mass sensing characteristics of composite thin Film Bulk Acoustic Resonator (FBAR) as a function of the side exposed to a mass perturbation. For NCD, the resonance frequency is increased while the electromechanical coupling coefficient remains high. At equivalent thickness, an enhancement of the mass sensitivity is reported for mass adsorption taking place on the piezoelectric actuation side of the composite device.

7.1 Introduction

The main challenge in the development of acoustic sensors for the detection of surface adsorbed mass in gaseous and liquid environments is to reach the smallest detection limit possible. Most of the time, this challenge is tackled by a selection of materials and structures for which

the acoustic energy is closely trapped at the sensing surface. In this case, a small perturbation due to the adsorption of a given mass causes a dramatic change in the acoustic field distribution in the entire vibrating structure and is detected through a given transduction mechanism. The thin film bulk acoustic resonator (FBAR) is a promising structure for highly mass sensitive miniature acoustic devices with application to gas and (bio)chemical detection as described in recent theoretical and experimental works corresponding to solidly mounted or membrane supported acoustic resonators [17, 62, 157, 164, 211]. In the latter case, little has been devoted to theoretically investigate the influence of the supporting membrane material on the mass sensitivity of a FBAR sensor although it forms a part of the resonator. By its presence, the supporting membrane traps a part of the acoustic energy, which physical effect is a key factor to understand the gravimetric sensitivity of the acoustic structure.

In this chapter, we assess the mass sensitivity of a membrane supported FBAR, referred in the present context as the *composite FBAR*, with an approach dedicated to provide an insight in the sensing mechanisms of this acoustic structure via the perturbation theory. We investigate theoretically the impact of introducing nanocrystalline diamond [151] (NCD) as a functional part of the device. NCD is an emerging material with high mechanical qualities and a chemical surface of interest for its application to biochemical and implanted sensors. The properties of a composite FBAR with NCD are presented and compared to AlN and SiO_2 within the frame of a systematic approach of composite FBAR.

7.2 Composite FBAR sensor

For its definition, a composite FBAR results from the electrical transduction of a longitudinal bulk acoustic wave in a piezoelectric layer mechanically supported by a second layer, referred to as the "loading layer", and air-backed ends as depicted in Figure 7.1. While the loading layer assures the mechanical stability of the structure, by its finite thickness it also influences acoustic and sensing properties of the resonator.

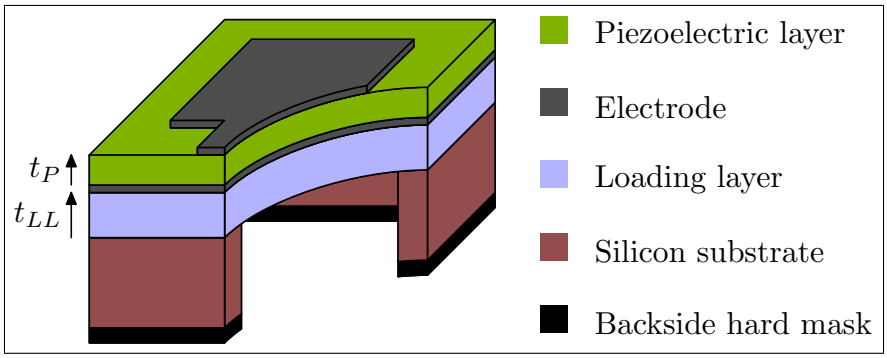


Fig. 7.1 – Schematic structure of the composite FBAR: a piezoelectric layer of thickness t_P is sandwiched between two metal electrodes to electrically excite a longitudinal wave resonance mode in the stack formed by the piezoelectric and a "loading layer" of thickness t_{LL}.

7.3 Theory

Since the composite FBAR presents two possible sensing surfaces, the mass adsorption can occur either on the piezoelectric side or on the loading layer side. In both cases, the properties of a given composite structure are theoretically assessed with the following generic approach:

1. Calculation of the relation of dispersion for the fundamental resonance mode;
2. Expression of the acoustic energy along the entire resonating structure;
3. Evaluation of the mass sensitivity by an analytical expression obtained from the perturbation theory.

For practical considerations, a composite FBAR with aluminum nitride - as a widely used piezoelectric material in FBAR - supported by a NCD loading layer (AlN/NCD) is investigated and compared to AlN/AlN and AlN/SiO_2 cases.

7.3.1 Relation of dispersion

The angular resonance frequency $\omega_C = 2\pi f_C$ is obtained via the mechanical model depicted in Figure 7.2, which consists in transmission lines of acoustic impedance $Z = \rho V$(material of density ρ and acoustic

velocity V) and wavenumber $k = \omega_C/V$. In this model, the piezoelectricity and the electrodes are ignored at first. The relation of dispersion solves the equation of opposite impedances at the interface between the two layers:

$$Z_2 \tan k_2 t_2 = -Z_1 \tan k_1 t_1. \tag{7.1}$$

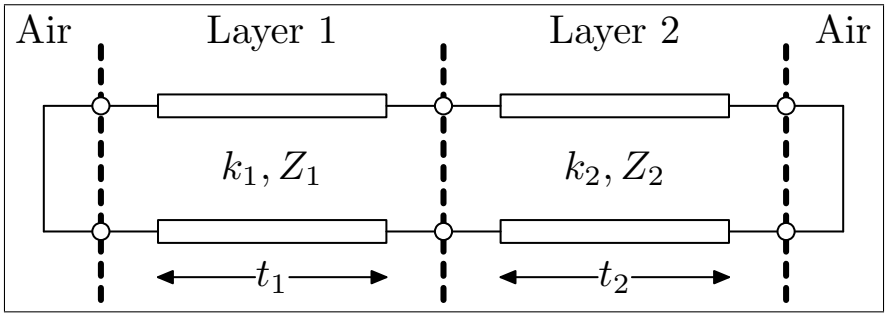


Fig. 7.2 – Equivalent transmission line model of the composite FBAR: a longitudinal acoustic wave with wavenumber k_i propagates in the two layers of acoustic impedance Z_i and thickness t_i. The air -backed ends are mechanically represented by shorted ends.

The particle velocity at a position x along the thickness of the structure, for an initial velocity v_0 at the sensing surface (i.e. $x = 0$), is:

$$v_1(x) = v_0 \cos k_1 x; \tag{7.2}$$

$$v_2(x) = v_0 \left(\cos k_1 t_1 \cos k_2 x - \frac{Z_1}{Z_2} \sin k_1 t_1 \sin k_2 x \right). \tag{7.3}$$

The resonance frequency f_C is found by taking $t_1 = t_P$ and $t_2 = t_{LL}$, where the subscripts P and LL refer to the piezoelectric and the loading layer, respectively. The material data used for the model are given in Table 7.1.

The frequency f_C is normalized to the resonance frequency of the AlN layer taken alone:

$$\boxed{f_P = \tfrac{V_P}{2t_P}.} \tag{7.4}$$

Figure 7.3 shows the relative frequency

$$R_f = \frac{f_C}{f_P}$$

Material	Density ρ kg/m^3	Ac. Velocity V m/s	Ac. Impedance Z MRayl.
AlN	3260	10400	34
NCD	3500	17700	62
SiO_2	2200	6400	14
Al	2700	5100	14

Table 7.1 – Material data used for simulations

as a function of the normalized thickness t_{LL}/t_P for AlN/NCD, AlN/AlN and AlN/SiO_2. Thanks to the normalization, the study of the composite FBAR is made independent of the actual thickness attributed to the piezoelectric layer.

A first advantage of NCD as loading layer is linked to the high acoustic velocity of the diamond material: at equivalent total thickness, the operating frequency of the AlN/NCD FBAR is the highest as the NCD gets thicker. A thick loading layer is also advantageous for a better mechanical stability. However, because the loading layer is only a mechanical loading a part of the acoustic energy in the structure is not effectively participating to the electromechanical transduction.

7.3.2 Energy distribution and coupling coefficient

The distribution of the acoustic energy in the structure is given in Figure 7.4 for an identical value of v_0 at the top surface of the piezoelectric. A second advantage of NCD is a larger trapping of the acoustic energy in the piezoelectric layer. From an electrical point of view, the electrical admittance of the device Y presents a maximum value at the resonance frequency, also called *series resonance* and denoted f_s, and a minimum value at the antiresonance frequency, also called *parallel resonance* and denoted f_p. The separation between both frequencies is called the *effective electromechanical coupling coefficient* K_e^2 and is linked to the electromechanical coupling constant of the piezoelectric material [119]. The relation between series and resonance frequency and the effective electromechanical coupling coefficient k^2 is given by the approximated

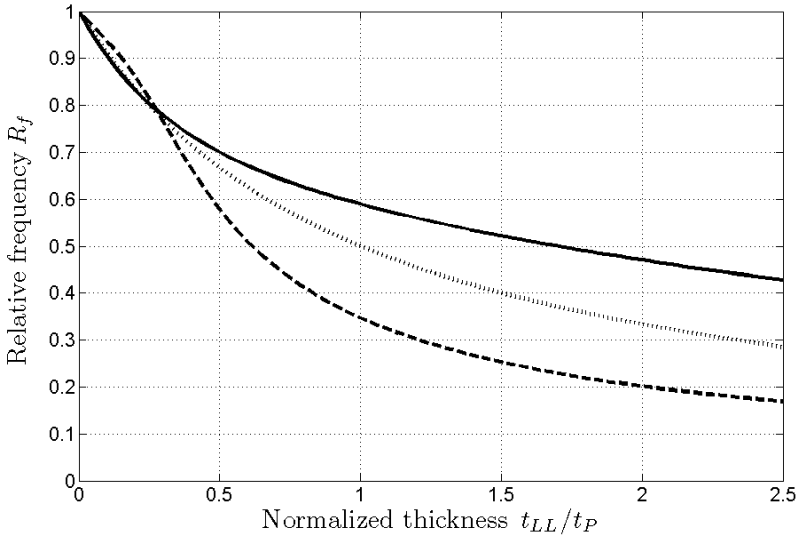


Fig. 7.3 – Relative frequency of composite FBAR as a function of the normalized thickness (solid line: AlN/NCD, dotted line: AlN/AlN, dashed line: AlN/SiO_2).

expression

$$K_e^2 \simeq \frac{\pi^2}{8}\frac{f_p^2 - f_s^2}{f_p^2}. \tag{7.5}$$

If the device is constituted only of a piezoelectric layer, its K_e^2 is close to k^2. The simulation of the composite structure indicates a high effective electromechanical coupling coefficient for AlN/NCD, close to pure AlN ($k^2 = 5.66\%$) as seen in Figure 7.5.

7.3.3 Mass sensitivity

The mass sensitivity S of the acoustic resonator is defined by the relative change of frequency for a perturbing mass of density ρ and Δh thickness :

$$S = \lim_{\Delta h \to 0} \frac{\Delta \omega}{\omega \rho \Delta h}. \tag{7.6}$$

According to the perturbation theory, the sensitivity can be written as a function of the total energy stored in the resonator U_v and the particle

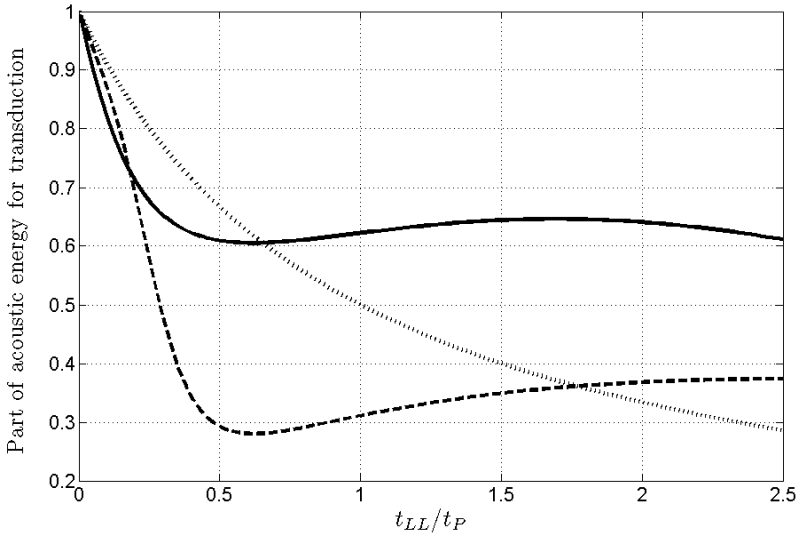


Fig. 7.4 – Part of the total acoustic energy trapped in the piezoelectric layer as a function of the normalized thickness (solid line: AlN/NCD, dotted line: AlN/AlN, dashed line: AlN/SiO_2).

velocity at the sensing surface of area A (e.g. Eq. 12.99 in [4]):

$$\frac{\Delta\omega}{\omega\rho\Delta h} = -\frac{1}{4U_v}\int_A |v|^2\, dA. \tag{7.7}$$

By assuming an infinite lateral extension of the acoustic field and no acoustic losses, the combination of Eqs. (3) and (4) gives:

$$S = -\frac{|v_0|^2}{2\int_0^t \rho(x)\,|v(x)|^2\, dx}. \tag{7.8}$$

We obtain the following analytical expression after replacement of Eqs. (1) and (2) in Eq. (5):

$$\boxed{S_C = -\frac{2Z_2\omega_C}{Z_1^2A_1+Z_2^2A_2+Z_1Z_2A_{12}}} \tag{7.9}$$

where:

$$A_1 = (2k_2t_2 - \sin 2k_2t_2)\sin^2(k_1t_1)\,; \tag{7.10}$$

$$A_2 = (2k_2t_2 + \sin 2k_2t_2)\cos^2(k_1t_1)\,; \tag{7.11}$$

$$A_{12} = 2k_1t_1 + \sin(2k_1t_1)\cos(2k_2t_2)\,. \tag{7.12}$$

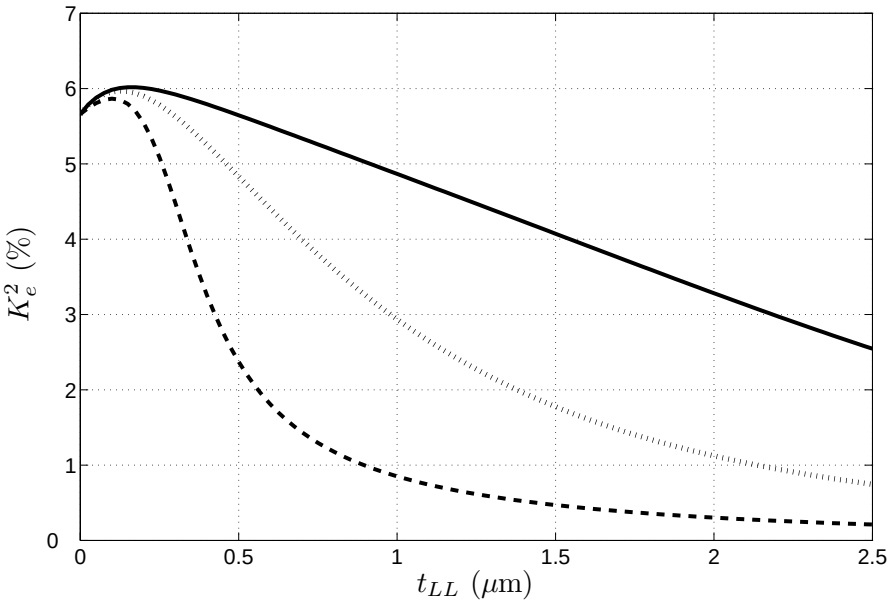


Fig. 7.5 – Effective eletromechanical coupling coefficient K_e^2 for a 1 μm thick piezoelectric AlN layer as a function of the loading layer thickness (solid line: AlN/NCD, dotted line: AlN/AlN, dashed line: AlN/SiO_2).

The composite device presents therefore two mass sensitivities: $S_{C,P}$ for ($t_1 = t_P$, $t_2 = t_{LL}$) and $S_{C,LL}$ for ($t_1 = t_{LL}$, $t_2 = t_P$), while the subscript P or LL mentions the sensing side. For a single layer, the mass sensitivity reduces to

$$\boxed{S_P = -\frac{1}{\rho_P t_P}.} \tag{7.13}$$

Figure 7.6 shows the evolution of the relative mass sensitivities

$$R_S = \frac{S_C}{S_P}$$

for low and high acoustic impedance loading layers and Table 7.2 summarizes the properties of a 2 μm thick composite FBAR.

FBAR	f_C [GHz]	$S_{C,P}$ [cm^2/g]	$S_{C,LL}$ [cm^2/g]	K_e^2 [%]
AlN/AlN	2.6	−1500	−1500	2.98
AlN/SiO_2	1.8	−700	−3800	0.85
AlN/NCD	3.1	−2200	−800	4.83

Table 7.2 – Summary of the properties of a 2 μm total thickness FBAR with $t_P = t_{LL} = 1$ μm

A third advantage of NCD is noticed in Figure 7.6: for a normalized thickness between 1 and 2, the $S_{C,P}$ of AlN/NCD varies by 10% while it varies by more than 50% for $S_{C,LL}$ in AlN/SiO_2. Therefore, the mass sensitivity of AlN/NCD is less influenced by thickness variations resulting from the fabrication process.

7.3.4 Ground detection limit

Although operating at high frequency results in an increased sensitivity, it often goes along with an increased noise. The minimum surface density detected σ_{min} is determined by the frequency noise f_n, it is considered that a signal at least three times higher than the frequency noise should be observed to unambiguously identify the frequency shift due to

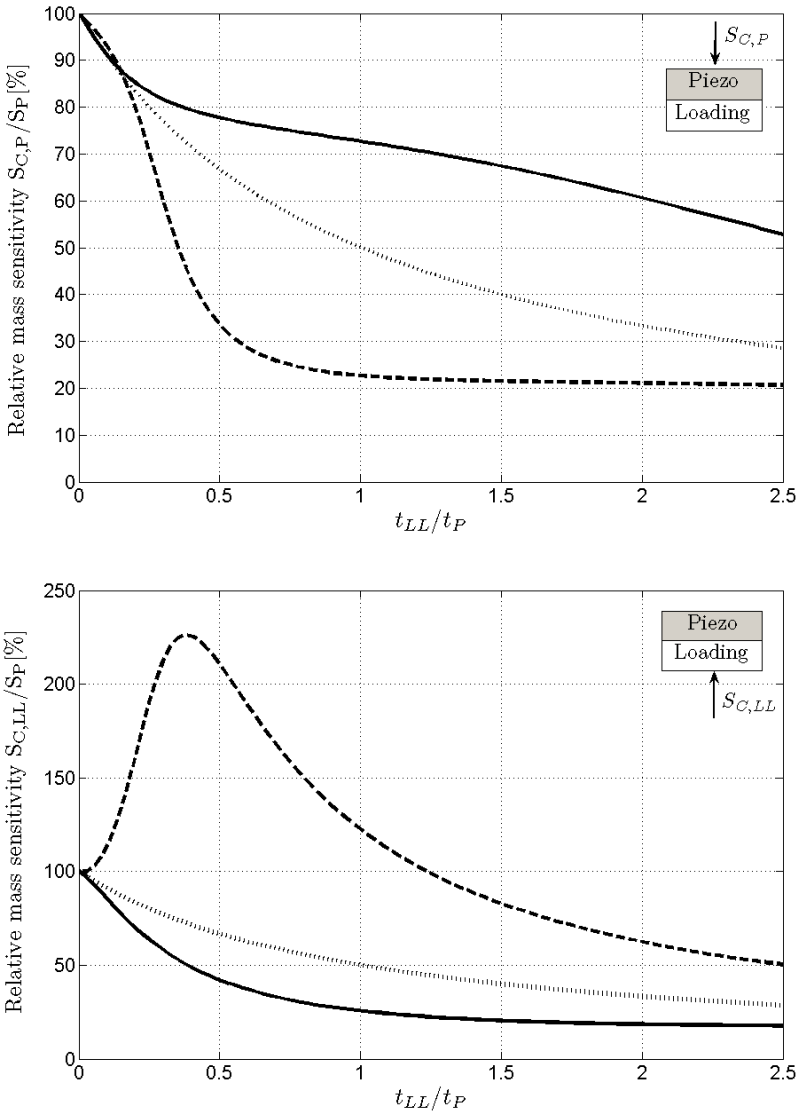


Fig. 7.6 – Relative mass sensitivity as a function of the normalized thickness for AlN/NCD (solid line), AlN/AlN (dotted line) and AlN/SiO_2 (dashed line) for a mass perturbation on the piezoelectric side (top graph) or on the loading layer side (bottom graph).

a sensing event. This is written

$$\sigma_{min} = \frac{3f_n}{f_C S_C}. \tag{7.14}$$

Because $f_C = R_f f_P$ and $S_C = R_S S_P$, it is also written as:

$$\sigma_{min} = \frac{3f_n}{R_f R_S f_P S_P}. \tag{7.15}$$

By replacing f_P and S_P by their expression from Eqs. (7.4) and (7.13), we have the ground detection limit:

$$\boxed{\sigma_{min} = \frac{6f_n}{R_f R_S} \cdot \frac{\rho_P t_P^2}{V_P}.} \tag{7.16}$$

The latter equation indicates that the detection limit is decreased with respect to a single piezoelectric FBAR at the condition that the product $R_f R_S$ is maximized. The value of σ_{min} for $f_n = 1$ Hz and $t_P = 1$ μm is reported for the best sensitivity of the three materials combinations in Figure 7.7.

According to this specific example, several conclusions can be drawn:

- the best detection limit is achieved with the sensing surface placed on the low acoustic impedance side of the composite device;
- for a loading layer thinner than the piezoelectric layer ($t_{LL} < t_P$), the best detection limit is achieved with AlN/SiO_2;
- for a loading layer thicker than the piezoelectric layer ($t_{LL} > t_P$), the best detection limit is achieved with AlN/NCD;
- in any cases and for the same total thickness, the detection limit of composite devices is always enhanced with respect to a single piezoelectric FBAR;
- a detection limit lower than 1 ng/cm^2 is possible for a noise level below 1 kHz.

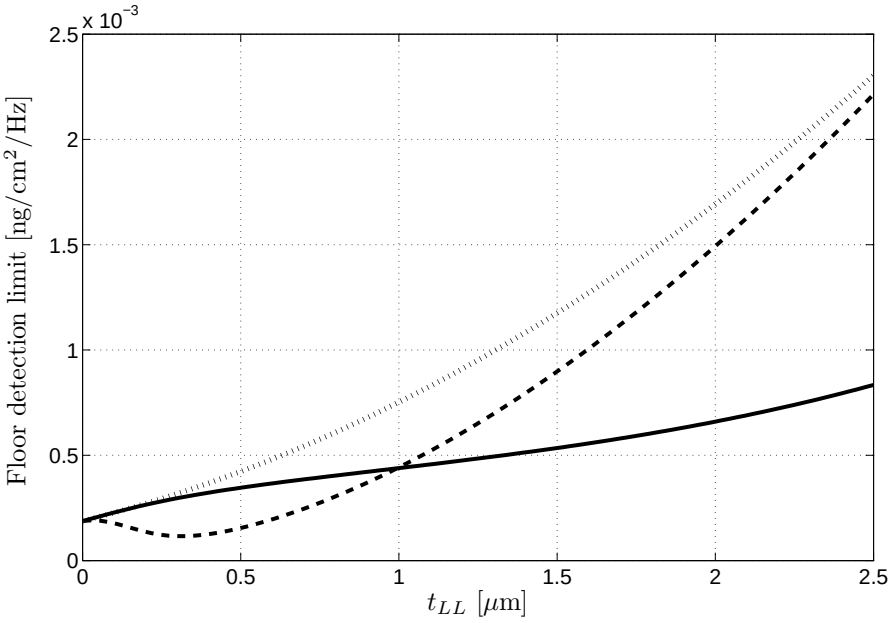


Fig. 7.7 – Ground detection limit as a function of the loading layer thickness for AlN/NCD (solid line), AlN/AlN (dotted line) and AlN/SiO_2 (dashed line) for the optimum sensitivity and a 1 μm thick piezoelectric layer.

7.4 Experimental results

An NCD/AlN FBAR has been fabricated as a demonstrator but, at this stage, the mass sensitivity has not been measured. In this section, we address the influence of the electrodes, as a first investigation.

7.4.1 Device fabrication

The composite FBARs were obtained by deposition of a nanocrystalline diamond thin film (t_{LL}=2.3 μm thick) on a clean 4 inches silicon substrate (film deposited by ρ-BeSt coating GmbH, Austria). The piezoelectric layer and its electrodes were obtained by the reactive sputtering of a Al/AlN/Al stack above the diamond surface (Nimbus310, Nexx Systems, MA). The aluminum layers are 200 nm thick and the aluminum nitride layer is t_P=800 nm thick. The top aluminum was patterned to form electrodes for the electrical RF measurement of the device. The composite structure was micromachined by subsequent back-side deposition of a masking layer (200 nm Al) with photo-defined patterns of the membranes followed by a silicon deep reactive ion etching (DRIE, Bosch Process). Diamond is an automatic etch stop material for this process. To avoid a degradation of the front side by the plasma of the DRIE, the entire wafer edge was protected with a Kapton tape that served equally to maintain the wafer on a 8 inches carrier wafer covered with aluminum.

7.4.2 Electrical performances

The electrical admittance Y of the composite AlN/NCD FBAR was measured with an HP85107B Network Analyzer. The values of the series and parallel resonances were measured on 8 different devices with electrodes shaped as squares of 200 and 300 μm edge size. The measured values are reported in Table 7.3 and plotted for the fundamental mode of resonance in Figure 7.8. The effective coupling coefficient K_e^2 and the quality factor Q of the resonators are calculated in Table 7.4. The quality factor is obtained using the following formula [119]:

$$Q_{s,p} = \frac{f}{2G} \cdot \left. \frac{\partial B}{\partial f} \right|_{f_{s,p}} \tag{7.17}$$

where G is the conductance (real part) and B is the susceptance (imaginary part) of the electrical admittance $Y = G + jB$.

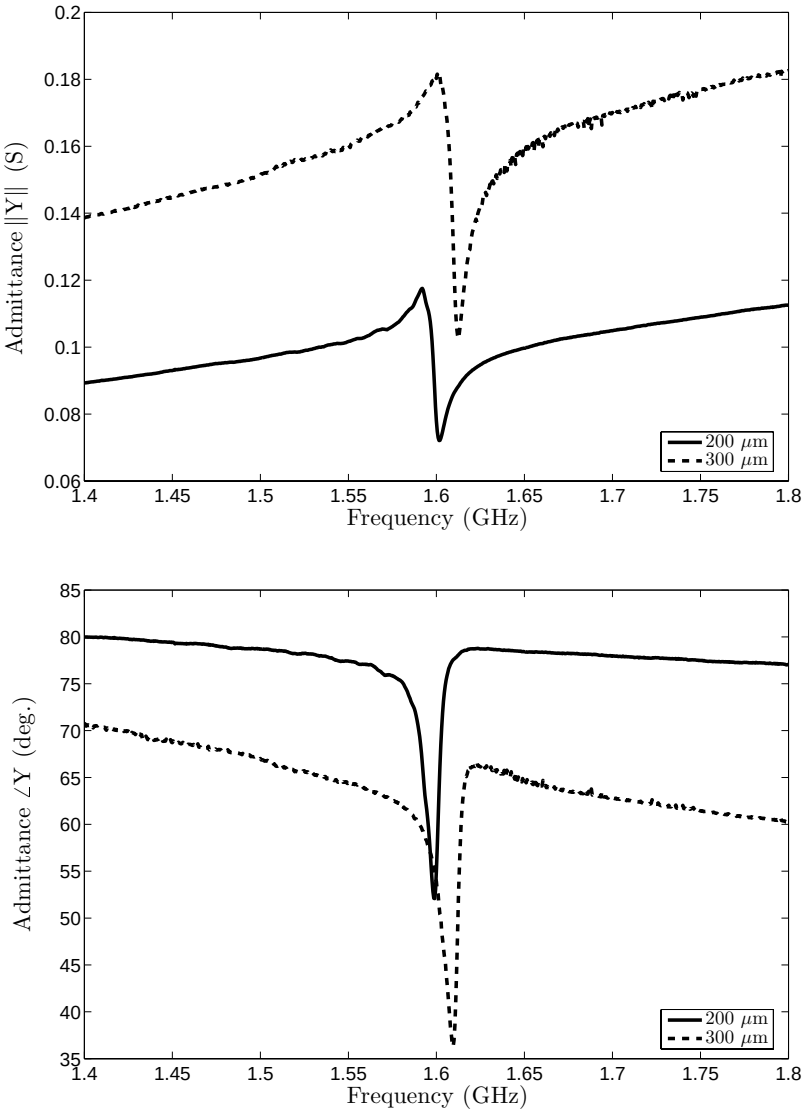


Fig. 7.8 – Electrical admittance Y of AlN/NCD composite FBAR with electrodes of edge size 200 and 300 μm as a function of the excitation frequency (top graph: magnitude of Y, bottom graph: phase angle of Y).

Mode	Electrode size (μm)	Device n°.	Series resonance				Parallel resonance				K_e^2
			f_s (GHz)	$\|Y_s\|$ (S)	$\angle Y_s$ (deg.)	Q_s	f_p (GHz)	$\|Y_p\|$ (S)	$\angle Y_p$ (deg.)	Q_p	(%)
1^{st}	200	1	1.589	0.123	64.0	98.8	1.600	0.0769	62.6	96.5	1.61
		2	1.592	0.118	66.4	127	1.602	0.0721	63.5	116	1.46
		3	1.597	0.117	62.3	110	1.605	0.0736	63.0	112	1.30
		4	1.599	0.116	68.6	135	1.609	0.0719	65.7	120	1.53
	300	1	1.596	0.173	49.5	80.4	1.605	0.100	50.1	112	1.38
		2	1.596	0.177	59.7	98.4	1.608	0.103	56.1	119	1.83
		3	1.601	0.182	52.9	80.3	1.613	0.103	52.4	118	1.83
		4	1.605	0.192	51.0	73.5	1.618	0.109	49.8	117	1.82
2^{nd}	200	1	3.230	0.295	39.6	58.6	3.263	0.142	37.6	212	2.48
		4	3.272	0.221	56.5	76.7	3.307	0.134	53.8	140	2.60
	300	4	3.308	0.310	43.0	49.3	3.342	0.182	43.9	142	2.53
3^{rd}	200	1	5.011	0.338	47.8	21	5.136	0.264	47.6	22	5.91
	300	4	4.962	0.319	22.5	13	5.158	0.274	21.0	16	9.20

Table 7.3 – Measured electrical performances of the three first modes of resonance of the AlN/NCD composite FBAR.

Mode	Electrode size (μm)		f_s (GHz)	Q_s	f_p (GHz)	Q_p	K_e^2 (%)
1^{st}	200	Mean	1.594	118	1.604	111	1.48
		Std. dev.	0.005	17	0.004	10	0.13
	300	Mean	1.599	83	1.611	116	1.72
		Std. dev.	0.005	11	0.006	3	0.22
	all	Mean	1.597	100	1.607	114	1.60
		Std. dev.	0.005	23	0.006	8	0.21
2^{nd}	all	Mean	3.27	62	3.30	165	2.54
		Std. dev.	0.04	14	0.04	41	0.06
3^{rd}	all	Mean	4.99	17	5.15	19	7.6
		Std. dev.	0.04	6	0.02	5	2.3

Table 7.4 – Mean values and standard deviations of the measured electrical performances given in Table 7.3 for the three first modes of resonance of the AlN/NCD composite FBAR.

7.4.3 Influence of the electrodes

The theoretical dispersion curves of the experimental structure for the 3 first modes is plotted in Figure 7.9 and the effective coupling coefficient for the first mode is plotted in Figure 7.10. The aluminum electrodes can not be neglected from the calculation since their thickness has a grand total equals to half the thickness of the piezoelectric layer. Their presence modifies the dispersion relation of the actual composite structure with respect to the modeled two-layered structure analyzed in the theoretical section. The aluminum has an acoustic impedance similar to silicon dioxide and, therefore, its presence as a low impedance material has an influence on the gravimetric sensitivity of the structure. To analyze this effect, the perturbation theory was used to assess the sensitivities of the actual structure, including the electrodes and the calculation is reported in Figure 7.11.

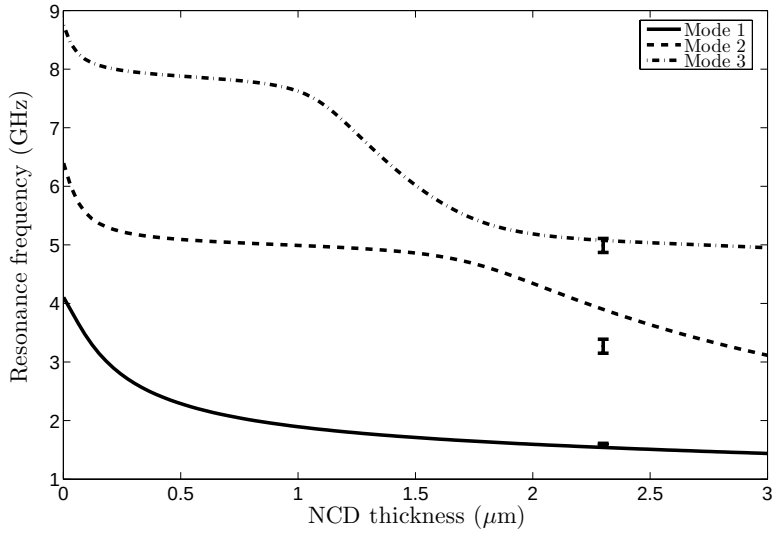


Fig. 7.9 – Theoretical dispersion curves of the 3 first modes of resonance as a function of the NCD layer thickness for the structure NCD/AlN including the presence of the Al electrodes. The experimental points at the NCD thickness of 2.3 μm – see Table 7.4 – are reported in the graph to indicate the correlation between theoretical calculations and measurement results. The 1^{st} and 3^{rd} modes are closely placed to the theoretical estimation while the 2^{nd} mode is below the expected value. The difference is most likely caused by the difference between the assumed and the actual mechanical values of the materials, and the error on their actual thickness.

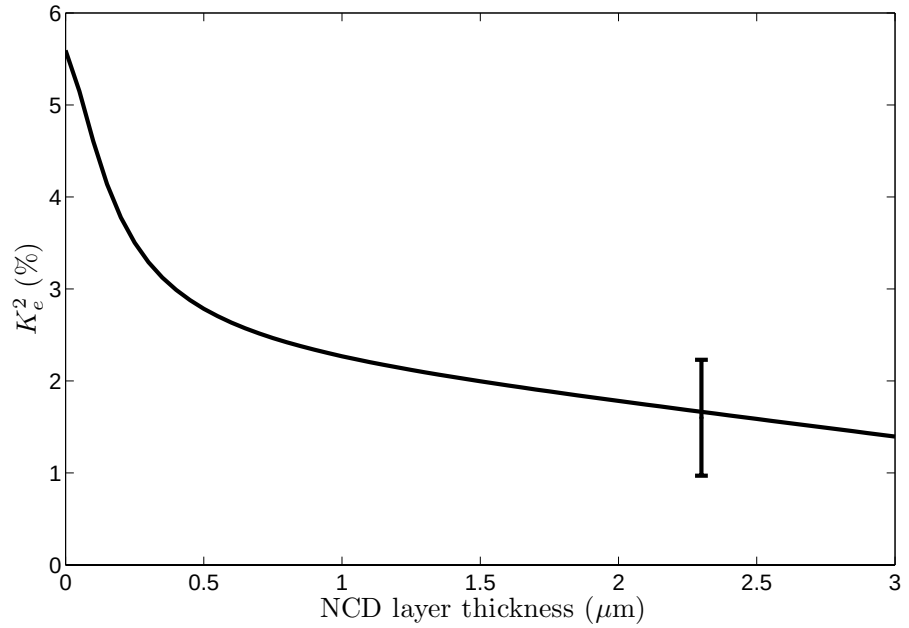


Fig. 7.10 – Theoretical evolution of the effective coupling coefficient K_e^2 *vs.* the NCD film thickness for the fundamental mode of resonance (mode 1). The experimental point at the NCD thickness of 2.3 μm – see Table 7.4 – is reported in the graph to indicate the correlation between the theoretical calculation and the measurement result.

7.4.4 Evolution of the sensitivity

The first overtone has not the same mass sensitivity as the fundamental mode due to a different distribution of the energy in the structure. Deducing an optimum sensitivity of the composite structure is complicated by schemes that strongly depends of the mechanical parameters of each material layers, their thicknesses and the mode of resonance. The experimental measurement of the mass sensitivity is left to future investigations.

Finally, the stress in the multilayered stack of the membranes causes a buckling as seen in the optical mapping (Veeco Wyko NT3000) images in Figures 7.12 and 7.13. The influence of the stress on the electrical and sensing performances has not been investigated presently.

7.5 Discussion

7.5.1 AlN/NCD FBAR mass sensor

The best composite FBAR sensor is obtained for the following conditions:

- a large acoustic impedance mismatch between piezoelectric and loading layers;
- a piezoelectric material with a low acoustic impedance and a high electromechanical coupling coefficient;
- a perturbation occurring on the lowest acoustic impedance side of the sensor.

The integration of NCD is advantageous as partial replacement of the AlN and for a sensing event taking place on the AlN side. The sensitivity enhancement is explained by the fact that a high acoustic impedance material has a low wavenumber and the AlN "sees" through NCD the impedance of the air backside, thus behave more like a single and thin AlN FBAR.

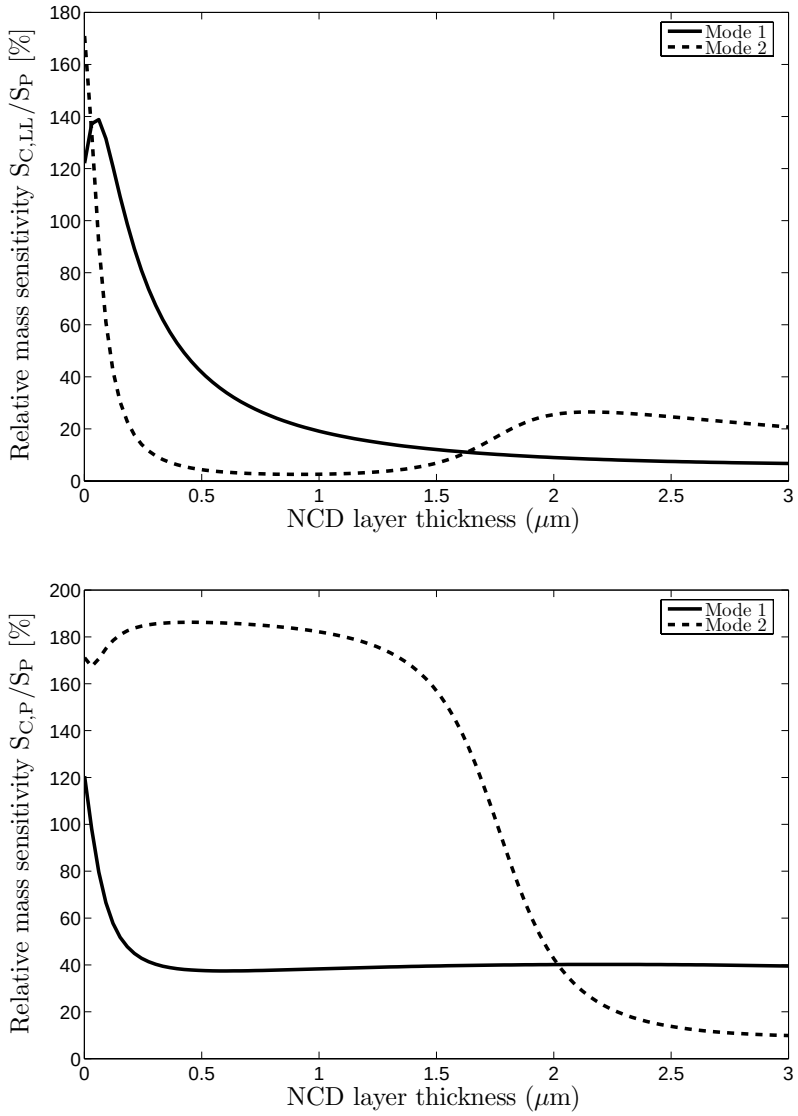


Fig. 7.11 – Theoretical mass sensitivities of the two first modes of the composite AlN/NCD FBAR including the presence of the Al electrodes (top graph: perturbation on the NCD side, bottom graph: perturbation on the top Al electrode side).

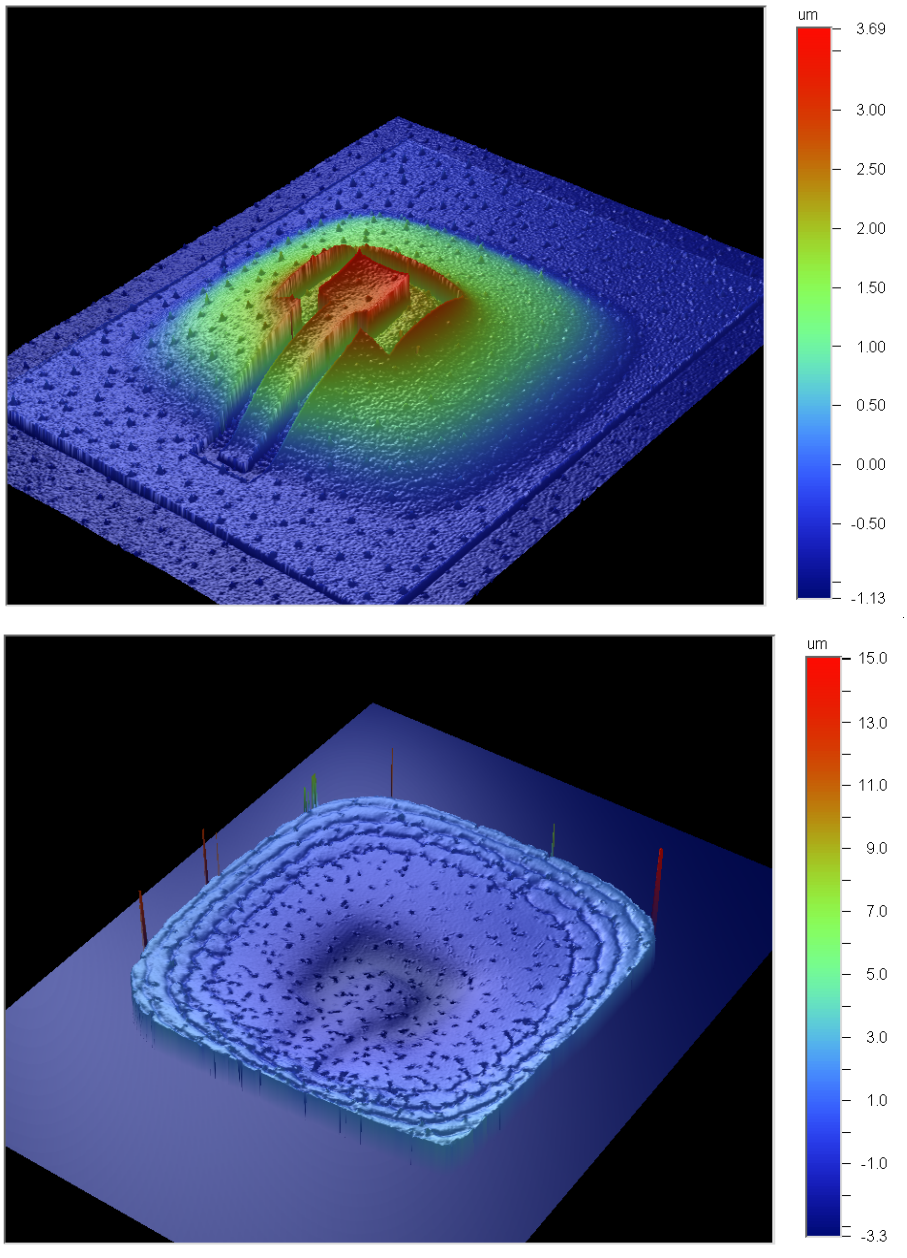


Fig. 7.12 – Optical mapping of the surface height of the 200×200 μm^2 electrode (top graph: top electrodes, bottom graph: backside).

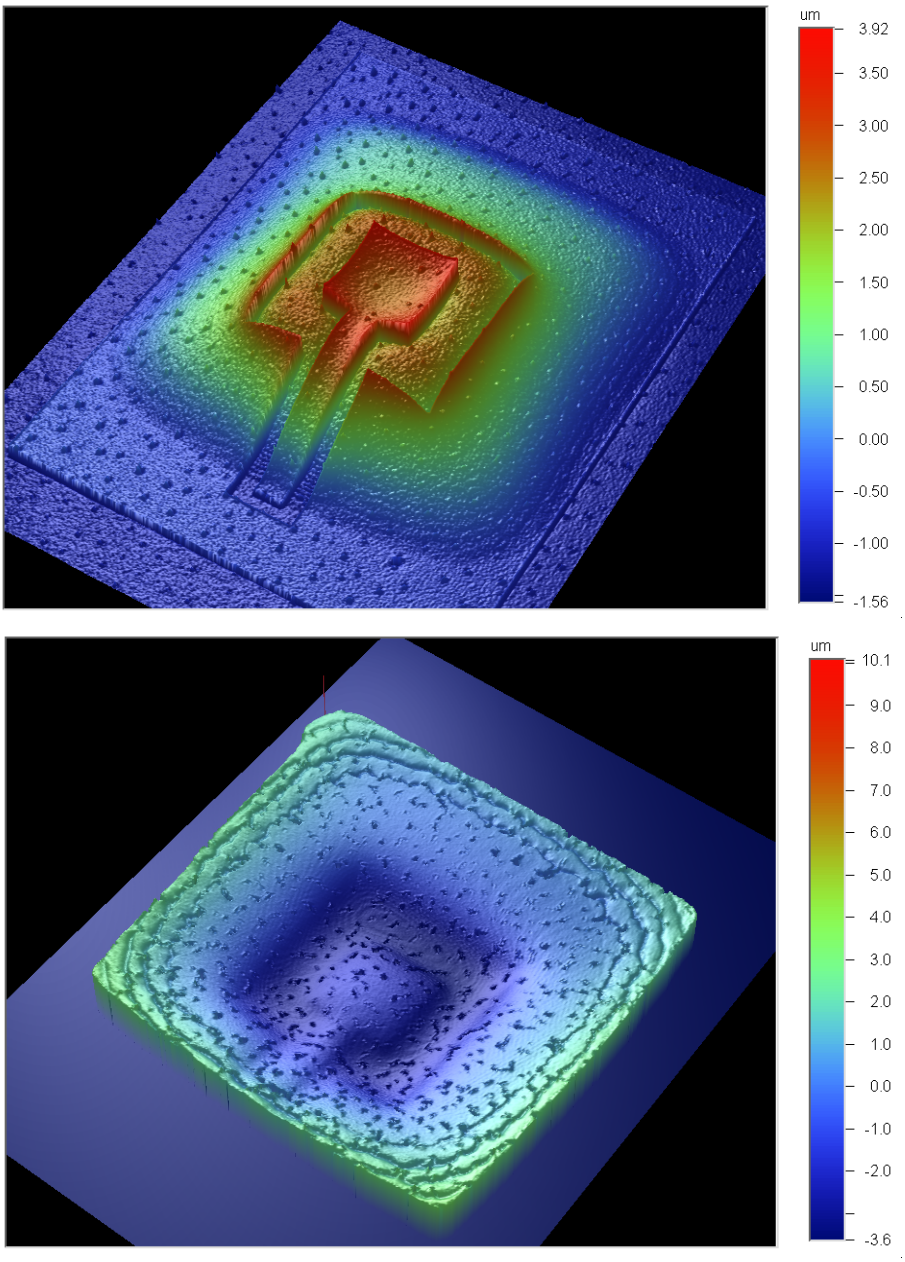


Fig. 7.13 – Optical mapping of the surface height of the 300×300 μm^2 electrode (top graph: top electrodes, bottom graph: backside).

7.5.2 FBAR-FPW sensor concept

The structure of the FBAR is compliant with the structure of Flexural Plate Wave (FPW) sensors [203]. We discussed in the last chapter of the opportunity to introduce nanocrystalline diamond in the fabrication of enhanced sensitivity FPW sensors. The identical fabrication process of FPW and FBAR devices allows the monolithic integration arrays of both acoustic sensors (FBAR-FPW).

The main interest of this combination will result from devices operating at very different frequencies: 1 to 10 MHz for FPW, and 1 to 10 GHz for FBAR. Consequently, FBAR-FPW provides additional information related to the mechanical properties of surface adsorbed layers, such as for instance in biosensors. Ongoing experimental work is directed towards the realization of this type of combined sensors.

7.6 Conclusion

The integration of nanocrystalline diamond in composite FBAR results in acoustic resonators with increased qualities: high resonance frequency, high electromechanical coupling coefficient, and better mechanical stability. A mass sensitivity enhancement occurs if the sensing event takes place on the piezoelectric side of the NCD-based structure but is comparable to other materials. However, NCD makes the characteristics of the structure less sensitive to thickness variations resulting from the fabrication process and more attractive for the achievement of real biosensor application where the mechanical robustness of the membrane structure is of crucial importance.

In comparison to other acoustic structures, in particular with respect to Love mode and Flexural Plate Waves sensors, a sensitivity enhancement is reached at the condition that the level of the frequency noise can be kept at an identical level; in such case, the detection limit reaches 1 pg/cm^2 instead of the typical 1 ng/cm^2 reported for Love mode devices. However, as the frequency of FBAR is a factor 10 higher, the frequency noise is expected to be higher as well, thus increasing the minimum mass amount detected. Finally, the sensing area of FBAR is one hundred times smaller than the one of the Love mode waveguide

or of the FPW resonator, an increased miniaturization of the acoustic sensor going along with its eventual integration with array technologies. Altogether, these features open a bright future to the FBAR gravimetric sensor.

Chapter 8

Final conclusions and outlook

> On a toujours tort d'essayer
> d'avoir raison devant des gens
> qui ont toutes les bonnes raisons
> de croire qu'ils n'ont pas tort !
>
> *Raymond Devos*

A biosensor is a variety of chemical sensor that performs a qualitative or a quantitative detection of specific biomolecules present in low concentration in an analyte solution. The detection of biomolecules can be achieved by several types of transducers, the acoustic method being one of them. In this thesis, we addressed acoustic structures in which the harmonic propagation of elastic deformations at frequencies comprised between 100 MHz to a few GHz is guided by a thin solid film, i.e. for film thicknesses lower or equal to the acoustic wavelength. Since the acoustic velocity in solid materials is comprised between 1 and 20 km/s, films with thicknesses in the range of hundreds of nanometers to a few micrometers were used. Thin films are more efficient to guide and to focus the acoustic energy at the surface where a specific adsorption of biomolecules takes place, thus leading to high sensitivities.

For an operation in liquid environments, the acoustic wave must present one of the two following conditions: 1) to be entirely shear-horizontally polarized (SH wave), or 2) to propagate at a phase velocity lower than the pressure wave velocity in the surrounding liquid. Under such condition, the acoustic energy is trapped in an evanescent wave at the surface-liquid interface and can therefore not dissipate in the liquid, which would result in a strong attenuation of the acoustic signal as it propagates in the guiding structure thus making it useless for most of the practical biosensor applications. The selection of one of the two conditions results in a given acoustic structure that guides the acoustic wave, namely an acoustic waveguide.

The first case is implemented by the Love mode acoustic waveguide, where a shear-horizontal wave is guided by the thin film deposited on a supporting substrate. The substrate, usually being piezoelectric, is also required to generate and to detect the acoustic wave that can be electrically excited thanks to interdigitated electrodes patterned on it. For better sensing characteristics, the Love mode device is fashioned with multilayered guiding thin films, some of the films being selected not only for an enhancement of the sensitivity but also to electrically shield the acoustic wave and its electrical transduction from the dielectric perturbation caused by the sensed environment. The sensing properties of the Love mode waveguide can be optimized by varying the thickness of the guiding films.

The second case is implemented under the form of a stand-alone thin film that can support, for instance, the propagation of the so-called Lamb mode. Since the mechanical stability of a stand-alone thin film would be impractical for the manipulation of the device, the actual implementation is better obtained under the form of a membrane supported by a thick rigid frame. In that later case, the thin film membrane can be operated in several modes. The flexural plate wave is a resonance mode close to the Lamb mode, which requires relatively long membranes; the same structure can be used for a second type of acoustic resonance: the thin film bulk acoustic resonator (FBAR). Because of the lack of supporting substrate, the concentration of acoustic energy in a thin film membrane results in a higher sensitivity than the fully supported film but the inherent fragility of a thin film membrane has been so far the clearest issue that limited their development for biosensor applications.

A first large part of this thesis has been devoted to the Love mode device, which is nowadays considered as an almost classical acoustic sensor. Despite a high sensitivity, a high versatility for mass and liquid sensing and a clear robustness, the Love mode device is not as widely spread as the famous quartz crystal microbalance (QCM) since it suffers from a more complicated fabrication process and from several packaging and instrumentation issues than the latter. A minimum 10-fold sensitivity gain is possible by switching from the QCM to the Love mode sensor, which might account for the large interest developed since the early '90s for this attractive waveguide. In a second and smaller part, the study of membrane based devices has taken a clear turn in direction of nanocrystalline diamond, an emerging material with fascinating properties. The high mechanical and chemical qualities of this material, close to the ones of pure diamond, in conjunction with its current fabrication method and relative easiness of processing makes it perfectly suited for the generation of novel micromachined devices and, in particular, of biosensors. Thanks to the highest acoustic velocity of all other materials, nanocrystalline diamond can be integrated as thin film membranes for the realization of flexural plate waves and FBAR sensors.
Although the two approaches described in the two main parts of this thesis may appear separate, they have a common global goal of clearly establishing the enormous potential for new materials in the development of novel acoustic wave devices and structures for application in biosensors. The integration of novel, emerging and tailored materials, together with a solid theoretical understanding of the underlying sensing mechanisms, leads to the realization of novel devices. However, we would also like to point to the fact that an other benefit could be obtained thanks to alternative actuation methods and innovative acoustic structures that are out of the scope of this thesis.

In the first Part, this thesis has deeply investigated the Love mode biosensor. The analysis of the propagation in the guiding structure made out of a stack of mechanically isotropic and generally viscoelastic layers was obtained thanks to a transmission line model. The model is efficient to calculate the acoustic wavevector by decoupling propagation and resonance directions of the structure using the standard transverse resonance principle. The real and imaginary parts of the wavevector are directly associated to, respectively, the attenuation and the acoustic velocity of

the guided wave. The model applies successfully to various configurations including the presence of lossy materials and for a liquid loading at the surface of the waveguide. The main limitation of the method is the lack of integration of electrical, piezoelectric and anisotropic effects. A discrepancy is expected for structures based on piezoelectric substrates with high values of the electromechanical coupling coefficient such as lithium compounds.

Thanks to the model, the variation of the electrical signal are correlated with the surface adsorption of a composite layer from a supporting liquid. Surface density and mass viscosity variations are fully integrated in the model while the rigid or viscous nature of the adsorbed layer are discriminated by the sensor depending of the relative shifts of amplitude and phase of the signal. This technique assumes in a novel approach with respect to known techniques that the biomolecules are forming on the surface a flat film of varying composition. Because of the varying composition, linked to the potential inclusion of solvent in the biofilm and the nature of the biomolecules, the mechanical characteristics of the film are varying as well and are reflected by the modification of the signal and the ratio of amplitude to phase shifts. A high ratio denotes a viscous film while a low ratio sustains a doubt about the rigid or viscous nature of the film. The uncertainty could be resolved by an additional and independent measurement of the film thickness. The numerical values of the ratio are determined by simulations that requires to know precisely the density, the shear stiffness and the thickness of the constituting layers of the waveguide. Once those properties known, simulations are sufficient to determine all sensing characteristics without requiring any experimental calibration methods.

The experimental calibration of the device should focus at determining the exact mechanical characteristics of the guiding layers since those directly determine the distribution of energy in the structure, the dispersion of the wave and, consequently, the variations in the propagation resulting from modifications happening above the sensing surface. We showed that most of the calibration methods intended to determine the gravimetric sensitivity have discrepancies between each others and with the actual sensing of biomolecules because of two reasons. The first reason is that the gravimetric sensitivity, that links the phase shift to the surface density shift, is not representative of the variation of density and viscosity induced by the adsorption of biomolecules. The second reason

is that the calibration methods induce variations representative of the material currently used for the calibration without direct link with the recognition of an other biochemical of other thickness or configuration on the surface. We conclude that calibrations should be avoided and stress should be put to determine the exact mechanical properties of the guiding layers instead and deduce directly from adequate simulations the variations of the acoustic signal resulting from variations in the composition of the sensed media.

During the experimental calibrations, the electromagnetic interferences had an impact on the variation of phase and amplitude as a function of the probing frequency and of the amplitude of the electromagnetic wave relatively to the one of the acoustic wave. A mathematical description of the interaction between the two waves yields two conclusions: the sensitivity experimentally evaluated at a constant value of the frequency (referring to the open loop configuration) is enhanced around interferences peaks and, when evaluated at a constant value of the phase (referring to the closed loop configuration), the interferences are almost not influencing the signal shift. The interference peaks allows to determine the actual value of phase velocity in the sensing area and their intensity is function of the design of the transducers, through their radiation conductance, and the coupling of the electromagnetic signal between input and output transducers. A substantial gain of sensitivity in the open loop configuration is attainable for a given bandwidth determined by the intensity of the interaction parameter.

The choice of materials used for guiding the acoustic wave in the Love mode structure has a direct influence on the sensitivity. A strong dispersion of the wave results in a high sensitivity that peaks for optimum thicknesses of the guiding layers. The strongest dispersion is obtained for a large difference in stiffness and density between the substrate and the guiding layers. A maximum is obtained for materials with the lowest value for both parameters and low losses dielectrics should be preferred. For practical achievements, the silicon dioxide still give the best results in our study if tailored properly during the deposition. Plasma-enhanced chemical vapor deposition of silica layers have different characteristics function of the gases used and others factors that must be optimized for each specific deposition tool. In the present case, a hydrogen-rich atmosphere resulted in very low shear stiffness of the guiding layer and therefore a relatively strong sensitivity. However, an acoustic device

with high sensitivity is also a device that suffers from a strong attenuation when loaded by the liquid, thus achieving the optimum thickness while keeping a sufficiently high level of the signal with a liquid loading is not possible.
The fabrication of actual sensors must also address the main issue of packaging and the protection of the electrical parts from the electrical influence of liquids. The original approach presented in this thesis and based on the photodefinition of SU-8 protection walls is the basis of a packaging method that needs further enhancements to be fully compatible with IC fabrication techniques.
The information issued from the SAW biosensor is not sufficient to quantitatively determine all the parameters of the composite layer lying on the surface. The composition of the layer and its thickness can not be determined out of a single SAW measurement. An additional biosensor technique that can be directly linked to the SAW parameters is required, such as a direct thickness measurement (e.g. AFM or capacitive techniques) or with an optical measurement such as ellipsometry or surface plasmon resonance (SPR). From literature, the combination of the quartz crystal microbalance with the SPR technique was known and, presently, the SPR method has been technically integrated with the Love mode biosensor in a single instrument for the *in situ*, real time and label-less monitoring of acoustic and optical data during the adsorption of biochemical material on a single sensing surface. Both techniques probes the adlayer within similar thicknesses and are linked by assuming a direct correlation between the refractive index and the density of the composite layer. Analytical methods were presented to determine out of these two measurements the thickness and the density of rigid or thin viscoelastic layers on one side, and the thickness, the density and the viscosity of Newtonian layers on the other side. To that end, simulations of both the SAW and the SPR signal are required and the only knowledge of the bulk values of refractive index and density of the component segregating in the composite layer. Investigation of S-layers and PNIPAAm demonstrated the potential of the method to determine nanometer range thicknesses and, from the density of the layer, the quantity of solvent diluted in the adlayer within 10% range. Beside that, the technique still operates for thermal cycling between 20 and 40 °C as seen by probing the evolution of PNIPAAm layers under such circumstances. Thanks to our method, an improved insight of the conformational transition of the

polymer around the Lower Critical Solution Temperature was obtained in agreement with previous studies reported in the literature.

In the second Part, this thesis has investigated thin film nanocrystalline diamond membrane for acoustic based sensors. Thin film suspended membranes concentrating more efficiently the acoustic energy to the sensing area have a higher sensitivity and a lower mass detection. Nanocrystalline diamond is a material of choice with respect to classically used materials due to the highest Young's modulus and other significant mechanical, optical and chemical properties. Its deposition as homogeneous thin films still happen at relatively high temperatures to allow IC integration but, for stand-alone devices, the fabrication and processing methods are fully compliant with current microfabrication techniques. The additional possibility to tune the material characteristics, and in particular its conductivity by doping, opens applications to a wide range of opportunities for microsystems and corresponding sensors.
In this thesis, the objective has been set to the development of flexural plate waves (FPW) in a first time for mass sensing in liquids, as a valuable competitor of the Love mode structure. Operation at lower frequencies similar to the ones of the quartz crystal device, with identical sensitivities and sensing area, facilitates the instrumentation. Due to a mechanical stiffness increasing faster than its density, nanocrystalline diamond is suited for the realization of FPW devices with increased sensitivity at the condition that the membrane could be thin enough (below 1 μm) and actuated appropriately. A piezoelectric actuation of the membrane, obtained by integrating a piezoelectric thin film like PZT-compounds, zinc oxide or aluminum nitride, in conjunction with interdigitated electrodes, is requested although any added layer deteriorates the sensing characteristics of the device because of the additional mass loading and the consequent decrease of acoustic energy density it causes. There are still efforts to place in such investigations since the experimental demonstration of a diamond-based FPW sensor was not reached yet during this thesis. However, as outcome of our investigations, an original dynamic characterization method of the relevant parameters for the design of FPW devices and the residual stress in the membrane was set. A stroboscopic measurement of the out-of-plane deflections of the membrane excited on the lower resonance modes is

used to determine the resonance frequencies function of the shape of the membrane and the residual stress in the thin film. By a simple regression technique, the exact value of a parameter involving the Young's modulus, the density and the Poisson's coefficient of the material is obtained as well as the residual stress in the film. This parameter enters directly the formulation of the FPW sensor and can therefore be used to assess the expected properties of a prototyping material intended for FPW sensors.
As a second step to the achievement of FPW sensors, the integration of piezoelectric aluminum nitride films was considered experimentally. Based on the same technology as the one needed for the fabrication of FPW device, thin film bulk acoustic resonators were fabricated in the frame of this thesis and tested. FBAR made of a supporting material, in this case the nanocrystalline diamond thin film, with the AlN layer is also an acoustic sensor to which we referred here as the composite FBAR. The sensing characteristics of the composite FBAR were assessed using the perturbation theory. From the theory, an unique feature of the composite FBAR structure is an asymmetric value of the mass sensitivity linked to the asymmetry of the structure itself, the best sensitivity being achieved with a sensing surface placed on the side of the material presenting the lowest density and the lowest acoustic velocity. The successful integration of AlN in the fabrication process of FBARs let us believe that the realization of operating diamond-based FPW sensor is at a stone thrown from our latest achievements. The gain in sensitivity of FBAR devices is about 1 000 times the sensitivity of the Love mode device, at the condition that the stability of the signal keeps identical performances. The miniature size of the FBAR sensor, with respect to acoustic waveguides, is an other advantage for its mechanical stability and for a drastic reduction in the absolute quantity of material required to shift the resonance frequency. Operation on overtones is also allowed by this type of nanoresonator. The integration of the FBAR or the FPW sensors with local probes techniques should be envisioned in future work dedicated to the achievement of multiparametric sensorial platforms.

For future work, the standardization of the fabrication procedure of Love mode devices should help to a faster spreading of this multipurpose sensorial platform. Packaging issues should be kept in mind while

reducing the measurement noise should be targeted to reduce the detection limit. The software implementation of techniques described in this thesis should also be done in order to help the understanding of the signal measured. A dedicated instrumentation of the device measuring continuously amplitude and phase of the electrical signal need to be implemented for a light and portable measurement with the sensor. Finally, integration with the optical technique, e.g. a white light SPR, with the SAW sensor is an additional but nonetheless useful feature of a biosensor! Finally, as mentioned previously, the integration of nanocrystalline diamond in the form of thin film membranes is opening large and appealing ways to design innovative biosensors.

References

[1] *Handbook of Chemistry andd Physics*. CRC Press, 56 edition, 1975.

[2] E. L. Adler. Matrix methods applied to acoustic waves in multilayers. *IEEE Trans. Ultrason., Ferroelect., Freq. Contr.*, 37(6):485–490, 1990.

[3] E. L. Adler, J. K. Slaboszewicz, G. W. Farnell, and C. K. Jen. PC for SAW propagation in anisotropic multilayers. *IEEE Trans. Ultrason., Ferroelect., Freq. Contr.*, 37(2):215–222, 1990.

[4] B. A. Auld. *Acoustic Fields and Waves in Solids*, volume 2. Krieger Publishing Company, Malabar, 2 edition, 1990.

[5] B. A. Auld. *Acoustic Fields and Waves in Solids*, volume 1. Krieger Publishing Company, Malabar, 2 edition, 1990.

[6] R. L. Baer, C. A. Flory, M. Tom-Moy, and D. S. Solomon. STW chemical sensors. In *IEEE Ultrason. Symp.*, pages 293–298, 1992.

[7] L.E. Bailey, D. Kambhampati, K.K. Kanazawa, W. Knoll, and C.W. Franck. Using surface plasmon resonance and the quartz crystal microbalance to monitor in situ the interfacial behavior of thin organic films. *Langmuir*, 18:479–489, 2002.

[8] C. D. Bain, E. B. Troughton, Y.-T. Tao, J. Evall, G. M. Whitesides, and R. G. Nuzzo. Formation of monolayer films by the spontaneous assembly of organic thiols from solution onto gold. *J. Am. Chem. Soc.*, 111(1):321–335, 1989.

[9] S. Balamurugan, S. Mendez, S. S. Balamurugan, M. J. O'Brien II, and G. P. López. Thermal response of poly(N-isopropylacrylamide) brushes probed by surface plasmon resonance. *Langmuir*, 19:2545–2549, 2003.

[10] D. S. Ballantine, R. M. White, S. J. Martin, M. J. Ricco, E. T. Zellers, G. C. Frye, and H. Wohltjen. *Acoustic wave sensors. Theory, design, and physico-chemical applications*. Academic Press, San Diego, 1997.

[11] C. Barentin, P. Muller, C. Ybert, J.-F. Joanny, and J.-M. di Meglio. Shear viscosity of polymer and surfactant monolayer. *Eur. Phys. J. E*, 2:153–159, 2000.

[12] N. Barié, M. Rapp, and H. Sigrist. The use of dextran as an intermediate layer: a new approach towards SAW biosensors. In *1999 Joint Meeting EFTF - IEEE IFCS*, pages 997–1000, 1999.

[13] D. R. Baselt, G. U. Lee, K. M. Hansen, L. A. Chrisey, and R. J. Colton. A high-sensitivity micromachined biosensor. In *Proc. IEEE*, volume 85, pages 672–680, 1997.

[14] R. Bashir, J. Z. Hilt, O. Elibol, A. Gupta, and N. A. Peppas. Micromechanical cantilever as an ultrasensitive pH microsensor. *Appl. Phys. Lett.*, 81(6):3091–3093, 2002.

[15] N. Baute, L. Martinot, and R. Jérôme. Investigation of the cathodic electropolymerization of acrylonitrile, ethylacrylate and methylmethacrylate by coupled quartz crystal microbalance analysis and cyclic voltammetry. *Journal of Electroanalytical Chemistry*, 472:83–90, 1999.

[16] F. Bender, K. Länge, N. Barié, J. Kondoh, and M. Rapp. Online monitoring of polymer deposition for tailoring the waveguide characteristics of Love-wave biosensors. *Langmuir*, 20(6):2315–2319, 2004.

[17] M. Benetti, D. Cannatà, A. D'Amico, F. Di Pietrantonio, V. Foglietti, and E. Verona. Thin film bulk acoustic wave resonator (TFBAR) gas sensor. In *IEEE Ultrason. Symp.*, pages 1581–1584, 2004.

[18] N. Benramdane, W. A. Murad, R. H. Misho, M. Ziane, and Z. Kebbab. A chemical method for the preparation of thin films of CdO and ZnO. *Materials Chemistry and Physics*, 48:119–123, 1997.

[19] E. Berkenpas, S. Bitla, P. Millard, and M. P. da Cunha. LGS shear horizontal SAW devices for biosensor applications. In *IEEE Ultrason. Symp.*, pages 1404–1407, 2003.

[20] J. Birrel, J. E. Gerbi, O. Auciello, J. M. Gibson, D. M. Gruen, and J. A. Carlisle. Bonding structure in nitrogen doped ultrananocrystalline diamond. *J. Appl. Phys.*, 93(9):5606–5612, 2003.

[21] J. P. Black, B. Chen, R. Quinn, M. Madou, and R. M. White. Comparison of the performances of flexural plate wave and surface acoustic wave devices as the detector in gas chromatography. In *IEEE Ultrason. Symp.*, pages 435–440, 2000.

[22] Robert D. Blevins. *Formulas for natural frequency and mode shape*. Krieger Publishing Company, Malabar, 1993.

[23] C. Boutris, E. G. Chatzi, and C. Kiparissides. Characterization of the LCST behaviour of aqueous poly(N-isopropylacrylamide) solutions by thermal and cloud point techniques. *Polymer*, 10:2567–2570, 1997.

[24] D. W. Branch and S. M. Brozik. Low-level detection of a Bacillus anthracis simulant using Love-wave biosensors on 36°YX $LiTaO_3$. *Biosensors and Bioelectronics*, 19:849–859, 2004.

[25] J. Brandrup and E. H. Immergut. *Polymer handbook*. John Wiley & Sons, New-York, London, Sydney, 1966.

[26] A. Bund, A. Baba, S. Berg, D. Johannsmann, J. Lübben, Z. Wang, and W. Knoll. Combining surface plasmon resonance and quartz crystal microbalance for the in situ investigation of the electropolymerization and doping/dedoping of poly(pyrrole). *J. Phys. Chem. B*, 107:6743–6747, 2003.

[27] A. Bund, O. Schneider, and V. Dehnke. Combining AFM and EQCM for the in situ investigation of surface roughness effects during electrochemical metal depositions. *Phys. Chem. Chem. Phys.*, 4:3552–3554, 2002.

[28] M. A. Butler, M. K. Hill, J. J. Spates, and S. J. Martin. Pressure sensing with a flexural plate wave resonator. *J. Appl. Phys.*, 85(3):1998–2000, 1999.

[29] C. Campbell. *Surface acoustic wave devices and their signal processing applications*. Academic Press, San Diego, 1989.

[30] A. P. Campitelli. *Investigation of a Shear Horizontal Surface Acoustic Wave Sensor System for Liquid Media*. PhD thesis, Royal Melbourne Institute of Technology, 1997.

[31] A. Caronti, H. Majjad, S. Ballandras, G. Caliano, R. Carotenuto, A. Iula, V. Foglietti, and M. Pappalardo. Vibration maps of capacitive micromachined ultrasonic transducers by laser interferometry. *IEEE Trans. Ultrason., Ferroelect., Freq. Contr.*, pages 289–292, 2002.

[32] F. Caruso, D.N. Furlong, K. Ariga, I. Ichinose, and T. Kunitake. Characterization of polyelectrolyte-protein multilayer films by atomic force microscopy, scanning electron microscopy, and Fourier transform infrared reflection-absorption spectroscopy. *Langmuir*, 14:4559–4565, 1998.

[33] P. F. Caton. *Microfiltration and Flexural Plate Wave Devices*. PhD thesis, University of California at Berkeley, 2001.

[34] B. A. Cavić, G. L. Hayward, and M. Thompson. Acoustic waves and the study of biochemical macromolecules and cells at the sensor-liquid interface. *Analyst*, 124:1405–1420, 1999.

[35] K.-H. Choi, J.-M. Friedt, F. Frederix, A. Campitelli, and G. Borghs. Simultaneous atomic force microscope and quartz crystal microbalance measurements: investigation of human plasma fibrinogen adsorption. *Appl. Phys. Lett.*, 81:1335–1337, 2002.

[36] D. K. T. Chu and R. G. Hunsperger. Piezoelectric and acoustic properties of potassium titanyl phosphate (KTP) and its isomorphs. In *IEEE International Frequency Control Symposium*, pages 732–743, 1992.

[37] S.-Y. Chu, W. Water, and J.-T. Liaw. An investigation of the dependence of ZnO film on the sensitivity of Love mode sensor in ZnO/Quartz structure. *Ultrasonics*, 41:133–139, 2003.

[38] A. J. Cunningham. *Introduction to bioanalytical sensors*. John Wiley & Sons, New York, 1998.

[39] R. Cush, J. M. Cronin, W. J. Stewart, C. H. Maule, J. Molloy, and N. J. Goddard. The resonant mirror: a novel optical biosensor for direct sensing of biomolecular interactions. *Biosensors and Bioelectronics*, 8:347–353, 1993.

[40] F. Paraguay D., W. Estrada, D. R. Acosta N., E. Andrade, and M. Miki-Yoshida. Growth, structure and optical characterizaion of high quality ZnO thin films obtained by spray pyrolysis. *Thin Solid Films*, 350:192–202, 1999.

[41] M. P. da Cunha and S. de A. Fagundes. Investigation on recent quartz like materials for SAW applications. In *IEEE Ultrason. Symp.*, pages 283–288, 1998.

[42] M. P. da Cunha, D. C. Malocha, D. W. Puccio, J. Thiele, and T. B. Pollard. LGX pure shear horizontal SAW for liquid sensor applications. *IEEE Sensors Journal*, 3(5):554–561, 2003.

[43] S. C. Deshmukh and E. S. Aydil. Investigation of low temperature SiO_2 plasma enhanced chemical vapor deposition. *J. Vac. Sci. Technol. B*, 14(2):738–743, 1996.

[44] S. M. Dickinson. The buckling and frequency of flexural vibration of rectangular isotropic and orthotropic plates using Rayleigh's method. *J. Sound Vibr.*, 61(1):1–8, 1978.

[45] P. D'Orazio. Biosensors in clinical chemistry. *Clinica Chimica Acta*, 334:41–69, 2003.

[46] B. Drafts. Acoustic wave technology sensors. *IEEE Trans. Microwave Theory Tech.*, 49(4):795–802, 2001.

[47] J. Du and G. L. Harding. A multilayer structure for Love-mode acoustic sensors. *Sensors and Actuators A*, 65:152–159, 1998.

[48] J. Du, G. L. Harding, A. F. Collings, and P. R. Dencher. An experimental study of Love-wave acoustic sensors operating in liquids. *Sensors and Actuators A*, 60:54–61, 1997.

[49] J. Du, G. L. Harding, J. A. Ogilvy, P. R. Dencher, and M. Lake. A study of Love-wave acoustic sensors. *Sensors and Actuators A*, 56:211–219, 1996.

[50] Y. F. Dufrêne, T. G. Marchal, and P. G. Rouxhet. Probing the organization of adsorbed protein layers: complementarity of atomic force microscopy, X-ray photoelectron spectroscopy and radiolabeling. *Appl. Surf. Sci.*, 144-145:638–643, 1999.

[51] T. W. Ebbesen, H. J. Lezec, H. F. Ghaemi, T. Thio, and P. A. Wolff. Extraordinary optical transmission through sub-wavelength hole arrays. *Nature*, 391:667–669, 1998.

[52] K. L. Ekinci, Y. T. Yang, and M. L. Roukes. Ultimate limits to intertial mass sensing based upon nanoelectromechanical systems. *J. Appl. Phys.*, 95(5):2682–2689, 2004.

[53] G. Feuillard, Y. Janin, F. Teston, L. Tessier, and M. Lethiecq. Sensitivities of surface acoustic wave sensors based on fine grain ceramics. In IEEE, editor, *Instrumentation and Measurement Technology Conference, 1996. IMTC-96. Conference Proceedings. Quality Measurements: The Indispensable Bridge between Theory and Reality*, volume 2, pages 1211–1215, 1996.

[54] D. Fischer, W. J. Varhue, J. Wu, and C. A. Whiting. Lamb-wave microdevices fabricated on monolithic single crystal silicon wafers. *J. Microelectromech. Syst.*, 9(1):88 – 93, 2000.

[55] C. M. Flannery, M. D. Whitfield, and R. B. Jackman. Characterisation of free-standing polycrystalline CVD diamond films by SAW-based laser ultrasonics. In *IEEE Ultrason. Symp.*, pages 729–732, 2000.

[56] L. A. Francis, J.-M. Friedt, C. Bartic, and A. Campitelli. An SU-8 liquid cell for surface acoustic wave biosensors. In *Proc. of the SPIE*, volume 5455, pages 353–363, 2004.

[57] L. A. Francis, A. Kromka, D. Steinmüller-Nethl, P. Bertrand, and C. Van Hoof. Rapid investigation of nanocrystalline diamond vibrating membranes with a stroboscopic interferometer. In D. Rocha, P. M. Sarro, and M. J. Vellekoop, editors, *IEEE Sensors 2004*, pages 146–149, 2004.

[58] D. M. Fraser. Biosensors: making sense of them. *Medical Device Technology*, 5(9):38–41, 1994.

[59] F. Frederix, K. Bonroy, W. Laureyn, G. Reekmans, A. Campitelli, W. Dehaen, and G. Maes. Enhanced performance of an affinity biosensor interface based on mixed self-assembled monolayers of thiols on gold. *Langmuir*, 19:4351–4357, 2003.

[60] J.-M. Friedt, L. Francis, K.-H. Choi, F. Frederix, and A. Campitelli. Combined atomic force microscope and acoustic wave devices: application to electrodeposition. *J. Vac. Sci. Technol. A*, 21:1500–1505, 2003.

[61] J.-M. Friedt, L. Francis, G. Reeckmans, R. De Palma, A. Campitelli, and U. B. Sleytr. Simultaneous surface acoustic wave and surface plasmon resonance measurements: electrodeposition and biological interactions monitoring. *J. Appl. Phys.*, 95(4):1677–1680, 2004.

[62] R. Gabl, E. Green, M. Shreiter, H. D. Feucht, H. Zeiniger, R. Primig, D. Pitzer, G. Eckstein, W. Wersing, W. Reichl, and J. Runck. Novel integrated FBAR sensors: a universal technology platform for bio- and gas-detection. In *Proc. of IEEE Sensors 2003*, volume 2, pages 1184–1188, 2003.

[63] E. Gizeli. Design considerations for the acoustic waveguide biosensor. *Smart Mater. Struct.*, 6:700–706, 1997.

[64] E. Gizeli. Study of the sensitivity of the acoustic waveguide sensor. *Anal. Chem.*, 72:5967–5972, 2000.

[65] E. Gizeli. Acoustic transducers. In E. Gizeli and C.R. Lowe, editors, *Biomolecular Sensors*. Taylor & Francis, London, 2002.

[66] E. Gizeli, F.Bender, A. Rasmusson, K. Saha, F. Josse, and R. Cernosek. Sensitivity of the acoustic waveguide biosensor to protein binding as a function of the waveguide properties. *Biosensors and Bioelectronics*, 18:1399–1406, 2003.

[67] E. Gizeli, A. C. Stevenson, N. J. Goddard, and C. R. Lowe. A novel Love-plate acoustic sensor utilizing polymer overlayers. In *IEEE Trans. on UFFC*, pages 657–659, 1992.

[68] E. Gizeli, A. C. Stevenson, N. J. Goddard, and C. R. Lowe. Acoustic Love plate sensors: comparison with other acoustic de-

vices utilizing surface SH waves. *Sensors and Actuators B*, 13–14:638–639, 1993.

[69] A. Gordijn, R. J. Zambrano, J. K. Rath, and R. E. I. Schropp. Highly stable hydrogenated amorphous silicon germanium solar cells. *IEEE Trans. Electron Devices*, 49(5):949–952, 2002.

[70] J. E. Graebner, H. F. Safar, B. Barber, P. L. Gammel, J. Herbsommer, L. A. Fetter, J. Pastalan, H. A. Huggins, and R. E. Miller. Optical mapping of surface vibrations on a thin-film resonator near 2 GHz. In *IEEE Ultrason. Symp.*, pages 635–638, 2000.

[71] D. Grigg, E. Felkel, J. Roth, X. Colonna de Lega, L. Deck, and P. de Groot. Static and dynamic characterization of MEMS and MOEMS devices using optical interference microscopy. In *Proc. of SPIE*, volume 5455, pages 429–435, 2004.

[72] T. M. A. Gronewold, S. Glass, E. Quandt, and M. Famulok. Monitoring complex formation in the blood-coagulation cascade using aptamer-coated SAW sensors. *Biosensors and Bioelectronics*, 20:2044–2052, 2005.

[73] P. Grossel, J.-M. Vigoureux, and F. Baïda. Nonlocal approach to scattering in a one-dimensional problem. *Phys. Rev. A*, 50:3627–3637, 1994.

[74] Y. V. Gulyaev. Review of shear surface acoustic waves in solids. *IEEE Trans. Ultrason., Ferroelect., Freq. Contr.*, 45(4):935–938, 1998.

[75] H. Guo and A. Lal. Characterization of micromachined silicon nitride membrane using resonant ultrasound spectroscopy. In *IEEE Ultrason. Symp.*, pages 863–866, 2001.

[76] A. Gupta, D. Akin, and R. Bashir. Single virus particle mass detection using microresonators with nanoscale thickness. *Appl. Phys. Lett.*, 84(11):1976–1978, 2004.

[77] E.S. Györvary, A. O'Riordan, A.J. Quinn, G. Redmon, D. Pum, and U.B. Sleytr. Biomimetic nanostructure fabrication: nanolithographic lateral patterning and self-assembly of functional bacterial S-layers at silicon supports. *NanoLetters*, 3:315–319, 2003.

[78] A. J. Haes and R. P. Van Duyn. A nanoscale optical biosensor: sensitivity and selectivity of an approach based on the localized surface plasmon resonance spectroscopy of triangular silver nanoparticles. *J. Am. Chem. Soc.*, 124:10596–10604, 2002.

[79] S.-S. Han and G. S. May. Using neural networks process models to perform PECVD silicon dioxide recipe synthesis via genetic algorithms. *IEEE Trans. Semiconduct. Manufact.*, 10(2):279–287, 1997.

[80] L. Hanley, O. Kornienko, E. T. Ada, E. Fuoco, and J.L. Trevor. Surface mass spectrometry of molecular species. *J. Mass Spectrom.*, 34:705–723, 1999.

[81] G. L. Harding. Mass sensitivity of Love–mode acoustic sensors incorporating silicon dioxide and silicon-oxy-fluoride guiding layers. *Sensors and Actuators A*, 88:20–28, 2001.

[82] G. L. Harding, J. Du, P. R. Pencher, D. Barnett, and E. Howe. Love wave acoustic immunosensor operating in liquid. *Sensors and Actuators A*, 61:279–286, 1997.

[83] M. R. Hart, R. A. Conant, K. Y. Lau, and R. S. Muller. Stroboscopic interferometer system for dynamic MEMS characterization. *J. Microelectromech. Syst.*, 9(4):409–418, 2000.

[84] A. Härtl, E. Schmich, J. A. Garrido, J. Hernando, S. C. R. Catharino, S. Walter, P. Feulner, A. Kromka, D. Steinmüller, and M. Stutzmann. Protein-modified nanocrystalline diamond thin films for biosensor applications. *Nat. Mater.*, 3:736–742, 2004.

[85] K.-Y. Hashimoto, Y. Watanabe, M. Akahane, and M. Yamaguchi. Analysis of acoustic properties of multi-layered structures by means of effective acoustic impedance matrix. In *IEEE Ultrason. Symp.*, pages 937–942, 1990.

[86] F. Herrmann and S. Büttgenbach. Temperature-compensated shear-horizontal acoustic waves in layered Quartz/SiO_2 structures. *Phys. Stat. Sol. (a)*, 170(2):R3–R4, 1998.

[87] F. Herrmann, D. Hahn, and S. Büttgenbach. Separate determination of liquid density and viscosity with sagitally corrugated Love-mode sensors. *Sensors and Actuators*, 78:99–107, 1999.

[88] F. Herrmann, M. Weinacht, and S. Büttgenbach. Properties of sensors based on shear-horizontal surface acoustic waves in $LiTaO_3/SiO_2$ and Quartz/SiO_2 structures. *IEEE Trans. Ultrason., Ferroelect., Freq. Contr.*, 48:268–273, 2001.

[89] S. L. Hietala, V. M. Hietala, and C. J. Brinker. Dual SAW sensor technique for determining mass and modulus changes. *IEEE Trans. Ultrason., Ferroelect., Freq. Contr.*, 48(1):262–267, 2001.

[90] J. Homola, S. S. Yee, and G. Gauglitz. Surface plasmon resonance sensors: review. *Sensors and Actuators B*, 54:3–15, 1999.

[91] F. Höök, B. Kasemo, T. Nylander, C. Fant, K. Scott, and H. Elwing. Variations in coupled water, viscoelastic properties, and film thickness of a Mefp-1 protein film during adsorption and cross-linking: a quartz crystal microbalance with dissipation monitoring, ellipsometry, and surface plasmon resonance study. *Anal. Chem.*, 73:5796–5804, 2001.

[92] F. Höök, J. Vörös, M. Rodahl, R. Kurrat, P. Böni, J.J. Ramsden, M. Textor, N.D. Spencer, P. Tengvall, J. Gold, and B. Kasemo. A comparative study of protein adsorption on titanium oxide using in situ ellipsometry, optical waveguide lightmode spectroscopy, and quartz crystal microbalance/dissipation. *Colloids and Surfaces B*, 24:155–170, 2002.

[93] W. P. Hu, S.-J. Chen, K.-T. Huang, J. H. Hsu, W. Y. Chen, G. L. Chang, and K.-A. Lai. A novel ultrahigh-resolution surface plasmon resonance biosensor with an Au nanocluster-embedded dielectric film. *Biosensors and Bioelectronics*, 19:1465–1471, 2004.

[94] B. Ilic, H. G. Craighead, S. Krylov, W. Senaratne, C. Ober, and P. Neuzil. Attogram detection using nanoelectromechanical oscillators. *J. Appl. Phys.*, 95(7):3694–3703, 2004.

[95] S.J. Ippolito, K. Kalantar-zadeh, D.A. Powell, and W. Wlodarski. A finite element approach for 3-dimensional simulation of layered acoustic wave transducers. In *2002 Conference on Optoelectronic and Microelectronic Materials and Devices*, pages 541–544, 2002.

[96] B. Ivarsson and M. Malmqvist. Surface plasmon resonance: development and use of BIACORE instruments for biomolecular interaction analysis. In E. Gizeli and C.R. Lowe, editors, *Biomolecular Sensors*. Taylor & Francis, London, 2002.

[97] R. J. Jackman, T. M. Floyd, R. Ghodssi, M. A. Schmidt, and K. F. Jensen. Microfluidic systems with on-line UV detection fabricated in photodefinable epoxy. *J. Micromech. and Microeng.*, 11:263–269, 2001.

[98] B. Jakoby and M. Vellekoop. Viscosity sensing using a Love-wave device. *Sensors and Actuators A*, 68:275–281, 1998.

[99] B. Jakoby and M. J. Vellekoop. Properties of Love waves: applications in sensors. *Smart Mater. Struct.*, 6:668–679, 1997.

[100] B. Jakoby and M. J. Vellekoop. Analysis and optimization of Love wave liquid sensors. *IEEE Trans. Ultrason., Ferroelect., Freq. Contr.*, 45:1293–1302, 1998.

[101] B. Jakoby and M. J. Vellekoop. Reducing the temperature sensitivity of Love-wave sensors. In *IEEE Ultrason. Symp.*, pages 447–450, 1998.

[102] B. Jakoby and M. J. Vellekoop. Viscous losses of shear waves in layered structures used for biosensing. In *IEEE Ultrason. Symp.*, pages 493–496, 1998.

[103] B. Jakoby and M. J. Vellekoop. FFT- based analysis of periodic structures in microacoustic devices. *IEEE Trans. Ultrason., Ferroelect., Freq. Contr.*, 47(3):651–656, 2000.

[104] Y. Janin, G. Feuillard, F. Teston, and M. Lethiecq. Effective surface permittivity of piezoelectric substrates coated with thin polymer films. In *IEEE Ultrason. Symp.*, pages 415–418, 1997.

[105] X. Jiang, J. V. Harzer, B. Hillebrands, Ch. Wild, and P. Koidl. Brillouin light scattering on chemical-vapor-deposited polycrystalline diamond: evaluation of the elastic moduli. *Appl. Phys. Lett.*, 59(9):1055–1057, 1991.

[106] K. Kalantar-zadeh, A. Trinchi, W. Wlodarski, and A. Holland. A novel Love-mode device based on a ZnO/ST-cut quartz crystal structure for sensing applications. *Sensors and Actuators A*, 2–3:135–143, 2002.

[107] K. Kalantar-zadeh, W. Wlodarski, Y. Y. Chen, B. N. Fry, and K. Galatsis. Novel Love mode surface acoustic wave based immunosensors. *Sensors and Actuators B*, 91:143–147, 2003.

[108] K. Kalantar-zadeh, W. Wlodarski, and K. Galatsis. Simulation of a Love mode surface acoustic wave transducer. In *IEEE Ultrason. Symp.*, pages 161–164, 1999.

[109] Y. Katsumoto, T. Tanaka, H. Sato, and Y. Ozaki. Conformations change of (N-isopropylacrylamide) during the coil-globule transition investigated by attenuated total reflection/infrared spectroscopy and density functional theory calculation. *J. Phys. Chem. A*, 106:3429–3435, 2002.

[110] D. J. Keller. Scanning force microscopy in biology. In A. Baszkin and W. Norde, editors, *Physical Chemistry of Biological Interfaces*. Marcel Dekker Inc., New York, 2000.

[111] P. Kielczynski and W. Pajewski. A new method for the determination of the shear impedance of viscoelastic liquids. In *IEEE Ultrason. Symp.*, pages 323–326, 1988.

[112] H. Kim, Y. Lee, Y. Roh, J. Jung, M. Lee, and H. Kwon. Development of ZnO thin films for SAW devices by the ultrasonic spray pyrolysis technique. In *IEEE Ultrason. Symp.*, pages 323–326, 1998.

[113] Y. T. Kim, S. M. Cho, Y. G. Seo, H. D. Yoon, Y. M. Im, and D. H. Yoon. Influence of hydrogen on SiO_2. *Cryst. Res. Technol.*, 37(12):1257–1263, 2002.

[114] M. M. Knock and C. D. Bain. Effect of counterion on monolayers of Hexadecyltrimethylammonium Halides at the air-water interface. *Langmuir*, 16:2857–2865, 2000.

[115] J. Kondoh, Y. Matsui, and S. Shiokawa. SH-SAW biosensor based on pH change. In *IEEE Ultrason. Symp.*, pages 337–340, 1993.

[116] J. Kondoh, T. Muramatsu, T. Nakanishi, and S. Shiokawa. Development of surface acoustic wave liquid sensing system and application for japanese tea measurements. In *IEEE International Frequency Control Symposium and PDA Exhibition*, pages 497 – 501, 2001.

[117] J. Koskela, S. Lehtonen, V. P. Plessky, and M. M. Salomaa. Surface transverse waves on langasite. *Appl. Phys. Lett.*, 72(21):2665–2667, 1998.

[118] R. Kötz, D. M. Kolb, and J. K. Sass. Electroreflectance spectra of Ag(111) electrodes. *Surf. Sci.*, 64:96–108, 1977.

[119] K. M. Lakin, G. R. Kline, and K. T. McCarron. High-Q microwave acoustic resonators and filters. *IEEE Trans. Microwave Theory Tech.*, 41(12):2139–2146, December 1993.

[120] K. Länge, F. Bender, A. Voigt, H. Gao, and M. Rapp. A surface acoustic wave biosensor concept with low flow cell volumes for label-free detection. *Anal. Chem.*, 75(20):5561–5566, 2003.

[121] K. Länge, G. Blaess, A. Voigt, M. Rapp, E. Hansjosten, and U. Schygulla. Packaging of surface acoustic wave (SAW) based biosensors: an important issue for future biomedical applications. In *Proceedings of the 2004 IEEE International Frequency Control Symposium and Exposition*, pages 321 – 325, 2004.

[122] A. Laschitsch, B. Menges, and D. Johansmann. Simultaneous determination of optical and acoustical thicknesses of protein layers using surface plasmon resonance spectroscopy and quartz crystal microweighing. *Appl. Phys. Lett.*, 77:2252–2254, 2000.

[123] V. Laude, A. Reinhardt, M. Wilm, A. Khelif, and S. Ballandras. Fast FEM/BEM simulation of SAW devices via asymptotic waveform evaluation. *IEEE Trans. Ultrason., Ferroelect., Freq. Contr.*, 51(3):359–363, 2004.

[124] R. M. Lec. Piezoelectric biosensors: recent advances and applications. In *IEEE International Frequency Control Symposium and PDA Exhibition*, pages 419–429, 2001.

[125] R. M. Lec and P. A. Lewin. Acoustic wave biosensors. In *Proceedings of the 20th Annual International Conference of the IEEE Engineering in Medicine and Biology Society*, volume 20, pages 2779–2784, 1998.

[126] C. S. Lee, K. No, D. M. Wee, J. H. Lee, and C. A. Choi. A novel angular rate sensor employing flexural plate wave. In *IEEE Ultrason. Symp.*, pages 493–496, 1999.

[127] D. L. Lee. Excitation and detection of surface skimming bulk waves on rotated Y-cut quartz. *IEEE Trans. Sonics and Ultrasonics*, SU27(1):22–30, 1980.

[128] A. Leidl, I. Oberlack, U. Schaber, B. Mader, and S. Drost. Surface acoustic wave device and applications in liquid sensing. *Smart Mater. Struct.*, 6:680–688, 1997.

[129] S. Li. The electromagneto-acoustic surface wave in a piezoelectric medium : the Bleustein-Gulayev mode. *J. Appl. Phys.*, 80(9):5264–5269, 1996.

[130] B. Liedberg, C. Nylander, and I. Lundström. Surface plasmon resonance for gas detection and biosensing. *Sensors and Actuators*, 4:299–304, 1983.

[131] S.-Y. Lin, K.-S. Chen, and L. Run-Chu. thermal micro ATR-FT-IR spectroscopic system for quantitative study of the molecular structure of poly(N-isopropylacrylamide) in water. *Polymer*, 40:2619–2624, 1999.

[132] J. R. Lu and R. K. Thomas. The application of neutron and X-ray specular reflection to proteins at interfaces. In A. Baszkin and W. Norde, editors, *Physical Chemistry of Biological Interfaces*. Marcel Dekker Inc., New York, 2000.

[133] R. Lucklum and P. Hauptmann. Generalized acoustic parameters of non-homogeneous thin films. In *IEEE International Frequency Control Symposium and PDA Exhibition*, pages 234–241, 2002.

[134] S. Makarov, E. Chilla, and H.-J. Fröhlich. Determination of elastic constants of thin films by dispersion of various SAW modes. In *IEEE Ultrason. Symp.*, pages 357–360, 1995.

[135] R.J. Marsch, R.A.L. Jones, and M. Sferrazza. Adsorption and displacement of a globular protein on hydrophilic and hydrophobic surfaces. *Colloids and Surfaces B*, 23:31–42, 2002.

[136] F. Martin, P. Muralt, M.-A. Dubois, and A. Pezous. Thickness dependence of the properties of highly c-axis textured AlN thin films. *J. Vac. Sci. Technol. A*, 22(2):361–365, 2004.

[137] G. McHale, F. Martin, and M. I. Newton. Mass sensitivity of acoustic wave devices from group and phase velocity measurement. *J. Appl. Phys.*, 92(6):3368–3373, 2002.

[138] G. McHale, M. I. Newton, and F. Martin. Theoretical mass, liquid, and polymer sensitivity of acoustic wave sensors with viscoelastic guiding layers. *J. Appl. Phys.*, 93(1):675–690, 2003.

[139] A. Milewska, J. Szydlowski, and L. P. N. Rebelo. Viscosity and ultrasonics studies of poly(N-isopropylacrylamide)-water solutions. *J. Polym. Sci. Pt. B-Polym. Phys*, 41:1219–1233, 2003.

[140] R. F. Milson, N. H. C. Reilly, and M. Redwood. Analysis of generation and detection of surface and bulk acoustic waves by interdigital transducers. *IEEE Trans. Sonics and Ultrasonics*, SU-24(3):147–166, 1977.

[141] S. P. Mohanty. Biosensors: a survey report. Technical report, University of South Florida, 2001.

[142] B.P. Nelson, A.G. Frutos, J.M. Brockman, and R.M. Corn. Near-infrared surface plasmon resonance measurements of ultrathin film. *Anal. Chem.*, 71:3928–3940, 1999.

[143] N.-T. Nguyen and R. M. White. Acoustic streaming in micromachined flexural plate wave devices: numerical simulation and experimental verification. *IEEE Trans. Ultrason., Ferroelect., Freq. Contr.*, pages 1463–1471, 2000.

[144] A. A. Oliner. Microwave Network Methods for Guided Elastic Waves. *IEEE Trans. Microwave Theory Tech.*, 17:812–826, November 1969.

[145] P. G. Pai, S. S. Chao, Y. Tagaki, and G. Lucovsky. Infrared spectroscopic study of SiO_x films produced by plasma enhanced chemical vapor deposition. *J. Vac. Sci. Technol. A*, 4(3):689–694, 1986.

[146] H. J. Pain. *The physics of vibrations and waves*. Wiley, New York, 5^{th} edition, 1999.

[147] E. Palik. *Handbook of optical constants of solids*. Academic Press, 1997.

[148] J. Y. Pan, P. Lin, F. Maseeh, and S. D. Senturia. Verification of FEM analysis of load-deflection methods for measuring mechanical properties of thin films. In *IEEE Solid-State Sensor and Actuator Workshop, 1990. 4^{th} Technical Digest.*, pages 70–73, 1990.

[149] P. S. Patil. Versatility of chemical spray pyrolysis technique. *Materials Chemistry and Physics*, 59:185–198, 1999.

[150] S. Petitgrand and A. Bossebœuf. Simultaneous mapping of phase and amplitude of MEMS vibrations by microsopic intereferometry with stroboscopic illumination. In *Proc. of SPIE*, volume 5145, pages 33–44, 2003.

[151] J. Philip, P. Hess, T. Feygelson, J. E. Butler, S. Chattopadhyay, K. H. Chen, and L. C. Chen. Elastic, mechanical, and thermal properties of nanocrystalline diamond films. *J. Appl. Phys.*, 93(4):2164–2171, 2003.

[152] M. A. Plunkett, P. M. Claesson, M. Ernstsson, and M. Rutland. Comparison of the adsorption of different charge density polyelectrolytes: a quartz crystal microbalance and X-ray photoelectron spectroscopy study. *Langmuir*, 19:4678–4681, 2003.

[153] M. A. Plunkett, Z. Wang, M. W. Rutland, and D. Johannsmann. Adsorption of pNIPAM layers on hydrophobic gold surfaces measured in situ by QCM and SPR. *Langmuir*, 19:6837–6844, 2003.

[154] D.A. Powell, K. Kalantar-zadeh, S. Ippolito, and W. Wlodarski. A layered SAW device based on $ZnO/LiTaO_3$ for liquid media sensing applications. In *IEEE Ultrason. Symp.*, volume 1, pages 493–496, 2002.

[155] H. Raether. *Surface plasmons on rough and smooth surfaces and on gratings*. Springer-Verlag, Berlin, 1988.

[156] A. Rasmusson and E. Gizeli. Comparison of poly(methylmethacrylate) and Novolak waveguide coatings for an acoustic biosensor. *J. App. Phys.*, 90:5911–5914, 2001.

[157] A. Reinhardt, V. Laude, Th. Pastureaud, and S. Ballandras. Numerical simulation and comparison of membrane and solidly mounted FBARs. In *IEEE Ultrason. Symp.*, pages 497–500, 2002.

[158] M. Rodahl, P. Dahlqvist, F. Höök, and B. Kasemo. The quartz crystal microbalance with dissipation monitoring. In E. Gizeli and C.R. Lowe, editors, *Biomolecular Sensors*. Taylor & Francis, London, 2002.

[159] Y. R. Roh, H. B. Kim, Y. J. Lee, H. M. Cho, J. S. Chung, and S. Baik. Development of SAW gas sensor for monitoring SOx gas. In *IEEE Ultrason. Symp.*, pages 473–476, 1995.

[160] D. Royer and E. Dieulesaint. *Ondes élastiques dans les solides*, volume 1. Masson, Paris, 1996.

[161] D. Royer and E. Dieulesaint. *Ondes élastiques dans les solides*, volume 2. Masson, Paris, 1999.

[162] K. Saha, F. Bender, and E. Gizeli. Comparative study of IgG binding to proteins G and A: nonequilibrium kinetic and binding constant determination with the acoustic waveguide device. *Anal. Chem.*, 75(4):835–842, 2003.

[163] K. Saha, F. Bender, A. Rasmusson, and E. Gizeli. Probing the viscoelasticity and mass of a surface-bound protein layer with an acoustic waveguide device. *Langmuir*, 19:1304–1311, 2003.

[164] S. Salgar, G. Kim, D.-H. Han, and B. Kim. Modeling and simulation of the thin film bulk acoustic resonator. In *IEEE International Frequency Control Symposium and PDA Exhibition*, pages 40–44, 2002.

[165] J. P. Santos, M. J. Fernández, J. L. Fontecha, J. Lozano, M. Aleixandre, M. García, J. Gutiérrez, and M. C. Horillo. SAW

sensor array for wine discrimination. *Sensors and Actuators B*, 107:291–295, 2005.

[166] M. Sára and U.B. Sleytr. Biotechnology and Biomimetic with crystalline bacterial cell surface layers (S-layers). *Micron*, 27:141–156, 1996.

[167] H.G. Schild. Poly(N-isopropylacrylamide): experiment, theory and applications. *Prog. Polym. Sci*, 17:163–249, 1992.

[168] M. D. Schlensog, T. M. A. Gronewold, M. Teves, M. Famulok, and E. Quandt. A Love-wave biosensor using nucleic acids as ligands. *Sensors and Actuators B*, 101:308–315, 2004.

[169] R. R. Seigel, P. Harder, R. Dahint, M. Grunze, F. Josse, M. Mrksich, and G. M. Whitesides. On-line detection of nonspecific protein adsorption at artificial surfaces. *Anal. Chem.*, 69:3321–3328, 1997.

[170] A. Sharma and K. R. Rogers. Biosensors. *Meas. Sci. Technol.*, 5:461–472, 1994.

[171] Y.-T. Shen, C.-L. Huang, R. Chen, and L. Wu. A novel SH-SAW sensor system. *Sensors and Actuators B*, 107:283–290, 2005.

[172] M. Shima, A. Terakawa, M. Isomura, M. Tanaka, S. Kiyama, and S. Tsuda. Effects of high hydrogen dilution at low temperature on the film properties of hydrogenated amorphous silicon germanium. *Appl. Phys. Lett.*, 71(1):84–86, 1997.

[173] M. Shinn and W. M. Robertson. Surface plasmon-like sensor based on surface electromagnetic waves in a photonic band-gap material. *Sensors and Actuators B*, 105:360–364, 2005.

[174] P. M. Smith. Dyadic Green's functions for multi-layer SAW substrates. *IEEE Trans. Ultrason., Ferroelect., Freq. Contr.*, 48(1):171–179, 2001.

[175] W. R. Smith, H. M. Gerard, J. H. Collins, T. M. Reeder, and H. J. Shaw. Design of surface wave delay lines with interdigital transducers. *IEEE Trans. Microwave Theory Tech.*, 17(11):865–873, 1969.

[176] W. R. Smith, H. M. Gerard, and W. R. Jones. Analysis and design of dispersive interdigital surface–wave transducers. *IEEE Trans. Microwave Theory Tech.*, 20(7):458–471, 1972.

[177] W. R. Smith and W. F. Pedler. Fundamental- and harmonic-frequency circuit-model analysis of interdigital transducers with arbitrary metallization ratios and polarity sequences. *IEEE Trans. Microwave Theory Tech.*, 23(11):853–864, 1975.

[178] E. Stenberg, B. Persson, H. Roos, and C. Urbaniczky. Quantitative determination of surface concentration of protein with surface plasmon resonance using radiolabeled proteins. *Journal of colloid and interface science*, 143:513–526, 1991.

[179] A. C. Stevenson, E. Gizeli, N. J. Goddard, and C. R. Lowe. Acoustic Love plate sensors: a theoretical model for the optimization of the surface mass sensitivity. *Sensors and Actuators B*, 13–14:635–637, 1993.

[180] P. Stöcker, B. Menges, U. Langbein, and S. Mittler. Multimode waveguide mode surface plasmon coupling: a sensitivity and device realizability study. *Sensors and Actuators A*, 116:224–231, 2004.

[181] L. Strong and G. M. Whitesides. Structures of self-assembled monolayer films of organosulfur compounds adsorbed on gold single crystals: electron diffraction studies. *Langmuir*, 4:546–558, 1988.

[182] X. Sun, S. Shiokawa, and Y. Matsui. Interactions of surface plasmons with surface acoustic waves and the study of the properties of Ag films. *J. Appl. Phys.*, 69(1):362–366, 1991.

[183] J. D. Swalen, J. G. Gordon II, M. R. Philpott, A. Brillante, I. Pockrand, and R. Santo. Plasmon surface polariton dispersion by direct optical observation. *Am. J. Phys.*, 48(8):669–672, 1980.

[184] O. Tabata, K. Kawahata, S. Sugiyama, and I. Igarashi. Mechanical property measurements of thin films using load-deflection of composite rectangular membranes. *Sensors and Actuators*, 20:135–141, 1989.

[185] O. Tamarin, C. Déjous, D. Rebière, J. Pistré, S. Comeau, D. Moynet, and J. Bezian. Study of acoustic Love wave devices for real time bacteriophage detection. *Sensors and Actuators B*, 91:275–284, 2003.

[186] F. Teston, G. Feuillard, L. Tessier, and M. Lethiecq. Mass sensitivity of acoustic plate mode in liquids. *IEEE Trans. Ultrason., Ferroelect., Freq. Contr.*, 45(5):1266–1272, 1998.

[187] D. V. Tsu, G. Lucovsky, and B. N. Davidson. Effects of the nearest neighbors and the alloy matrix on $SiO_r : H$ $(0 < r < 2)$ alloy system. *Phys. Rev. B*, 40(3):1795–1805, 1989.

[188] M. Urbakh and L. Daikhin. Roughness effect on the frequency of a quartz-crystal resonator in contact with a liquid. *Phys. Rev. B*, 49(7):4866–4870, 1994.

[189] K. Van De Rostyne, C. Glorieux, W. Gao, V. Gusev, M. Nesladek, W. Lauriks, and J. Thoen. Investigation of elastic properties of CVD-diamond films using the lowest order flexural leaky Lamb wave. *Phys. Stat. Sol. (a)*, 172:105–111, 1999.

[190] W. M. van Spengen, R. Puers, R. Mertens, and I. De Wolf. Characterization and failure analysis of MEMS: high resolution optical investigation of small out-of-plane movements and fast vibrations. In *Microsystem Technologies*, volume 10, pages 89–96. Springer-Verlag, 2004.

[191] M. J. Vellekoop, B. Jakoby, and J. Bastemeijer. A Love-wave ice detector. In *IEEE Ultrason. Symp.*, pages 453–456, 1999.

[192] M.J. Vellekoop, G.W. Lubking, and A. Venema. Acoustic-wave based monolithic microsensors. In *IEEE Ultrason. Symp.*, pages 565–574, 1994.

[193] P. Ventura, J. M. Hodé, and M. Solal. A new efficient combined FEM and periodic Green's function formalism for the analysis of periodic SAW structures. In *IEEE Ultrason. Symp.*, pages 263–268, 1995.

[194] P. Ventura, J. M. Hodé, M. Solal, J. Desbois, and J. Ribbe. Numerical methods for SAW propagation. In *IEEE Ultrason. Symp.*, pages 175–186, 1998.

[195] J. Vöröss, J. J. Ramsden, G. Csúcs, I. Szendrö, S. M. De Paul, M. Textor, and N. D. Spencer. Optical grating coupler biosensors. *Biomaterials*, 23:3699–3710, 2002.

[196] J. L. Vossen and W. Kern. *Thin film processes*. Academic Press, New-York, 1978.

[197] Z. Wang, J. D. N. Cheeke, and C. K. Jen. Sensitivity analysis for Love mode acoustic gravimetric sensors. *Appl. Phys. Lett.*, 64:2940–2942, 1994.

[198] M. S. Weinberg, B. T. Cunningham, and C. W. Clapp. Modeling flexural plate wave devices. *J. Microelectromech. Syst.*, 9(3):370–379, 2000.

[199] M. Weygand, M. Schalke, P.B. Howes, K. Kjaer, J. Friedmann, B. Wetzer, D. Pum, U.B. Sleytr, and M. Lösche. Coupling of protein sheet crystals (S-layers) to phospholipid monolayers. *J. Mater. Chem.*, 10:141–148, 2000.

[200] M. Weygand, B. Wetzer, D. Pum, U.B. Sleytr, N. Cuvillier, K. Kjaer, P.B. Howes, and M. Lösche. Bacterial S-layer protein coupling to lipids: X-ray reflectivity and grazing incidence diffraction studies. *Biophys. J.*, 76:458–468, 1999.

[201] R. M. White. Acoustic sensors for physical, chemical and biochemical applications. In *IEEE Frequency Contr. Symp.*, pages 587–594, 1998.

[202] R. M. White and F. W. Voltmer. Direct piezoelectric coupling to surface elastic waves. *App. Phys. Lett.*, 7:314–316, 1965.

[203] M. D. Whitfield, B. Audic, C. M. Flannery, L. P. Kehoe, G. M. Crean, C. Johnson, P. R. Chalker, and R. B. Jackman. Polycrystalline diamond films for acoustic wave devices. *Diam. Relat. Mat.*, 7:533–539, 1998.

[204] A. Witvrouw and F. Spaepen. Viscosity and elastic constants of amorphous Si and Ge. *J. Appl. Phys.*, 74(12):7154–7161, 1993.

[205] Y. Wu, M. de Labachelerie, and F. Bastien. Investigations on excitation and detection methods for Lamb wave sensors. *Sensors and Actuators A*, 100(2–3):214–222, 2002.

[206] J. Z. Xie, S. P. Murarka, X. S. Guo, and W. A. Lanford. Stability of hydrogen in silicon nitride films deposited by low-pressure and plasma enhanced chemical vapor deposition techniques. *J. Vac. Sci. Technol. B*, 7(2):150–152, 1989.

[207] I. Yonenaga and K. Sumino. Mechanical strength of GeSi alloy. *J. Appl. Phys.*, 80(6):3244–3247, 1996.

[208] S. Y. Yurish, N. V. Kirianaki, and I. L. Myshkin. World sensors and MEMS markets: analysis and trends. *Sensors and Transducers Magazine*, 62(12):456–461, 2005.

[209] C. Zhang, J. J. Caron, and J. F. Vetelino. The Bleustein-Gulyaev wave mode in potassium niobate for liquid sensing applications. In *IEEE Ultrason. Symp.*, pages 263–268, 2000.

[210] C. Zhang, S. Schranz, R. Lucklum, and P. Hauptmann. Mass effects of quartz resonant sensors with different surface microstructures in liquids. *IEEE Trans. Ultrason., Ferroelect., Freq. Contr.*, 45(5):1204–1209, 1998.

[211] H. Zhang and E. S. Kim. Micromachined acoustic resonant mass sensor. *J. Microelectromech. Syst.*, 14(4):699–706, 2005.

[212] J. Zhang and S. O'Shea. Tuning forks as micromechanical mass sensitive sensors for bio- or liquid detection. *Sensors and Actuators B*, 94:65–72, 2003.

[213] V. Y. Zhang, J.-E. Lefebvre, C. Bruneel, and T. Gryba. A unified formalism using effective surface permittivity to study acoustic waves in various anisotropic and piezoelectric multilayers. *IEEE Trans. Ultrason., Ferroelect., Freq. Contr.*, 48(5):1449–1461, 2001.

[214] V. Y. Zhang, J. E. Lefebvre, and T. Gryba. Two true surface acoustic waves and other acoustic modes in (110) plane of $Li_2B_4O_7$ substrate. *J. Appl. Phys.*, 86(6):3361–3370, 1999.

[215] C. Zimmermann, P. Mazein, D. Rebière, C. Déjous, F. Josse, and J. Pistré. A theoretical study of Love wave sensors mass loading and viscoelastic sensitivity in gas and liquid environments. In *IEEE Ultrason. Symp.*, pages 813–816, 2004.

Appendix A

Acoustic waves in solids

A.1 Introduction

This appendix presents the propagation of acoustic waves in solids, it is the theoretical support for the modeling [1]. Waves propagation is ruled by Christoffel's equation that is derived from Newton's dynamic equation and from the constitutive relations for solids. The propagation of *time-harmonic plane waves* is investigated since their comportment is well suited to waves that can be generated in solids. These waves present three orthogonal displacement components, also called polarizations. Each polarization has its own phase velocity. Polarizations are largely influenced by the materials characteristics. For that reasons, propagation in isotropic, anisotropic and piezoelectric solids will be detailed and also attenuation effect in viscous solids. An intuitive graphic representation of the inverse of velocity as a function of direction of propagation is given. This representation will help further comprehension of the mechanisms involved in the propagation of the waves.

In bounded media, reflection and refraction occur at boundaries. Snell's law rules the relation between incident and scattered waves. The link between the waves is given by introducing the definition of the acoustic impedance. The impedance gives a direct relation between stresses and local particle velocity for a given direction of propagation of the waves. The definition of that impedance is a starting point for the modeling and the investigation of resonant structures. Entrapment of

[1] The sources for this appendix are found in [5], [146], and [160]

the waves in a multi-reflective structure such as the Love mode structure form an acoustic waveguide supporting resonant fields. Finally, power flow of the waves is considered while the well-known Poynting's Theorem will found a direct equivalent in acoustic.

Although any wave can propagate in a media, propagation of time-harmonic plane waves makes the study easier. The mechanical fields that are generated and that propagate under harmonic solicitations at angular frequency ω with wavevector $\vec{k}$ are described as functions of the position $\vec{r}$ and the time t by functions proportional to $e^{i(\omega t - \vec{k}\cdot\vec{r})}$, describing well-known time-harmonic plane waves. The angular frequency ω and the wavenumbers k_i $(i = 1, 2, 3)$ are related by a function called *relation of dispersion*.

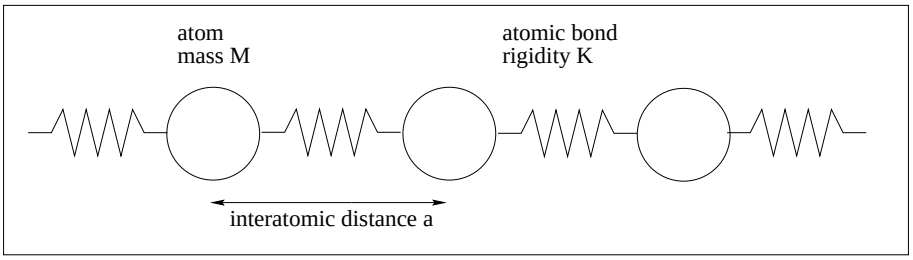


Fig. A.1 – Linear model of solid : atoms with mass M linked by elastic bonds of constant K

A preliminary note before entering the subject is necessary. A simple model of solid is a linear arrangement of atoms with mass M, separated by a distance a and connected together by elastic bonds of rigidity constant K (see Figure A.1). The relation of dispersion for this model is

$$\omega = 2\sqrt{\frac{K}{M}} \left|\sin\frac{ak}{2}\right| \tag{A.1}$$

and it presents for considerably low values of the wavenumber ($ka << 1$) a linear relation

$$\omega \cong \sqrt{\frac{K}{M}}\, ak = Vk$$

with V the propagation velocity of low frequency acoustic waves. Since

$|\sin ka/2| < 1$, a cut-off frequency exists:

$$f_c = \frac{V}{\pi a}.$$

As the phase velocity V for low frequency acoustic waves lies between 1 000 m/s and 20 000 m/s and inter-atomic distances (a) are of a few Å, the cut-off frequency is in the range of the terahertz. Discussions in this report will be limited to frequencies in the range of 1 MHz to 1 GHz, in the linear approximation of the dispersion curve (A.1) where the wavelength $\lambda = V/f$ is longer than inter-atomic distances. The conclusion of this preliminary note is that solids will always be considered as a *continuous media* for waves propagation; quantum considerations are irrelevant and therefore not considered.

A.2 Propagation of time-harmonic plane waves

A.2.1 Elastic fields in solids

Description of acoustic waves requires description of the linear behavior of elastic solids. The action of a force on a solid body of density ρ induces a displacement field $\vec{u}$; this field is accompanied by a strain field $\mathbf{S}$ defined by

$$\mathbf{S} = \frac{1}{2}\left(\nabla\vec{u} + \widetilde{\nabla\vec{u}}\right) \equiv \nabla_s\vec{u} \tag{A.2}$$

where the tilde ($\sim$) denotes transposition and subscript s is an abbreviated indication of the symmetry in the displacement gradient. The mechanical stress is defined as a vector equals to the force applied per unit surface. For an arbitrarily oriented surface, the mechanical stress is expressed by a symmetric stress matrix $\mathbf{T}$. In an acoustically vibrating solid, Newton's law rules the displacement-stress relation:

$$\boxed{\nabla \cdot \mathbf{T} = \rho\frac{\partial^2\vec{u}}{\partial t^2} - \vec{F}} \tag{A.3}$$

and this equation is called the *translational equation of motion* for a vibrating medium. The vector $\vec{F}$ represents the body forces, for instance the gravitational field.

The constitutive equation of the solid is determined by *Hooke's law* for elastic solids. This law states the strain-displacement relation:

$$\boxed{\mathbf{T} = \mathbf{c} : \mathbf{S} = \mathbf{c} : \nabla_s\vec{u}} \tag{A.4}$$

where **c** is the elastic stiffness constants matrix. The matrix **c** is a fourth rank tensor with 81 components, symmetries of **S** and **T** reduce to 36 the number of independent constants. The double scalar (or double dot) product between a fourth rank and a second rank tensor is defined by the summation over pairs of subscripts in Eq. (A.4). Reduction in number of independent coefficients allows to write the equations with an abbreviated subscript notation by replacing pairs of subscript by single subscript using the convention reported in Table A.1. For instance, Hooke's law in subscript notation becomes $T_i = c_{ij}S_j$ with $i, j = 1, 2, \cdots, 6$ instead of $T_{ij} = c_{ijkl}S_{kl}$ with $i, j, k, l = 1, 2, \cdots, 6$.

$(11) \leftrightarrow 1$	$(22) \leftrightarrow 2$	$(33) \leftrightarrow 3$
$(23) = (32) \leftrightarrow 4$	$(13) = (31) \leftrightarrow 5$	$(12) = (21) \leftrightarrow 6$

Table A.1 – Voigt notation of subscripts.

A.2.2 Christoffel equation

The wave equation is obtained by substitution of Eq. (A.4) in Eq. (A.3) and the assumption of no source-induced forces ($\vec{F} = 0$),

$$\nabla \cdot \mathbf{c} : \nabla_s \vec{u} = \rho \frac{\partial^2 \vec{u}}{\partial t^2}. \tag{A.5}$$

The propagation of uniform plane waves along the direction

$$\boxed{\vec{l} = l_x \vec{x} + l_y \vec{y} + l_z \vec{z}} \tag{A.6}$$

is now considered. The field is assumed to be a time-harmonic plane wave proportional to $e^{i(\omega t - k\vec{l}\cdot\vec{r})}$. The representation of time-harmonic plane waves allows to replace directly time and space derivative as following (the field is represented by the $\bullet$):

$$\frac{\partial \bullet}{\partial t} = i\omega \bullet \tag{A.7}$$

$$\frac{\partial \bullet}{\partial x_i} = -ik_i \bullet \tag{A.8}$$

with $i = 1, 2, 3$ that relates respectively to direction x, y,and z. The assumption of propagation of that kind of waves let the wave equation (A.5) to be written as here after, in Voigt notation:

$$\boxed{k^2(l_{iK}c_{KL}l_{Lj})u_j = k^2\Gamma_{ij}u_j = \rho\omega^2 u_i} \tag{A.9}$$

with

$$l_{iK} = \begin{bmatrix} l_x & 0 & 0 & 0 & l_z & l_y \\ 0 & l_y & 0 & l_z & 0 & l_x \\ 0 & 0 & l_z & l_y & l_x & 0 \end{bmatrix} = \widetilde{l}_{Lj}. \tag{A.10}$$

Equation (A.9) is called the *Christoffel equation* and the second rank tensor $\mathbf{\Gamma}$ is called the *Christoffel matrix*. The Christoffel equation is valid for both isotropic and anisotropic solids; it allows determination of polarizations and velocities. Effectively, the Christoffel equation is modified by introducing the phase velocity definition

$$V = \lambda f = \omega / k \tag{A.11}$$

and assuming no variation of c and ρ with time, this is an eigenvalue problem:

$$\boxed{\Gamma_{ij} u_j = \rho V^2 u_i.} \tag{A.12}$$

Phase velocities V and polarizations $\vec{u}$ of plane waves propagating along direction $\vec{l}$ in a solid of elastic stiffness $\mathbf{c}$ *are respectively the eigenvalues and the eigenvectors of the second rank tensor $\Gamma_{ij} = l_{iK} c_{KL} l_{Lj}$.*

A.2.3 Isotropic solids

For isotropic solids, the stiffness matrix presents the following shape:

$$\mathbf{c} = \begin{bmatrix} c_{11} & c_{12} & c_{12} & 0 & 0 & 0 \\ c_{12} & c_{11} & c_{12} & 0 & 0 & 0 \\ c_{12} & c_{12} & c_{11} & 0 & 0 & 0 \\ 0 & 0 & 0 & c_{44} & 0 & 0 \\ 0 & 0 & 0 & 0 & c_{44} & 0 \\ 0 & 0 & 0 & 0 & 0 & c_{44} \end{bmatrix}. \tag{A.13}$$

Furthermore, stiffness constants are submitted to the invariance rotation condition described as

$$c_{12} = c_{11} - 2c_{44}. \tag{A.14}$$

From this latter condition, only two independent constants are necessary to describe the elastic comportment of isotropic solids, namely the Lamé's constants $\mu \equiv c_{44}$ and $\lambda \equiv c_{12}$. The two Lamé's constants are linked to the Young's modulus E and the Poisson ratio ν by the relations:

$$\lambda = \frac{\nu E}{(1+\nu)(1-2\nu)}, \tag{A.15}$$

$$\mu = \frac{E}{2(1+\nu)}. \tag{A.16}$$

The relation between Young's modulus E, Poisson's ratio ν, Lamé's constants λ and μ are summarized in Table A.2.

	E, ν	E, μ	λ, μ	c_{11}, c_{12}
λ	$\frac{E\nu}{(1+\nu)(1-2\nu)}$	$\frac{\mu(E-2\mu)}{3\mu-E}$	λ	c_{12}
μ	$\frac{E}{2(1+\nu)}$	μ	μ	$\frac{c_{11}-c_{12}}{2} = c_{44}$
E	E	E	$\frac{\mu(3\lambda+2\mu)}{\lambda+\mu}$	$c_{11} - 2\frac{c_{12}^2}{c_{11}+c_{12}}$
ν	ν	$\frac{E-2\mu}{2\mu}$	$\frac{\lambda}{2(\lambda+\mu)}$	$\frac{c_{12}}{c_{11}+c_{12}}$

Table A.2 – Relation between elastic constants for isotropic solid.

Without loss of generality, the specific case of $\vec{l} = \vec{x}$ is considered. The Christoffel matrix $\mathbf{\Gamma}$ with stiffness matrix (A.13) is a purely diagonal matrix, the eigenvalue problem is reduced to solutions of:

$$k^2 \begin{bmatrix} c_{11} & 0 & 0 \\ 0 & c_{44} & 0 \\ 0 & 0 & c_{44} \end{bmatrix} \begin{bmatrix} u_x \\ u_y \\ u_z \end{bmatrix} = \rho\omega^2 \begin{bmatrix} u_x \\ u_y \\ u_z \end{bmatrix}. \tag{A.17}$$

Equation (A.17) is related to a set of three independent equations with two independent eigenvalues. The first solution consists in a x-polarized x-propagating wave that satisfies the dispersion equation

$$\boxed{k^2 c_{11} = \rho\omega^2}$$

This is the description of a longitudinal wave

$$\vec{u_l} = \vec{x}\ u_l^\circ e^{i(\omega t - kx)} \tag{A.18}$$

that has a phase velocity

$$\boxed{V_l = \sqrt{\frac{c_{11}}{\rho}}} \tag{A.19}$$

The second solution consists in two degenerated waves: a y-polarized x-propagating wave and a z-polarized x-propagating wave. These waves satisfy the dispersion equation

$$\boxed{k^2 c_{44} = \rho\omega^2}$$

They finally consist in two pure shear modes

$$\vec{u}_s = \vec{y}\ u_s^\circ e^{i(\omega t - kx)} \tag{A.20}$$

$$\vec{u}_{s'} = \vec{z}\ u_{s'}^\circ e^{i(\omega t - kx)} \tag{A.21}$$

that have a single phase velocity

$$\boxed{V_s = \sqrt{\frac{c_{44}}{\rho}}} \tag{A.22}$$

A.2.4 Anisotropic solids

The propagation in anisotropic solids, for instance in crystals, still satisfy Christoffel's equation. The stiffness matrix has a different number of independent constants, depending upon the symmetries present in the crystal. The stiffness matrix is a symmetric 6 by 6 matrix with a maximum of 21 independent constants. This corresponds to the triclinic classes which does not present any further symmetries. Solutions of Christoffel equation need more often to be solved numerically for anisotropic solids and receive simple analytical solutions only for a certain number of directions that depends of the symmetries. Anyway, plane waves propagation can still be considered to be along direction $\vec{l} = \vec{x}$ at the condition that stiffness matrix would be aligned to this direction by a rotation and solving the Christoffel equation with this new stiffness matrix.

In general, for a given direction, there are three phase velocities. Due to the symmetry of stiffness matrix $\mathbf{c}$, the Christoffel matrix is also symmetric ($\Gamma_{ij} = \Gamma_{ji}$) and its eigenvectors and eigenvalues are all real numbers. In addition, eigenvectors are orthogonals. It can be also demonstrated, by energetic considerations, that eigenvalues are positives. Consequently, *in solid media, three plane waves with orthogonal polarization and different phase velocities propagate along the same direction*.
Generally, $\vec{u}$ is not aligned or perpendicular to $\vec{l}$. The wave with polarization close to $\vec{l}$ is called *quasilongitudinal* and the others are called *quasishear*. Those latter propagate slower than the quasilongitudinal wave.

A.2.5 Piezoelectric solids

In piezoelectric solids, electrical and mechanical values are related. The relation implies a coupling between acoustic waves and electromagnetic waves. Finding solutions that simultaneously satisfy Newton's mechanical equation and Maxwell's electric equations will theoretically solve the propagation. These solutions have a coupled-wave behavior: acoustic waves propagating at phase velocity V are accompanied by an electric field $\vec{E}$, and electromagnetic waves propagating at speed of light (that is almost 10^5 times faster than V) are accompanied by a mechanical deformation.

The electric field created by the acoustic waves has the velocity V, the magnetic field can be neglected. From Maxwell's equation:

$$\text{curl } \vec{E} = -\frac{\partial \vec{B}}{\partial t} \cong 0 \tag{A.23}$$

and so the electric field is deduced to be the gradient of a scalar potential like in electrostatic:

$$\boxed{\vec{E} = -\nabla \cdot \Phi} \tag{A.24}$$

For the electromagnetic field, the high speed reduces the accompanying acoustic field, so that the elastic energy can be neglected in comparison to the electromagnetic energy. The treatment of the electromagnetic waves and coupled acoustic waves can be done separately. This hypothesis is known as the *quasistatic approximation*, it is a useful hypothesis since it reduces the complexity of the analysis for piezoelectric media.

The constitutive equations for piezoelectric solids incorporate the effect of the coupling between electric field and acoustic field:

$$\vec{D} = \varepsilon^S \cdot \vec{E} + \mathbf{e} : \mathbf{S} \tag{A.25}$$

$$\mathbf{T} = -\widetilde{\mathbf{e}} \cdot \vec{E} + \mathbf{c}^E : \mathbf{S}. \tag{A.26}$$

where $\vec{D}$ is the electric displacement, ε^S the electric dielectric constants at constant mechanical strain, $\mathbf{e}$ the *piezoelectric strain constants* and $\mathbf{c}^E$ the elastic stiffness at constant electric field. The piezoelectric constants matrix is a third rank tensor that can be reduced to a 3 by 6 matrix with subscript convention over the last two subscripts (see Table A.1). Introducing the quasistatic approximation in Eq. (A.26), the

translational equation of motion (A.3) comes out:

$$\nabla \cdot \mathbf{c}^E : \nabla_s \vec{u} = \rho \frac{\partial^2 \vec{u}}{\partial t^2} - \nabla \cdot (\widetilde{\mathbf{e}} \cdot \nabla \Phi)\,. \tag{A.27}$$

In addition, from the first constitutive equation for piezoelectric solids (A.25) and Poisson's equation for insulating solids ($\nabla \cdot \vec{D} = 0$), we have:

$$\nabla \cdot \left(\varepsilon^S \cdot \nabla \Phi\right) = \nabla \mathbf{e} : \nabla_s \vec{u}. \tag{A.28}$$

We now consider propagation along direction $\vec{l}$ of uniform plane waves as in page 250, Eqs. (A.27) and (A.28) can then be written with abbreviated subscript notation as:

$$k^2 (l_{iK} c^E_{KL} l_{Lj}) u_j = \rho \omega^2 u_i - k^2 (l_{iK} e_{Kj} l_j) \Phi, \tag{A.29}$$

$$(l_i \varepsilon^S_{ij} l_j) \Phi = (l_i e_{iL} l_{Lj}) u_j. \tag{A.30}$$

The last equation is interesting since the term that multiplies the electric potential is a scalar, this relation gives the potential in term of the particle displacement:

$$\Phi = \frac{l_i e_{iL} l_{Lj}}{l_i \varepsilon^S_{ij} l_j} u_j.$$

Christoffel equation for piezoelectric solids is directly found by eliminating the electric potential between Eqs. (A.29) and (A.30), the final result looks like that:

$$\boxed{\left(l_{iK} \left\{ c^E_{KL} + \frac{[e_{Kj} l_j][l_i e_{iL}]}{l_i \varepsilon^S_{ij} l_j} \right\} l_{Lj} \right) \; u_j = \rho V^2 \; u_i} \tag{A.31}$$

One can clearly see from the Christoffel equation for piezoelectric solids a resemblance with the non piezoelectric case except the presence of an additional term in the Christoffel matrix. The elastic stiffness has been replaced by the expression enclosed in the curly brackets,

$$c^E_{KL} + \frac{[e_{Kj} l_j][l_i e_{iL}]}{l_i \varepsilon^S_{ij} l_j}$$

which is often called a *piezoelectrically stiffened elastic constant*. In the same way, the Christoffel matrix $\mathbf{\Gamma}$ is replaced by a *stiffened Christoffel matrix* $\overline{\mathbf{\Gamma}}$ defined by

$$\boxed{\overline{\Gamma}_{ij} = \Gamma_{ij} + l_{iK} \left(\frac{[e_{Kj} l_j][l_i e_{iL}]}{l_i \varepsilon^S_{ij} l_j} \right) l_{Lj}} \tag{A.32}$$

and that enters the *stiffened Christoffel equation*:

$$\boxed{\overline{\Gamma}_{ij}u_j = \rho V^2 u_i} \tag{A.33}$$

A.2.6 Attenuation

The equation of motion has solutions that would never decrease with propagation distances. This description is valid under the restricting case of "ideal" materials. Materials with weak damping are compared to this model but most of the real materials present a damping of the wave, *i.e. attenuation*. Damping is a complicated function of temperature, mode of vibration and frequency. At room temperature, the constitutive equations can be modified to introduce acoustic losses. The model is based on Maxwell's mechanical model of damping and relates to viscoelastic comportment of material. As the damping results from deformations rather than rigid displacements, the model is based on the time derivatives of the strains rather than the time derivatives of the particle displacements. The model states the following equation:

$$\boxed{\mathbf{T} = \mathbf{c} : \mathbf{S} + \eta : \frac{\partial \mathbf{S}}{\partial t}} \tag{A.34}$$

where η is the viscosity matrix. This matrix is a fourth rank tensor as the stiffness matrix $\mathbf{c}$.

We will now consider effect of damping on the propagation of plane waves in isotropic materials. The motional equation with introduction of Eq. (A.34) accepts solutions of type (for the $y-$polarized $x-$ propagating wave):

$$\vec{u} = e^{-\alpha x} e^{i(\omega t - kx)}\ \vec{y} \tag{A.35}$$

with a damping coefficient α that reduces the field amplitude along distance of propagation and represent viscous loss and energy absorption in the medium. The ratio of field amplitudes between x_1 and $x_2 > x_1$ is $e^{-\alpha(x_1 - x_2)}$. The exact expression of attenuation factor α is obtained by replacing the assumed solution (A.35) in the equation of motion. The obtained solution has often a complex shape that can be reduced to a simpler form by stating the *low-loss approximation* for shear waves in isotropic media:

$$\boxed{\left(\frac{\omega \eta_{44}}{c_{44}}\right) \ll 1} \tag{A.36}$$

This statement is valid for most solids with a viscosity coefficient sufficiently small even at frequencies as high as 1 GHz. The attenuation per wavelength $\alpha\lambda = 2\pi\alpha/k$ is function of the *acoustic quality factor* (or *acoustic* Q)

$$Q = \frac{c_{44}}{\omega\eta_{44}}.$$

The attenuation is known to be proportional to the square of the frequency. At high frequencies, high quality materials have to be used to avoid large acoustic damping.

A.2.7 Slowness surfaces

For a given angular frequency ω, the wavenumber k is a function of the direction $\vec{l}$ called the *wave vector surface* in the $k-$space. This surface is the *slowness surface* because of the relation $k/\omega = 1/V$. Solutions to the Christoffel equation usually require help of computational methods except for some cases (propagation along symmetry axes, isotropic media, ...). We illustrate here after the slowness surface for some materials including amorphous silicon dioxide (SiO_2 , isotropic), quartz ($\alpha - SiO_2$) and lithium niobate ($LiNbO_3$). Selection of these materials is due to their illustrative example but, and also, because they are widely present in acoustic sensors.

Amorphous silicon dioxide is an isotropic material. As considered before, this kind of material supports pure modes: a longitudinal wave with phase velocity V_l and two shear waves with phase velocity V_s. Reporting the materials data from Table A.3 for silicon dioxide, the slowness surfaces in the $k-$space are represented in Figure A.2, for a plane cut the slowness surface takes the name of *slowness curve*. Figure A.2 shows two curves, due to the degeneration of the shear waves. The outer curve is the slowest velocity and is related to the shear waves. The inner surface is the longitudinal wave, faster than the two others. Numbering of the k direction is purely arbitrary and any direction can be chosen. In the whole $k-$space, slowness surfaces are spheres; whatever the cut and the direction of propagation, slownesses remain the same.

Anisotropic and piezoelectric cases are showed simultaneously here after. The slowness curves are strongly dependent on the chosen direction of propagation. We consider first lithium niobate, which belongs to

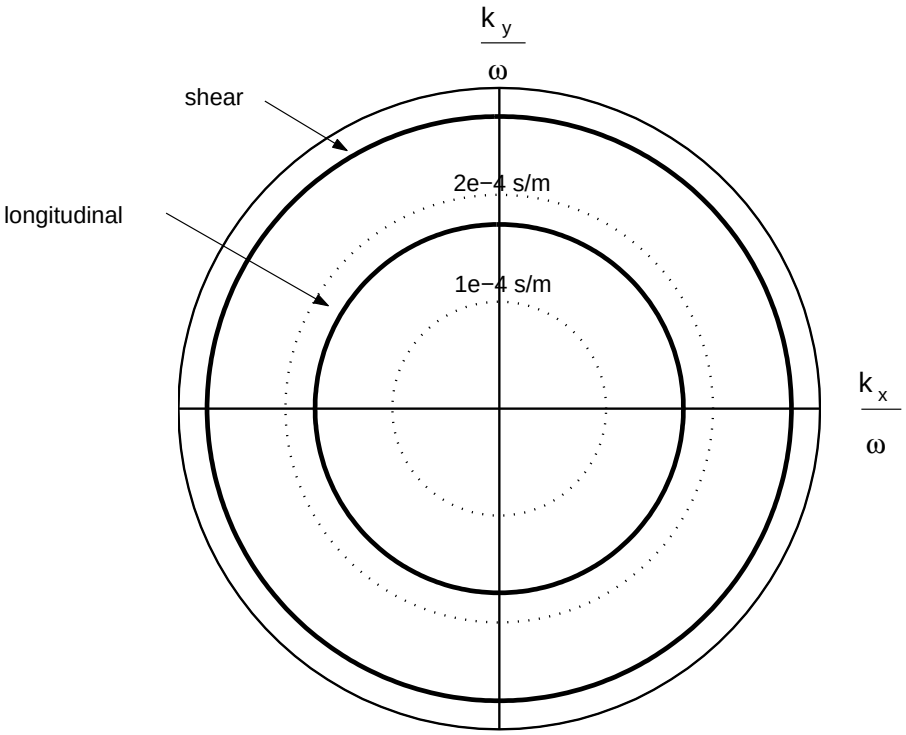


Fig. A.2 – Slowness curves for silicon dioxide.

Material	**Class**	**Density**	c_{11}	c_{12}	c_{13}	c_{33}	c_{44}	c_{14}
Aluminum	$m\bar{3}m$	2702	10.73	6.08			2.83	
Gold	$m\bar{3}m$	19300	19.25	16.30			4.24	
Silica	isotropic	2203	7.85	1.61			3.12	
Lithium niobate	$3m$	4700	20.3	5.3	7.5	24.5	6.0	0.9
Lithium tantalate	$3m$	7450	23.3	4.7	8.0	27.5	9.4	-1.1
Quartz α	32	2648	8.67	0.70	1.19	10.72	5.79	-1.79

Table A.3 – Density (in $\mathrm{kg} \cdot \mathrm{m}^{-3}$) and elastic constants (in $10^{10}\ \mathrm{N} \cdot \mathrm{m}^{-2}$) [4].

Material	**Class**	e_{11}	e_{14}	e_{15}	e_{22}	e_{31}	e_{33}	ε_{11}^S	ε_{33}^S
Lithium niobate	$3m$	0	0	3.7	2.5	0.2	1.3	38.9	25.7
Lithium tantalate	$3m$	0	0	2.6	1.6	$\simeq 0$	1.9	36.3	38.1
Quartz α	32	0.171	-0.0406	0	0	0	0	3.92	4.10

Table A.4 – (Piezo)electric constants (in $\mathrm{C \cdot m^{-2}}$) and dielectric constants (in 10^{-11} $\mathrm{F \cdot m^{-1}}$) of materials [4].

the $3m$ crystallographic class. Slowness curves in the plane YZ are shown in Figure A.3. They are drawn with (solid line) and without (dashed line) taking piezoelectricity of this compound into account. The material data for simulations are given in Tables A.3 and A.4. From Figure A.3,

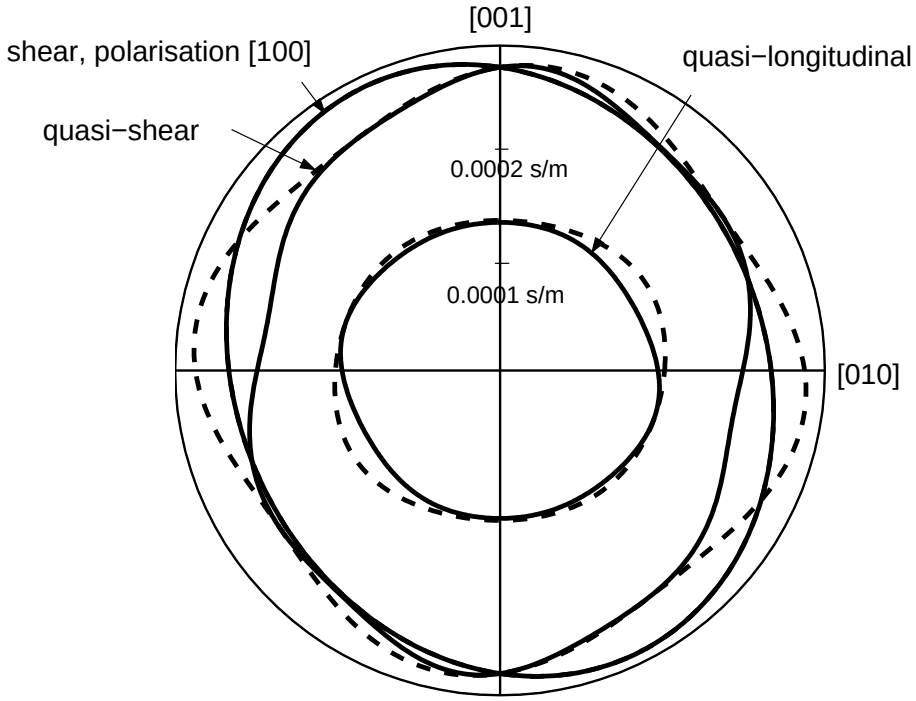


Fig. A.3 – Slowness curves for YZ-plane in $LiNbO_3$ with (solid lines) and without (dashed lines) taking account of piezoelectricity.

three observations can be withdrawn:

- There are three curves that present some symmetry around the central point but these curves are no more circles like in the isotropic case;
- The dashed and the solid curves for the pure shear wave are superimposed in the Figure. This wave has polarization along direction X ([100]).
- Along some directions, slowness for transversal waves crosses but those directions change when considering or not piezoelectricity.

One can deduce from those observations that, for a given direction and a specific polarization, an electrical field either accompanies or not the acoustic wave and this modify the phase velocity of the wave. This effect is quantified by the following relation taken from the expression (A.31):

$$c_{KL}^{E}\left(1+\frac{[e_{Kj}l_j][l_ie_{iL}]}{(c_{KL}^{E})(l_i\varepsilon_{ij}^{S}l_j)}\right) \tag{A.37}$$

where the fractional change in the elastic constant is given by coefficients called *electromechanical coupling constants* K_{KL}:

$$\boxed{(K_{KL}(\vec{l}))^2=\frac{[e_{Kj}l_j][l_ie_{iL}]}{(c_{KL}^{E})(l_i\varepsilon_{ij}^{S}l_j)}} \tag{A.38}$$

The very expression of K_{KL} depends on the considered wave and direction. The constant determines the maximum variation in phase velocity by Ingebritsen's relation:

$$\boxed{\frac{\Delta V}{V}\simeq\frac{K^2}{2}} \tag{A.39}$$

The $\alpha-SiO_2$ belongs to crystallographic class 32. The slowness curves are presented for propagation of waves in the plane corresponding to the ST-cut. This cut contains the $\vec{X}$ axis and the normal is inclined of 47.5° with respect to the $\vec{Z}$ axis. Slowness curves are presented in Figure A.4, the coupling constants in $\alpha-SiO_2$ are very small so that only not piezoelectric slowness curves are presented in the Figure. The material data for simulations are given in Tables A.3 and A.4.

The two piezoelectric materials presented enter in sensors as transducing elements. A large value of the coupling constant indicates a strong effect between electric and acoustic fields. Electrodes plated to the surface of the material can do excitation of acoustic waves and the coupling constants are related to the conversion of electric energy to acoustic energy. Efficiency of the acoustic transducer is really dependent on this factor. We will discuss of the importance of coupling constants latter, when considering design of the transducer.

The dependence of the coupling constants with direction of propagation is used to launch preferentially one kind of wave instead of one another. For instance, in the case of lithium niobate: the coupling constant along direction $\vec{Y}+163°$ in the **YZ**−plane is null. Shear waves are

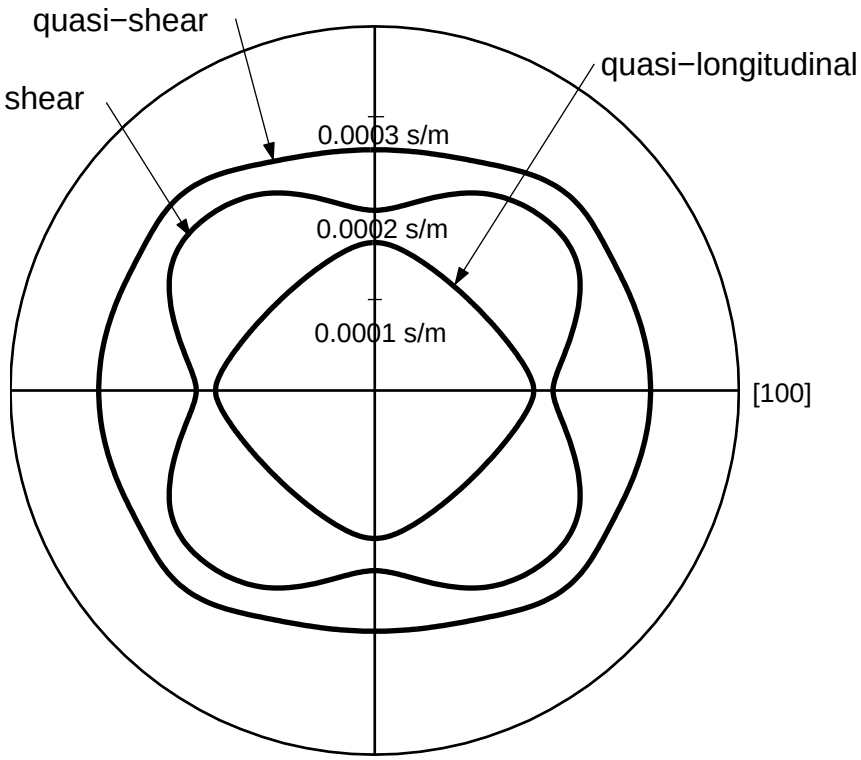


Fig. A.4 – Slowness curves for ST-cut $\alpha - SiO_2$ without taking account of piezoelectricity.

generated in lithium niobate crystal with cut $\vec{Y}+163°$ and faces covered with metallic electrodes. Although longitudinal waves are still allowed to propagate, electric sources can not induce their existence.

For the ST-cut $\alpha - SiO_2$, the coupling constants for both quasi-longitudinal and quasi-shear waves are null for direction orthogonal to the $\vec{X}$ axis and only of $K^2 = 0.11\%$ for the pure shear wave. That direction can be used to launch and propagate shear waves that have a polarization parallel to the cut plane, they are called *shear-horizontal waves* (or SH-waves). Anyway, it will be too restrictive to talk only about lithium niobate and quartz for generation of acoustic waves. Other materials are under investigation for that goal and receive much attention like berlinite ($AlPO_4$), gallium phosphate ($GaPO_4$), aluminum nitride (AlN), gallium arsenide (GaAs), ... In addition, the two materials showed here are also under investigations for finding new cuts [41]. These cuts depend obviously of the final application they want to receive.

A.3 Reflection and refraction

A.3.1 Snell's law

At boundaries, acoustic waves experience a change in propagation properties. They can propagate faster or slower, being partially reflected. We assume a plane boundary between two solids, with normal $\vec{n}$; displacements and traction forces have to be continuous across the boundary (quoted values are relative to the second medium):

$$\vec{u} = \vec{u}' \tag{A.40}$$

$$\mathbf{T} \cdot \vec{n} = \mathbf{T}' \cdot \vec{n} \tag{A.41}$$

and as plane wave fields are described by wave functions

$$e^{-i\vec{k}\cdot\vec{r}} = e^{-i(k_x x + k_y y + k_z z)}$$

incident and scattered waves must all have the same component of $\vec{k}$ tangential to the boundary. The remaining component of the wavevector is determined by a relation called *acoustic Snell's law*, which is the acoustic pendant of the well known Snell's law in electromagnetism. For isotropic solids, the acoustic Snell's law takes a very simple form that

can be compared to the electromagnetic Snell's law:

$$\boxed{\frac{\omega}{V_l}\sin\theta_l = \frac{\omega}{V_s}\sin\theta_s = \frac{\omega}{V_l{}'}\sin\theta_l{}' = \frac{\omega}{V_s{}'}\sin\theta_s{}'} \tag{A.42}$$

where θ is the angle between the normal to the boundary plane and the direction of propagation. For anisotropic solids, a simple analytical expression of Snell'law is often difficult to obtain and numerical methods have to be used.

The slowness surface give a useful representation to find directly both directions and number of reflected and refracted waves by a simple geometrical construction. Figure A.5 shows schematically that construction for two isotropic materials with different slowness surfaces. The axis on this Figure are components tangential ($k_{\parallel}/\omega$) and perpendicular ($k_{\perp}/\omega$) to the boundary plane. The plane perpendicular to the boundary plane contains an incident shear wave. This wave arrives at the interface from the solid represented below on the Figure. Conservation of the tangential component of $\vec{k}$ give rise to two reflected waves (both shear waves) in the first solid and three refracted waves (one longitudinal and two shear waves) in the second solid, which has phase velocities slower than in the first solid. All the waves are contained in the same plane perpendicular to the interface plane. Extension of this effect to anisotropic solids is direct: up to three reflected and three refracted waves might arise from boundaries and the direction of each one is geometrically deduced from the slowness surfaces or from analytical solution to the boundary value problem.

In piezoelectric solids, the problem is more difficult since two additional boundary conditions are necessary for the electrical values. These two additional conditions can be expressed with use of the quasistatic approximation:

$$\Phi = \Phi' \tag{A.43}$$

$$\vec{D}\cdot\vec{n} = \vec{D}'\cdot\vec{n} \tag{A.44}$$

Those conditions give rise to up to five reflected and five refracted waves (three acoustic waves and two electromagnetic waves). Solutions can be deduced geometrically by adding electromagnetic slowness curves to the acoustic slowness curves.

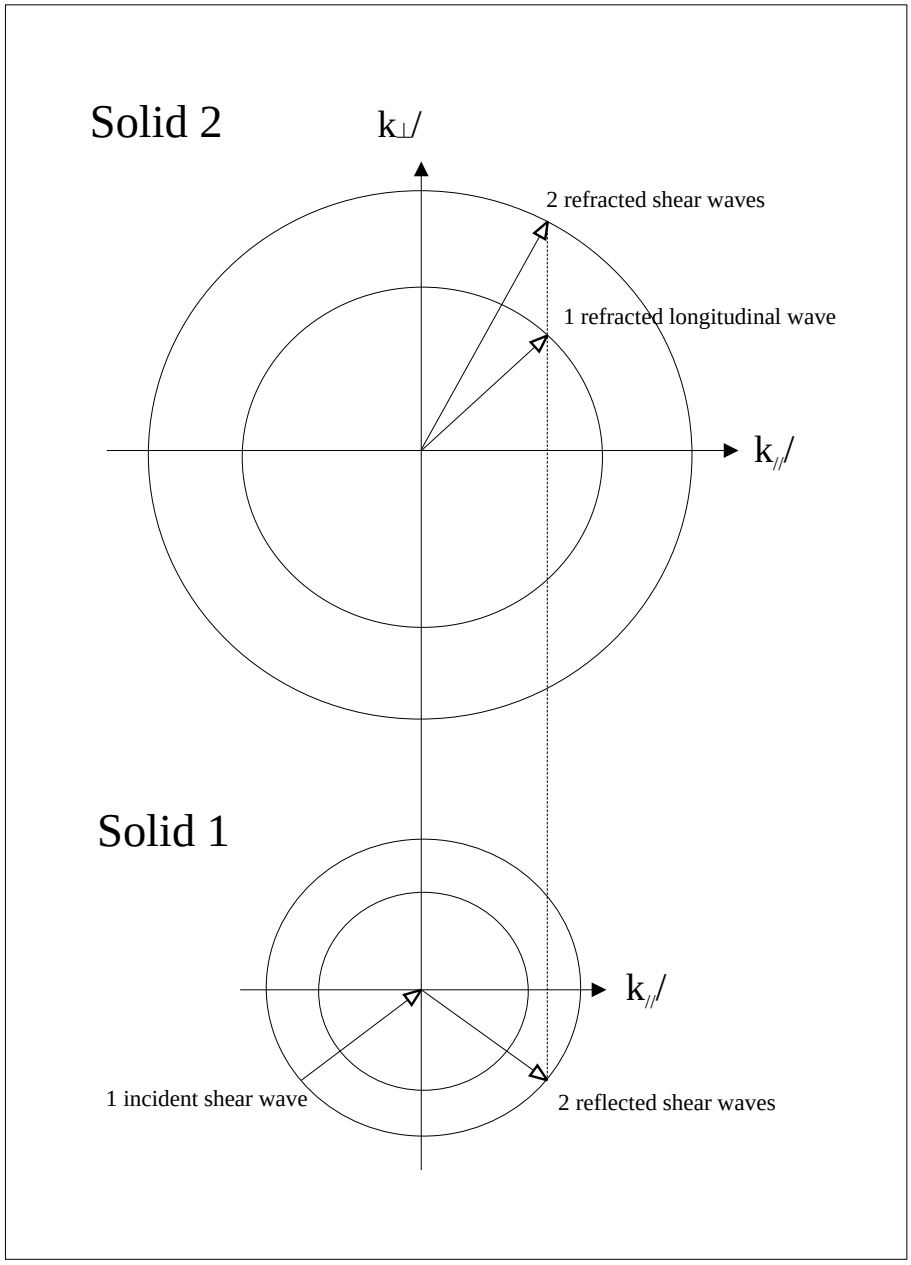


Fig. A.5 – Reflections and refractions at boundary between two isotropic solids.

A.3.2 Critical angle

The geometrical constructions in Figure A.5 do not always give real intersections with the slowness surface for all of the scattered waves. Physical significance is deduced from the dispersion relation for transmitted wave for isotropic solids:

$$k_{\parallel}{}'^2 + k_{\perp}{}'^2 = \left(\frac{\omega}{V'}\right)^2 \tag{A.45}$$

In this equation, the tangential component $k_{\parallel}$ is greater than (ω/V') leading to a pure imaginary perpendicular component $k_{\perp}$:

$$k_{\perp} = \pm i \left({k_{\parallel}}^2 - \left(\frac{\omega}{V'}\right)^2 \right)^{1/2}, \tag{A.46}$$

the sign is chosen to satisfy the physical requirement of getting a signal that reduces to zero as distance trends to infinite. From this consideration, one can see that the wave is totally reflected; the refracted wave is *evanescent*. For isotropic solids and from Snell's law (A.42), total reflection occurs for incidence angles greater than a *critical angle* defined by:

$$\boxed{\theta_{\text{critical}} = \arcsin\left(\frac{V}{V'}\right)} \tag{A.47}$$

A.3.3 Acoustic impedances

Previous sections have shown a relation between stress fields $\mathbf{T}$ and particle displacement fields $\vec{u}$, or equivalently between stress fields and particle velocities [2] $\vec{v} = \frac{\partial \vec{u}}{\partial t}$. For a given direction of propagation, each plane wave solution has three stress components and three velocity components. If we consider, for a direction $k\vec{l} = \vec{k}$, the following definition

$$(\mathbf{T}_k)_i = T_{ik}$$

with $i = x, y, z$, the relation between the two fields is given by:

$$-T_{ik} = (Z_a^k)_{ij} v_j \tag{A.48}$$

and the 3 by 3 matrix (Z_a^k) is called the *acoustic impedance matrix*. Acoustic impedance coefficients have dimension $[\mathrm{kg} \cdot \mathrm{m}^{-2} \cdot \mathrm{s}^{-1}]$ that is called *Rayleigh* (Rayl.) in acoustic. As values of acoustic impedances

[2] the factor ω has to be introduced in the relations

are usually large, the use of MRayl. $= 10^6 \cdot$ Rayl. is relatively spread.

For a given direction, there are three different acoustic impedance matrices, corresponding to one (quasi)longitudinal and two (quasi)shear waves. Elements of matrix (A.48) are found from the acoustic field equations. Explicit calculation of this matrix is given here after. For further resolution of scattering at boundaries, the relation (A.48) is generalized to measurement of acoustic impedance in direction $\vec{n} = [n_x \; n_y \; n_z]$ for plane wave propagating in direction $\vec{k}$:

$$-T_{in} = \frac{n_{iK} c_{KL} k_{Lj}}{\omega} \; v_j \tag{A.49}$$

where

$$n_{iK} = \begin{bmatrix} n_x & 0 & 0 & 0 & n_z & n_y \\ 0 & n_y & 0 & n_z & 0 & n_x \\ 0 & 0 & n_z & n_y & n_x & 0 \end{bmatrix} \tag{A.50}$$

and $k_{Lj} = k l_{Lj}$ is defined by (A.10). Elements of the acoustic matrix for that direction are:

$$\boxed{(Z_a^k)_{ij} = \frac{n_{iK} c_{KL} k_{Lj}}{\omega}} \tag{A.51}$$

and one can see that impedance matrix elements can be obtained by a slight modification of the Christoffel matrix in (A.9).

A.4 Energy considerations

A.4.1 Acoustic Poynting's Theorem

Wave propagation requires for a complete description the formulation of an energy conservation relation. In electromagnetism, this relation is derived from Maxwell's equations and is known as *Poynting's Theorem*. For acoustic fields, using the strong analogy with electromagnetic fields results in a similar relation. The scalar product of the translational equation of motion (A.3) with $-\vec{v}$ is taken and added to the double scalar product of (A.2) (differentiated with respect to t) with $-\mathbf{T}$. The result can be expressed as:

$$-\nabla \cdot (\vec{v} \cdot \mathbf{T}) = -\rho \vec{v} \cdot \frac{\partial \vec{v}}{\partial t} - \mathbf{T} : \frac{\partial \mathbf{S}}{\partial t} + \vec{v} \cdot \vec{F} \tag{A.52}$$

and then integration is carried out over a volume V and the divergence theorem is used to introduce an integral over the bounding surface S:

$$\oint_S (-\vec{v}\cdot\mathbf{T})\cdot\vec{n}\, dS = -\int_V \rho\vec{v}\cdot\frac{\partial\vec{v}}{\partial t}\, dV - \int_V \mathbf{T} : \frac{\partial\mathbf{S}}{\partial t}\, dV + \int_V \vec{v}\cdot\vec{F}\, dV. \quad \text{(A.53)}$$

We assume first that surface S is stress-free so that the surface integral in (A.53) goes to zero. Only volume integration terms remain, in which the term $\int_V \vec{v}\cdot\vec{F}\, dV = P_s$ is the power supplied to the volume V by the sources. For a system without loss, the expression

$$\int_V \rho\vec{v}\cdot\frac{\partial\vec{v}}{\partial t}\, dV + \int_V \mathbf{T} : \frac{\partial\mathbf{S}}{\partial t}\, dV \quad \text{(A.54)}$$

is the rate of change of of stored energy in the system, $\partial U/\partial t$. The first term in (A.54) can be identified as the rate of change of *kinetic energy density*,

$$\frac{\partial u_v}{\partial t} = \rho\vec{v}\cdot\frac{\partial\vec{v}}{\partial t} = \frac{\partial}{\partial t}\left(\frac{1}{2}\rho v^2\right), \quad \text{(A.55)}$$

and the other term is the rate of change of the elastic energy stored energy density, u_s. For a viscously damped medium, the term $\int_V \left(\mathbf{T} : \frac{\partial\mathbf{S}}{\partial t}\right) dV$ contains both stored energy and power loss term. With all those considerations, the *acoustic Poynting's Theorem* can be written for the general case as

$$\boxed{\oint_S(-\vec{v}\cdot\mathbf{T})\cdot\vec{n}\, dS + \tfrac{\partial U}{\partial t} + P_d = P_s} \quad \text{(A.56)}$$

where

$$U = \int_V (u_v + u_s)\, dV \quad \text{(A.57)}$$

is the total kinetic and elastic stored energy in V. The surface integral is the total power flow outward through closed surface S. The integrand

$$\vec{P}\cdot\vec{n} = -\vec{v}\cdot\mathbf{T}\cdot\vec{n}$$

is the power flow density in the direction $\vec{n}$ and we can thereby define an *acoustic Poynting vector*

$$\boxed{\vec{P} = -\vec{v}\cdot\mathbf{T}} \quad \text{(A.58)}$$

that has dimension $[\mathrm{W}\cdot\mathrm{m}^{-2}]$.

A.4.2 Complex acoustic Poynting's Theorem

Poynting's Theorem (A.56) relates to instantaneous power flow and energy storage. For time-harmonic fields, Poynting's Theorem is found to be

$$\oint_S \frac{(-\vec{v}^* \cdot \mathbf{T})}{2} \cdot \vec{n}\ dS = i\omega \int_V \left(\frac{\mathbf{T} : \mathbf{S}^*}{2} - \rho \frac{|\ v\ |^2}{2} \right)\ dV + \int_V \frac{\mathbf{v}^* \cdot \vec{F}}{2}\ dV \tag{A.59}$$

In this equation, we can replace terms by definitions for commodity. The complex power supplied by the source:

$$\int_V \frac{\mathbf{v}^* \cdot \vec{F}}{2}\ dV = P_s \tag{A.60}$$

and the peak kinetic stored energy in the system:

$$\int_V \rho \frac{|\ v\ |^2}{2}\ dV = (U_v)_{peak}. \tag{A.61}$$

The peak strain energy $(U_s)_{peak}$ and the time average power loss due to viscous damping $(P_d)_{AV}$ can be defined by:

$$i\omega \int_V \frac{\mathbf{T} : \mathbf{S}^*}{2}\ dV = i\omega \int_V \left(\frac{\mathbf{S} : \mathbf{c} : \mathbf{S}^*}{2} + i\omega \frac{\mathbf{S} : \eta : \mathbf{S}^*}{2} \right)\ dV \tag{A.62}$$

$$= i\omega (U_s)_{peak} - (P_d)_{AV}. \tag{A.63}$$

Finally, the *complex acoustic Poynting's Theorem* is

$$\boxed{\oint_S \frac{(-\vec{v}^* \cdot \mathbf{T})}{2} \cdot \vec{n}\ dS - i\omega \{(U_s)_{peak} - (U_v)_{peak}\} + (P_d)_{AV} = P_s} \tag{A.64}$$

and the *complex acoustic Poynting vector* is defined as

$$\boxed{\vec{P} = \frac{-\vec{v}^* \cdot \mathbf{T}}{2}} \tag{A.65}$$

A.4.3 Energy transport of plane waves

For the specific case of time-harmonic plane waves, the expression of Poynting's Theorem takes a simpler form. The relation of dispersion for those waves implies interchange between kinetic and potential density of energy; equivalent peaks are exactly balanced and the relation (A.64) reduces to a simpler power balance:

$$\oint_S \frac{(-\vec{v}^* \cdot \mathbf{T})}{2} \cdot \vec{n}\ dS + (P_d)_{AV} = P_s \tag{A.66}$$

and when there is no attenuation, the complex acoustic Poynting vector is a real number that represents the average power flow density $\vec{P}_{AV}$. From this latter condition, the equation that can be obtained is rather interesting:

$$\boxed{\oint_S \vec{P}_{AV} \cdot \vec{n}\ dS = P_s} \tag{A.67}$$

If the *energy velocity* is the vector defined by the ratio of the average power flow to the peak (kinetic or potential) energy

$$\vec{V}_e = \frac{\vec{P}_{AV} \cdot \vec{n}}{U_{AV}},$$

and an other relation that can be derived is

$$\vec{k} \cdot \vec{V}_e = V. \tag{A.68}$$

Usually, the energy velocity is equal to the group velocity defined by

$$V_g = \frac{\partial \omega}{\partial k}.$$

The energy velocity direction, or the group velocity direction, is the normal to slowness surface at the point given by the intersection between the wavevector and the slowness surface. With that point of view, pure modes are the directions where energy velocity direction is aligned with direction of propagation. When the medium is dispersive, the phase velocity and the group velocity are different. The relation between them can be deduced by differentiating the phase velocity with regard to wavenumber:

$$\boxed{V_g = V + k \cdot \frac{dV}{dk}} \tag{A.69}$$

This relation gives the influence of the dispersion on the group velocity. Figure A.6 gives the representation of the phase and the group velocity as a function of the dispersion relation. For a given wavenumber, the phase velocity is the slope between the origin (wavenumber null) and the considered point; the group velocity is the slope of the line tangent at the considered point.

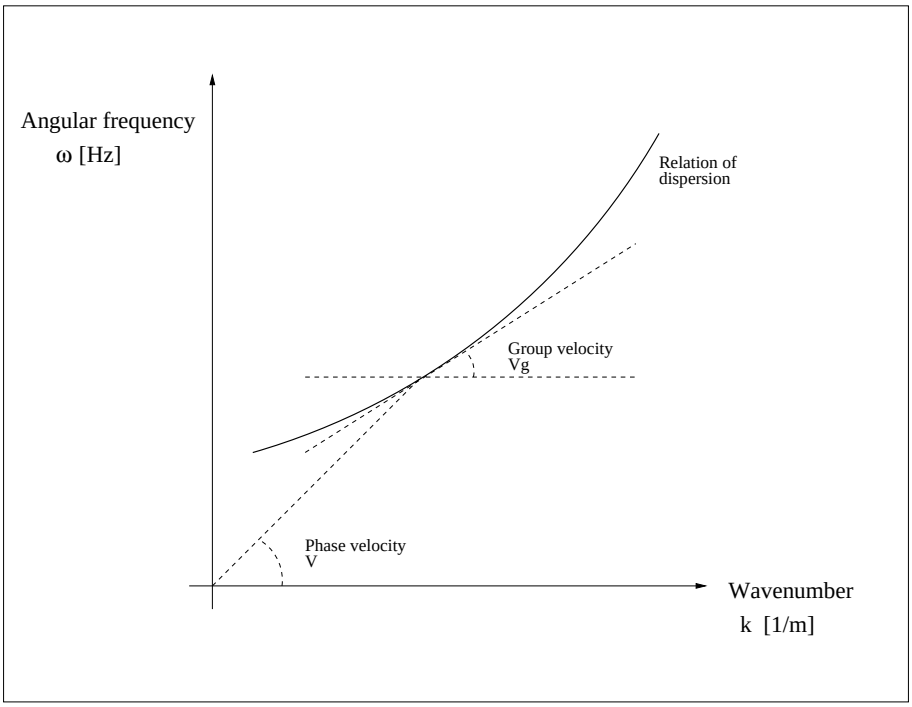


Fig. A.6 – Relation of dispersion: phase velocity V and group velocity V_g are represented

Appendix B

Electrical model of the SAW device

Surface acoustic wave devices and interdigital transducers have been described abundantly in the literature [29, 161]. We use the electrical model to evaluate the effect a liquid loading on the electrical instrumentation of the device. The ideal transducer is modeled by a radiation conductance $G_a(f)$ that is function of the frequency f connected in parallel with a static capacitance C_T. The electrical admittance of the transducer is written as

$$Y_{IDT}(f) = G_a(f) + j2\pi f C_T \tag{B.1}$$

and an expression for C_T is NWC_0, where N is the number of finger pairs with an acoustic aperture W corresponding to the overlap length of the fingers and C_0 the capacitance per finger pair and per unit length. The *synchronous frequency* f_0 is the ratio between the acoustic velocity V and the finger pairs periodicity λ (i.e. $f_0 = V/\lambda$). For frequencies near the synchronous frequency, the radiation conductance is approximated by

$$G_a(f) \simeq 8K^2 f_0 N^2 W C_0 \left(\frac{\sin x}{x}\right)^2, \tag{B.2}$$

where $x = N\pi(f - f_0)/f_0$ and K^2 is the electromechanical coupling constant of the piezoelectric substrate. The transfer function $H(f)$ of a lossless SAW delay line relates the output (or load) voltage V_L to the source voltage V_S and is given by

$$H(f) = \frac{V_L}{V_S} = \frac{Y_{DL}R}{(1 + Y_{IDT}R)^2 - (Y_{DL}R)^2} \tag{B.3}$$

where R is the source and load impedances supposed identical and equal to 50 Ohms, and Y_{DL} is a transfer admittance given by

$$Y_{DL} = G_a(f) \exp\left\{j\left(\pi - 2x - 2\pi f L/V\right)\right\}.$$

The electrical model of the SAW device allows us to evaluate the effect of water loading on the transducers. In a rough estimation, the capacitance per finger pair and per unit length is given by $C_0 = (\varepsilon_{rS} + \varepsilon_{rL}) \times \varepsilon_0$, where ε_0 is the dielectric constant of vacuum (8.854 pF/m), ε_r is the relative permittivity and the subscripts S and L refer to the substrate and the loading, respectively. We compare the effect of water loading ($\varepsilon_r = 80$) of the transducers for two classical substrates with low and high K^2: quartz and lithium niobate (LNO). The maximum amplitude of the transfer function, that is $20 \log \|H(f)\|$, is simulated as a function of the value of C_0. The parameters of the simulation are given in Table B.1 and with $W = 3.2$ mm, $L = 9$ mm and $\lambda = 40$ μm.

	Quartz	LNO
K^2	0.0011	0.046
f_0	126.5 MHz	87.2 MHz
V	5060 m/s	3488 m/s
N	100	40

Table B.1 – Simulation parameters

Figure B.1 displays the net change of the amplitude with air and with water above the electrodes of the transducers. The attenuation is more pronounced on the quartz with a loss about 12 dB, while for LNO the loss is lower with a value of 6.9 dB. This difference is mainly due to the high value of both the dielectric constant and the electromechanical coupling constant of LNO.

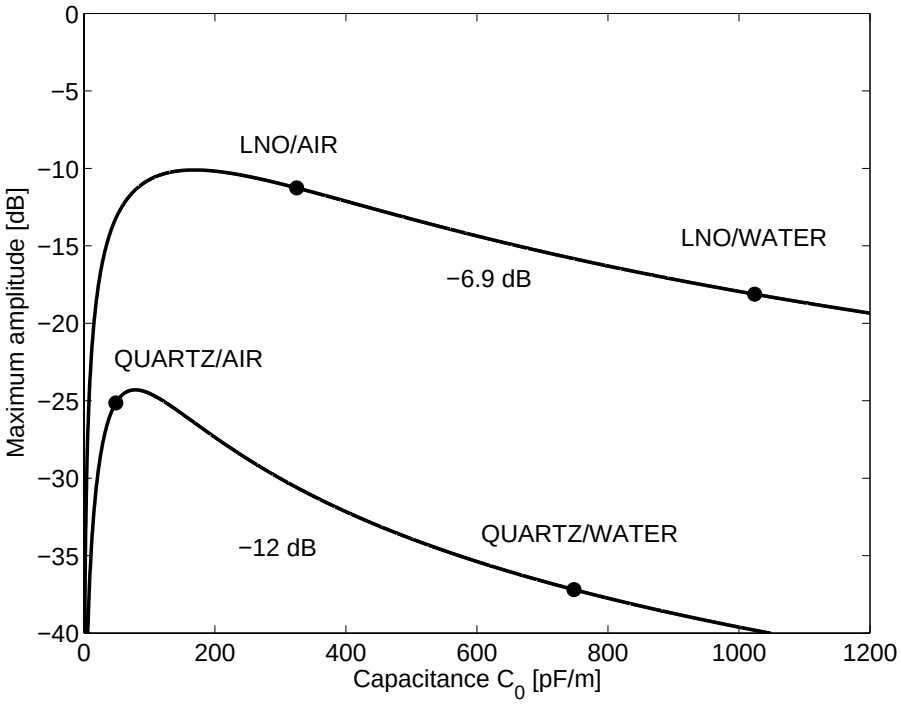


Fig. B.1 – Theoretical evolution of the maximum electrical amplitude of the SAW device as a function of the capacitance per finger pair and per unit length (C_0) for lithium niobate (LNO, upper curve) and quartz (lower curve). The dots are the values corresponding to air and water above the finger electrodes.

Appendix C

List of scientific communications

C.1 Peer-reviewed publications

P. Ekkels, R. Puers, **L. A. Francis**, and H. A. C. Tilmans. "Realisation of planar platinum bridges for high temperature", submitted to *J. Micromech. Microeng.*, December 6^{th}, 2005.

L. A. Francis, J.-M. Friedt, C. Zhou and P. Bertrand. "In situ evaluation of density, viscosity and thickness of adsorbed soft layers by combined surface acoustic wave and surface plasmon resonance", submitted to *Anal. Chem*, July 11^{th}, 2005.

L. A. Francis, A. Kromka, D. Steinmüller-Nethl, P. Bertrand, and C. Van Hoof. "Non-destructive dynamic characterization of nanocrystalline diamond membranes for flexural plate wave sensors", *IEEE Sensors Journal*, in print.

L. A. Francis, J.-M. Friedt, and P. Bertrand. "Influence of electromagnetic interferences on the mass sensitivity of Love mode surface acoustic wave sensors", *Sensors and Actuators A* **123–124**, 2005, pp. 360–369.

L. Huang, G. Reekmans, D. Saerens, J.-M. Friedt, F. Frederix, **L. Francis**, S. Muyldermans, A. Campitelli, and C. Van Hoof. "Prostate-specific antigen immunosensing based on mixed self-assembled mono-

layers, camel antibodies and colloidal gold enhanced sandwich assays", *Biosensors and Bioelectronics* **21**, 2005, pp. 483–490.

C. Zhou, J.-M. Friedt, A. Angelova, K.-H. Choi, W. Laureyn, F. Frederix, **L. A. Francis**, A. Campitelli, Y. Engelborghs, and G. Borghs. "Human Immunoglobulin Adsorption Investigated by Means of Quartz Crystal Microbalance Dissipation, Atomic Force Microscopy, Surface Acoustic Wave, and Surface Plasmon Resonance Techniques", *Langmuir* **20** (14), 2004, pp. 5870–5878.

J.-M. Friedt, **L. Francis**, G. Reeckmans, R. De Palma, A. Campitelli, and U. B. Sleytr. "Simultaneous surface acoustic wave and surface plasmon resonance measurements: electrodeposition and biological interactions monitoring", *J. Appl. Phys.*, 95(4) (2004), pp. 1677–1680.

J.-M. Friedt, **L. Francis**, K.-H. Choi, F. Frederix and A. Campitelli. "Combined atomic force microscope and acoustic wave devices: application to electrodeposition", *J. Vac. Sci. Technol. A* 21(4) (2003) pp. 1500–1505. This article was selected by the Virtual Journal of Nanoscale Science & Technology 8(2) (2003).

J.-M. Friedt, K.-H. Choi, **L. Francis** and A. Campitelli. "Simultaneous atomic force microscope and quartz crystal microbalance measurements: interactions and displacement field of a quartz crystal microbalance", *Jpn. J. Appl. Phys.* Vol. 41 (2002) pp. 3974–3977.

C.2 Patent

J.-M. Friedt, A. Campitelli, and **L. Francis**. "Apparatus and methods for simultaneous surface acoustic wave and surface plasmon resonance measurements", patent no. WO2004113882.

C.3 Conferences

L. A. Francis, W. Pan, C. Geuens, A. Kromka, H.A.C. Tilmans, D. Steinmueller-Nethl, and C. Van Hoof. "Theoretical investigation of nanocrystalline diamond thin film bulk acoustic resonators (FBAR) for

mass sensing applications." *16th Workshop on Micromachining, Micromechanics and Microsystems (MicroMechanics Europe 2005)*, Göteborg, Sweden (September 4-6, 2005), oral and poster presentation and proceedings (4 pages).

J.-M. Friedt, **L. A. Francis**, and S. Ballandras. "Thickness and viscosity of organic thin films probed by combined surface acoustic Love wave and surface plasmon resonance." *IEEE International Ultrasonics Symposium 2005*, Rotterdam, The Netherlands (September 18-21, 2005), oral presentation and proceedings (4 pages).

L. A. Francis, A. Kromka, D. Steinmüller-Nethl, P. Bertrand, and C. Van Hoof. "Rapid investigation of nanocrystalline diamond vibrating membranes with a stroboscopic interferometer." in *Proc. of the IEEE Sensors Conference*, 2004, pp. 146–149.
IEEE Sensors 2004, Vienna, Austria (October 24-27, 2004), poster presentation and proceedings (4 pages).

L. A. Francis, J.-M. Friedt, R. De Palma, P. Bertrand, and A. Campitelli. "Influence of electromagnetic interferences on the mass sensitivity of Love mode surface acoustic wave sensors." *Eurosensors XVIII*, Roma, Italy (September 13-15, 2004), poster presentation and proceedings (2 pages).

L. A. Francis, J.-M. Friedt, R. De Palma, C. Zhou, C. Bartic, P. Bertrand, A. Campitelli. "Techniques to evaluate the mass sensitivity of Love mode surface acoustic wave biosensors", in *Proc. of the IEEE International Ultrasonics, Ferroelectrics, and Frequency Control. 50th Anniversary Joint Conference*, 2004, pp. 241–249.
IEEE International Frequency Control Symposium Montreal, Canada (August 24-27, 2004), oral presentation, poster presentation (**Best Student Poster Award – section Sensors and Transducers**) and proceedings (9 pages).

L. Francis, J.-M. Friedt, C. Bartic, P. Bertrand, A. Campitelli. "A novel biosensor platform integrating Love mode acoustic wave and surface plasmon resonance for the investigation of protein layers", *Biosensors 2004*, Grenada, Spain (May 24-26, 2004), oral presentation.

L. A. Francis, J.-M. Friedt, C. Bartic, A. Campitelli. "An SU8 liquid cell for surface acoustic waves biosensors", *Proc. of SPIE*, vol. 5455 (MEMS, MOEMS and Micromachining), 2004, pp. 353–363.
SPIE Photonics Europe Conference, section MEMS, MOEMS and Micromachining, Strasbourg, France (April 25-29, 2004), poster presentation and proceedings (11 pages).

G. Reekmans, L. Huang, F. Frederix, J.-M. Friedt, **L. Francis**, R. De Palma, D. Rooyackers, R. Wirix-Speetjens, W. Laureyn, D. Saerens, C. Bartic, K. Bonroy, J. Suls, C. Zhou, S. Muyldermans, U.B. Sleytr, A. Campitelli. "Assay development for Prostate Specific Antigen detection", *Synthetic Receptors 2003*, Lisbon, Portugal (October 15-17, 2003), poster presentation.

A. Campitelli, C. Bartic, J.-M. Friedt, K. De Keersmacker, W. Laureyn, **L. Francis**, F. Frederix, G. Reeckmans, A. Angelova, J. Suls, K. Bonroy, R. De Palma, Z. Cheng, and G. Borghs. "Development of microelectronics based biosensors", in *Proc. IEEE 2003 Custom Integrated Circuits Conference*, 2003, pp. 505–512.
IEEE Custom Integrated Circuits Conference, San Jose, California (September 21-24, 2003), invited paper.

R. De Palma, J.-M. Friedt, **L. Francis**, W. Laureyn, A. Campitelli, U.B. Sleytr, G. Maes. "Calibration of the mass Sensitivity of Love-mode surface acoustic wave sensors for probing biological interactions", *Euresco 2003: Biological Surfaces and Interfaces: Euroconference on Understanding and Improving Specific Interactions*, Castelvecchio Pascoli, Italy (June 21-26, 2003), poster presentation.

J.-M. Friedt, **L. Francis**, K.-H. Choi, A. Campitelli. "The metrology of biosensors: a multiparameters approach to characterizing protein layers", *Nanoscience Workshop*, Egmond aan Zee, The Nederlands, (June 1-3, 2003), poster presentation.

R. De Palma, **L. Francis**, J.-M. Friedt, W. Laureyn, A. Campitelli, U.B. Sleytr, G. Maes. "Mass sensitivity calibration of Love mode surface acoustic wave sensors for immunosensing", *Nanoscience Workshop*, Egmond aan Zee, The Nederlands, (June 1-3, 2003), poster presentation.

J.-M. Friedt, **L. Francis**, K.-H. Choi, A. Campitelli. "Combined atomic force microscope and acoustic wave devices: application to electrodeposition", *49^{th} AVS meeting*, Denver, Colorado, USA (November 4-8, 2002), oral presentation.

J.-M. Friedt, K.-H. Choi, **L. Francis**, F. Frederix, A. Campitelli. "Simultaneous AFM and QCM measurements of biological and electrochemical processes", *QCM2002*, Brighton, United Kingdoms (July 24-25, 2002), poster presentation.

J.-M. Friedt, K.-H. Choi, F. Frederix, **L. Francis**, A. Campitelli, G. Borghs. "Simultaneous AFM and QCM measurements: application to the adsorption of proteins on metallic surfaces". *IV^{th} Annual Linz Winter Workshop*, Linz, Austria (February 1-4, 2002), poster presentation.